UNIVERSITÀ DEGLI STUDI DI TRIESTE

DOCTORAL THESIS

Particle Identification with the Cherenkov imaging technique using MPGD based Photon Detectors for Physics at COMPASS Experiment at CERN

Author:
Shuddha Shankar DASGUPTA

Supervisor:
Dr. Fulvio TESSAROTTO

A thesis submitted in fulfillment of the requirements for the degree of Doctor of Philosophy

Università degli Studi di Trieste, Dipartimento di Fisica

March 6, 2017

Declaration of Authorship

I, Shuddha Shankar DASGUPTA, declare that this thesis titled, "Particle Identification with the Cherenkov imaging technique using MPGD based Photon Detectors for Physics at COMPASS Experiment at CERN" and the work presented in it are my own. I confirm that:

- This work was done wholly or mainly while in candidature for a research degree at this University.
- Where any part of this thesis has previously been submitted for a degree or any other qualification at this University or any other institution, this has been clearly stated.
- Where I have consulted the published work of others, this is always clearly attributed.
- Where I have quoted from the work of others, the source is always given. With the exception of such quotations, this thesis is entirely my own work.
- I have acknowledged all main sources of help.
- Where the thesis is based on work done by myself jointly with others, I have made clear exactly what was done by others and what I have contributed myself.

Signed: Shuddha Shankar Dasgupta

Date: 12/01/2017

UNIVERSITÀ DEGLI STUDI DI TRIESTE

Abstract

Università degli Studi di Trieste, Dipartimento di Fisica

Doctor of Philosophy

Particle Identification with the Cherenkov imaging technique using MPGD based Photon Detectors for Physics at COMPASS Experiment at CERN

by Shuddha Shankar DASGUPTA

A novel technology for the detection of single photons has been developed and implemented in 2016 in the Ring Imaging Cherenkov (RICH) detector of the COMPASS Experiment at CERN SPS. Some basic knowledge in the field of particle identification and RICH counters, Micro Pattern Gaseous Detectors (MPGDs) in general and their development for photon detection applications are provided. The characteristics of the COMPASS setup are summarized and the COMPAS RICH-1 detector is described and shown to provide hadron identification in the momentum range between 3 and 55 GeV/c. The THGEM technology is discussed illustrating their characterization as gas multipliers and as reflective photocathodes: large gains and efficient photodetection collections are achieved when using optimized parameters and conditions (hole diameter = THGEM thickness = 0.4 mm; hole pitch = 0.8 mm and no rim; CH4-rich gas mixtures and electric field values > 1 kV/cm at the CsI surface). The intense R&D program leading to the choice of a hybrid THGEM + Micromegas architecture for the novel detectors is summarized: prototypes construction and test results are presented. The beam test performed at CERN with two 300 mm $\times$ 300 mm active area hybrid prototypes validated this new technology and allowed to demonstrate efficient detection of Cherenkov photons. The optimal design of the detector, consisting in two layers of THGEMs, the first of which is coated with 300 mm thick layer of CsI, couple with a Micromegas on a pad segmented anode with an original design of capacitive – resistive readout is presented. All aspects of the construction, test and assembling from the raw material selection to the procedures applied for the quality assessment are described in detail. The challenges encountered during the detectors assembly, the test in the laboratory and the transportation of the chambers to CERN for the assembly and mounting are then illustrated. The production of the photocathode and the final assembly of the four hybrid detectors, covering an active area of 1.4 m^2 are presented. The adventurous installation of the combined Hybrid PDs and Multi Anode Photo Multiplier Tubes with fused silica lenses onto COMPASS RICH-1 and the work for equipping the new detectors with all needed services are presented. The description of the HV control system and of the other services is illustrated and the APV25-based frontend electronics is described together with the studies performed to understand the electronic and physical noises of the new chambers. A preliminary on-line analysis of the detector response and of the performance are presented: an indication that the average number of photons is larger than the neighboring traditional MWPC-based PDs is obtained. The success of the first MPGD-based large area photon detector operating in a physics experiment opens new perspectives in the field of single photon detection.

Acknowledgements

My grateful thanks to Fulvio Tessarotto and to Silvia DallaTorre for giving me this unique opportunity to work in a very advanced laboratory with state of the art equipments and for their guidance and support during these five years. Without there kindest help it would not be possible to write this thesis: they helped by taking out their precious time from their very busy schedule and gave precious advises and corrections for this thesis. A special thanks to my supervisor Fulvio Tessarotto and to my father who helped me and inspired me to keep my tenacity and helped to continue until this point. I will also like to thank with my heart, Stefano Levorato, who is much more than a colleague: he is a friend, an elder brother, a philosopher and a guide to me.

I will like to show my gratefulness to Renato Birsa, Piero Ciliberti and to Benigno Gobbo for helping me during these years with their maximum efforts.

I want to specially thank Franco Bradamante, Anna Martin, Andrea Bressan, Giulio Sbrizzai and others of the Trieste COMPASS team for their dearest support and teaching.

A large fraction of the work presented in this thesis could not be realized without the dearest help of my friends and colleagues, technicians of INFN Trieste. I will like to thank deeply Giorgio Menon, Mauro Gregori, Livio Rinaldi, Claudio Azzan and their colleagues, who helped me with their professional expertise and made me being more knowledgeable about many technical issues.

I want to express my gratitude towards the whole Istituto Nazionale di Fisica Nucleare, Sezione di Trieste for the opportunities and support in all aspects of my work.

I would like to thank my friends and colleagues of INFN Trieste lab: Carlos Santos, Fabio Pireira, Gergo Hamar and others.

I would like to specially acknowledge my very good friends Michela Chiosso and Maxim Alexeev and our other colleagues from INFN Torino, for their support and help during the whole period of my stay in Italy and at CERN.

I would like to thank Matrivani Institute of Experimental Reasearch & Education, Kolkata and colleagues there, as without their support and motivation, it would not be possible to have this horizon neither the chance.

I would like to thank all colleagues from the COMPASS experiment at CERN and my friends Joseph Novy, Martin Bodlak, Michael Pesek, Marketa Peskerova, Didier Cotte for their support during my Ph.D. period.

My dearest greetings for our Aveiro colleagues who were always helpful. Special thanks to Dr. J.F.C.A. Veloso for his recommendation and support during this year. Thanks to Dr. carlos Azevedo for being a supportive friend.

This acknowledgment cannot be completed without giving thanks to my parents and family. Thank you “BABA”, “Ma”, “Mamma”, “Va”, “Didi” and “Aich Da” for their supports and help during all these years.

I will also like to thank my very good friends from India and from Italy: Suvro, both of the Sudip, Samik, Kaustav, and Vito, Giulia, Roberto, Elisa, Francesco, Monika, Siewei, Mariano, Alessio, Miko and other friends for their help and support for these years.

Contents

List of Figures

List of Tables

To my beloved "Putu" and "Pute"

Chapter 1

Introduction

This thesis reports on the work performed within the Trieste COMPASS RICH group in the period between April, 2012 and Oct, 2016, in the INFN Trieste THGEM laboratory and at CERN. A large part of this work was dedicated to the R&D activity aiming at the development of a novel Micro Pattern Gaseous Detector (MPGD) based Photon Detector (PD), to be used for the upgrade of COMPASS RICH-1. The final detector architecture, result of the long R&D, is based on a hybrid technology, combining THick Gas Electron Multipliers (THGEMs) and MicroMegas (MM). The second part of the work consisted in building and commissioning the new large PDs on COMPASS RICH-1.

My work for the R&D was dedicated to build and test several different prototypes, in the INFN Trieste Laboratory or at CERN Test Beam facilities. New tools (e.g. custom built wireless picoamperometers) and concepts (e.g. a special capacitive/resistive anode for reading the MM signals) were developed with my help during this activity. Dedicated studies of spark rate and gain response uniformity and stability were performed for the optimization of the final hybrid PD design.

The work to build and commission the new PDs was very complex. Building activities were distributed between Industries, Workshops and Laboratories. The part in which I contributed significantly is also discussed in this thesis. The commissioning of these new PDs has been done at CERN. Studies of the APV-25 based readout electronics response and of the COMPASS on-line analysis software were needed to perform the work. I also installed this software in the Trieste computing farm, for a more convenient analysis of the on-line data. Brief descriptions of this analysis and its first results are also presented.

The structure of this thesis is the following: Chapter-1 presents a short overview of the Particle Identification Techniques (PID), Cherenkov imaging counters (RICH), MPGDs in general and gaseous PDs in particular. In chapters 2 and 3 a description of the COMPASS Experiment at CERN and of the COMPASS RICH-1 before the upgrade are presented. The following chapters describe the original work of building, mounting and commissioning of the newly developed hybrid detectors in COMPASS RICH-1. In Chapters 4 and 5 the information about the R&D performed for THGEMs and Micromegas in these last years is summarized. In Chapter-5 the test of the newly made hybrid prototype at the T10 beam line at CERN is presented. The studies related to the final THGEMs and Micromegas characterization are described in Chapter-6. The whole story of building and assembling the final hybrid detectors and mounting them on COMPASS RICH-1 is presented in Chapter-7. Chapter-8 is showing the first results from this new upgrade. The activity is partially supported

by the H2020 project AIDA2020 GA no. 654168. My activity was also part of the scientific program of the RD51 Collaboration. Part of the laboratory studies described in Chapters 4 to 6 were performed in a largely autonomous way while my contributions to beam tests described in Chapter-5 and my work during the commissioning phase, illustrated in Chapter-7, were performed in strict collaboration with my colleagues. The first results, extracted by online analysis of raw data are presented in Chapter-8.

1.1 Particle Identification

Particle Identification (PID) is an essential tool for experimental investigation of fundamental physics. A particle or an ion can be experimentally identified by one of the following techniques:

- via the kinematic reconstruction of the particle decay: this method can be applied when the particle lifetime is short enough, so that the decay products are detected within the experimental setup;
- via the specific interaction mode with matter; for instance, a high energy muon can be identified via its penetration in matter, an intermediate energy muon via its travel range, low energy protons again from their travel range, high-energy electromagnetic particles (electrons, gamma rays) via the development of their shower in calorimeters; high energy electrons from the response of a transition radiation detector;
- by determining the particle mass from the equation

$$E^2 \quad = \quad (m \cdot c^2)^2 + (p \cdot c)^2 \tag{1.1}$$

  For this purpose, two kinematical quantities of the particles have to be measured: the momentum and the velocity or the energy and the velocity or the momentum and the value of γ=E/m or the energy and the momentum. The momentum is always obtained measuring the trajectory bending in magnetic field, the energy from the particle range or the energy deposited in a calorimeter; the velocity can be obtained from Time Of Flight (TOF) measurements, or from repeated measurements of the specific particle ionization or from the velocity-dependent Cherenkov effect. The choice of the most convenient approach depends on the particle species to be determined and on the energy range of these particles. The Cherenkov imaging technique discussed in the next sections is the most effective approach to identify hadron species in a wide momentum range and wide angular region.

The following equation is obtained by differentiating eq.1.1:

$$(\frac{dp}{p})^2 = (\frac{dm}{m})^2 + (\frac{d(\beta\gamma)}{\beta\gamma})^2 = (\frac{dm}{m})^2 + (\frac{\gamma^3 db}{\beta\gamma})^2 = (\frac{dm}{m})^2 + (\frac{\gamma^2 d\beta}{\beta})^2 \tag{1.2}$$

where γ is the Lorentz factor and β is the ratio of the particle velocity to the velocity of light c. The large value of γ for relativistic particles clearly indicate that, when the momentum and the velocity of a particle are measured in order to identify a relativistic particle, the resolution of the velocity measurement is the crucial parameter.

1.1.1 The Cherenkov effect

The basic elements of the Cherenkov effect are recalled in this section.

The effect is due to the undulatory nature of the electromagnetism and it is a typical shock-wave effect, which is present when a charged particle travels through a transparent medium with velocity larger than the group velocity of the light in the medium itself. Analogous phenomena are the mechanical shockwave events of the "triangular" wake of a speedboat traveling faster than the wave propagation speed on the sea surface (2-D) or the shockwave produced in air by supersonic flying objects (3-D).

The fundamental Cherenkov's equation:

$$cos(\theta_C) \quad = \quad 1/(\beta \cdot n) \tag{1.3}$$

where θ_C is the Cherenkov angle, namely the angle between the produced Cherenkov photon direction and the particle trajectory and n is the refractive index of the medium, can be obtained from the Huygen's construction shown in Fig.1.1. The threshold nature manifests itself in the requirement to have $\beta > 1/\mathrm{n}$ in order to get $cos(\theta_C) < 1$. When β approaches 1, namely for ultra-relativistic particles, θ_C reaches a maximum value $\theta_{C_{max}}$ = arccos(1/n).

The distribution of the Cherenkov photons was obtained by Frank and Tamm in 1937; here the distribution is provided through various equations useful for the applications in Cherenkov detectors. The double differential distribution of the energy W radiated per unit path length is:

$$d^2W/(dxd\omega) \quad = \quad Z^2 \cdot e^2 \cdot \omega/c^2 \cdot (1 - 1/(\beta^2 \cdot n(\omega)^2)) \tag{1.4}$$

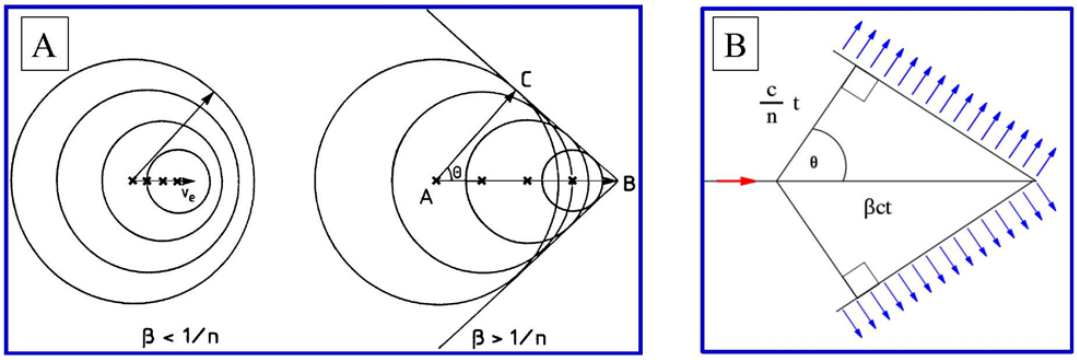

FIGURE 1.1: *(A) Huygen's construction: spherical wavelets emitted along the particle track. A coherent wavefront is formed, at a specific angle with respect to the particle track, in the case of a particle moving faster than the light in the medium. (B) Geometrical construction to obtain the Cherenkov equation.*

where x is the path length, ω is the radiation frequency, $Z \cdot e$ is the particle charge. n is a function of ω because of the medium chromatic dispersion. For a radiator of

given length L, the resulting distribution is:

$$dW/d\omega \quad = \quad L \cdot Z^2 \cdot e^2 \cot \omega / c^2 \cdot (1 - 1/(\beta^2 \cdot n(\omega)^2) \tag{1.5}$$

The number of Cherenkov photons N in a given range of the radiation energy is obtained integrating 1.5:

$$N \quad = \quad (L \cdot Z^2 \cdot \alpha / c) \cdot \int (1 - 1/(\beta^2 \cdot n(\omega)^2) \cdot d\omega \tag{1.6}$$

From equations 1.3, and 1.5 it results that N is proportional to $sin^2(\theta_C)$: N is the average value, which is affected by large fluctuations, because it follows a Poisson distribution. Therefore, a fine resolution measurement of β cannot be based on the measurement of N: a direct measurement of θ_C is needed.

In a detector, the number of detected photons N_{det} has to take into account several reduction factors: the Quantum Efficiency (QE) of the photon converter, the photo-electron detection efficiency ϵ, the radiator transparency T and the mirror reflectance R, when mirrors are present.

Fig.1.2 shows θ_C and N for three different hadrons versus γ; the values are normalized respectively to θ_{max} , namely the θ_C for β = 1, and N to N_{max}, the number of photons for β = 1; γ is normalized to its value γ_{thr} at the threshold of the Cherenkov effect; thanks to these normalizations the curves are valid for any radiator.

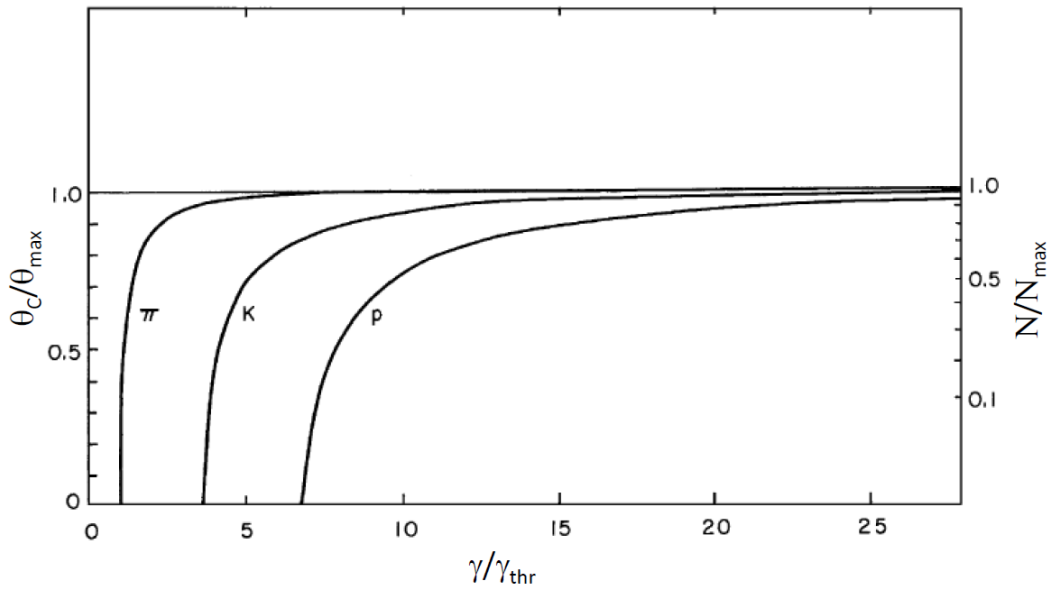

FIGURE 1.2: *θ_C and N for three different hadrons versus γ. The values are normalized respectively to θ_{max} , namely the θ_C for β = 1, and N to N_{max}, the number of photons for β = 1; γ is normalized to its value γ_{thr} at the threshold of the Cherenkov effect for pions.*

1.1.2 Radiators for Cherenkov detectors

The characteristics of the radiator material play a major role in the performance of the detector radiator. In fact, the normalizations of the variables in the plot of Fig.1.2 depend on the refractive index of the medium. For low n-values, namely n near to

1, the threshold is at high particle velocity, the maximum θ_C value is small requiring fine angular resolution to separate particle species and the number of produced photons for unit length is small, requiring long radiators. For large n-values, thresholds are at low particle velocity and, at the same time, the saturation value of θ_C is reached at moderate β-values, limiting the PID power to low momenta particles; the number of photons per unit radiation length is large and thin radiators can be used.

Another relevant feature is the chromatic dispersion of the transparent material; in fact, the dispersion represents the intrinsic resolution limit of a Cherenkov device. Fluorocarbons considered in the following are appreciated because of their low chromaticity.

The available radiators can be grouped as follows:

- $1 <$ n < 1.12; this group includes gases, cryogenic liquids as He or Ne, and silica aerogel, a manmade material formed by fused silica bubbles that can be used only for photons in the visible range;
- $1.2 <$ n < 1.35; mainly flour-carbon compounds in liquid phase are used;
- $1.35 <$ n < 1.46; transparent liquids, as water, alcohol, glycerin and hydrocarbons are considered;
- n > 1.46; this group includes transparent solid materials as crystals, glass, plastic materials and fused silica, the last one with transparency extended to the Ultra Violet (UV) region.

1.1.3 Photon Detectors

The photon detectors used so far to equip Cherenkov counters used in experiments are vacuum-based detectors or gaseous photon detectors. The former include Photo-Multiplier Tubes (PMT), Multi-Anode PMTs (MAPMT) and Hybrid Photon Detectors (HPDs), where a vacuum photo-cathode and a solid-state pixel sensor are used; a relevant voltage, applied between the photo-cathode and the pixel sensor, accelerates the photoelectrons extracted from the photo-cathode so that they can release in the sensor enough energy to make their detection possible. The photo-converters used in the vacuum-based devices convert photon in the visible or near UV range. The latter, namely the gaseous PDs, are discussed in the dedicated Section-1.3. They detect photons in the UV domain.

The use in Cherenkov counters of other photon detector types, namely Silicon PMTs (SiPMT) and Micro Channel Plate PMTs (MCP-PMT), is being studied and proposed for future applications.

1.1.4 Cherenkov Detectors

The fact that the Cherenkov angle depends on the β of the charged particle suggests that the detection of the Cherenkov photons can be used to obtain information about the particle velocity, a typical ingredient required for particle identification, as illustrated in Sec-1.1. Three approaches are possible, the second and third ones making used of the Cherenkov angle, as shortly discussed in the following.

The simplest approach is to detect the Cherenkov radiation for a charged particle, if it is produced. In this way it is possible to discriminate between particles with velocity above or below a given velocity threshold and these detectors are referred to as **threshold Cherenkov counters**. Two such detectors with different radiators and thus with different thresholds can be can be combined to increase the PID capabilities. A relevant example is provided by the couple of gigantic threshold Cherenkov counters C1 and C2 [1] (Fig.1.3) used in the experiment E-691 at Fermilab, dedicated to study the charmed particle photo- production. The radiators were different gases at atmospheric pressure: N_2, 3755 cm long in C1 and N_2 : He = 20 : 80, 6604 cm long in C2. Only a few photons per particle could be collected due to the radiator low density: typically, 2-3 photons in C1, resulting in an inefficiency ∼8% and 3-4 in C2, corresponding to an inefficiency ∼3%. Globally, the combined system made it possible effective K/π and p/K separation in the momentum range 5-35 GeV/c.

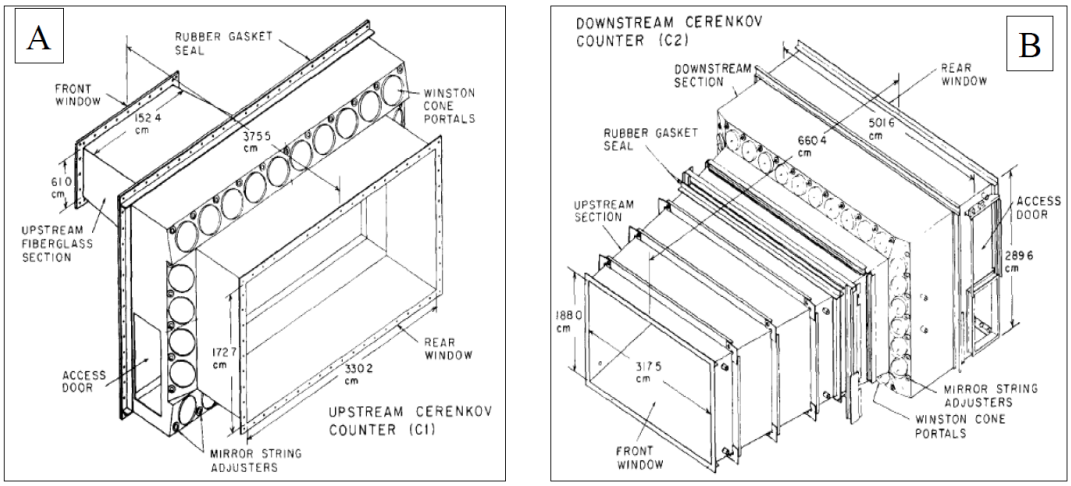

FIGURE 1.3: *The Cherenkov counters C1 (A) and C2 (B) of the experiment E-691 [1].*

When the experimental request is to tag particles of a selected specie all having the same velocity, a Cherenkov detector selecting a specific Cherenkov angle can be used. This is the case of tagging one particle specie in a secondary beam, where, in general, more particle species are present, all with momenta in a restricted range. These detectors are named **differential Cherenkov counters**. An example is given in Fig.1.4 [2]. This kind of detectors are positioned where the beam line has a section where the particle trajectories are parallel, so that all the Cherenkov photons from particles of the same specie are emitted at the same polar angle with respect to the beam axis. A spherical mirror, orthogonal to the beam axis, focuses all these photons in the same annulus region at the focal plane. A diaphragm with annulus aperture at this plane intercepts the photon produced by unwanted particle species. The resolution can be increased adding optical correctors to the basic scheme.

When all the Cherenkov photons are detected by a detection system with adequate space resolution, it is possible to reconstruct images and, knowing the particle trajectory, to infer the Cherenkov angle from the images. It is so possible to identify by the same counter several particle species. This counters are known as **Ring Imaging CHerenkov (RICH) counters**. The various technologies of RICHes are presented in the next section.

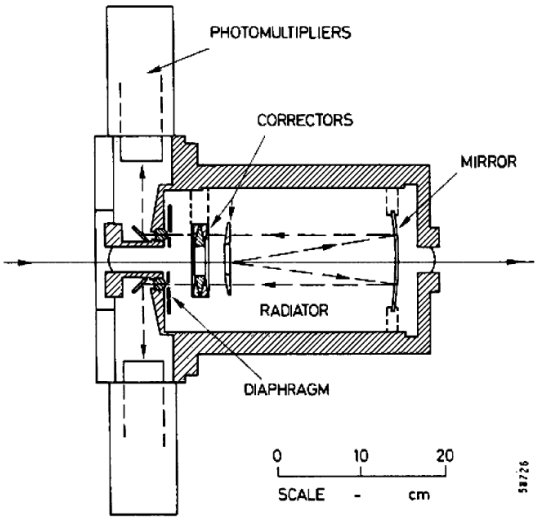

FIGURE 1.4: *Differential Isochronous Self-Collimating (DISC) counter used at CERN on the 20 GeV/c hyperon beam [2].*

1.1.5 Cherenkov imaging counters

Three different implementation of the RICH counters have been used in experiments.

RICHes with gaseous radiator are used for particle separation at high momenta. The refractive index is small and, therefore, the radiator is long, namely 1 m or more. An image can be formed only using an adequate optical system, namely mirrors focusing the photons at the focal plane where the photon detectors sit. This approach is illustrated by the scheme principle shown in Fig.1.5. Some relevant examples of focusing RICHes are COMPASS RICH-1 (Chapter-3), the RICH of the OMEGA spectrometer [3] at CERN SPS used for hadron and heavy ion physics, the RICHes of the Delphi experiment [4] at CERN LEP, the CRID of the SLD experiment [5] at SLAC, the HeraB RICH [6] at Desy HERA , the two twin RICHes of the HERMES experiment [7] again at Desy Hera, and the two RICHs of the LHCb experiment [8] at CERN LHC.

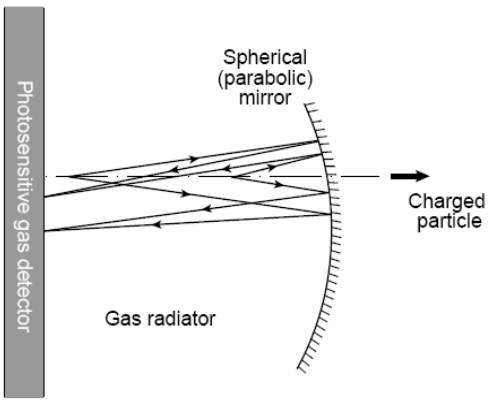

FIGURE 1.5: *Schematic principle of a focusing RICH.*

When a liquid or solid state radiator is used, the radiator can be very thin: 1 or a few cm. In this case, the proximity focusing scheme is usually preferred. The radiator is followed by an expansion gap placed between the radiator and the photon detectors, in order to let the photon image open to resolve the different photon angles. The principle is illustrated in Fig.1.6. Remarkable examples of proximity focusing RICHes are the High Momentum PID (HMPID) detector [9] of the ALICE experiment at CERN LHC and the RICH of the experiment CLEO III [10] at Cornell.

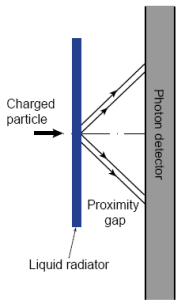

FIGURE 1.6: *Schematic principle of a proximity focusing RICH.*

The concept of the Detection of Internally Reflected Cherenkov light (DIRC) illustrated in Fig.1.7 is based on the use of fused silica bars both as radiator and as light transmitters: a large fraction of the Cherenkov photons generated by the particles crossing the fused silica bar in nitrogen atmosphere are trapped in the bar itself because of total internal reflection; therefore, these photons are transmitted along the bar till one of its terminal faces where the light is extracted by the use of a medium with a much larger refractive index: water. The extracted photons travel through a water-filled expansion region till the photon detectors. The only DIRC which operated in an experiment is BABAR DIRC [11].

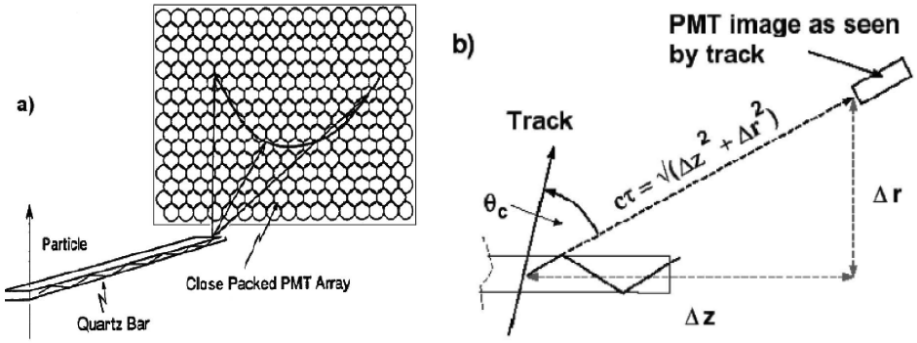

FIGURE 1.7: *Schematic principle of a DIRC.*

1.2 The main MicroPattern Gaseous Detector technologies

The Micro Pattern Gaseous Detectors have been invented in the last two decades of the twentieth century to answer to the quest of gaseous detectors with increased space resolution and rate capabilities by decreasing the basic cell-size.

The Micro-Strip Gas Chamber (MSGC) [12] is the first MPGD; the anode and cathode electrodes are formed by a pattern of alternated metallic strips on a dielectric support with a pattern pitch of 200 μm (Fig.1.8). The anode strips are thin (10 μm) to ensure a strong electric field at the anode in order to obtain the electron multiplication cascade. Initially, the MSGCs were affected by serious problems. In case of discharges,

the high electric field at the edges between the insulator areas and the metallic strips made these discharges very powerful and they could damage the detector. The abundant charge accumulation at the insulator surface caused important gain evolution versus time. Later, the passivation of the cathode edges was introduced: the detectors became more stable and could be used in experiments and applications.

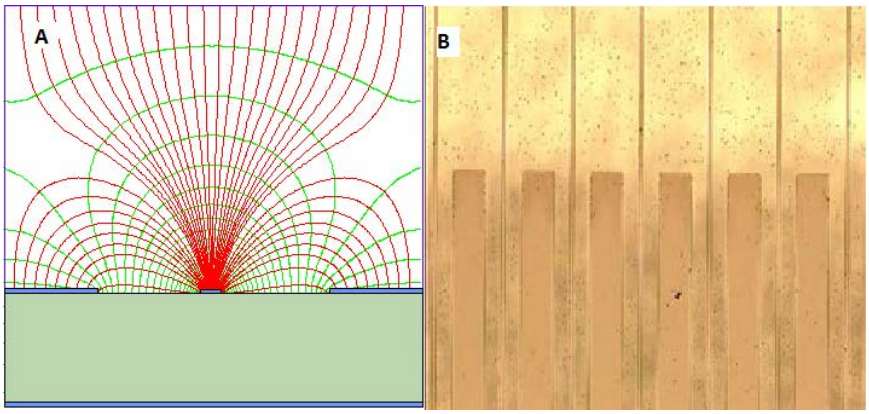

FIGURE 1.8: *(A) Scheme of a MicroStrip Gas Chamber with electric field lines (not to scale); (B) a MicroStrip Gas Chamber foil, picture.*

In the very last years of the twentieth century, two successful MPGD technologies were introduced: MicroMegas [13] and Gas Electron Multipliers (GEM) [14].

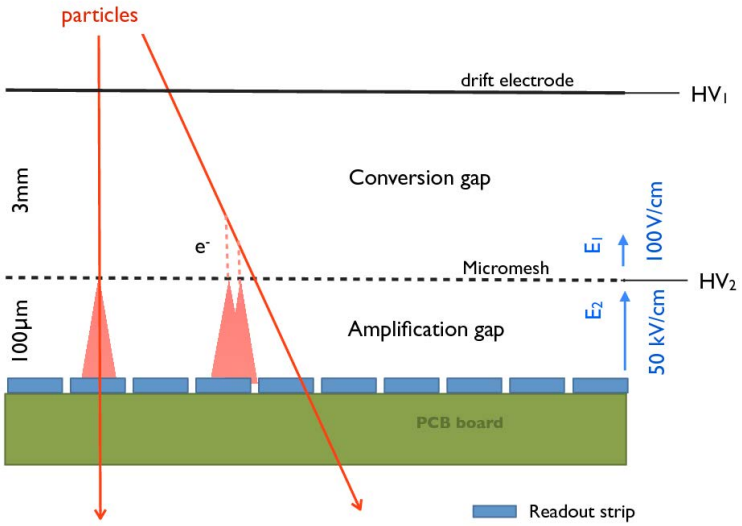

FIGURE 1.9: *Scheme of a MICROMEGAS (not to scale).*

The multiplication in the MM detector (Fig.1.9) is obtained with a parallel-plate electrode geometry. Nevertheless, there is a fundamental difference between a standard parallel-plate detector and an MM. In standard parallel-plate chambers a single gap is present, where both ionization and multiplication take place. In a MM two gaps are present separated by a metallic micromesh. The conversion gap, a few mm tick, where the ionization takes place, and where the electric field is low ($<$ 1kV/cm) to let the electrons drifts towards the mesh. The amplification gap, located between the mesh and the anode, is very thin (of the order of 100 μm) and here the electric field is high (30-50 kV/cm or more). The electric field is largely different in the two

regions above and below the mesh: the resulting field configuration makes the mesh almost fully transparent to the electrons from the ionization region, while a very large fraction of the ions generated in the amplification process are collected at the mesh. Therefore, the ion drift path is short (« the amplification gap) and the signal development is correspondingly fast, (∼100 ns or less). The high rate capability is related to the fast ion collection, while the space resolution is obtained with a fine segmentation of the anode electrode.

The GEM multiplier (Fig.1.10) is a thin dielectric foil, typically polyimide with 50 μm thickness, with Cu coated surfaces, where a regular pattern of holes is produced by photolithography. When a bias voltage (a few times 100 V) is applied between the two foil faces, a large electric field is present in the holes: here the electron multiplication takes place. In general, a detector includes more than one GEM multiplication foil, typically three; the multilayer approach is chosen in order to obtain a large gain limiting the discharge rate in each single foil. A moderate electric field above the first layer is present to collect the ionization electrons; the detector is completed by an anode plane with read-out elements positioned below the last GEM layer.

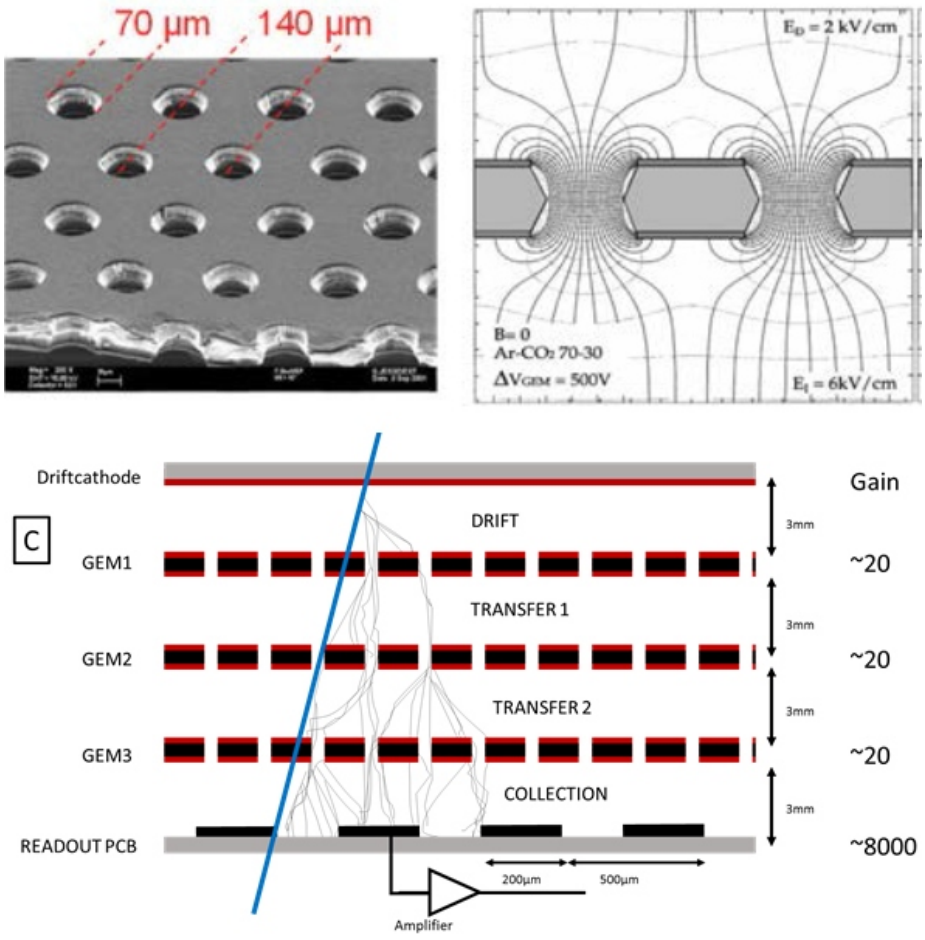

FIGURE 1.10: *(A) GEM-foil, picture; (B) GEM-foil, cross-section and electric field lines when a 500 V bias is applied between the two foil faces; (C) scheme of a triple GEM detector (not to scale).*

The THick GEM is an electron multiplier derived from the GEM design, scaling the geometrical parameters; it is typically made from Printed Circuit Board (PCB) with

0.2 mm - 1 mm thickness by standard drilling and etching techniques. As THGEMs are one of the fundamental ingredients of this thesis, they are described widely in Chapters 4, 5 and 6.

1.2.1 Dictionary for hole type and parallel plate type MPGDs

A hole type MPGD (e.g. GEM, THGEM) (Fig.1.11) is formed by one or more layers. For each layer, we indicate as **top** and **bottom** faces respectively, the surface at the hole entrance and hole exit, where entrance and exit refer to the electron path. Above the first layer, a **drift electrode**, namely a wire plane or a grid, defines the electric field in the region above the first electron multiplier; the field established in this region is indicated as **drift field**, $\mathbf{E_D}$ and, in general, it points towards the **drift electrode**. When the field is pointing towards the **top**, the electric configuration is indicated as **reversed field**. The voltage applied between the two faces (**top** and **bottom**) of a multiplication layer ($\Delta\mathbf{V} = |V_{top} - V_{bottom}|$) defines a field, called **dipole field**. The **dipole field** present in the multiplication holes is called $\mathbf{E}_{hole}$. The field between two multiplication layers is called **transfer field**,

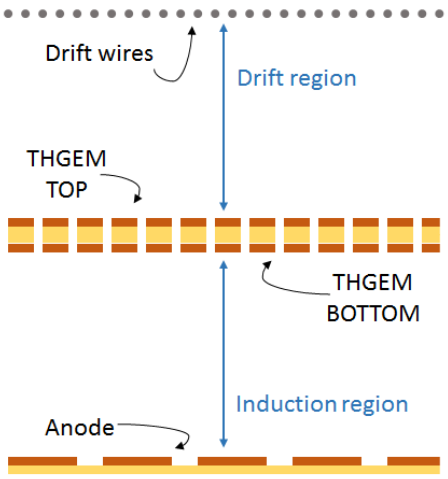

FIGURE 1.11: The scheme of a THGEM setup for measurements

$\mathbf{E}_{trans}$ (in case of multi layer structure (Fig.1.10), the **transfer fields** will be indicated as $\mathbf{E}_{T1}$ and $\mathbf{E}_{T2}$). The field between the bottom face of the last multiplication layer and the anode electrode is the **induction field**, $\mathbf{E}_{ind}$. In the standard detector configuration, the readout element is the anode itself. The geometrical parameters of such detectors are referred to as **t** (dielectric thickness), **p** (hole pitch), **d** (hole diameter) and **rim** (the clearance ring around the hole for THGEMs only). When a **photo-cathode** is present, two possible schemes can be implemented: the **Semi Transparent** (**ST**) and the **Reflective** (**Ref**) ones: in the **ST** case, the photo-converter layer is place above the multiplication layers and it is obtained coating with a CsI film an UV transparent window; in the **Ref** configuration, the CsI film is deposited on the top surface of the first multiplication layer.

For large area Detectors the electrodes are divided in segments with independent high voltage connectors in different segments. These segments are called sectors.

For parallel plate type MPGDs (e.g. MicroMegas), the concept of **drift field** remains the same as for the hole type MPGDs described above. The field between the μ-Mesh and the anodic readout PCB is called **mesh field** ($\mathbf{E}_{MESH}$) and is responsible for multiplication as well as for drifting of electrons.

The ions created in the multiplication process, which drift back to the drift region constitute the **Ion Back Flow** (**IBF**). In case of MPGDs with a photo-cathode, the **IBF Ratio** (**IBFR**), is the fraction of ions reaching the photo-cathode: a more precise definition is described in Chapter-4.

1.2.2 The dissemination of MicroPattern Gaseous Detector in fundamental research

The first large scale application in an experiment of MM and GEM trackers was at the COMPASS experiment [15] at CERN SPS. Then, GEM detectors have been used in two CERN LHC experiments, namely in LHCb [16] and in TOTEM [17]. The Time Projection Chamber (TPC) of the T2K (J-PARC, Japan) neutrino makes use of MMs as read-out sensors [18].

Recently, MPGDs have been chosen for relevant High Energy Physics (HEP) experiment upgrades. At LHC, ATLAS and CMS are equipping the forward regions with novel MPGD trackers with triggering capabilities. Large-size, about 1×2.5 m^2, resistive MM will cover a total surface of 1200 m^2 in ATLAS [19]. Triple GEM detectors with size up to 1.2×2.5 m^2 are being produced for CMS; the GEM foils will cover a total area of 1000 m^2 [20]. ALICE has approved the upgrade of the TPC read-out sensors by 4-layer GEM counters; the total area to be instrumented is 130 m^2 [21]. The replacement of 1.4 m^2 of gaseous photon detectors of COMPASS RICH-1 with hybrid MPGD based PDs which took place in 2016, is the main topic of this thesis.

1.2.3 Improving the MicroPattern Gaseous Detector performance

At present, the performance in running experiments of MM and GEM, are similar: space resolution better than 100 μm, time resolution around 10 ns, operative gain in experiments of a few time 10^3, always below 10^4, material budget of a 10^{-3} of X_0 and rate capabilities up to 100 kHz/cm^2. Better performance can be obtained with specific parameter choices; for instance, the time resolution of the GEM tracker in LHCb is 4.5 ns [16], and the rate capability of pixelized GEMs [22] and pixelized MM [23] used at the COMPASS experiment is two orders of magnitude higher than the standard limit.

In the following, some relevant R&D studies to substantially improve the MPGD performance are mentioned.

Extremely fine space resolution is the goal of the GridPix detector [24], obtained building a miniaturized micromesh over the Timepix chip [25] by wafer post processing. Recently, GridPixes have being used to read-out the EUDET TPC prototype: preliminary results indicate a space resolution of the TPC of about 100 μm, fully driven by the electron diffusion in the TPC with a negligible intrinsic contribution by the GridPix.

The Fast Timing Micro Pattern (FTM) Detector [26] makes use of a stack of multiple amplification gaps by fully resistive components in order to make the single gap transparent to fast signals, which are read out by external planes: fine time resolution is obtained by multiple measurements as in multilayer RPCs and a first two-layer prototype has provided 1.5 ns resolution. Fine time resolution is also the goal of a different approach: Cherenkov light is produced in a thin solid state radiator with fully negligible time jitter; O(100) photoelectrons can be detected when a minimum ionizing particle crosses a 1 cm-thick crystal; minimizing the photo-electron drift path a time resolution O(10 ps) is expected; the principle feasibility has been verified by extracting photoelectrons from an Al cathode illuminated by 100 fs long laser pulses and detecting them in an MM prototype [27].

High rate capabilities are requested for a large number of applications and, therefore, several different R&D are performed. The Micro-Resistive-Well detector, μ-RWELL [28], a single layer resistive device characterized by fine space resolution, of about 60 μm, and a simple assembly procedure aims at reaching rate capabilities up to 1 MHz/cm^2. Resistive MM with pad read-out, developed within the SCREAM project [29] and the High Performance MICROMEGAS project [30] also aim at 1 MHz/cm^2 rate capability.

Two application domains require to have low rates of IBF from the multiplication region. This is needed to operate TPC at high rates; in fact, the TPC rate is limited by the need to apply voltage at the gate electrode to avoid a high IBF flux in the drift TPC volume: detectors with intrinsic IBF suppression can allow to operate without gate. Two approaches have been proposed for TPC sensors, both offering similar performance: IBF below 1% is obtained without compromising the energy resolution. The first one, to be used for the upgrade of the ALICE TPC, is by four-layer GEMs with different geometries, standard GEMs and double pitch ones [31], the other by a hybrid detectors formed by two GEM-layers and a MM one [32]. The other field of application is the detection of single photons, where the IBF bombardment damages the photo-cathode; this is discussed in Section-1.3.

Large gains are required to detect intrinsically feeble signals, as those generated by single photoelectrons and to favour the MPGD dissemination beyond HEP. The μ-RWELL aims at gains as large as 10^5 by a single multiplication stage, while the development of the hybrid single photon detectors already able to operate at gains as high as 10^5 will be further continued to increase the present gain limit by one order of magnitude (Chapter-4).

1.2.4 The wide MicroPattern Gaseous Detector application domain

MPGDs are developed for the requirements of experiments in fundamental research, in particular in the HEP sector. Some of this applications have been given in Sec.1.2.2. More examples are provided in the following. GEMs are being implemented at the HallA experiment at JLab [33]. MSGC trackers have been operated at the DIRAC [34] and at the HeraB experiment [35]. An MM detector has been operated at the axion experiment CAST [36]. A triple GEM cylindrical detector instruments the vertex region of the KLOE2 experiment [37] and a second cylindrical detector inspired by this one is under construction for BESSIII in Beijing [38]. Cylindrical MMs have been developed for the experiment CLAS12 [39] at JLab and are now one of the options for tracking at the future Electron Ion Collider (EIC) [40]. Different MPGDs are being tested as sensors for the TPC at ILC: GEMs [41], MMs [42] and GridPIXes [24].

MPGDs are becoming popular in low energy nuclear physics experiments. GEMs will read-out a TPC operated at low pressure using light gases at the National Superconducting Cyclotron Facility (NSCL) in Michigan [43], MMs are the read-out sensors of the double-sided TPC of the Neutron Induced Fission Fragment Tracking Experiment (NIFFTE) at Los Alamos Neutron Science CEnter (LANSCE) [44].

Neutron detection is another field of application of MPGDs. The first example is the MSGC-based D0 reflectometer in operation at the Institut LaueLangevin (ILL) [45]. More recently, neutrons have been detected using GEM detectors and polyethylene converter [46] at Frascati ENEA Tokamak. High-efficiency n-detectors based on

GEMs where the neutrons are converted in a set of $^{10}B_4C$-coated lamellas orthogonal to the GEM planes [47] are under developments for applications at the European Spallation Source (ESS).

THGEMs are considered as sensors for large volume noble liquids TPCs in rare event experiments. In two-phase liquid Ar TPCs, THGEMs operated in gaseous Ar atmosphere are proposed for the DUNE experiment [48]. The read-out by GAPD of the electroluminescence produced during the amplification process in THGEMs [49] is used in the CRyogenic Avalanche Detector (CRAD). Recently, THGEMs have been successfully operated in liquid Xe detecting by PMTs the light produced by electroluminescence in the liquid [50]; moreover, coating the THGEM with a CsI film, it is possible to detect both the ionization and the scintillation signal produced in the liquid Xe.

Other applications in rare-event experiments are being considered. Micro-bulk MM, built making use of radiopure materials, are studied for the neutrino less double beta decay experiment PANDAX-III [51] at the Jinping Underground Laboratory, China. The NEWAGE Detector at the Kamioka mine, Japan, is developing a negative-ion TPC [52] using a μ-PIC detector coupled to a GEM foil. MMs are foreseen for axion search in the experiment IAXO [53] for WIMPs search at TREX-DM [53] and for dark photon search at P348 [54]. The experiment PADME [55], also dedicated to dark photon search, will use GEMs.

MPGDs are considered for applications of social interest: medical imaging, non-destructive and large-size object inspection, nuclear plant and radioactive waste monitoring, micro-dosimetry, medical beam monitoring, tokamak diagnostic and geological studies by muon radiography. There are MPGD architectures which are specifically developed in view of these applications. For example: the Resistive Plate WELL (RPWELL) [56], the Scintillating GLASS-GEM detector [57], the GEMpix [58] and the resistive μ-PIC [59].

1.3 Gaseous photon detectors

1.3.1 The motivations for the development of gaseous photon detectors

Gaseous photon detectors are the most effective solution for what concerns the cost of large detector area applications, namely they represent a cheap approach to extended photon detection systems. Moreover, they can operate in magnetic field thanks to their low sensitivity to the magnetic field itself. Another important feature is the limited material budget of these detectors, an important parameter when the photon detectors have to seat in the experiment acceptance.

Historically, the development of gaseous photon detectors has been guided by the requirements of the Cherenkov imaging counters for PID, namely the goal has been the challenging detection of **single photons**. More recently, gaseous photon detectors are also considered for the detection of scintillation light, mainly in rare-event noble liquid counters and for the detection of electroluminescence photons produced in the multiplication process in the gaseous detector itself for application in fundamental research and beyond.

1.3.2 Historical overview of the gaseous photon detectors

1.3.3 Gaseous photon detectors with photoconverting vapours

Gaseous photon detectors with photoconverting vapours have greatly contributed to establishing RICH counters as reliable detectors for experimental physics. Two photoconverting vapours have been used: (i) Tetrakis-Dimethylamine-Ethylene (TMAE) and (ii) Tri-Ethyl-Amine (TEA).

(i) TMAE has been used in the photon detectors of a large number of RICH detectors: among them, the RICHes of the experiments OMEGA [3], DELPHI [4] and SLD [5]. TMAE QE is non negligible below 200 nm and, therefore, only UV light is converted. When the detector windows are made of good quality fused silica, with transparency threshold at about 165 nm, the effective wavelength range of the detector is 165-220 nm. The vapour pressure of TMAE at room temperature is very low: the amount of TMAE in the atmosphere inside the gaseous detectors is limited: exceeding vapour amount can result in condensation drops, that can damage the detector. In order to obtain high photoconversion rate the detector has to be long introducing parallax errors in the measurement of the detection point and slowing down the detector response (for instance, 5 cm in the photon detectors of DELPHI barrel RICH) or it has to be operated at a temperature higher than the room temperature, a technically complex implementation (for instance, detectors were operated with TMAE vapour saturated at 40 ^{o}C in the CERES RICH [60]. More difficulties are related to the conversion of photons produced in the multiplication process in the gas and to the extreme chemical reactivity of TMAE, which imposes precise choice of detector materials and great care in its tightness.

(ii) TEA has been used in the photon detectors of two RICH detectors, in the experiments E605 [61] at Fermilab and CLEOIII [10] at Cornell. TEA vapour pressure at room temperature is high and thin detectors can be built. Its QE is however non negligible only in the very far UV domain, for wavelengths shorter than 170 nm. This fact imposes to use delicate and expensive windows, which are transparent in the far UV domain, namely CaF_2 or LiF, and to face all the technical challenges of the far UV domain. In the far UV domain the chromatic dispersion of the radiators is large and, therefore, TAE can be used only in those detectors where the chromatic dispersion is not the major resolution limitation or with radiators where the chromatic dispersion is very small, as it is the case for He.

MWPC-based photon detectors with solid state photoconverters

Gaseous photon detectors with a solid state photoconveter have been developed by the CERN-based RD26 Collaboration [62]: they consist of MWPCs where a cathode plane is formed by a PCB segmented in pads and coated with a CsI film. These PDs have been adopted by several experiments: NA44 [63], HADES [64], [65], [66], COMPASS [67] (described in detail in Chapter-3) with a total active surface of 5.3 m^2, STAR [68], JLab-HallA [69], and ALICE [9] with photon detectors covering a surface larger than 10 m^2. CsI has been selected as photo-cathode material because its relatively high work function makes it more robust than other ones commonly used in vacuum-based detectors.

CsI quantum efficiency is non-negligible below 210 nm (Fig. 1.12). When good quality fused silica windows are used, the resulting range for effective photon detection is 165-210 nm. The QE of the CsI photo-cathodes depends on the substrate and production procedure: both parameters have been optimized in the context of the RD26 development. Presently, QE as high as about 28% at 170 nm is routinely obtained [70] employing the plants and procedure developed at CERN [71] and used for the new COMPASS hybrid PDs (Chapter-7).

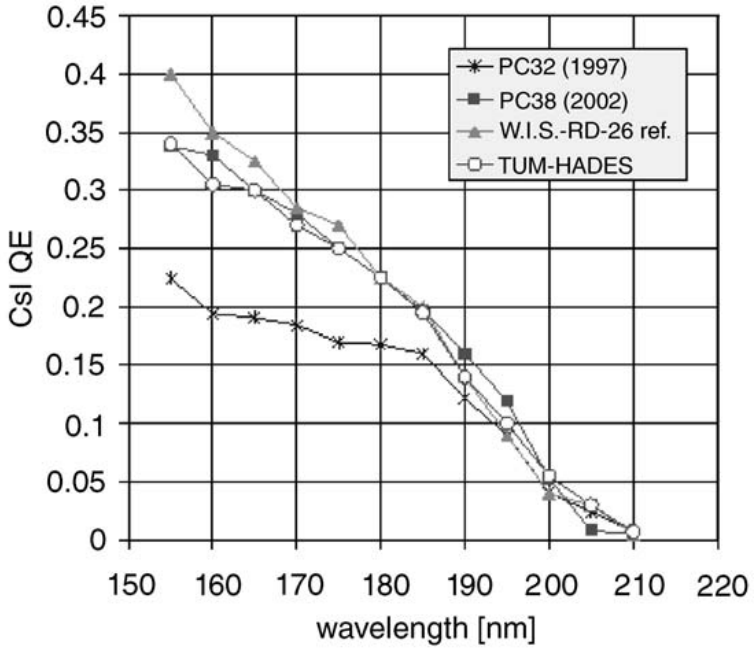

FIGURE 1.12: *The quantum efficiency of large size CsI photo-cathodes produced at CERN for ALICE (PC32 and PC38) and at the Technical University of Munich for HADES (TUM-HADES), compared to that measured at the Weizmann Institute of Science on small samples (W.I.S.-RD26 ref.) [70]. The relevant increase of the QE from PC32 to PC38 corresponds to the progress in optimising the procedure to produce large size photo-cathode on a PCB substrate.*

The effective quantum efficiency obtained in a gaseous detector depends on the gas used and the normal component of the electric field at the photo-cathode surface: when the photoelectron scattering off a gas molecule is elastic, the back scattering probability is high and part of the photoelectrons impinge back on the photo-cathode where they are absorbed. The characteristics of the gas molecules and the value of the electric field accelerating the photoelectrons determine the elastic scattering rate and thus the effective quantum efficiency. Both parameters have been studied in the context of RD26 [72, 73] and newly explored more recently [74, 75]. The response in different gas atmosphere has also been reproduced by calculation [73, 76]. An example of the measurements performed by our group is shown in Fig. 1.13. At atmospheric pressure, the effective quantum efficiency increases very steeply up to electric field values of about 1000 V/cm. At higher field values, this rate of increase of the effective QE versus field is reduced, even if it remains non-negligible. The highest QE is obtained in pure methane or in methane-Ar mixtures, provided that the methane fraction is high ($> 40\%$). The majority of the RD26-like photon detectors are operated in pure methane. At the typical applied voltage of 2000 V, the field at the photo-cathode is about 7000 V/cm, ensuring good photoelectron extraction.

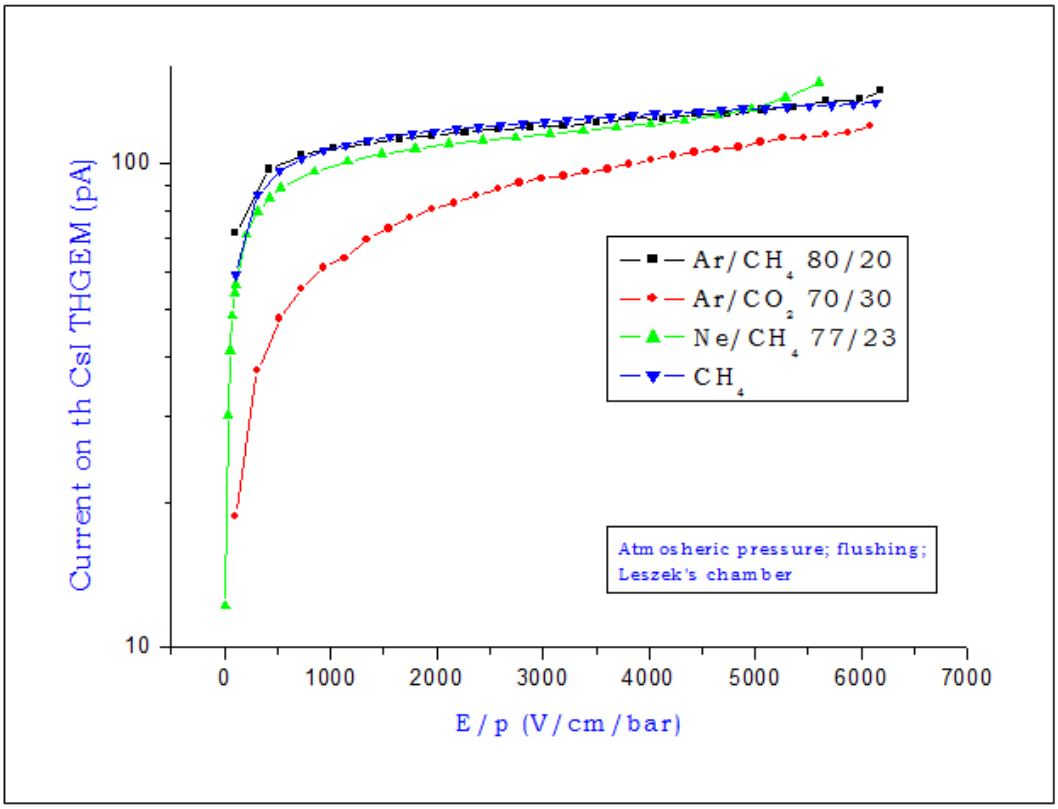

FIGURE 1.13: *CsI photocurrent versus applied electric field in various gases and gas mixtures at atmospheric pressure; the systematic uncertainty is ∼1% level [74].*

The basic scheme of the photon detectors is very similar in all applications and it is illustrated in Fig. 1.14. An important choice at the base of this detector architecture is to adopt reflective instead of semi-transparent photo-cathodes. This configuration is preferred as it results in a larger photo-conversion rate. In fact, a semitransparent photo-cathode requires the application, onto the detector window, of a thin metallic film to keep the entrance window at a fix potential: this film absorbs photons; also, the probability of photo-electron absorption is lower in a reflective photo-cathode than in a semitransparent one as the conversion probability is maximum at the entrance surface of the photoconveter layer. Another consideration is of great relevance when aiming at large surface detectors: while the thickness of the photoconverting film is very critical for semitransparent configurations, this is not the case for the reflective photo-cathodes, opening the way to the production of large size photo-cathodes up to 0.35 m^2 (COMPASS RICH-1 [77]) and to 0.27 m^2 (ALICE HMPID [9]).

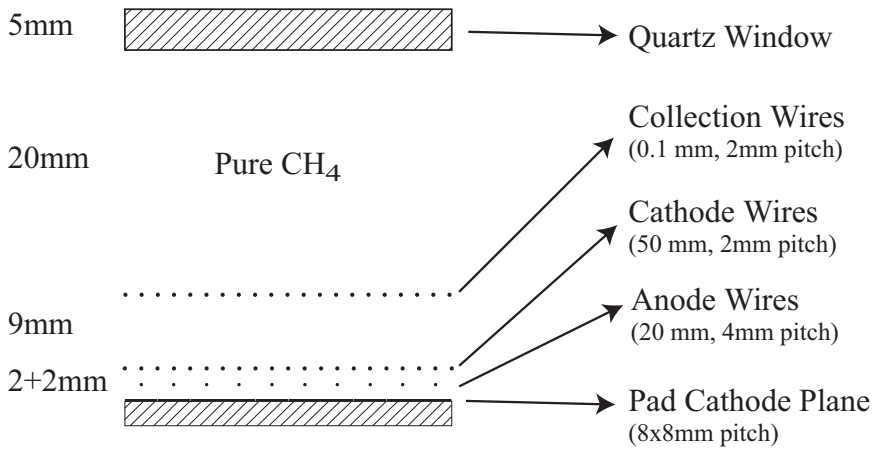

FIGURE 1.14: *Schematic cross-section of the COMPASS RICH-1 gaseous photon detectors (not to scale).*

In spite of the remarkable success of proving that solid state photo-converters can operate in gaseous atmospheres, MWPCs with CsI photo-cathodes suffer because of some performance limitations.

- Ageing, resulting in a severe decrease of the quantum efficiency, is reported after a collected charge of the order of some mC/cm^2 [78].
- The presence of the CsI layer causes electrical instabilities of the MWPCs accompanied by long recovery time (O(1 d)) [77].

The detectors must be operated at low gain to overcome as much as possible the effects described above; this limits the single photo-electron detection efficiency. Low gain is required also to keep the after-pulse rate low. The operation at low gain imposes to integrate a relevant fraction of the signal, namely integrating over several hundred ns. The long integration time acts as a detector memory: these photon detectors are not adequate for high rates. Ageing is related to the bombardment of the CsI layer by the positive ions generated in the multiplication process, namely the IBF to the photo-cathode elements. Electrical instabilities are due both to IBF and the feedback of photons generated in the multiplication region.

1.3.4 MPGD-based photon detectors

Two basic requirements must be matched to progress with respect to the MWPC-based photon detectors: reduced photon back-flow and IBF rates, in order to overcome aging and to make possible high gain operation, and intrinsically fast detector operation, so to obtain detectors adequate for high rate environments. MPGD detector architectures look promising under this respect: the signal generation is intrinsically fast (Chapter "MPGD") and various architectures, as, for instance, multilayer GEM detectors ensure no photon feedback, while a good fraction of the ions is trapped in the intermediate layers and do not reach the photo-cathode. These detectors have been studied both coupled to ST photo-cathodes [79] and Ref photo-cathodes [80] (Fig. 1.15).

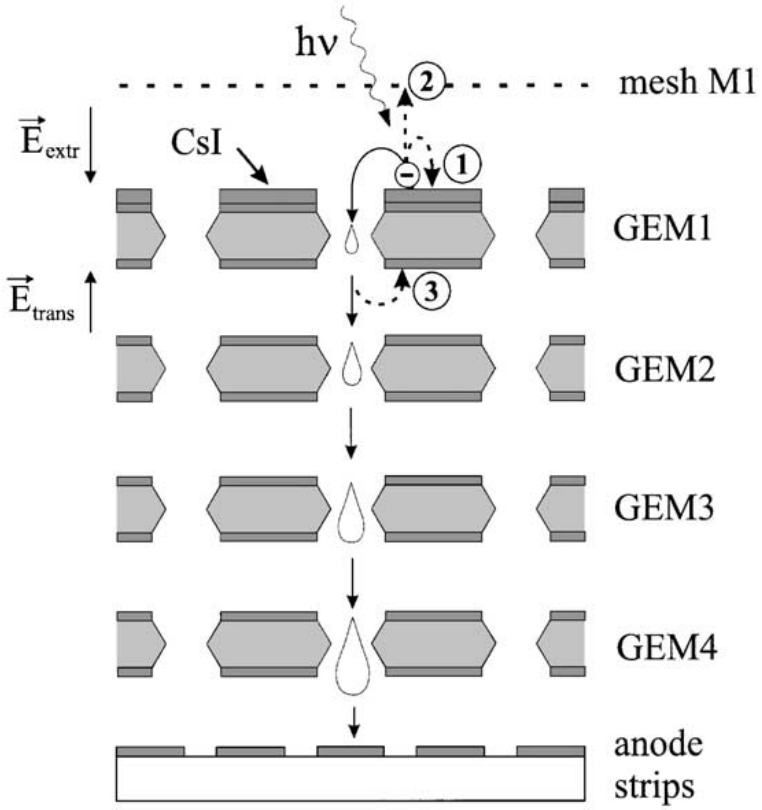

FIGURE 1.15: *Sketch of a quadruple GEM photon detector with the photo-cathode evaporated on the top face of the first GEM. The dashed arrows illustrate the different photoelectron loss mechanisms: backscattering (1), transfer to the mesh (2) and collection at the bottom of the GEM (3) [81].*

The threshold Cherenkov counter Hadron Blind Detector (HBD) [82] of the Phenix experiment represents the first application of these ideas: the photon detectors are triple GEM counters covering a total area of about 1.5 m^2. The first GEM foil is coated with a CsI film and acts as reflective photo-cathode. The photon detectors are window-less and the same radiator gas (CF_4) forms also the detector atmosphere. The read-out elements are large pads (6.2 cm^2) and 5-10 photoelectrons per pad are collected. They are operated at low total gain (about 4000), while the noise level is at about 1000 electrons equivalent. It is important to notice that the signals due to minimum ionizing particles crossing the photon detectors are suppressed thanks to the reverse electric bias in front of the photo-cathode: reversed bias would not be compatible with a semitransparent photo-cathode configuration. The successful operation of the HBD is encouraging, but several features are not directly exportable to imaging devices: the detection of several photoelectrons per channel makes it possible to operate at a gain which is only a factor four larger than the noise level, the window-less architecture, which makes it possible to convert photons down to about 110 nm and thus to increase the number of converted photons, would result in a high chromatic dispersion.

The IBF has been studied in detail for GEM-based photon detectors [83]: rates as low as 10^{-3} have been obtained only applying very low values of the electric field at the photo-cathode surface. This condition is incompatible with good effective quantum efficiency (Sec. 1.3.3). IBF cannot be reduced to less than a few % in effective GEM-based photon detectors. More elaborate structures have been introduced to

obtain better IBF figures: one of the two surfaces of a GEM foil is no longer a single electrode, but it is segmented in electrodes with different functions: part of them are there to establish the dipole field in the holes, while the inter-laid electrodes shape the electric field so to trap the ions. This is the principle of the Micro-Hole & Strip-Plate elements (MHSP) [84] and the Cobra plates [85]: IBF rates below 10^{-4} have been obtained.

GEM-based photon detectors have been operated in laboratory studies at gain up to about 10^5, but is unlikely that such high gain can be preserved in the environment of an experiment. This consideration is based on the fact that the HBD GEM detectors operate at a total gain of 4000 and that GEM trackers used in experiments operate at gains around at most 10^4.

THGEM-based photon detectors can allow to obtain higher gains (O(10^5)) also in beam and the intrinsic stiffness of the boards allows easier handing, a relevant characteristic for the delicate operations related to the CsI coating, the photo-cathode storage and the detector assembly. An IBF rate of a few % can be obtained with triple THGEM detectors applying a high electric field (typically 5 kV/cm) as transfer field between the second and third multiplication layer [86]. The drawback of this approach is the maximum voltage to be applied to the detector electrodes, which is as high as 7-8 kV (absolute value), imposing more restrictive detector design requirements to guarantee the electrical insulation: the dead areas result increased. An alternative option is to use as third multiplication layer a MPGD concept with intrinsically small IBF rate, namely an MM stage: reduced IBF rates analogous to those obtained with triple THGEM detectors or better, can be achieved without applying voltage higher than 5 kV (absolute value). The novel PDs for the upgrade of COMPASS RICH-1 described in this thesis are based on this design.

The use in gaseous detectors of photo-cathodes with sensitivity in the visible light range is problematic due to the extreme fragility of the typical photo-converters, which have work function lower than CsI and the QE is degraded after an integrated charge of a few $\mu C/mm^2$ [87]. The concept of gaseous PMTs with sensitivity to visible light based on MPGDs has been introduced by the group active at the Weizmann Institute: they introduced the already mentioned structures MHSP and Cobra in order to reduce the IBF rate at the O(10^{-4}) level. In recent years, further progress has been obtained in Japan, by a collaboration between scientific institutions and Hamamatsu. The most successful approaches are by the use of metallic micro-meshes: for instance, small-size devices using double mesh layers with different geometrical parameters provide IBF rate at the 6×10^{-4} level and gains as high as 10^4 [88]. It has to be stressed that gaseous PMTs for visible light are largely insensitive to the presence of the magnetic field; therefore, these developments are pursued even if the effective QE is lower in gaseous detectors than in vacuum-based detectors [89] .

Chapter 2

The COMPASS Experiment at CERN

The Common Muon and Proton Apparatus for Structure and Spectroscopy (COMPASS) (NA58) is a high rate, fixed target experiment at the Super Proton Synchrotron (SPS) of CERN. COMPASS is a collaboration of 24 Institutes from 13 Countries with $\sim$250 physicists. Initiated with the proposal of 1996, COMPASS is born from the merging of two collaborations, CHEOPS and HMC, that shared similar demands to the experimental apparatus but addressing different physics topics, focusing around structure and spectroscopy of hadrons. The aim of COMPASS is to study in detail the nucleon spin structure using a high energy muon beam and to perform hadron spectroscopy, Drell-Yann and Primakoff measurements using hadron beams.

The first experiment proposal [90] was accepted in 1998. The broad physics program of the first phase of COMPASS (2002-2011 data taking period), included studies of spin structure with longitudinally polarized ^{6}LiD and NH_3 targets, for inclusive and semi-inclusive Deep Inelastic Scattering (DIS) to measure parton helicity distribution functions, gluon polarization function and transversity together with hadron spectroscopy and Primakoff reaction measurements. The measurements of Primakoff reaction allowed to extract the most precise direct value of the π polarizability to date.

In a second phase, which started in 2012 [91], it was decided to extend the study to the generalised parton distributions (GPDs) through deeply virtual Compton scattering (DVCS), to the nucleon transverse momentum dependent distributions (TMDs) through Drell-Yan process and also to the chiral perturbation theory through Primakoff reactions.This chapter will describe the experimental setup used with a muon beam for spin structure or for DVCS measurements.

2.1 The COMPASS layout

The COMPASS physics program imposes specific requirements to the experimental setup, (Fig.2.1) which are: large angle and momentum acceptance, including the request to track particles scattered at extremely small angles, precise kinematic reconstruction of the events together with efficient particle identification and good mass resolution. Operation at high luminosity imposes capabilities of high beam intensity and counting rates, high trigger rates and very large data flows. To cope with these requirements the apparatus is organized in a two stage spectrometer setup: tree different parts can be distinguished. The first part includes the detectors upstream of

the target, which measure the incoming beam particles and the target region. The second and the third part of the setup are located downstream of the target, and extend over a total length of 50 m. These are the Large Angle Spectrometer (LAS) and the Small Angle Spectrometer (SAS), respectively. The use of two spectrometers for the outgoing particles is a consequence of the broad momentum range and the wide angular acceptance requirements.

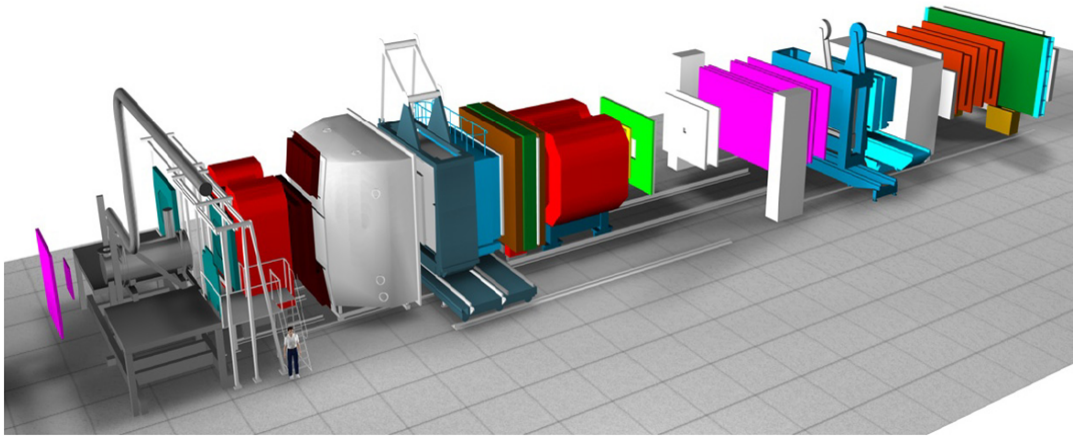

FIGURE 2.1: Artistic view of the COMPASS spectrometer for COMPASS phase-1

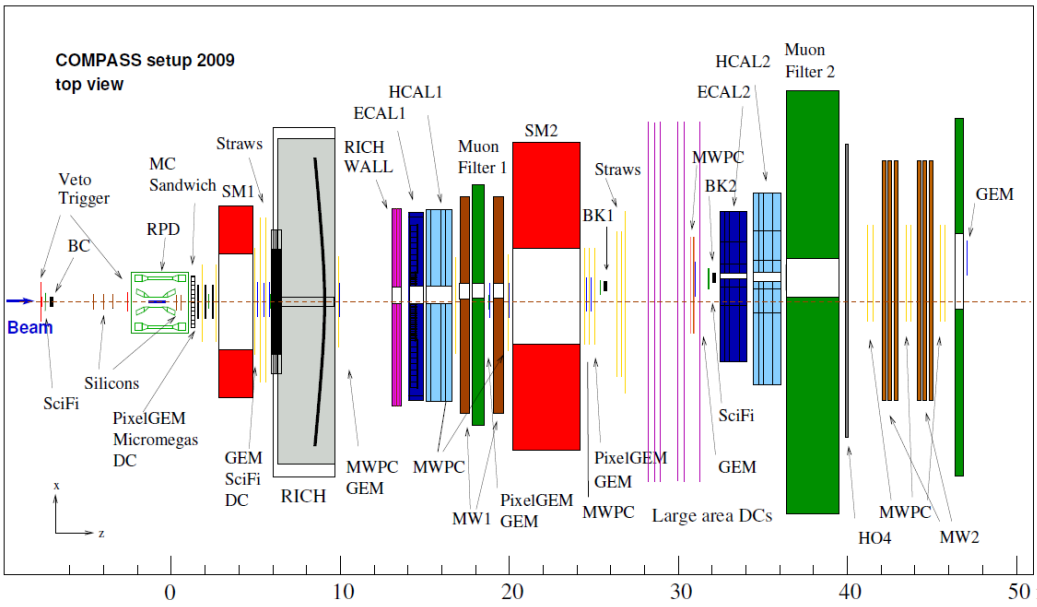

FIGURE 2.2: Top view of the COMPASS spectrometer for Primakoff studies in 2009

The new COMPASS spectrometer setup specific for the 2016 DVCS data taking is shown in Fig.2.3.

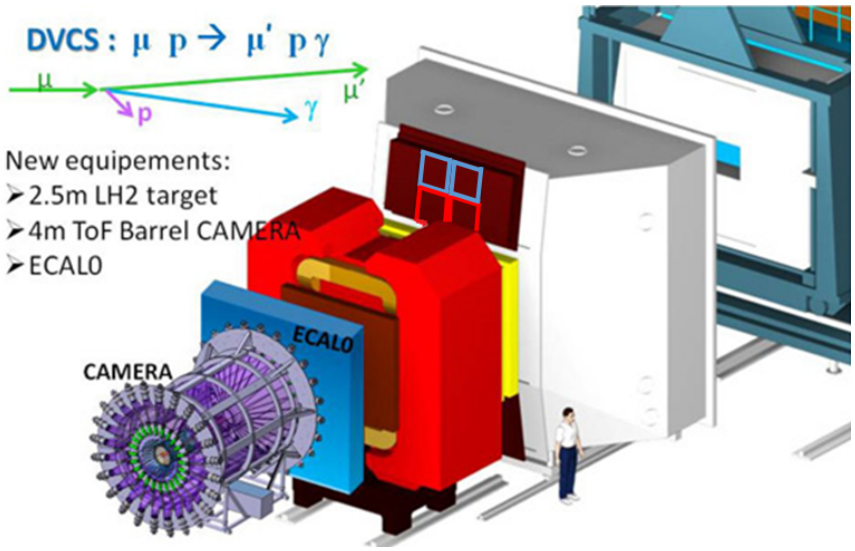

FIGURE 2.3: New detectors (CAMERA and ECAL0) needed for DVCS studies in 2016 are shown (zoom of front part of the spectrometer)

The LAS, has been designed to ensure 180 mrad polar acceptance. It is built around the SM1 magnet, which is preceded and followed by telescopes of trackers. SM1 is a dipole magnet located 4 m downstream of the target center. The main component of the field goes from top to bottom. Its field integral was measured to be 1.0 T.m and corresponds to a deflection of 300 mrad for particles with a momentum of 1 GeV/c. The bending due to the field allows for momentum measurement. The information from the RICH-1 detector, placed just after SM1 is used in combination with the momentum measurement to perform particle identification as explained in the following chapter. Particles then travel through the gaseous volume of the RICH reaching the electromagnetic and hadronic calorimeters.

The SAS detects particles at small angles (± 30 mrad) and momenta larger than 5 GeV/c. It's structure is similar to the LAS one: its central element is the 4 m long SM2 magnet, located 18 m downstream the target center and preceded and followed by telescopes of trackers. SM2 is a rectangular shape dipole magnet with a gap of $2 \times 1\ m^2$ and a total field integral of 4.4 T.m for its nominal current of 4000 Amperes. As for SM1 the main component of the field is in the vertical direction. The downstream part of the SAS includes electromagnetic and hadronic calorimeters and a muon filter. A second muon filter is positioned at the downstream end of the spectrometer.

The flexibility required by the broad spectrum of the COMPASS physics program has been implemented by mounting huge setup elements on rails, allowing them to be positioned at variable distances from the experimental target: the RICH, the first hadron calorimeter, the first muon filter, the second analysing magnet and the trackers fixed to it can move longitudinally on rails.

2.2 The M2 beam line

The muon beam is derived from a very intense primary proton beam, extracted from the CERN SPS at 400 GeV/c momentum, that impinges on a beryllium target with 500 mm thickness (T6). Thinner targets can be selected for lower fluxes, if required.

The nominal proton flux available for COMPASS is $1.2 \cdot 10^{13}$ protons/spill, during $\sim$ 5 s long spills, within a typical 16.8 s long SPS cycle. A section of six acceptance quadruples and a set of three dipoles select a high pion flux within a momentum band of up to $\pm$10% around a nominal momentum up to 225 GeV/c and within a geometrical acceptance of about $3\pi\mu$sr. The pions are transported along a 600 m long channel, consisting of regularly spaced alternately focusing and defocussing quadrupole Along this channel a fraction of the pions decay into a muon and a neutrino. Both pions and a large fraction of the muons produced in the decays are transported until the muons are focused and the hadrons are stopped in a hadron absorber. Before entering the experimental hall, the μ momentum (nominal value 160 GeV/c) is measured for each particle by the Beam Momentum Station (BMS), consisting of a bending magnet and six hodoscope stations located downstream and upstream the magnet. Four stations are made of horizontal cope with the different flux in the regions around the beam axis; two stations are made of scintillating fibres with 2 mm diameter. The time resolution achieved by the system is around 0.3 ns; the momentum resolution is better than 1%. After the BMS, the muons are focused on the target. The incoming muon flux is of the order of $4{\cdot}10^8$ muons per spill. The beam is also accompanied by a large halo, composed of muons outside the beam-line acceptance: the "near" halo, in the region within 15 cm from the beam line, accounts for $\sim$16% of the beam intensity, while the "far" halo accounts for about 7%. The beam is naturally polarized with a polarization $P_\mu \sim 80\%$.

2.3 The polarised Target and the liquid H_2 target

The majority of the COMPASS data were collected using a polarized target in a cryostat inside a solenoid magnet. The superconducting solenoid has an acceptance of $\pm$180 mrad. The target configuration has three cells and a microwave cavity. The COMPASS muon program aims to measure cross section asymmetries $\Delta\sigma/2\sigma$ where $\Delta\sigma$ is the difference between the cross sections of a given process for two different spin configurations and σ the spin averaged cross section. The corresponding observable counting rate asymmetry is $A_{obs} = (P_\mu \cdot PT \cdot f \cdot (\Delta\sigma/2\sigma))$, where P_μ and PT are the beam and target polarizations respectively, and f is the fraction of polarizable material inside the target. The use of a polarized target is thus mandatory and, in addition the factors PT and f must be made as large as possible in order to optimize the statistical significance of the results. While electron spins can be aligned in a magnetic field and give rise to a large polarization at equilibrium for a low enough temperature, only a negligible nuclear spin polarization can be reached by high field and low T only. Therefore, solid state polarized targets rely on dynamic nuclear polarization (DNP)[92] which transfers the electron polarization to the nuclear spins by means of a microwave field. This process requires a material containing some amount of paramagnetic centers, a temperature below 1 K and a strong and homogeneous magnetic field. Deuterated lithium (^6LiD) and ammonia targets (NH_3) have been used by COMPASS. ^6LiD allows to reach a high degree of deuteron polarization ($\geq$40%) and has a very favorable composition: ^6LiD can be considered to a good approximation as a spin-0 ^{4}He nucleus and a deuteron, the fraction of polarizable material f is of the order of 0.35, taking into account also the He content in the target region. The irradiated ammonia (NH_3), which has been used as polarized proton target, has a less favorable composition (f $\sim$ 0.15) but can be polarized to a higher degree ($\geq$80%). The spin directions were frequently inverted by rotating the

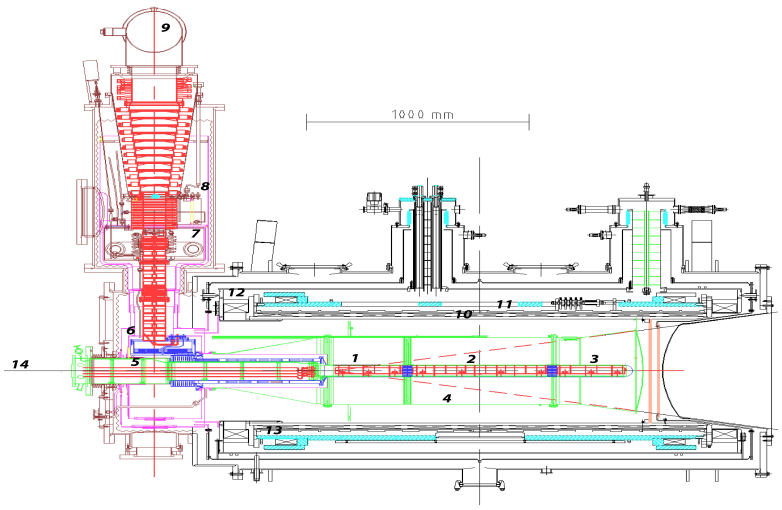

FIGURE 2.4: Side view of the COMPASS polarized target: upstream target cell 1, central 2 and downstream target cell 3 inside mixing chamber, microwave cavity 4, target holder 5, still or ^{3}He evaporator 6, ^{4}He evaporator 7, ^{4}He liquid/gas phase separator 8, ^{3}He pumping port 9, solenoid coil 10, correction coils 11, end compensation coil 12, dipole coil 13, muon beam entrance 14. The tree halves of the microwave cavity are separated by a thin microwave stopper.

solenoid field in the longitudinal target configuration, rebuilding the polarizations with opposite microwave frequencies in the transverse target polarization case.

During transverse data taking the target material is kept in frozen spin mode below 90 mK and the spin direction is maintained by the 0.42 T transverse dipole field. The polarization is reversed by exchanging the microwave frequencies of the tree cells.

In 2016, for the DVCS run, a special non polarized liquid H_2 target has been used.

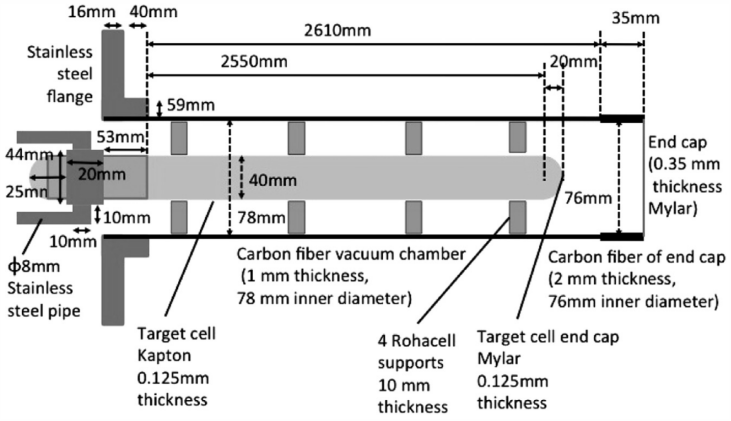

FIGURE 2.5: A schematic side view of the target cell and vacuum chamber of the COMPASS liquid H_2 target.

The liquid H_2 target apparatus (Fig.2.5)[93] consists of a 2668 mm long cylindrical target cell with a diameter of 40 mm and a volume of ∼3.3 l made of 0.125 mm thick Kapton, a vacuum chamber with an end-cap which is a hemisphere made of 0.125

mm thick Myler, a refrigerator system (consisting of cryo-coolers with cooling power of 30W at 20K) and 5 H_2 tanks with a volume of 1000 l each.

To reduce the material budget of the liquid H_2 target, thin Kapton and Myler foils are used to construct the target cell. To construct the vacuum chamber a thin-walled 1 mm thick and 80 mm outer diameter Carbon Fiber Reinforced Plastic (CFRP) has been used (consisting of 10 layers of two different types of CFRP sheets made of carbon fiber): this guarantees 2.0 bar of maximum inner pressure in the vacuum chamber.

The liquid H_2 target was tested during the pilot run data taking period of 2012 with satisfactory outcomes and was used during the 2016 DVCS run.

2.4 The Recoil Proton Detector

The Camera detector is designed to detect particles that leave the target with a high polar angle. Developed for the DVCS runs, it detects and measures the recoiled proton and its momentum. However, it can detect other charged particles as well including cosmic muons (or pions) that were used to calibrate the Camera detector. The detector as shown in Fig.2.6 [94] consists of two concentric cylinders of scintillator stripes (in the following "ring A" for the inner cylinder and "ring B" for the outer one) that are connected to PMTs (The main properties of the scintillators used are listed in Table.2.1).

TABLE 2.1: Camera ring A and B properties and dimensions

Property	A Ring	B Ring
Length	275 cm	360 cm
Width	0.4 cm	5 cm
Radius	25 cm	110 cm
Model	EJ-200	BC-408
Refractive index	1.58	1.58
PMT	ET9823	ET9823

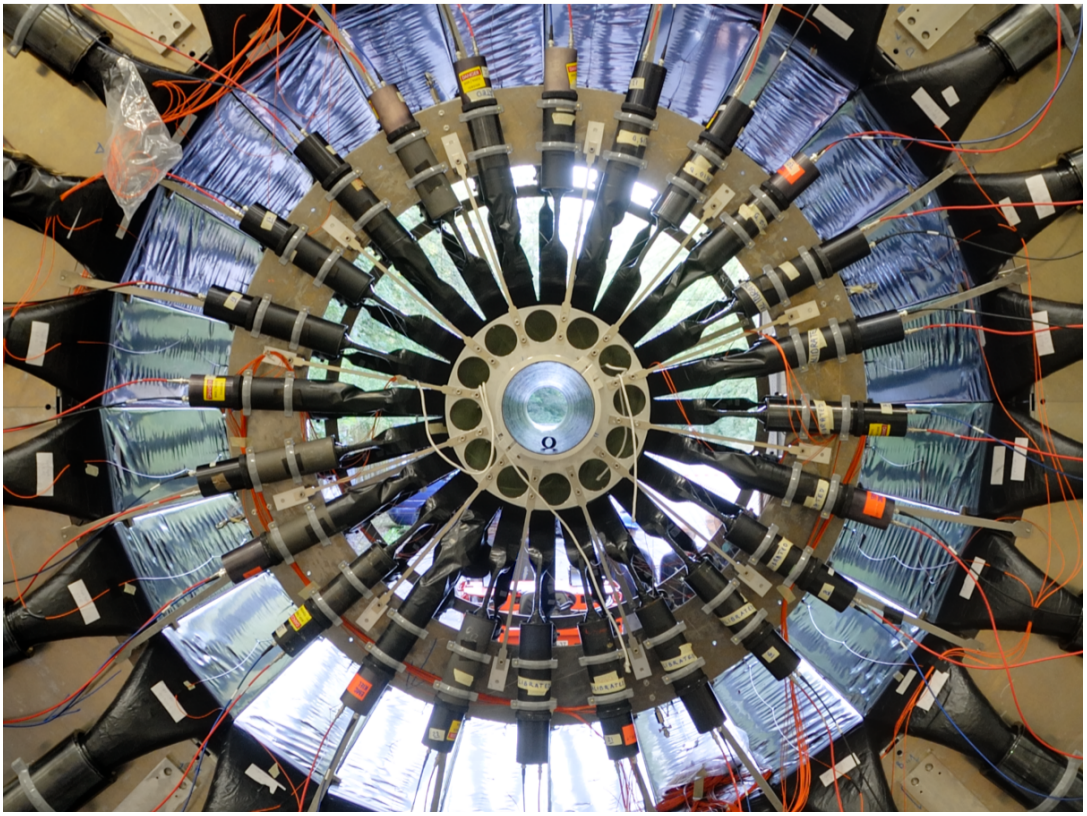

FIGURE 2.6: Camera setup visualization, upstream view. The inner ring A consists of 24 scintillators around the target, each connected with light guides to two photomultiplier tubes. The outer ring B is built around the ring A and consists of 24 scintillators and PMTs as well.

A good performance of the CAMERA recoil detector is essential for the delicate DVCS measurement: after 2012 pilot run data taking, the detector has been refurbished and during 2016 run its performance was highly improved.

2.5 Tracking

The tracking system of COMPASS comprises many tracking stations, distributed over the entire length of the spectrometer for a total of $\sim$ 350 sensitive plains. Each tracking station consists of a set of detectors of the same type, located at approximately the same z-coordinate along the beam. In a station, the trajectory of a charged particle is measured in several projections transverse to the beam direction in order to reduce ambiguities. Due to the large overall acceptance of the spectrometer, the region to be covered by the detectors is large and the requirements for the tracking change with the distance from the beam axis. Near the beam axis region, detectors should stand high particle flux and they must provide good timing and position resolution; in the region far from the beam axis, the particle flux is less intense and the requirements for the detectors can be relaxed. In this way three main tracking detector types can be identified: the very small, small and large area trackers.

2.5.1 Very Small area tracker

The Very Small Area Trackers (VSAT) cover the beam region up to a radial distance of 2,5 - 3 cm. The very high rate of beam particles in this area, up to about $10^5 s^{-1} mm^{-2}$ in the center of the muon beam requires excellent time or position resolution of the corresponding detectors in order to identify hits belonging to the same track in a highly crowded environment. Scintillating fibers (SciFi), silicon micro-strip detectors and pixelized MPGDs fulfil this task.

The scintillating fibers have a diameter between 0.5 and 1 mm; each station is made by different planes in order to measure more than one projection. In each plane several layers, shifted one with respect to the other, are used in order to avoid low efficiency zones. Hits belonging to different tracks can be assigned to the corresponding track by time correlation only. Time correlation is also used to link the incoming muon with the scattered muon track, as well as with the trigger and the information from the beam momentum station. A total of eleven SciFi detector stations were used. The obtained time resolution ranges between ∼300 ps and 450 ps for the central regions of the various detector planes with a detection efficiency above 99%.

The silicon micro-strip detectors are made of a wafer 300μm thick n-type with an active area of 5×7 cm^2. The 1280 readout strips on the n-side are perpendicular to the 1024 readout strips on the p-side so that with one wafer two-dimensional position information can be obtained. Two detectors make up one silicon station. They are mounted back-to-back on a fibre-glass frame such that one detector measures the horizontal (X) and vertical (Y) coordinates of a particle trajectory, while the other is rotated around the beam axis by 5°, providing two additional projections (U,V). The average spatial resolution is about 10 μm, the time resolution is about 2.5 ns.

The pixel GEMs and pixel MMs will be discussed in the next sub-section along with the standard GEMs and MMs.

2.5.2 Small Area Tracker

The intermediate region at a radial distance of 2.5 cm to 30 - 40 cm is covered by the Small Area Trackers (SAT), and is the domain of MPGDs (Chapter-1). Both MicroMegas and GEM detectors were employed for the first time in a large-scale particle physics experiment by COMPASS since 2002.

11 GEM stations each consisting of 2 detectors with 2D strip readout having 31 × 31 cm^2 active area are used in the COMPASS spectrometer. They have a thickness of 0.4% X_0 and provide 12 ns time resolution and 70 μm space resolution per plain. Both standard strip Micromegas and GEM detectors have central dead zones with 5 cm diameter.

The DVCS program needs measurements at low Q^2, meaning at very small angles with better spatial resolution than the scintillating fibers (150 μm), and with less material reducing the probability of interaction of the real photons. To achieve this goal, the pixelized GEMs and MMs detectors have been introduced in the COMPASS spectrometer, also for the first time in a large experiment. The rate in the beam region is ∼20 MHz·cm^{-2}.

The novel GEM read-out structure has been realized on a polyimide basis using the GEM patterning and wet-etching PCB technologies. The central area of 32×32 mm^2 is segmented into 1024 pixels, each of size 1×1 mm^2. Signals, which are read from the pixels are routed to the readout electronics via traces with an extremely small width of only 50 μm and a pitch of 100 μm, which is on the other side of the foil. The rest of the total active area of 100×100 mm^2, where the occupancy is sufficiently low, is covered by two orthogonal sets of 512 strips with a pitch of 400 μm, realized on a second 50 μm thick polyimide foil.

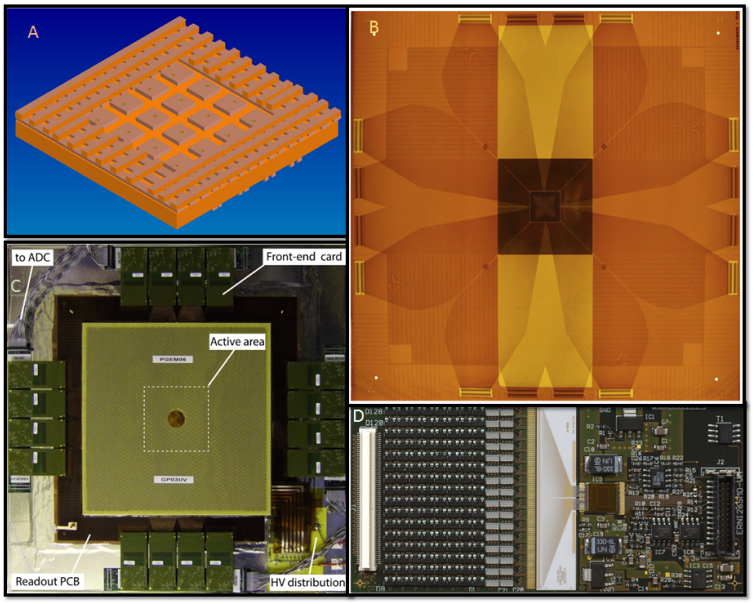

FIGURE 2.7: A. Schematic view of the pixel and strip region of the readout circuit. Note that the pixel region consists of 32×32 pixels of 1 mm^2 size each, while only 4×4 are shown for clarity. Figure not to scale.; B. The PixelGEM read-out foil. The inner 10×10 cm^2 darkest part is the active area. The symmetric wires connecting the pads and the strips to the read-out electronics surround this part; C. A fully assembled PixelGEM detector, equipped with 16 APV front-end cards. The digitisation of the analog signals from the APVs is done at an external ADC card, which is connected via the grey cables; D. Front-end card carrying (from top to bottom) the 130-pin connector, the protection network, a ceramic pitch adapter, and the APV25-S1 ASIC for analog sampling of the signals induced on the readout electrodes.

The strip foil is then glued onto the one with the pixels, with the central area completely removed from the strip foil in order to open the pixels for charge collection. The strips are split in the middle and read out on both sides, in order to equalize their capacitances. The same idea has been realized also for the ones not ending at the pixel region. In Fig.2.7.A, the pixel and strip regions are displayed schematically, while Fig.2.7.B shows a photograph of the complete readout foil. The readout foil is glued onto a light honeycomb sandwich panel of 610×610 mm^2 size, which serves as a support plate and also carries the front-end electronics, the high voltage distribution circuit, and the GEM stack which consists of three GEM foils of 10×10 mm^2 active area (t = 150 μm and p = 350 mum). The efficiency of the pixel GEMs is very high. They are in operation since 2008.

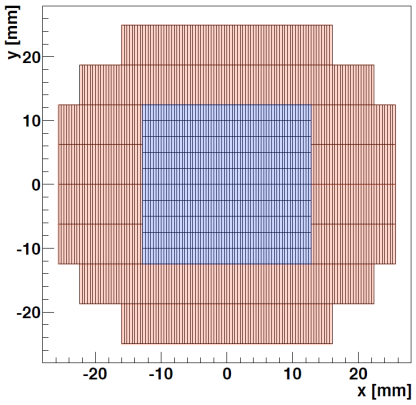

(A)

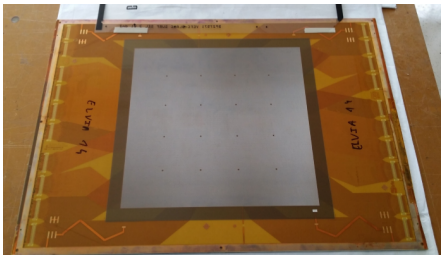

(B)

FIGURE 2.8: A. Geometry of the pixelised region of the new Micromegas detectors. The blue region consists of 400 μm$\times$2.5 mm pixels and the red region consists of 400 μm$\times$6.25 mm pixels; B. Picture of the Pixel MM with 25$\times$25 mm^2 pixel readout.

At COMPASS, twelve Micromegas detectors are used in the LAS region, between the target and SM1. The detectors of this region are exposed to a high flux of low energy electromagnetic showers, which is not screened by SM1 (up to 300 kHz·cm^{-2}) and to the influence of the fringe field of SM1. The detectors have an active area of 40$\times$40 cm^2 and consist of 1024, (200 μm thick) Cu readout strips. The typical gas mixture which is used is Ne:C_2H_6:CF_4 80:10:10. COMPASS MMs provide an efficiency $\sim$96%-98%, 5 ns of time resolution and 90 μm of space resolution.

The first prototypes used 32$\times$32 square pixels of 1 mm^2, but a study showed that the spatial resolution was not sufficient [95]. Rectangular pixels with the same width than the strips (400 μm) and with variable length depending on the proximity to the center as shown in (Fig.2.8a and Fig.2.8b) have been adopted. They showed good efficiency and space resolution $\sim$100 μm. Furthermore the use of a hybrid GEM + MM detector allowed to greatly reduce the discharge rate.

2.5.3 Large area tracker

The reduced flux in the outermost regions, covered by the Large Area Tracker allows the use of detectors such as drift chambers, straw tube chambers, and multi wire proportional counters.

Three identical drift chambers (DC) were installed in COMPASS. Their design was optimized for operation upstream of the first dipole magnet (SM1), where the total particle flux through the chamber is higher by almost a factor of three compared to the downstream side due to the low-energy background which is bent away by the magnet. One DC is installed upstream, and two DCs downstream of the SM1 magnet. All three DCs have an active area of 180 $\times$ 127 cm^2 with a central dead zone of 30 cm diameter, fully covering the acceptance of the target magnet upstream as well as downstream of SM1. The spatial resolution of a DC is 190 μm. From 2006 downstream SM1 a Drift Chamber (DC4) was installed and put into operation. Characterized by the same construction parameters of the other DCs but with increased

dimensions bringing the horizontal acceptance from 1200 to 2000 mm. A new DC, DC5 has been built and installed for COMPASS2.

To provide tracking for charged particles detected in the COMPASS SAS a system of six large area drift chambers is used. Each chamber has an active area of 500 $\times$ 250 cm^2; the spatial resolution has been evaluated in $\sim$500 μm.

Straw tube drift chambers are used for the tracking of charged particles produced at large scattering angles (15 $\div$ 200 mrad) in the Large Area Tracking section (LAT) of COMPASS downstream of the first spectrometer magnet. In total 12440 straw tubes were assembled into 15 detectors. Each detector had an active area of about $9m^2$ with a a central dead zone of 20×20 cm^2. In order to measure three projections of a particle trajectory, one station consists of three detectors, one with vertical, one with horizontal and one with inclined straw tubes. The detectors with inclined straws are rotated by 10° with respect to the vertical ones. For one straw detector (two layers), the average resolution is $\sim$200μm.

The tracking of particles at large radial distances to the beam in the SAS is mainly based on a system of multi wire proportional chambers (MWPC). A total of 34 wire layers, corresponding to about 25000 detector channels, is installed and operational. The active area is of 178$\times$120 cm^2, while the distance between anodic wires is 2 mm, allowing a spatial resolution of 1.6 mm. The diameters of their insensitive central zones increase along the beam line from 16 to 22 cm before SM2, from 50 cm to 100 cm in the last spectrometer part.

2.6 Muon identification

The muon identification is performed by two detector systems, one in the LAS and one in the SAS part. Both systems are made of a set of tracking stations and a hadron absorber followed by a second set of tracking stations covering large surfaces ($\sim$4$\times$2 m^2). Muon Wall 1 uses 8+8 stations of aluminum Mini Drift Tubes (MDT) with square cross section, measuring two projections and the absorber is a 60 cm long iron block. Muon Wall 2 employs 6+6 planes of drift tubes measuring three projections and a 2.4 m long concrete block. The MW1 averaged tracking efficiency per plane is typically 91%, while for MW2 it is between 81 and 84%.

2.6.1 Rich Wall

A large-size (4.86$\times$4.22 m^2) tracking station (Rich Wall), is positioned downstream of RICH-1, directly in front of the ECAL1 electromagnetic calorimeter. It consists of eight layers of MDT modules. Mechanically, the Rich wall detector is similar to one station of Muon Wall 1. The tracking planes are alternated to converter layers made of a sandwich of three plates (steel/lead/steel), resulting in a total converter thickness of about 3 radiation lengths. The Rich wall tracker station performs a twofold function in the COMPASS spectrometer. First, it measures the particle trajectories downstream of RICH-1, thus allowing a better reconstruction of the particle trajectories in the RICH-1 volume. Second, it acts as preshower for the ECAL1 electromagnetic calorimeter, thus improving the spatial resolution of the calorimeter itself.

2.7 Calorimetry

2.7.1 Hadron calorimeters

The COMPASS spectrometer is provided with two hadron calorimeters positioned before the Muon Wall detectors. They are used both for the hadron energy measurement and for trigger purposes in semi inclusive muon scattering events. HCAL1 has a modular structure, each module consisting of 40 layers of iron and scintillator plates, 20 mm and 5 mm thick respectively, amounting to 4.8 nuclear interaction lengths. The hadron calorimeter 2 (HCAL2) takes the form of a matrix of 22 $\times$ 10 modules, arranged on a mobile platform. The overall thickness of the counters is 5 nuclear interaction lengths for pions and 7 for protons. The linearity of the energy response is of the order of a few percents for both calorimeters over different energy ranges: 0-25 GeV for HCAL1 and 10-100 GeV for HCAL2. The energy resolution can be parametrized as:

- HCAL1 σ/E =59.4%/$\sqrt{E}\otimes$ 7.6% for pions;
- HCAL2 σ/E =65%/$\sqrt{E}\otimes$ 5% for pions;

where E is expressed in GeV.

2.7.2 Electromagnetic calorimeters

An electromagnetic calorimeter (ECAL1), with overall dimensions of 4.0$\times$2.91m^2 is assembled and positioned upstream of the HCAL1 hadronic calorimeter. The ECAL1 calorimeter is formed by blocks of lead glass of different size: centrally 576 blocks of 38.2×38.2 mm^2, in the intermediate region 580 blocks of 75×75 mm^2 and the most external region is equipped with 320 blocks with dimensions of 143×143 mm^2. It allows measurements of reaction channels with the production of low energy prompt photons and/or neutral pions.
The electromagnetic calorimeter ECAL2 in the SAS part of the COMPASS spectrometer consists of 2972 lead glass modules with 38$\times$38$\times$450 mm^3 dimensions amounting to 16 radiation lengths. A high energy gamma ray (or electron) incident on ECAL2 develops an electromagnetic shower inside the lead glass. The electrons and positrons from a shower emit Cherenkov light on their way through the glass. The amount of Cherenkov light is proportional to the energy deposited in each counter. Each lead glass block is viewed at one end by a PMT. Linearity response is better than 1% until 40 GeV; the energy and spatial resolutions have been measured as:

- σ/E =5.5%/$\sqrt{E}\otimes$ 1.5%;
- σ_x =6 mm/$\sqrt{E}\otimes$ 0.5 mm;

with E in GeV.

For the 2016 DVCS run a new electromagnetic calorimeter (ECAL0) was introduced to perform precise DVCS measurements. ECAL0 is a device of "shashlyk"-type (scintillator, lead), in which Micro-pixel Avalanche Photo Diodes (MAPD) with ultra-high pixel density (up to 15 thousand pixels / mm^2) are used, instead of the traditional photomultiplier tubes for the first time in the electromagnetic calorimeter of a large physical experiment. This type of photon detectors has been developed

and tested for more than 20 years. The MAPD with the pixel density of 15 thousand pixels.mm^{-2} were developed at JINR by the Z. Sadygov's team.

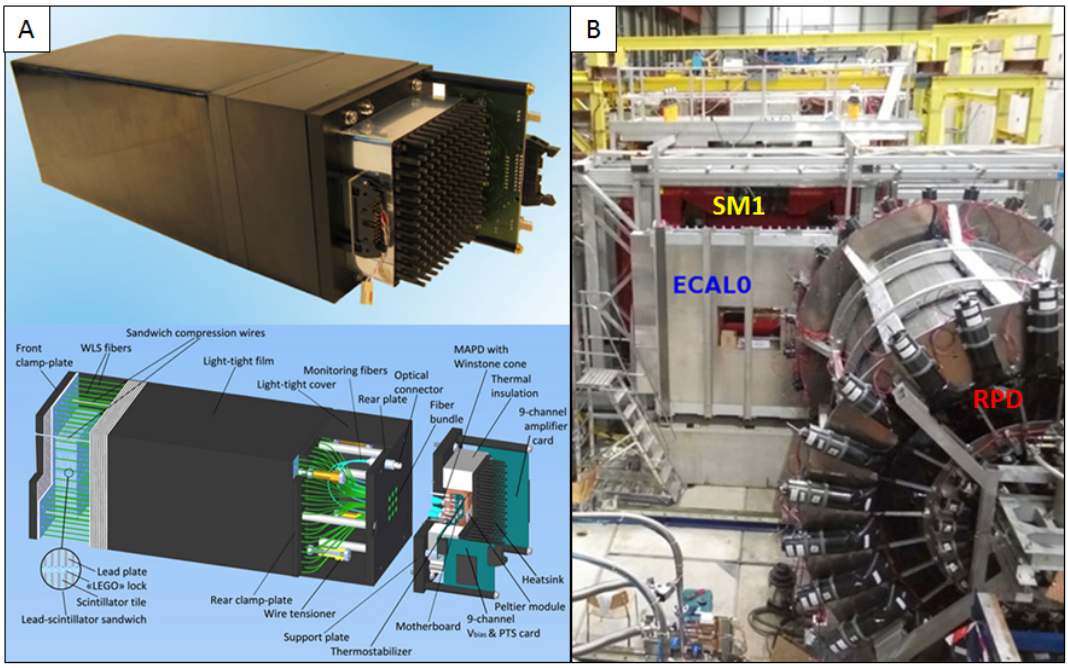

FIGURE 2.9: A. Top: a Shashlyk module with the MAPD connected to it. Bottom: Schematic of the Shashlyk module and MAPD system; B. View of COMPASS spectrometer setup inside the experimental hall 888 at CERN. Part of RPD detector, ECAL0 and the SM1 magnet (red color behind the frames) can be seen.

In April 2016 the ECAL0 was fully assembled, tested and included in the COMPASS setup. ECAL0 effectively registers direct photons from the DVSC reactions in a wide energy range (0.2 – 40 GeV); and together with ECAL1 effectively registers π^0.

2.8 Triggering

The COMPASS trigger system is used to perform several tasks: select event candidates in a high rate environment with a decision time $\sim$1 μs and minimum dead time, provide an event time reference and generate the signals for the analog to digital converters, finally to trigger the readout of detectors and front end electronics. The setup for the muon beam is designed for an as large kinematic acceptance in Q^2 as possible ranging from $Q^2 \sim 0$ to the maximum allowed by kinematics. A large range in the muon energy loss is required too. The trigger system is based on fast hodoscope signals, energy deposits in calorimeters and a veto system (see fig. 2.10). Depending on the kinematics of the reactions different elements are combined to form the trigger signal. Due to the high rate in the central region of the spectrometer the hodoscope is segmented in four subsystems consisting of two hodoscope stations each, the inner (H4I, H5I), the ladder (H4L,H5L) , the middle (H4M, H5M) and the outer system (H3O, H4O). Events belonging to the kinematics regime with $Q^2 >\sim 0.5$ GeV/c^2 are mainly triggered by using the scattered muon information only. The muons are measured in two horizontal scintillator hodoscopes in order

to determine the projection of the muon scattering angle in the non-bending plane and to check its compatibility with the target position (vertical target pointing). To suppress events due to halo muons, a veto system is added to the trigger system.

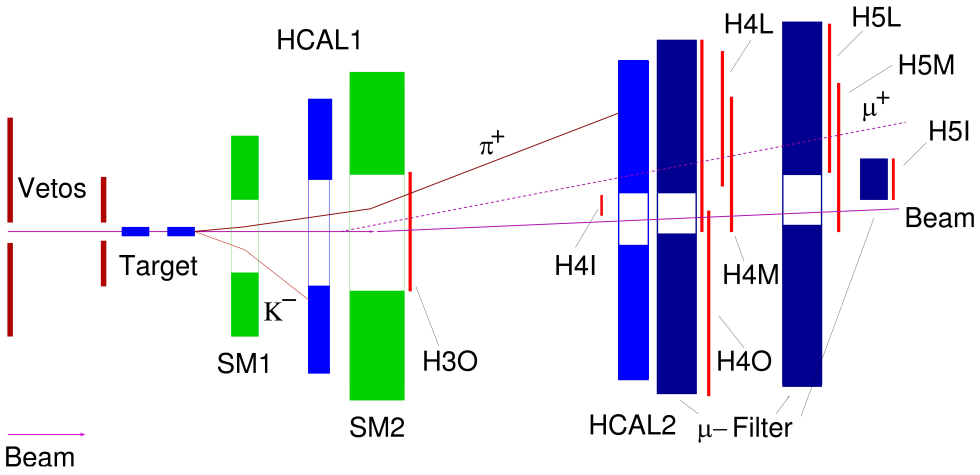

(A)

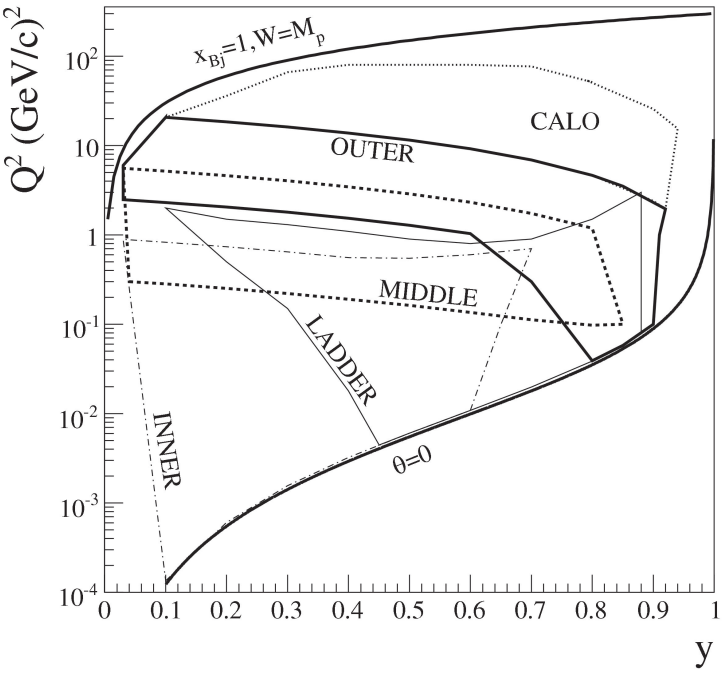

(B)

FIGURE 2.10: A. Schematic view of the location of the trigger components in the setup; B. The range in y and Q^2 for the four hodoscope trigger subsystems and the standalone calorimeter trigger.

For the quasi-real photon regime (low Q^2) the target pointing technique can not be used since muon scattering angles are close to zero. These events are selected by measuring the energy loss with two vertical scintillator hodoscopes using the bending of the muon track in the spectrometer magnets.

2.9 Data Acquisition

The hardware of the Data Acquisition System consists of several layers of different electronics. The layer closest to the detector is called frontend electronics (FEE). It's task is to capture signals directly from the detectors and convert them to digital values. There are approximately 300000 data channels coming from the first layer. This data is readout by roughly 250 of **CATCH**, **GeSiCA**, and **Gandalf** concentrator modules based on **VME standard** and grouped into sub-events (i.e. partial information about the progress of particle in the detector). The readout of sub-events and assembly and buffering of events is carried out by modern **FPGA cards** (Field Programmable Gate Array) which replaced original and nowadays performance wise obsolete hardware based on PCs. Data taking process is synchronized by the **TCS** (Trigger Control System).

The new software of DAQ is conceptually inspired by the ALICE software, however it is more lightweight and thus easier to use and to maintain. The new software consists of five main types of processes:

1. **Master process** - a Qt console application.
2. **Slave process** - an application that controls and monitors a custom hardware (e.g FPGA, ...).
3. **GUI** - a Qt GUI application designed for controlling and monitoring of the whole DAQ.
4. **Message Logger** - a console application that receives informative and error messages and stores them into the MySQL database.
5. **Message Browser** - a GUI application that provides an intuitive access to messages from system (stored in the database) with an addition of online mode (displaying new messages in real time).

The trigger signals from the TCS were transferred via the CATCH to all connected FEE boards. At the beginning of a data taking run the CATCH initializes all connected front-end boards. The GeSiCA works similar to the CATCH, but is optimized for the readout of GEM and Silicon and RICH-1 gaseous PDs. Through optical fibres (S-link)[1]the data collected from CATCH or GeSiCA are then transferred to FPGA based special multiplexers and then via a special multiplexer switch it is connected to the event builders. Before the upgrade of the DAQ the signals were received by readout buffer PCs (ROB). The ROBs stored the received data on PCI cards called "spill buffers". For further processing the information of each sub-event in the ROBs, which do not contain the full information from all detectors, are transferred via three Gigabit Ethernet switches to the event builder (EB) computers.

The finalized and filtered events in the EBs are asynchronously transferred through the network via a dedicated 10 GBps Ethernet switch to the CERN central data recording system, where they are temporarily stored on disk, before they get migrated to the tapes of the CERN Advanced STORage system[1] (CASTOR).

[1]CASTOR - CERN Advanced STORage system web page, http://castor.web.cern.ch/

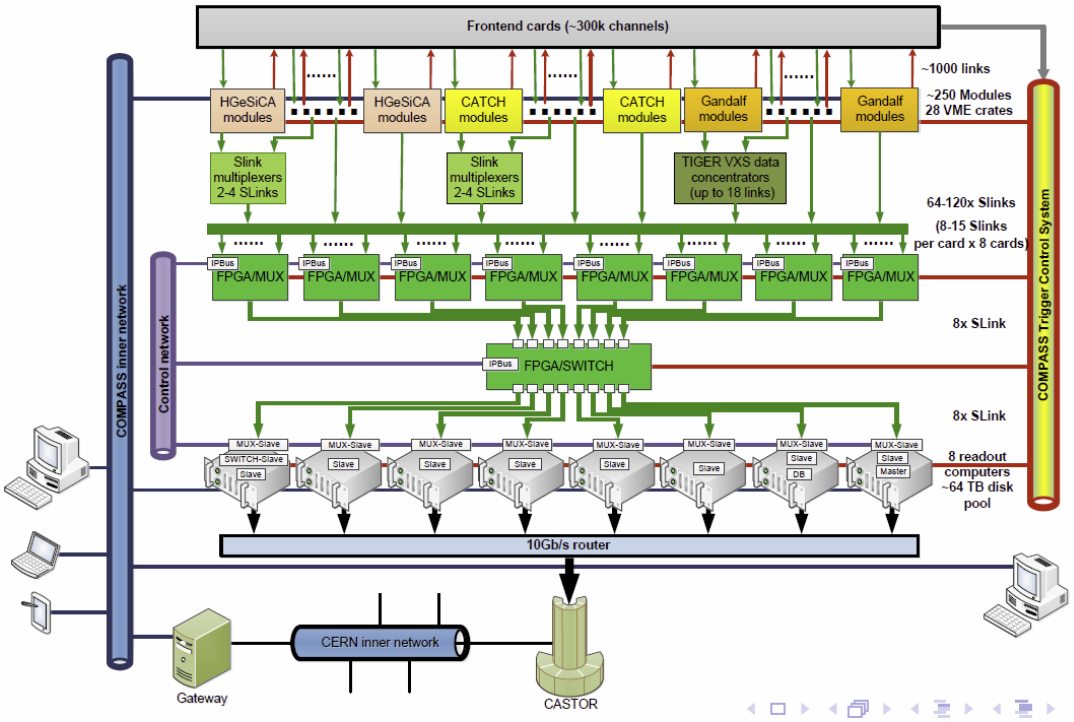

FIGURE 2.11: Working principle and schematic diagram of COMPASS DAQ

2.10 Event reconstruction

The huge amount of data ($\sim$ 1PB/y) collected by the experiment requires the availability of sufficient computing power to reconstruct the events at a rate comparable to the data acquisition rate. The required CPU power is estimated to be 200k SPECint2000 units[2], which are provided currently by 200 Linux Dual-CPU PCs out of the CERN shared batch system. Event reconstruction is performed by a fully object oriented program, CORAL[3], with a modular architecture and written in C++. The input of the reconstruction software is represented either by the raw data collected by the experiment or Monte Carlo data. The data files produced by the COMPASS acquisition software contain the raw information from the detectors, digitized by the front-end electronics. Two initial processing phases are needed to prepare the input to the track finding algorithm. In the first phase, called decoding, the information on the fired detector channel (either wire, pad, or cell, depending on the detector type) is extracted from the raw data. In the second phase, called clustering, detector channels that are fired by the same particle are grouped together. The result of the reconstruction phase (track parameters, vertexes, calorimeter clusters, PID probabilities, detector hit patterns, etc.) is stored in output ROOT trees, called mini Data Summary Tapes (mDST), that are distributed to home computing centers and serve as input for all the physics data analysis. The data reduction factor between the input raw data and the output mDSTs is about 100. Large DST files, storing the detector

[2]Standard Performance Evaluation Corporation, http://www.spec.org/ http://www.spec.org/cpu2000/CINT2000/

[3]The COMPASS Reconstruction and AnaLysis Program (CORAL), COMPASS Collaboration. Available at: http://coral.cern.ch.

digits and clusters in addition to the tracking, vertex, and PID information are also created and kept at CERN on tape.

A dedicated Detector Control System (DCS) provides slow control and logging the running informations of all the detectors and stores the information in a dedicated ORACLE based database at CERN computing facility. Alignment, calibrations, event quality selection are performed before the full analysis chain.

Chapter 3

COMPASS RICH-1

COMPASS RICH-1 [96] [97] [67] [98] [99] is an unique and extraordinary detector. Before the HMPID of the ALICE experiment at CERN, it had the largest single photon detection surface based on gaseous PDs. It is equipped with all main state of the art technologies in the field. It has been an honor and an amazing experience in this five years to work on and even inside of this very special complex system. In this chapter an overview of COMPASS RICH-1 components and a brief summery of its performance before the hybrid PD upgrade are presented.

Two gaseous RICH counters were originally foreseen in the COMPASS proposal [90] (see Fig.3.1) to provide hadron identification in a very large momentum range; RICH-1 (see Fig.3.2) has successfully been built and improved in order to meet the challenging COMPASS PID requirements while the construction of COMPASS RICH-2 has been postponed and never done. As explained in Section-3.4, a gaseous RICH with fluorocarbon radiator is the optimal choice for π-K separation in a momentum range between 3 and 55 Gev/c as required for COMPASS RICH-1 over an angular acceptance of $\pm$250 mrad in the horizontal plane and $\pm$180 mrad in the vertical plane, with beam rates up to 40 MHz and trigger rates up to 30 kHz.

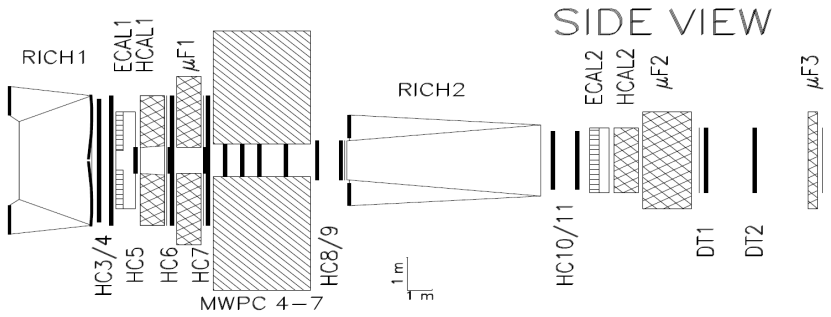

FIGURE 3.1: Part of the COMPASS set-up from the Proposal of the Experiment: two RICH counters were foreseen.

The RICH-1 detector uses a 3 m long gaseous C_4F_{10} radiator, a 21 m^2 large focusing VUV reflecting surface and two kinds of photon detectors (PDs) (Fig.3.3): MAPMTs and MWPCs with CsI photocathodes, placed outside of the acceptance and covering a total surface of 5.5 m^2. It was designed in 1996 and it operates since 2002; its performance has increased in time thanks to progressive optimization and in particular to a major upgrade which was implemented in 2006.

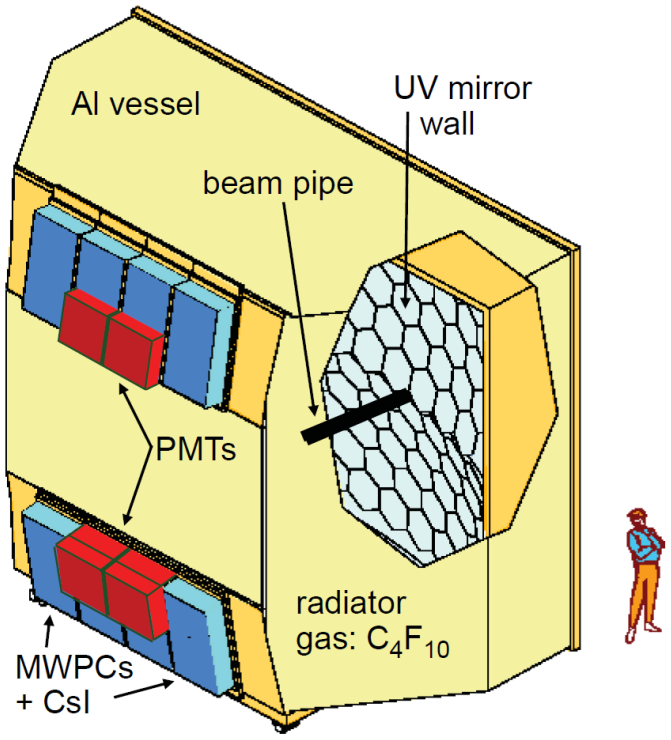

FIGURE 3.2: Artistic view of COMPASS RICH-1.

The new upgrade described in this thesis and implemented in 2016 completes the outstanding performance of the COMPASS RICH-1 detector.

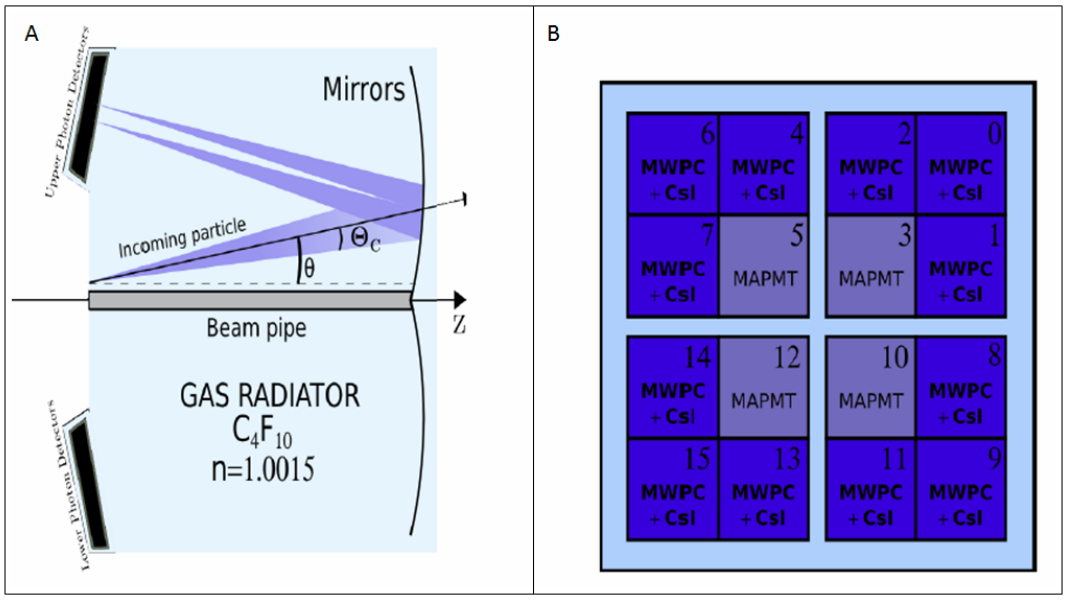

FIGURE 3.3: A. The Cherenkov photon propagation and focusing. B. Photon detectors (not to scale).

3.1 Description of different parts of RICH1

3.1.1 The RICH-1 vessel and the gas radiator

Fig. 3.4 shows the RICH vessel: it consists in an aluminum structure closed by Al plates; it has a length of 3 m, a width of 6 m and a height of about 5 m. The front and rear windows need to hold the radiator gas hydrostatic pressure with a minimum amount of material, being in the spectrometer acceptance. They consist in a sandwich of two aluminum foils and a layer of rigid foam, for a total of 2% X_0. In the central region, where the beam is passing, their contribution to the material budget is reduced to 0.6% X_0 each.

FIGURE 3.4: picture of the RICH-1 vessel during transport

A cylindrical pipe of 100 mm diameter has been installed (see Fig. 3.5) and filled with helium to reduce the amount of material in the beam region (>10% X_0 from the radiator gas) and to protect the RICH from the large amount of Cherenkov photons generated by the beam particles. The original beam pipe, made of 150 μm thick stainless steel, has been replaced in 2012 by a lighter pipe, (see Fig. 3.6) made of 4 layers of metalized BoPET (25 μm BoPET + 0.2 μm Al): the contribution to the total material budget by the new pipe for beam particles is 0.08% X_0 (plus 0.06% due to helium). The installation of this pipe was the start of my work regarding RICH-1 and was a unique opportunity to work inside the RICH vessel.

To guarantee both low Cherenkov thresholds (2.5, 9, 17 GeV/c for π, K, p respectively) and low chromatic dispersion, C_4F_{10}, the heaviest fluorocarbon in gaseous phase at STP, was chosen as the RICH-1 radiator gas. To avoid excessive stress on the vessel windows the gas is kept at atmospheric pressure (plus 100 Pa with a 10 Pa maximum allowed deviation at a reference point, on the top of the vessel). A dedicated gas system [100] continuously circulates the gas in a closed loop circuit at a rate of about 2 m^3/h.

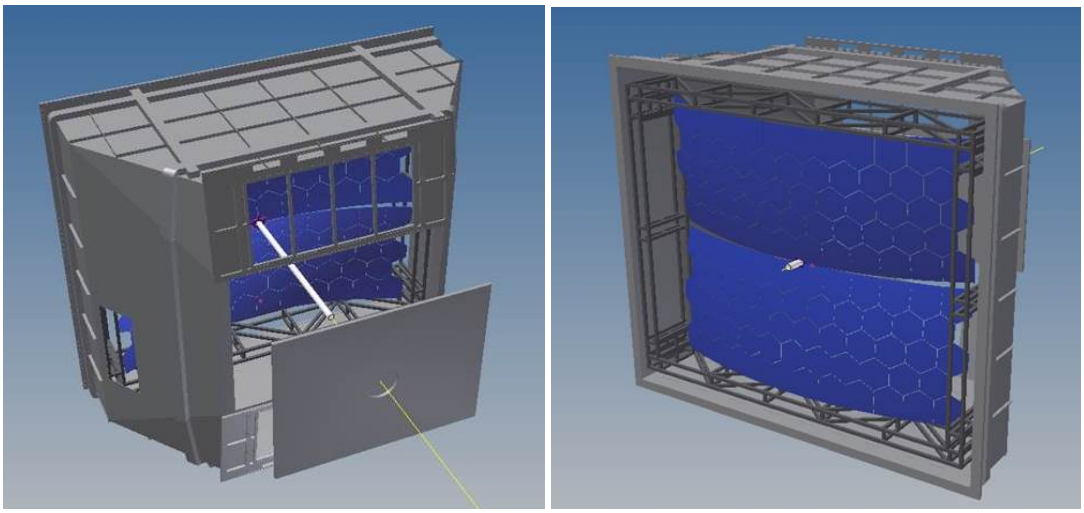

FIGURE 3.5: Two views of the opened RICH-1 vessel with the mirrors in blue and the beam pipe in white done with CAD software.

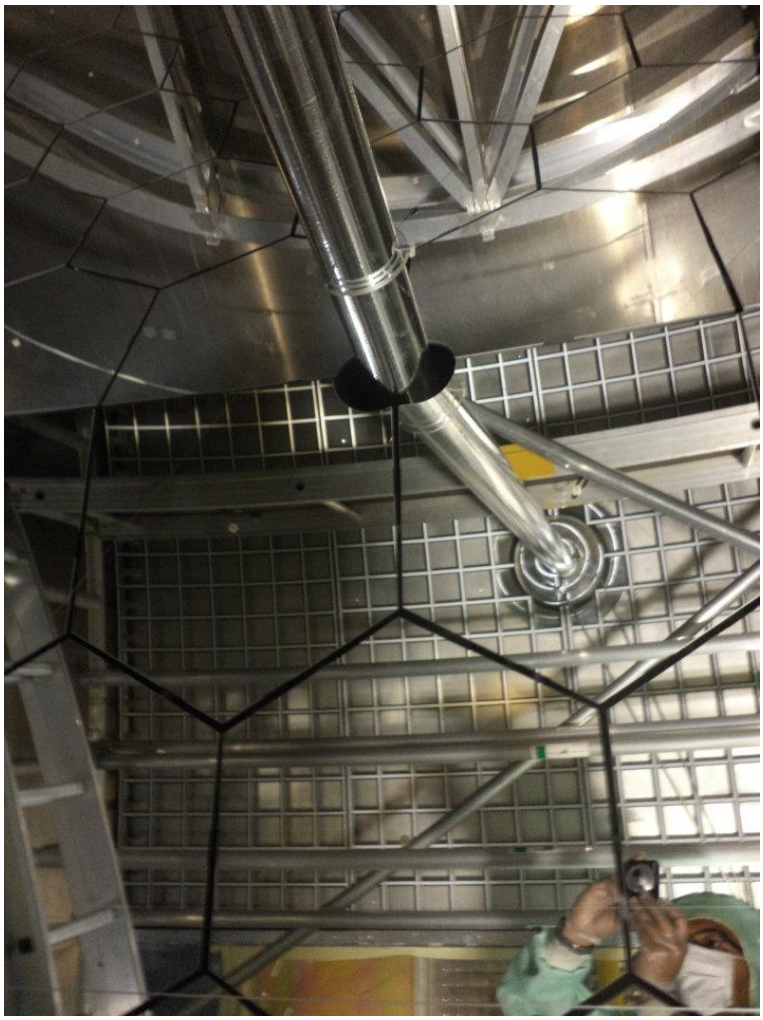

FIGURE 3.6: Picture of a part of the light beam pipe inside RICH-1 and mirrors (picture credit: the author).

High transmittance for Cherenkov photons is guaranteed by reducing the contamination from UV absorbing impurities using Cu catalyst filters (operated at 40°C) and 5A molecular sieves (at 15°C) to keep moisture and oxygen contamination levels below 1 ppm and 3 ppm respectively.

Before and after the COMPASS running periods, a storage tank keeps the C_4F_{10} in liquid phase; during normal operation the compressors of the gas system suck the C_4F_{10} from the vessel at a fixed rate and force it through the filters and a liquefier to the storage tank, where it evaporates and it is sent back to the vessel at the rate needed to exactly compensate for compressor sucking, atmospheric pressure variations and temperature effects on the vessel and the gas. The leaks of the precious radiator gas are kept at the level of $\sim$60 l/day.

The vessel has to be kept at atmospheric pressure during the C_4F_{10} filling and recovery operations too, at the beginning and at the end of the running periods: efficient separation between N_2 and C_4F_{10} is obtained by operating the liquefier at a pressure larger than 6 bars and at a temperature lower than -35°C, where the equilibrium vapour pressure of C_4F_{10} is $\leq$ 20 kPa.

A continuous monitoring of the levels of O_2 and H_2O contamination and the total amount of C_4F_{10} in the system is performed and the transparency is frequently checked by measuring the light transmission in an automated system based on a D_2 lamp, a monochromator and UV sensitive PMs. The stability of the radiator gas mixture (typically: C_4F_{10}/N_2 = 97/3) is measured by a sonar-based system in the same set-up. [101]

Fig. 3.7 shows an example of a radiator transparency measurement: light transmission values larger than 88% in the VUV wavelength domain of the CsI-based photon detectors (165-210 nm), close to the limit provided by Rayleigh scattering process, are routinely obtained.

A cleaning operation is applied before usage to the commercially available C_4F_{10}, which is full of impurities [102]: a system in which the C_4F_{10} circulates in closed loop through activated carbon and 3A molecular sieves and condenses in a cold section where the gas component is vented out has been built for this purpose; the fraction of material, which is lost in this cleaning operation can vary between 0.1 and 0.4 depending on the level of the initial contamination.

A dedicated system is providing up to 20 m^3/h circulation flow between the top and the bottom of the vessel: it has been implemented to avoid the formation of thermal or composition gradients in the radiator gas volume.

An on-call expert is always available during the whole data taking period for regular checks and immediate intervention in case of an emergency.

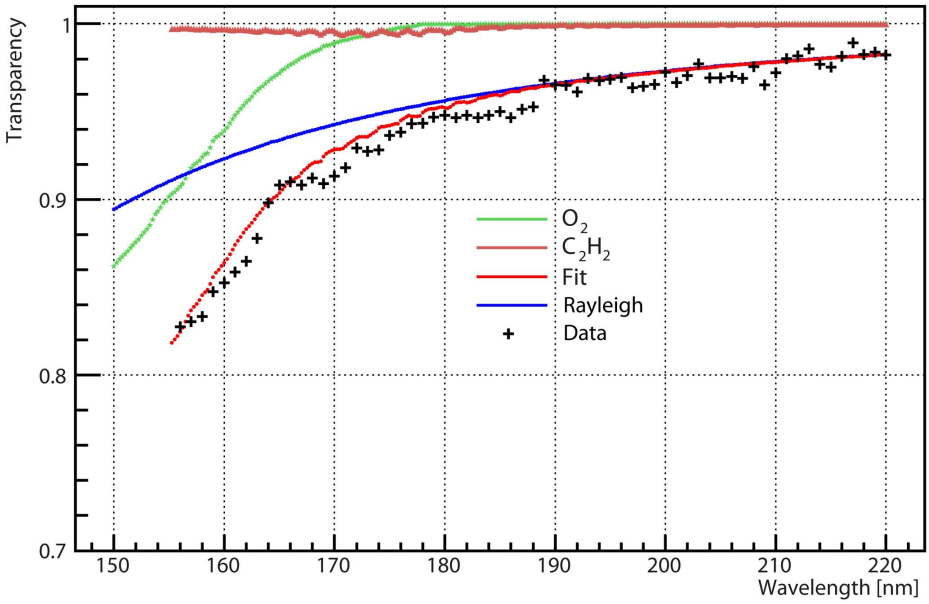

FIGURE 3.7: Typical example of a transparency curve for the C_4F_{10} of COMPASS RICH-1: the fitted transparency curve (in red) corresponds to contamination levels of O_2 = 2.3 ppm, H_2O = 0.0 ppm, C_2H_2 = 0.03 ppm.

3.1.2 The mirrors

A 21 m^2 mirror wall [103] (see Fig. 3.8) reflects the Cherenkov photons generated inside the RICH-1 and focuses them on the photon detectors placed above and below the acceptance region. The mirror wall is divided in two spherical surfaces of 6.6 m radius and formed by 116 spherical mirror units: 68 regular hexagons with 522 mm long diagonal and 48 larger pentagons. The reflecting surface consists of an 80 nm thick Al layer deposited on a 7 mm thick borosilicate glass substrate and covered by a 30 nm tick MgF_2 protective layer.

Each mirror has been fully characterized before installation and provides a VUV reflectance of 83-87% in the range between 165 and 200 nm. The reflectance of COMPASS mirrors has remained stable in time except an initial degradation for the smallest wavelengths.

Fig. 3.10 shows the mechanical structure supporting the mirrors. It was designed to minimize the amount of material in the acceptance while preserving the accurate positioning of the mirrors. It has a net-like configuration, with nodal points laying on a sphere with a precision better than 1 mm.

The mirrors are arranged in a mosaic-type composition with small clearance between them, corresponding to 4% of the total reflecting surface. They are suspended at the center to the nodal points of the support structure via a joint which allows for small angular adjustments to be applied rotating two fine screws [103] (see Fig. 3.9)

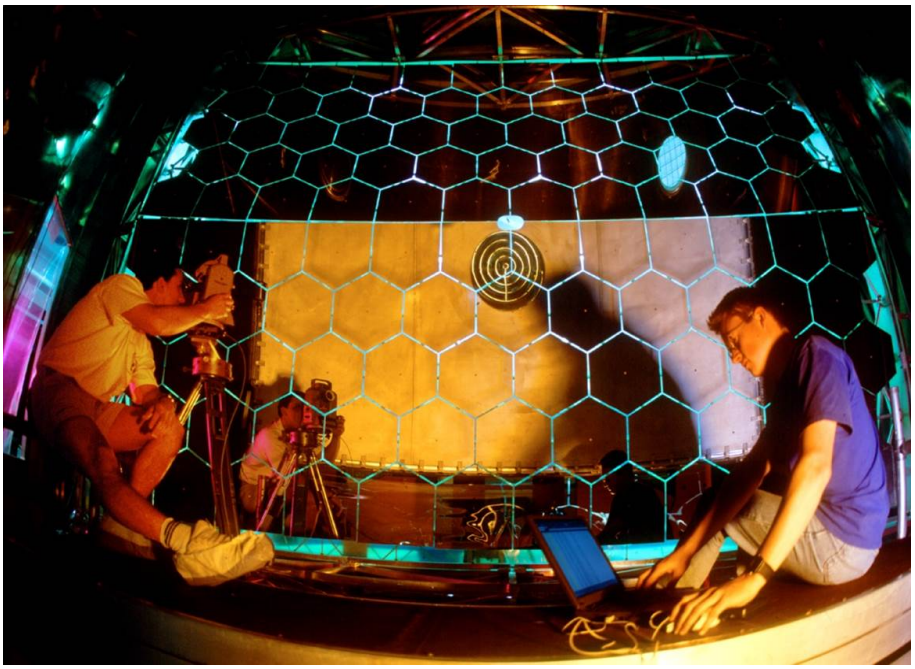

FIGURE 3.8: Picture of the mirror wall taken during the mirror alignment operation

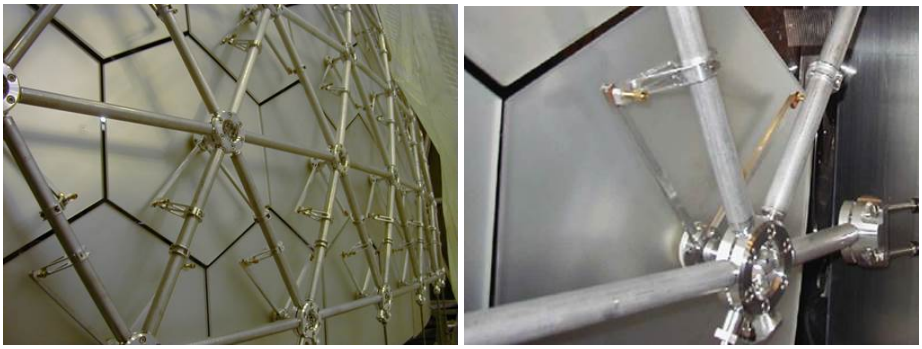

FIGURE 3.9: Picture of the back side of the mirrors and of the adjustment screws

3.2 The CLAM system

To avoid the long, risky and difficult alignment operations using "theodolite autoreflection" procedure (opening the RICH-1 vessel, mounting a scaffolding structure inside it and working close to the mirrors) and to frequently monitor the mirror alignment during the data taking, an original method, called CLAM [**lsteiger**] [104] [105], was developed and implemented in 2007. Four high resolution cameras, fixed on the corner of the vessel and facing the mirror wall (see Fig. 3.11) record the reflected image of a rectangular grid which is placed inside the vessel, close to the front wall. To increase the contrast of the images the grid is made of retro reflective material and equipped with optical targets while the scene illumination is provided for each camera by LED light sources located near the camera positions.

FIGURE 3.10: Picture of the mirror support structure: the nodal points are connected by light Al pipes

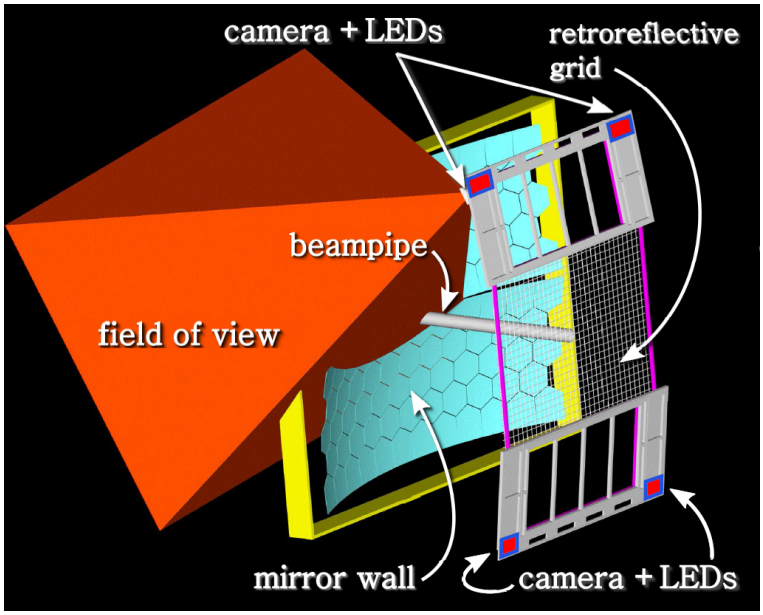

FIGURE 3.11: The CLAM hardware components; in red the field of view of one camera

The rectangular grid image (see Fig.3.12a) is seen by a camera (see Fig.3.12b) as a set of intersected conics: whenever neighboring mirrors have a relative misalignment, the conics lines appear to be broken and the shift of the line images provides the direction and amount of the relative misalignment. Individual calibration constants are needed for each mirror position to apply this procedure: they have been previously evaluated with accurate laboratory measurements.

The stability of the mirror orientation during the running period is checked by comparing images collected at different times: many slow continuous motions have been

detected with maximum observed tilts of about 150 μrad.

It is possible to extract from the images the absolute position of the center of curvature of each individual mirror [106] [**lsteiger**] using photogrammetry tools for the complete characterization of each CLAM camera (with its optical system) and for the description of the geometrical position of each optical target inside the RICH.

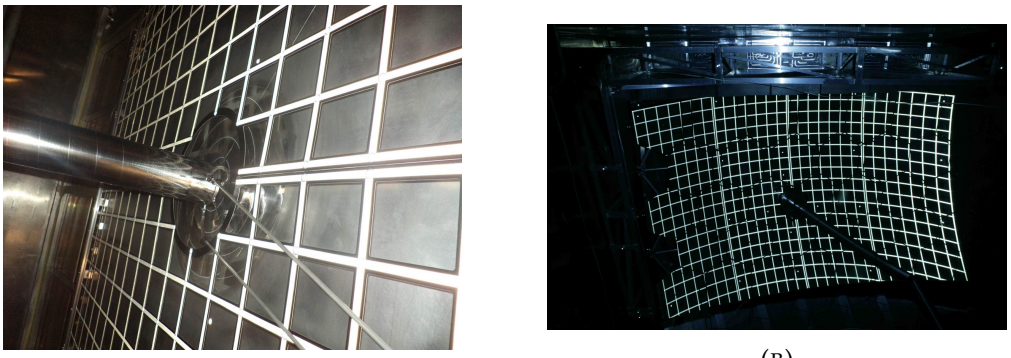

(A) (B)

FIGURE 3.12: A. Picture of the retro reflective grid used for CLAM with a part of the light beam pipe; B. Typical CLAM photo showing the image of the retro-reflective grid on the mirrors.

3.3 Photon detectors

3.3.1 The MWPC-based Photon Detectors

Between 2006 and 2010 RICH-1 [96] [97] used as photon detectors eight MWPCs [107] (see Fig. 3.15) having 576 $\times$ 1152 mm^2 active area, each equipped with two square CsI-coated photocathodes (see Fig. 3.13), segmented in pads.

The principle of operation and the main parameters of this PDs [108] as defined and optimized by the RD26 Collaboration have already been discussed in Chapter-1) and shown in Fig.1.14. The parameters are: 2 mm for each anode-cathode gap, anode wires with diameter = 20 μm and pitch = 4 mm, cathode wires with diameter = 50 μm and pitch = 2 mm, cathode pads of 8$\times$8 mm^2. Each photocathode has 72$\times$72 pads which are individually read by the electronics, for an original total of 82944 channels. Tight mechanical tolerances have been imposed in the construction phase to all components of the PDs and to their assembly (see Fig. 3.15), (50 μm for the anode-cathode gaps, for instance), and great care has been put to all aspects of the construction of the MWPCs and the large quartz windows which separate the radiator gas from the pure methane used in the MWPCs (see Fig. 3.13).

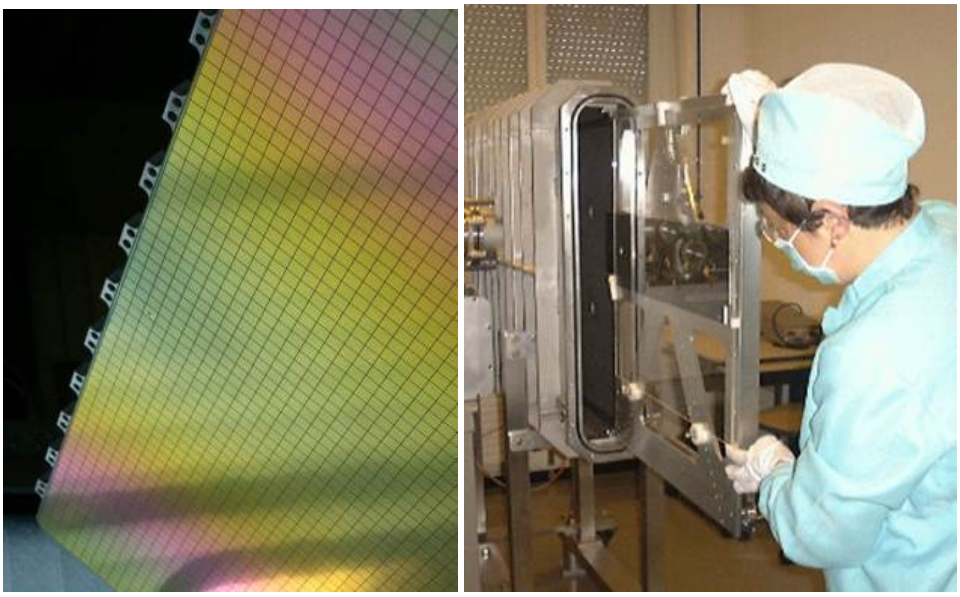

FIGURE 3.13: Picture of a CsI-coated photocathode and of a quartz window during the transparency measurement operation performed by Silvia DallaTorre.

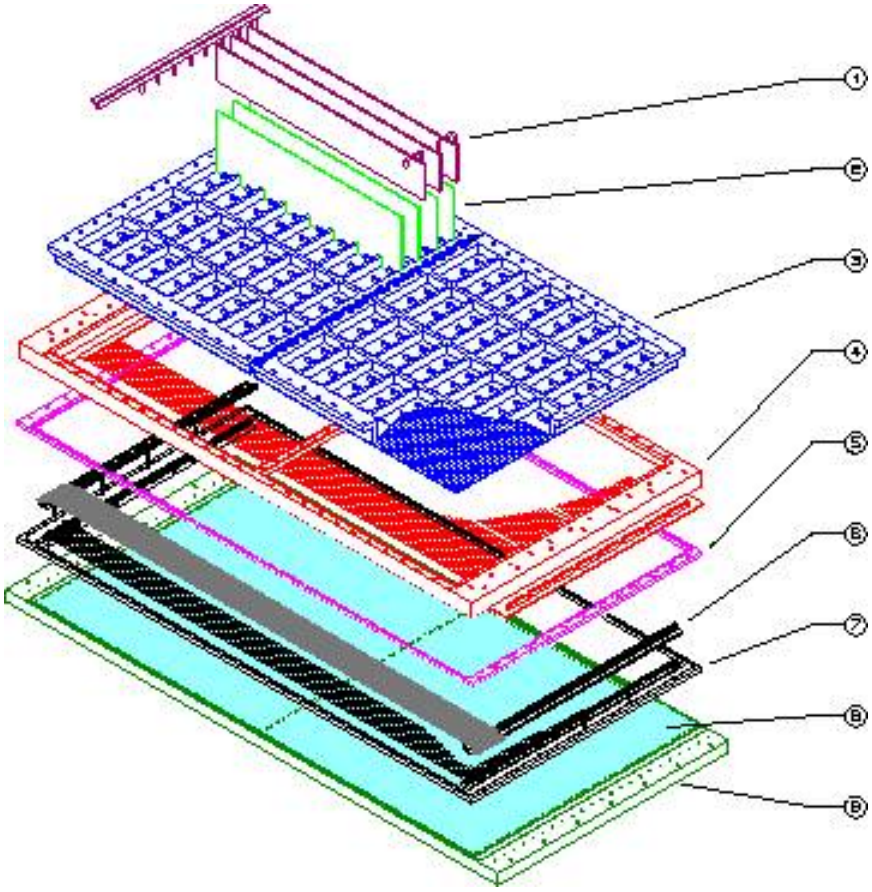

FIGURE 3.14: Computer Aided Design of COMPASS RICH-1 MW-PCs. Performed by Giorgio Menon

FIGURE 3.15: The structure and some details of RICH-1 MWPCs.

The CsI coating of the photocathodes (see Fig 3.16) was performed at CERN using the evaporation setup, which will be described in details in Chapter-7, and dedicated tools and procedures were developed for the transport and handling of the photocathodes (see Fig 3.17), in order to avoid exposure to air, in particular to water vapour, which would result in a degradation of the quantum efficiency. [78] [109], as already described in Chapter-1. During all phases of the handling and storage they were kept in a controlled atmosphere with O_2 level below 50 ppm and flushed with clean, dry gas.

(A)

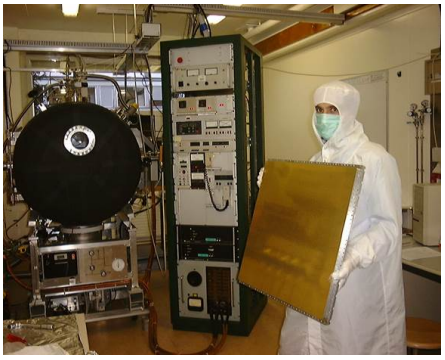

(B)

FIGURE 3.16: Pictures of the CERN CsI evaporation plant and of the COMPASS photo-cathode in hand of my supervisor.

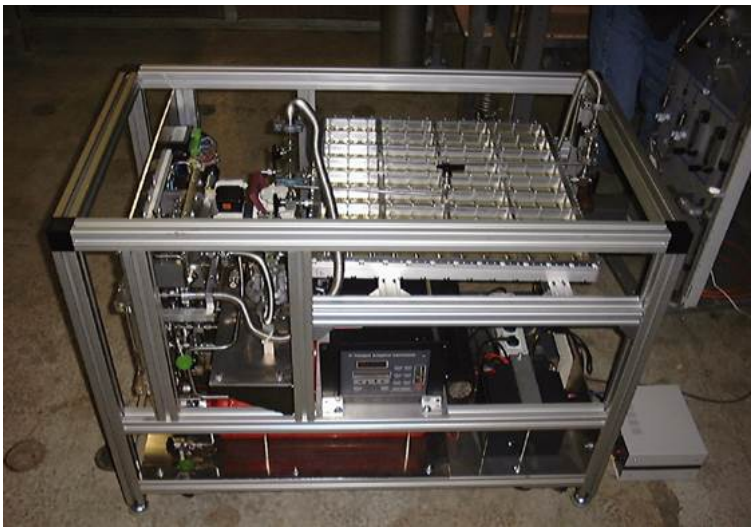

(A)

(B)

FIGURE 3.17: Pictures of the COMPASS photocathode transport system and of the the installation glove-box.

The MWPCs with CsI photocathodes were providing gains between 10^5 and 10^6 when tested in the laboratory, but they can only be operated stably in the COMPASS experimental environment at gains not exceeding 3×10^4: for larger gains they exhibit occasional electrical instabilities with long ($\sim$1 day) recovery time, clearly related to the combined effect of the level of the applied voltage and the ionizing particle flux, as demonstrated by a series of dedicated studies and validation tests performed on these PDs at the CERN Gamma Irradiation Facility.

The readout [110] [111] in use before 2006 had an integration time of 0.6 μs, which was also acting as a detector memory and a 3.5 μs long baseline restoration time, generating a significant data acquisition dead-time. For this reason the MWPCs with CsI photocathodes covering the outer region (75% of the photon detection surface, corresponding to 62208 channels) have been equipped in 2006 with the readout system [112] based on the APV25-S1 chip [113]: which is used also for the new hybrid PDs and will be presented in Chapter-8, before discussing the performance of the new hybrid PDs. With this electronics, the measured noise level of the MWPC based PDs is $\sim$680 e^-, to be compared with the average collected signal amplitude of $\sim$9000 e^-.

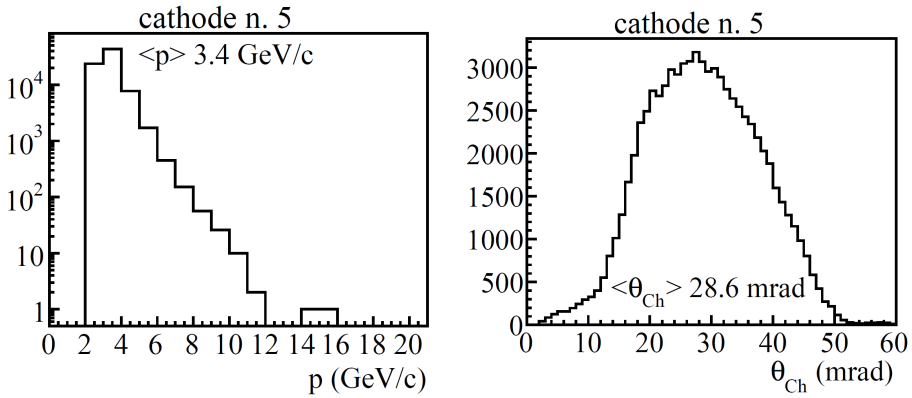

FIGURE 3.18: Momentum distribution and Cherenkov angle distribution of the pions with a ring fully contained in one of the photocathodes (cathode n. 5).

The variation of the CsI QE versus time has been studied [114] by monitoring the mean number of detected photons per incoming charged pion in the COMPASS data for the period from 2006 to 2011.

The data taking conditions were different each year (different triggers, targets and beams); to select samples as homogeneous as possible, the same cuts have been applied to the reconstructed particle trajectories.

After selecting tracks identified as pions by means of the particle identification criteria described in [115], based on a likelihood analysis, a Cherenkov ring has been associated to each track by the standard patter recognition algorithm.

The amount and distribution of the background photons in the detectors is non-homogeneous and depends on the data taking conditions; variations in the the radiator gas characteristics, in the electronics settings and in the MWPC HV induce systematic effects which have been estimated to be small, apart from those due to a reduction by 20 V of the HV anodic bias of the MWPCs for 2010 and 2011. A correction (about 2% of the number of detected photons) has been evaluated and applied to compensate for the HV reduction.

The IBF to the photocathodes, integrated over the considered period, is smaller than 10 μC/cm^2, corresponding to less than 1% of the flux reported in literature [78] [109] to cause significant QE reduction as described in Chapter-1.

A set of tracks has been selected for each of the twelve CsI photo-cathodes requiring that the associated Cherenkov ring is completely accepted to the photo-cathode: the selected tracks are characterized by low momenta (with mean values between 3 and 4 GeV/c) and therefore the Cherenkov angle distributions are statistically poor in the region of the largest values of the Cherenkov angle, as can be seen in Fig. 3.18, where the distribution of the pion momenta for rings fully contained in one of the cathodes (cathode n. 5) is presented. In the same figure the Cherenkov angles distribution for the associated rings is shown.

The value of the Cherenkov angle θ_{Ch} and the number of detected photons N_{ph} for each ring are obtained. The data are grouped in 1 mrad wide θ_{Ch} bins and for each bin the mean value of the N_{ph} distribution is computed. In Fig. 3.19 the mean value of the N_{ph} for each θ_{Ch} bin and for all cathodes is plotted for year 2006. The detected photons N_{ph} are expected to include a background contribution, N_B, with a uniform

distribution, corresponding to a linear dependence on θ_{Ch} and a signal component, N_S following the Frank and Tamm distribution (Eqn.3.1), implying a $\sin^2(\theta_{Ch})$ dependence. The fit to the N_{ph} distribution is performed with the function:

$$N_{ph}(\theta_{Ch}) = p_0 \cdot sin^2(\theta_{Ch}) + p_1 \cdot \theta_{Ch} \tag{3.1}$$

where p_0 and p_1 are free parameters; the fit allows to separately determine the signal N_S and the background N_B contributions. It is applied to the distribution of $N_{ph}(\theta_{Ch})$ in the central range of θ_{Ch} values, as shown by the continuous red lines in Fig. 3.19, because for the large θ_{Ch} bins the statistics is poor and for small θ_{Ch} bins the measured distribution is not following the Frank and Tamm law, due to the missing detection of Cherenkov rings with no photons.

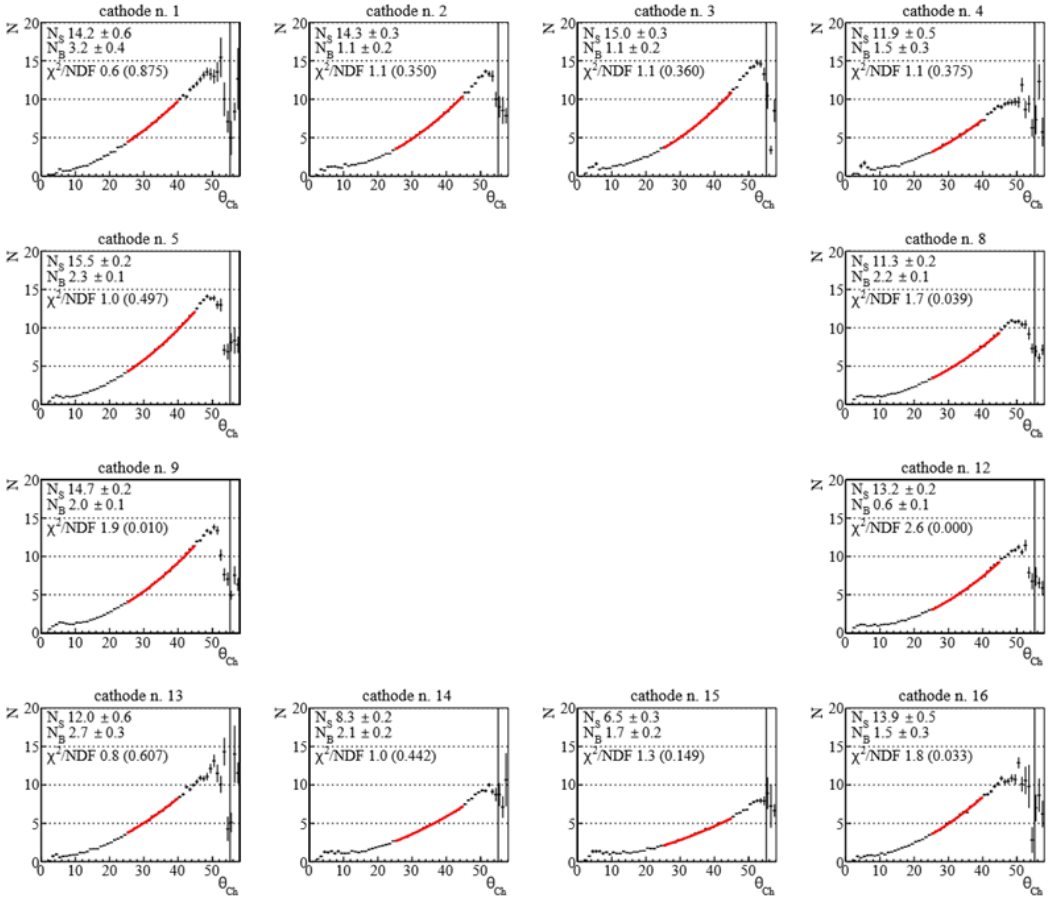

FIGURE 3.19: Distributions of the number of photons as a function of the Cherenkov angle, for each cathode. The result of the best fit procedure is shown as the red bold line superimposed to the graph. The vertical line indicates the saturation angle Θ_{Ch}^{max}, at which the number of signal and background photons are evaluated.

The number of detected photons is expected to follow Poisson statistics as does the number of emitted Cherenkov photons, if the effects of photon signal overlap and other sources of distortions are negligible. The mean value of the measured distribution is however biased because the zero-photon rings are not detected: this effect is very relevant for the small θ_{Ch} bins; after applying a correction for this effect the

average number of detected signal photons decreases and approaches zero at small θ_{Ch} as expected; this effect becomes negligible for θ_{Ch} > 25 mrad.

The fits are good, in general, for all years and all cathodes, with one exception, corresponding to cathode no.15, which is affected by electrical instabilities and exhibits low efficiency: this cathode has been excluded from the further analysis. The low performance of this chamber is one of the motivation for the upgrade described in this thesis. From the study of the χ^2 distribution of the fits an estimate of the systematic uncertainty σ_{syst} = 0.7 σ_{stat} has been obtained. The dependence of the results on the θ_{Ch} range used in the fit is negligible.

To compare data from different years, with different running conditions, signal distributions are evaluated at a fixed reference value of θ_{Ch}: θ_{Ch}^{ref} = 55.2 mrad, corresponding to the Cherenkov angle at saturation θ_{Ch}^{max} in 2006 data; the different values of the radiator gas refractive index (mainly due to slightly different nitrogen contamination) result in different θ_{Ch}^{max} in the range from 55.2 mrad to 55.4 mrad in different years.

Fig. 3.20 shows the values of $N_S(\theta_{Ch}^{ref})$ and $N_B(\theta_{Ch}^{ref})$ evaluated for each of the 12 photocathodes [114] and for each year. Apart from cathode no.15 which was excluded from the analysis, also cathodes no. 2 and 14 show a low efficiency. The error bars represent the statistical plus the systematic contribution which include a set of effects (temperature and pressure variations, electronic threshold setting, etc.) none of which contributes more than 1% of the measured number of detected photons.

In Fig. 3.21 the mean number of photons per ring at saturation, averaging the information from the 11 cathodes is presented as function of the year. The error bars not only include the evaluated systematic error contribution but also an enlargement factor obtained requiring the fit of a first order polynomial to provide a probability value of 0.5.

No evidence for a substantial decrease of the CsI QE is observed, and the points are consistent (33.4% CL) with a constant value, represented in the plot by the dashed line. The first order polynomial fit provides a slope of -0.28 photons/year, corresponding to an estimated decrease rate of the QE of 2.3% per year.

It can thus be said that the CsI photo-cathodes used by COMPASS RICH-1 are robust and preserve their QE over several years of operation with at most a moderate decrease.

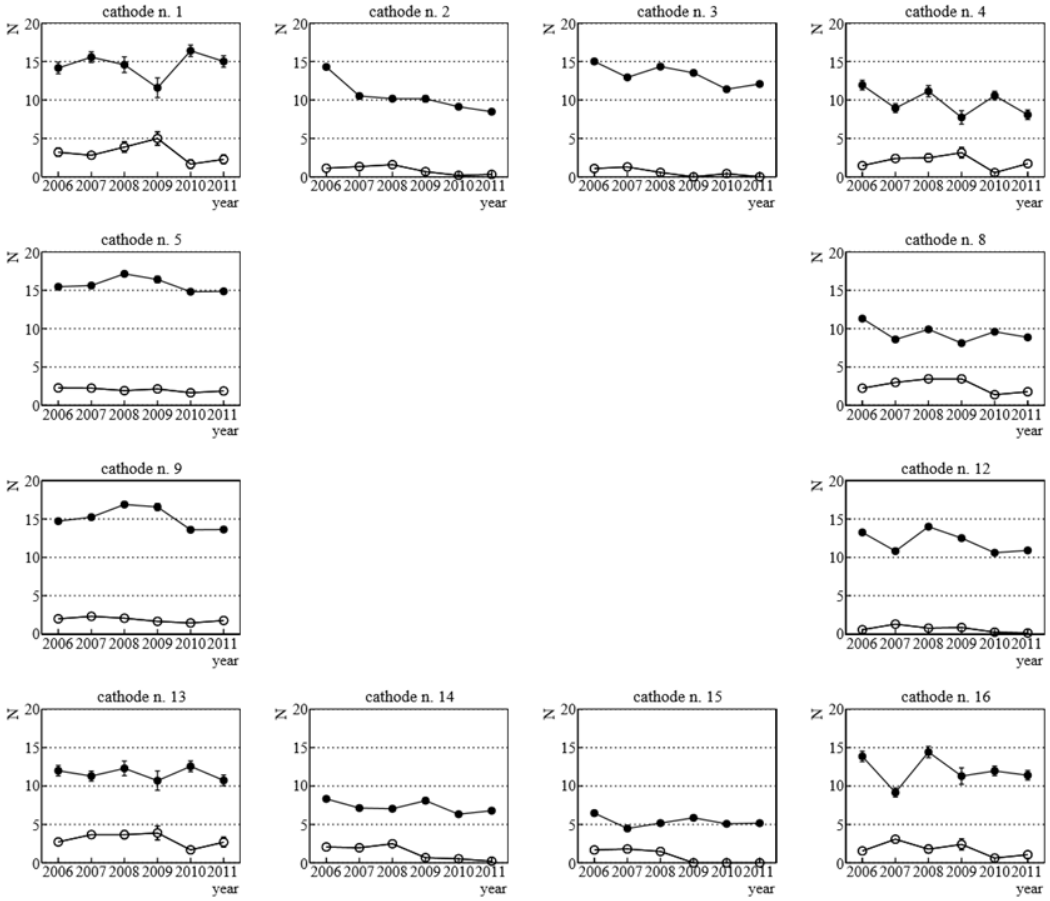

FIGURE 3.20: Distributions of the number of signal (closed points) and background (open points) photons as a function of year, for each cathode.

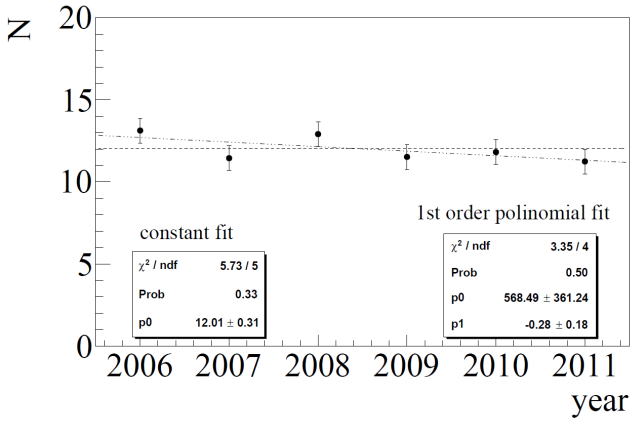

FIGURE 3.21: Mean number of detected signal photons for θ_{Ch} = 55.2 mrad as function of the year averaged over 11 photocathodes. Results from a best fit procedure with a constant and a first order polynomial function are shown.

3.3.2 The MAPMT-based Photon Detectors, the readout and DAQ

In 2006, to overcome the problem of low PID efficiency for very forward particles, to provide higher rate capability and to get rid of the large uncorrelated background, the MWPCs with CsI photocathodes in the central region (25% of the detector surface) have been replaced by a fast detection system [116][117][118] [119][120][121] based on MAPMTs coupled to individual fused silica lens telescopes and read out via sensitive front-end digital electronics and high resolution TDCs.

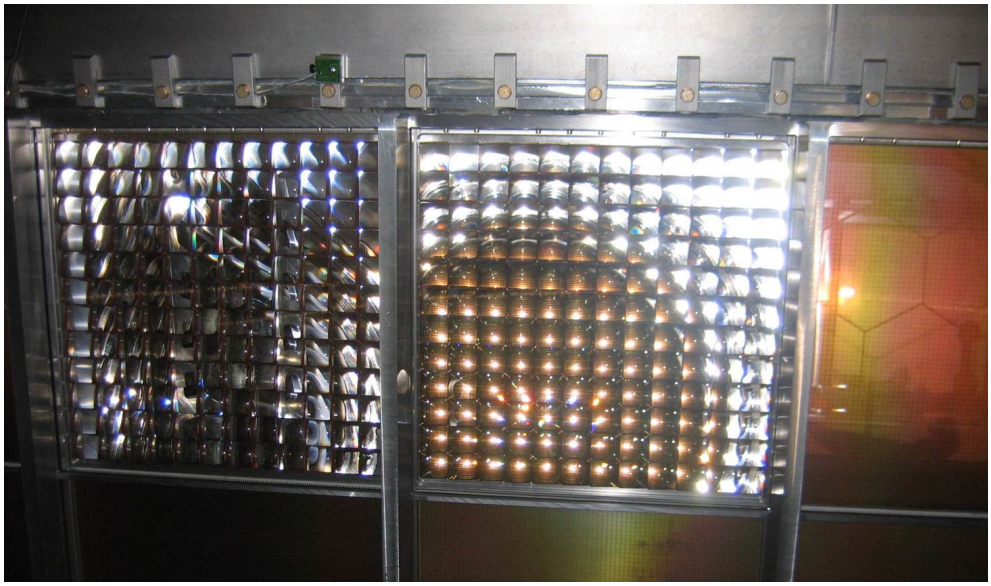

FIGURE 3.22: Two panels with lens telescopes and MAPMTs seen from inside of the RICH-1 vessel.

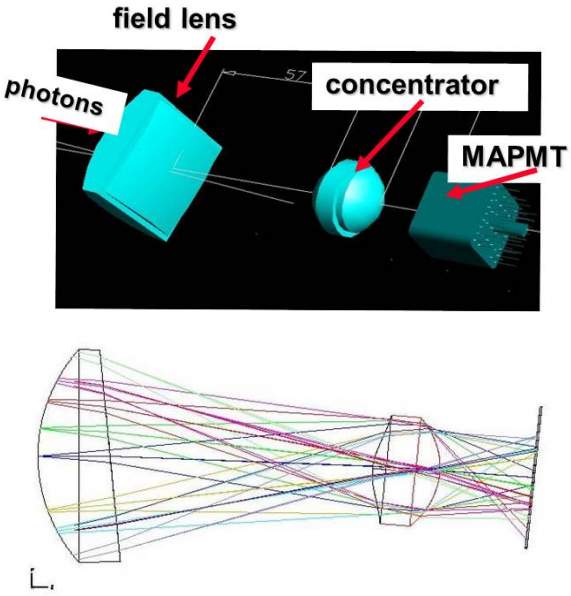

FIGURE 3.23: Artistic view and scheme of the individual fused silica lens telescope.

Four panels of 144 MAPMTs, (Hamamatsu R7600-03-M16 with 16 channels and a UV extended glass window), equipped with custom voltage dividers have been installed in place of the four central CsI coated photocathodes (see Fig. 3.22).

A total of 612 MAPMTs have been submitted to a complete quality control protocol [122] [116] including visual inspection, measurements of dark currents and of gain at 5 different voltages. The typical gain is about 10^7 at 900 V, with excellent uniformity; no gain reduction is observed up to a single photoelectron rate of at least 5 MHz per channel. Individual soft iron boxes have been installed to screen the magnetic field of about 200 Gauss present at the PDs location.

A light concentration system in front of the MAPMTs transmits photons with wavelength in the range from 200 to 700 nm with a wide angular acceptance provides an image reduction of a factor 7.3 in area with minimal distortion, and complies with the space limitations at the detector (11.5 cm total length). It consists of individual optical telescopes [123] [116] for each MAPMT, made of two fused silica lenses (see Fig. 3.23): a plano-convex field lens, placed in the focal plane of the mirrors and a biconvex condenser lens with one aspherical surface, providing the large demagnification with reduced image distortions.

The fused silica lenses are made by grinding and polishing procedure with tight tolerances for surface quality and shape, and are coated with a MgF_2 antireflection layer which provides an increase of about 8% in the number of the collected photons. Each lens and each telescope have been tested [124] [116] in a custom setup employing the Hartmann method [125] [126]. A careful mechanical design of the lens support frames (see Fig.3.24) allowed to reduce the dead areas below 2% of the surface.

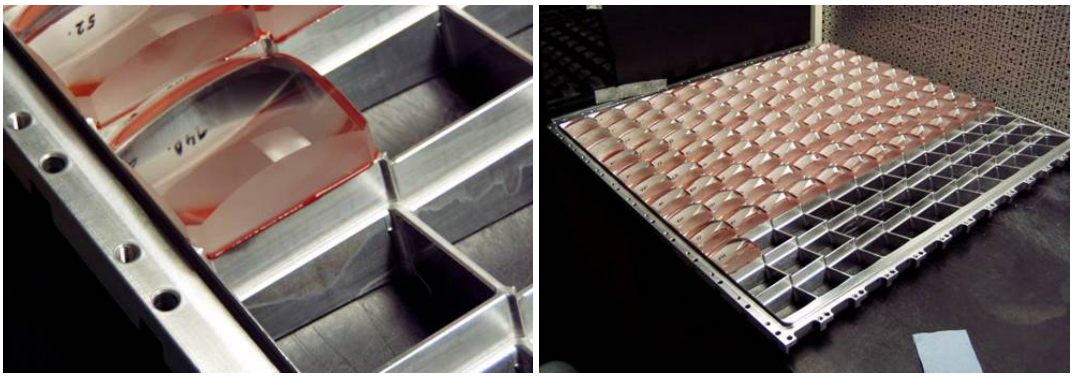

FIGURE 3.24: Picture of a lens and of a lens panel during the lens glueing operation.

The signals from the MAPMTs are read by a fast digital electronics system [127] [128] based on the 8 channels CMAD [129] preamplifier-discriminator, developed for COMPASS RICH-1 as an upgraded version in CMOS technology of the MAD4 [130] front-end chip. The CMAD has a small noise level ($\sim$1 fC), the possibility to set individual channel thresholds, a good time resolution and high rate capability: it provides full efficiency up to an input rate of 5 MHz per channel. The design of the front-end boards and the optimization of the thresholds setting allows to completely suppress the MAPMTs cross talk signals while keeping the single photoelectron detection efficiency at a $\sim$95% level.

The good MAPMT time resolution is fully exploited with the help of digital cards, called DREISAM, housing the dead-time free F1 TDC [131] , which has a time resolution of $\sim$ 110 ps and can stably operate up to 10 MHz per channel input rate and 100 kHz trigger rate.

All the electronics components of the RICH-1 readout system are directly mounted on the detector and form a very compact setup. Each PCB is coupled to a copper plate providing both efficient electromagnetic shielding and good cooling power: thermalized water circulates in underpressure condition in thin copper pipes brazed onto the copper plates [127] (described in detail in Chapter-7).

Data from the front-end cards are transferred via optical links to a set of CATCH readout-driver modules which concentrate the data and send them via S-LINK transmitters and optical fibers to the COMPASS DAQ system.

3.4 PID performance

The RICH reconstruction and analysis package, called RICHONE [115], has been developed by Prof. Paolo Schiavon to perform data reduction,

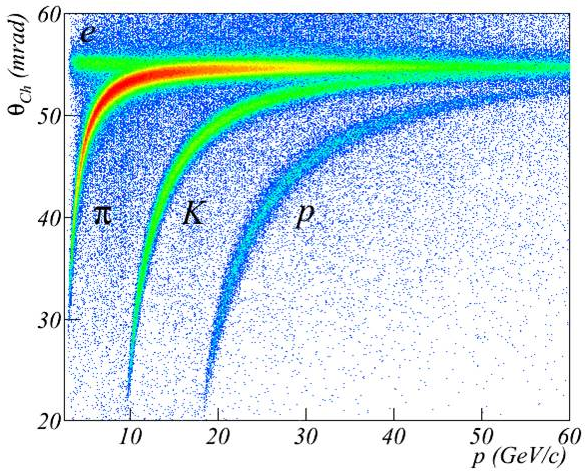

(A)

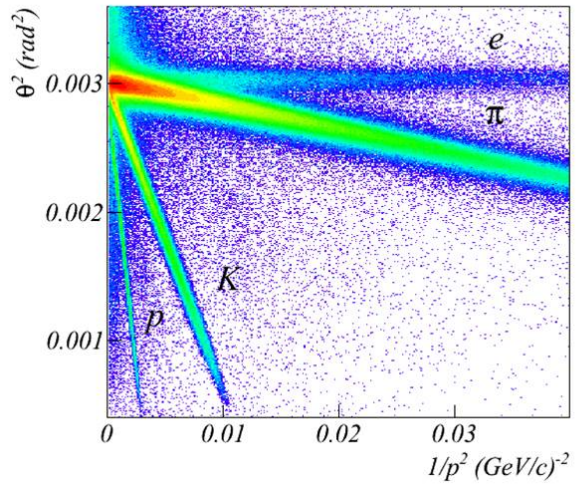

(B)

FIGURE 3.25: A. The measured ring Cherenkov angle versus particle momentum p; B. The measured ring Cherenkov angle squared versus $1/p^2$.

pattern recognition and hadron identification in COMPASS; it is also used to perform several accessory tasks, including tuning and calibrations and to study the RICH-1 detector performance. Its software is part of CORAL, the COMPASS reconstruction and analysis package [132].

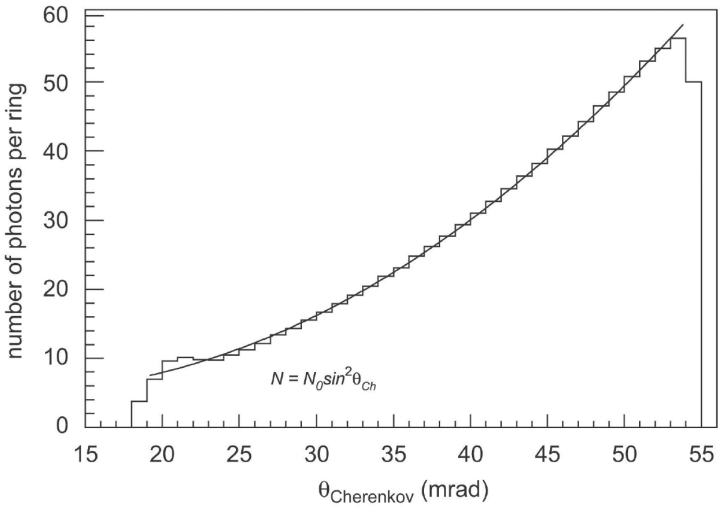

FIGURE 3.26: Number of photons per ring as function of the Cherenkov angle.

For each event the RICH-1 data are decoded, the MAPMT hits are selected on the basis of the time information and the MWPCs hits are selected on the base of the time and amplitude information and clustered; all accepted particles, namely tracks within the RICH angular acceptance and having a momentum between 1.8 and 180 GeV/c, are then correlated to the RICH reconstructed coordinates.

For each particle a wide fiducial area of the photon detectors is defined, where its Cherenkov photons could have arrived, which can sometimes cover both part of the MAPMT and part of the MWPC or part of the upper and part of the lower photon detector set; for each reconstructed hit inside the fiducial area an algorithm is used to compute the Cherenkov polar and azimuthal angles in the particle reference frame: this are the reconstructed photon parameters used in the analysis. Corrections for the individual mirror parameters and the MAPMT optical system crossed by the photon are included.

The reconstructed photons are relative to the considered particle and the reconstruction algorithm is repeated for each particle in the event.

The value of an extended likelihood function is computed for five mass hypotheses (e,μ,π,K,p) and one for the absence of signal hypothesis: the maximum is assumed to correspond to the best hypothesis. The identification purity can be improved by requiring the ratio of best to second best hypothesis likelihood to be larger than a fixed value.

In Fig. 3.25a the measured ring Cherenkov angle θ_{Ch} as a function of the particle momentum is shown. The e,π,K and p band are clearly separated. In Fig. 3.25b another relationship between the Cherenkov angle and the particle momentum is shown, which emphasises the small momentum region: θ^2_{Ch} as a function of $1/p^2$. In the small angle approximation, the relationship between these two variables is linear, with a slope proportional to the squared mass of the corresponding particle.

For an accurate likelihood evaluation the average refractive index of the radiator gas needs to be know at about 10^{-6} level for both detector types: it is experimentally determined from the RICH-1 data at fixed time intervals and evolved during the

intermediate time periods according to the measured changes in the radiator temperature and pressure.

A ring pattern recognition is also performed by the RICHONE package since it is needed for a detailed study of the RICH response and for the fine tuning and optimization of both the RICH detector hardware and the data analysis program.

in Fig.3.26, the number of detected photons per ring as function of the Cherenkov angle is shown for rings fully contained in the MAPMT part of the photon detectors. For particles with $\beta = 1$ the average number of detected photons is 56.

The measured single photon resolution in the central region is 2.0 mrad and the global resolution on the measured Cherenkov angle[133] is less than 0.3 mrad for particles at saturation, in agreement with the single photon resolution value scaled by the square root of the number of photons: this confirms that the background contribution is minimal, thanks to the excellent time resolution of the MAPMTs.

In the central region, where the ring images produced by high momentum particles are formed, the 2σ π-K separation defined according to the recipe of ref. [134] is up to 55 GeV/c.

The efficiency for π (K) identification has been evaluated as function of particle momenta making use of a sample of kinematically reconstructed K^0_S ($\phi(1020)$) mesons. Fig.3.27 and Fig.(3.28) show the efficiency and the misidentification probability for π (K) for the three most commonly used cuts on the ratio of the best to L to the second best L^{2nd} hypothesis likelihood. For particle momenta below 30 GeV/c the efficiencies are larger than 90% and the misidentification probabilities smaller than 1%; for higher momenta the cut on the likelihood ratio can be tuned to optimize efficiencies or sample purities.

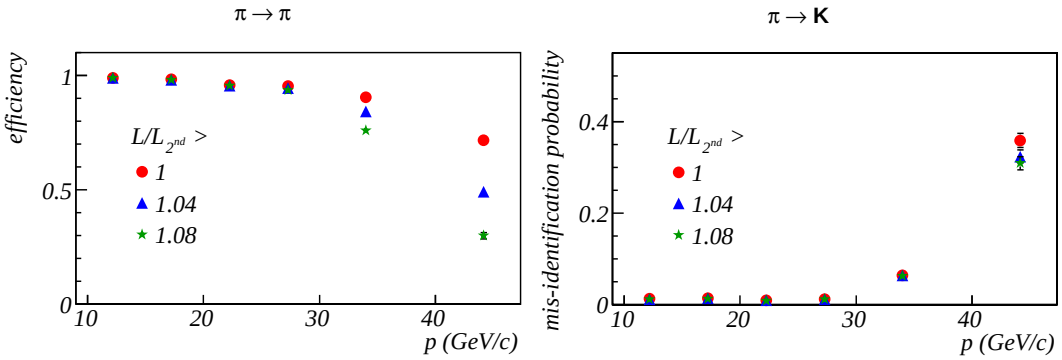

FIGURE 3.27: Efficiency (left) and misidentification probability (right) for π as function of momentum.

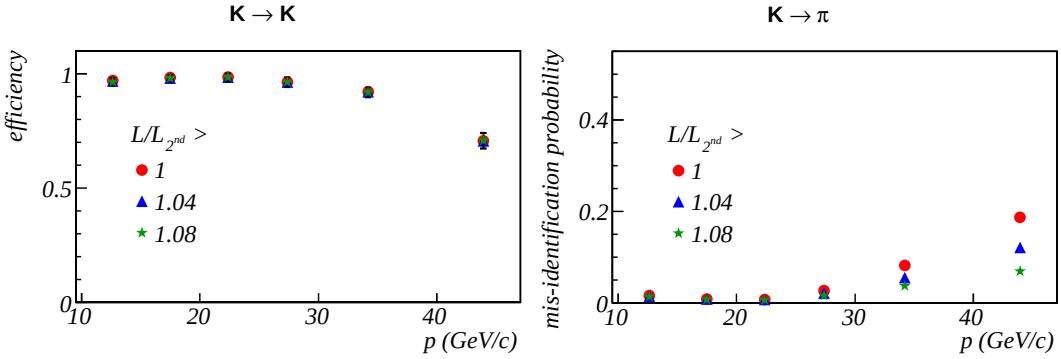

FIGURE 3.28: Efficiency (left) and misidentification probability (right) for K as function of momentum.

The purity of identified K samples depends on the physics channel under consideration: Fig. 3.29 shows it for standard COMPASS deep inelastic scattering events. In the momentum range below 30 GeV/c the purity is always above 80%, for all cuts on the likelihood ratio.

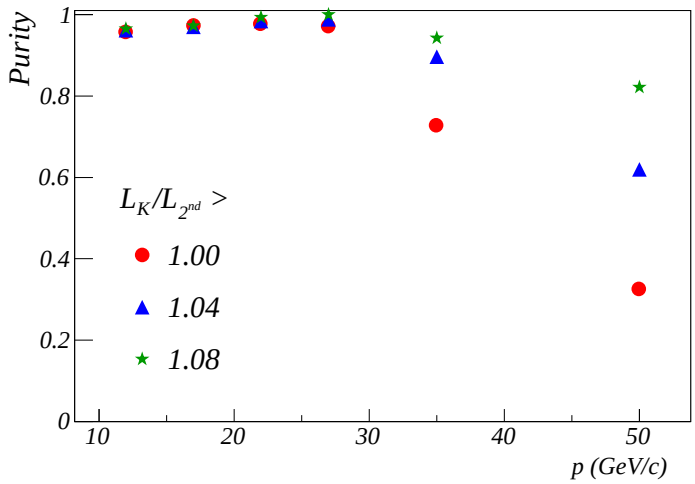

FIGURE 3.29: Purity of K samples as function of momentum.

Charged hadrons with momenta below the Cherenkov threshold are identified by using the likelihood for the absence of signal hypothesis; the low background level in that region allows a good evaluation of the particle yields. This identification turns out to be very effective too: K samples with momenta below 9 GeV/c from the decay of $\phi(1020)$ show identification efficiencies larger than 90%.

During 2014 run, The RICH detector was filled with N_2 instead of C_4F_{10} as radiator. In Fig.3.30, the measured ring Cherenkov angle θ_{Ch} as a function of the particle momentum is shown: the separation between the μ and π was very efficient.

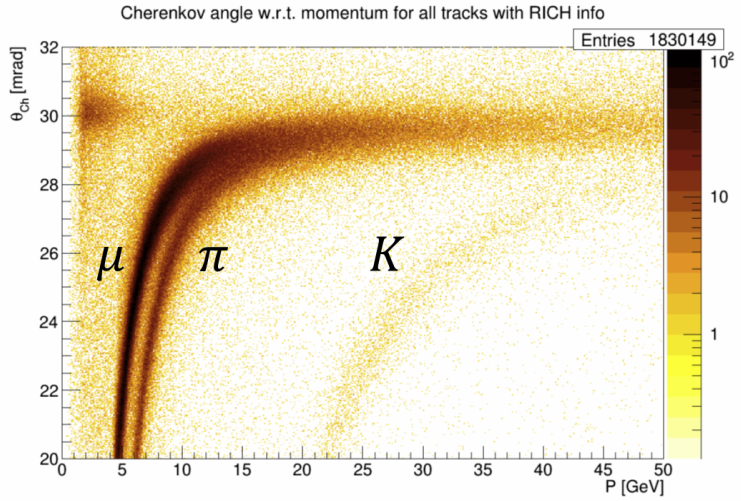

FIGURE 3.30: The measured ring Cherenkov angle versus particle momentum p.

3.5 Summary

COMPASS RICH-1 is an extraordinary detector and it provides efficient hadron PID in the momentum range between 3 and 55 GeV/c, in the difficult conditions of COMPASS data taking.

In view of the challenges imposed by the measurement of DVCS on 2016 and 2017 COMPASS data taking periods, the performance of the MWPC based PDs needs to be improved, in particular in the central region where three of the four chambers showed a critically low average value of the number of detected photons (Fig.3.31) as described in Section-3.3.1. For these chambers it was not possible to guaranty the level of stability of the efficiency which is essential for the delicate measurements of the new COMPASS program.

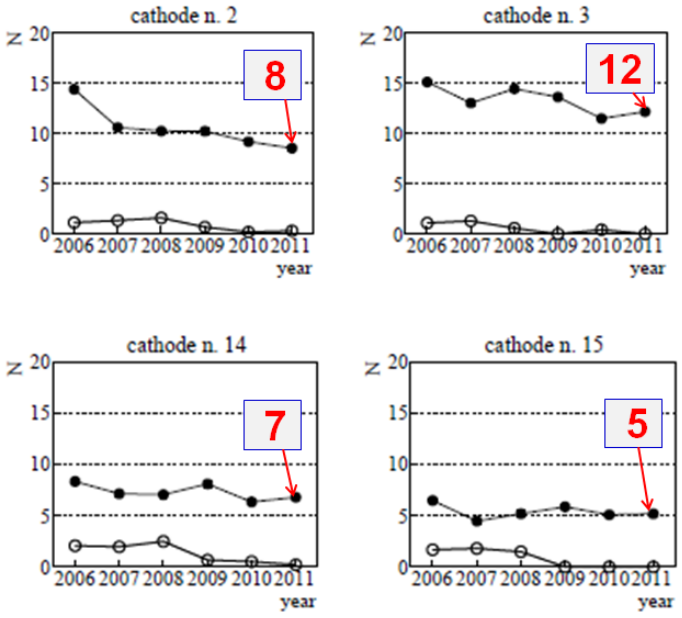

FIGURE 3.31: Detected average number of photo-electrons (full circles) and average background (empty circles) for central chambers with MWPCs

As described in the next chapters only a change in the photon detection technology could allow to cope with the new requirements and in particular to provide a faster signal generation time to achieve a better signal to noise ratio in higher rate environment.

A dedicated R&D program aimed to develop novel PDs to be used for the upgrade of COMPASS RICH-1 was started 8 years ago. The main results of this large effort, my contribution to this effort and the successful implementation of the novel PDs on the COMPASS RICH-1 are described in the next chapters.

Chapter 4

R&D for THGEM based Detector of Single Photon

In this chapter, a brief summary of the work performed before my arrival in Trieste and of the work I performed on the R&D project to develop THGEM based PDs is presented. I started working in THGEM Trieste lab 2 years before the start of my Ph.D., after finishing my master degree. During these five years I took part in all aspects of the R&D project.

In Section-4.1 the motivations and the goals of the R&D program are discussed. A brief description of THGEMs and their characteristics is provided in the next section, followed by the main results relevant for the R&D obtained by the Weizman group on THGEM characterization before the start of our R&D.

The full study of single and triple THGEM based detectors performed within the dedicated R&D is summarized in Section-4.4.

A very important element of the detector performance is the control over the IBF: the study of the IBFR in triple THGEM detectors, done by me, is described at the end of this chapter along with the illustration of the picoammeters specifically developed for this purpose.

4.1 Goals of the THGEM based PDs R&D

In view of the challenges imposed by the new physics program of the COMPASS Experiment, the use of MWPCs with CsI photo-cathodes was considered inadequate because of the intrinsic limitations of this technology as already described in Section-1.3.3.

Replacing them with MAPMTs was not an option, because the acceptance of the MAPMT lens system ($\sim 9^0$) would not be large enough for the Cherenkov photons impinging on the external chambers and because they are very expensive. In view of their large dark counting rate SiPMs were also not a viable option.

A dedicated R&D program was started to investigate the available technologies and chose the optimal solution; the requirements on the new technologies to be used for the upgraded PDs were:

- a small signal formation time to provide a time resolution ≤ 10 ns,
- a closed geometry to avoid photon feedback,

- a large effective gain ($\sim 10^5$) to guarantee high single photo-electron detection efficiency and avoid critical dependence on the front-end electronics threshold,
- a reduced ion back-flow to the CsI photo-cathode ($\leq$ few $\%$) to guarantee stability and avoid aging problems,
- a good uniformity and stability of the response both in time and under different irradiation conditions to guarantee high and constant efficiency.

As discussed in Section-1.2 MPGD based technologies were the natural choice to meet these needs. MPGD based PDs had already been built and installed in the PHENIX experiment at RHIC: PHENIX HBD [82] (Section-1.3.4) is based on GEM technology, provides collective signals from 5-10 photo-electrons with a gain $\sim$4000. A higher gain alternative was needed for the single photon detection in COMPASS RICH-1: The THGEM technology was thus investigated for the upgrade.

In what follows, the definitions provided in section-1.2.1 will be widely used.

4.2 THick Gas Electron Multipliers (THGEMs)

THGEMs are electron multipliers derived from the GEM design, scaling the geometrical parameters and changing the production technology. The Cu coated kapton foil of the GEM multipliers is replaced by standard Printed Circuit Boards (PCB) and cylindrical holes are produced by drilling. The conical shape of the GEM holes that gives origin to the uncoated polyiamide rings around the holes itself is replaced by a clearance ring, the rim, surrounding the hole and obtained by Cu etching. Typical values of the geometrical parameters are PCB thickness **t** = 0.2 - 1.2 mm, hole diameter **d** ranging between 0.15 and 1 mm, hole pitch **p** of 0.4 - 1mm and rim width between 0 and 0.1 mm (Fig.4.1).

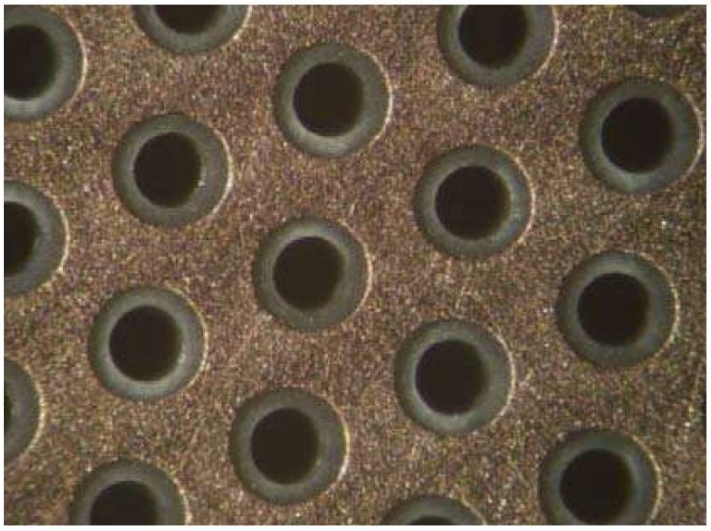

FIGURE 4.1: Picture of THGEM with d = 0.3 mm, p = 0.7 mm, t = 0.4 mm and rim = 0.1 mm.

THGEMs have been proposed by several groups independently [135] [136] [137] [138] [139]. Since the beginning, high gain and high rate capability were reported

for detectors made with one or more layers of THGEMs. Other specific characteristics are:

- Intrinsic mechanical stiffness, which allows easier mounting, handling and removes the need of gluing and stretching.
- Making a THGEM is simple (instead of chemically etched holes in GEMs, the use of PCB drilling technique makes it possible to produce THGEMs by industry). The production cost depends on the number of holes to be drilled ($\sim 10^6$holes.m^2) and is $\sim$1€/10^3 holes.
- Unlike GEMs, THGEMs are robust and they are not damaged in case of large electrical discharges.
- Due to the large pitch ($\sim$ 1mm) of the holes, THGEMs cannot achieve space resolution as good as GEMs do; this however is not a problem for RICH applications.
- As the gaps between different layers of THGEMs are small, the detector is insensitive to magnetic field.
- It is possible to make a staggered configuration of holes between different layers of THGEMs, which helps in reducing the IBF.
- As the signal is generated mainly by the movement of electrons in the induction region($\sim$few mm), it is fast and a small time resolution ($\sim$10 ns) can be achieved.

4.3 THGEM studies at Weizmann Institute

First systematic studies with THGEMs were performed at Weizman Institute (Tel-Aviv, Israel). In this section, a brief summery of the results [140] [141] [142] [143] [144] relevant for this thesis is presented.

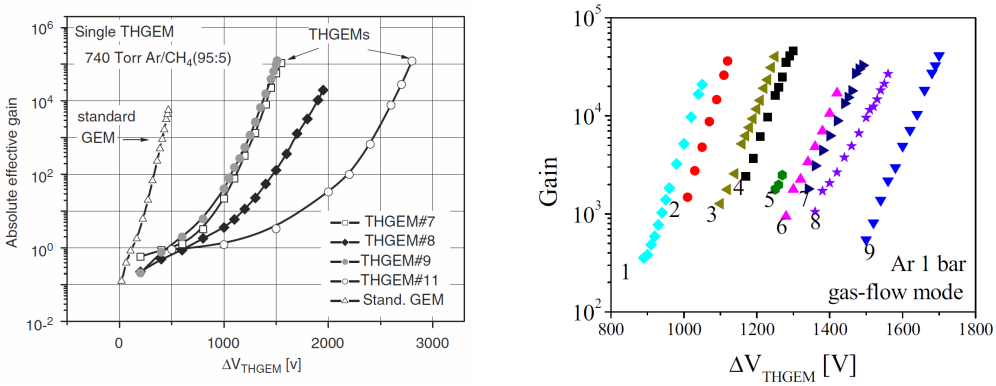

(A) (B)

FIGURE 4.2: (A) Gain measurement versus ΔV_{THGEM} for detectors based on THGEMs with different geometries (Table-4.1); gas mixture: Ar/CH_4 (95:5). UV photons are detected [140]. (B) gain measurements versus ΔV_{THGEM} for detectors based on THGEMs with different geometries (Table 4.1); gas used: pure Ar; X-ray from a ^{55}Fe source are detected [143].

TABLE 4.1: Details of THGEMs geometrical parameters used in Fig.4.2a and Fig.4.2b

Curve #	Diameter (mm)	Pitch (mm)	Thickness (mm)	Rim (mm)
1	0.3	0.7	0.4	0.1
2	0.3	0.8	0.4	0.1
3	0.5	0.9	0.4	0.1
4	0.6	1.2	0.4	0.1
5	0.8	1.3	0.4	0.1
6	0.4	0.9	0.8	0.1
7	0.6	1.2	0.8	0.1
8	0.8	1.3	0.8	0.1
9	0.6	1.0	0.8	0.1
11	1	1.5	1.2	0.1

The influence of the geometrical parameters on THGEM performance has been extensively studied. In Fig.4.2a the effective gain of single THGEM detector as a function of applied ΔV_{THGEM} using an UV light source in 1 bar Ar:CH_4 95:5 gas mixture is plotted. In Fig.4.2b the effective gain vs ΔV_{THGEM} is plotted for an ^{55}Fe X-Ray source and 1 bar of pure Ar. The different THGEM parameters are listed in Table-4.1. Gains exceeding 10^5 in case of single photo-electrons are observed (Fig.4.2a); for the X-Ray source ($\sim$220 primary e^-) case in pure Ar, gains of few$\times 10^4$ were achieved ((Fig.4.2b)).

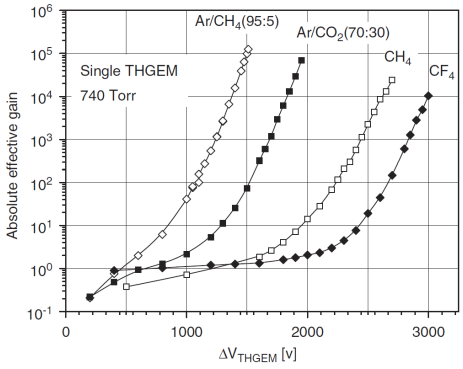

FIGURE 4.3: Gain measurement for a THGEM (d= 0.5 mm, p= 0.9 mm, t= 0.4 mm, rim= 0.1 mm.) employing different gas mixtures [140].

The effective gain variation behaviour of THGEM with d= 0.5 mm, p= 0.9 mm, t= 0.4 mm, rim= 0.1 mm, in different gas mixtures, is shown in Fig.4.3. Maximum effective gains above 10^4 were achieved for all gas mixtures; $\sim 10^5$ was achieved only for Ar:CH_4 95:5.

The gain response of a single layer of THGEM was measured for different rates of an UV source in a reflective photo-cathode configuration. In Fig.4.4a, the measurements performed with two different ΔVs show that, for the gain of $\sim 10^3$ no drop is seen, and for the gain of $\sim 10^4$ a drop occurs only for rates larger than $\sim 10^7 e^-.mm^{-2}.s^{-1}$, which clearly demonstrates that THGEMs are adequate for high rate applications. The energy resolution was measured using a single THGEM layer and an ^{55}Fe X-Ray source, providing a FWHM = 18.8% (Fig.4.4b).

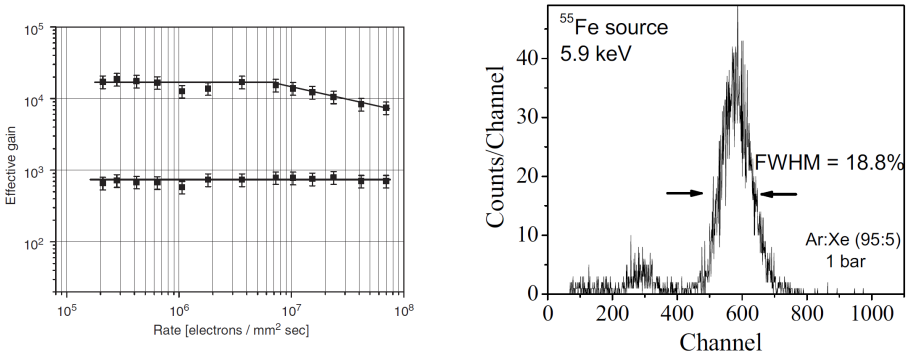

(A) (B)

FIGURE 4.4: (A) Rate capability for a single THGEM (d = 0.3 mm, p = 1 mm, t = 0.4 mm, rim = 0.1 mm) with a reflective photo-cathode in Ar/CO_2 (70:30) [140]. (B) Pulse height spectrum for a double THGEM detector in Ar/Xe (95:5) irradiated with ^{55}Fe 5.9 KeV X-rays [143].

As the electron counting inefficiency directly translates into a counting rate deficiency, the pulsed counting mode was used for Electron Transfer Efficiency (ETE) measurements. With the setup shown in Fig.4.5a the ETE for a reflective photo-cathode configuration has been measured. The measurement was done in two steps:

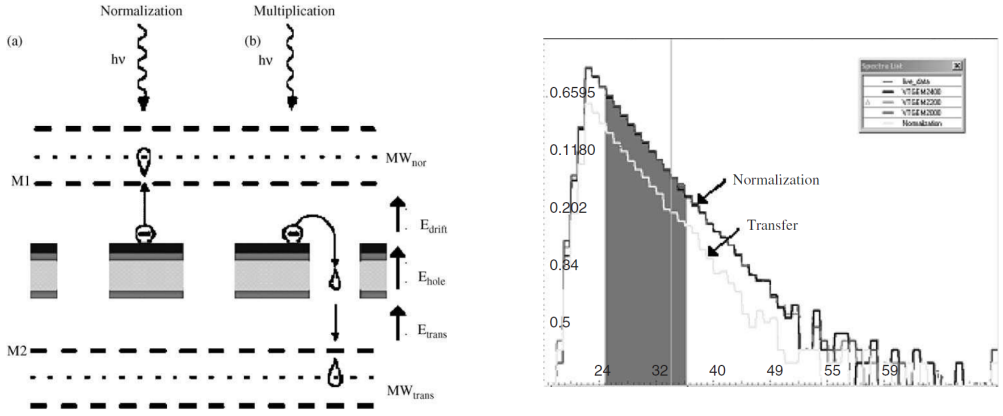

(A) (B)

FIGURE 4.5: (A) scheme of the experimental setup for the Electron Transfer Efficiency (ETE) measurement, Ref photo-cathode configuration (details are given in the text) [140]. (B) single photo-electron spectra of the normalization and electron transfer measuring steps, recorded on MW_{nor} and MW_{trans} respectively [140].

1. To collect and multiply all the photoelctrons originating from the photo-cathode to the first MWPC (made with wire planes M1 and MW_{nor}) by using a high value of $E_{drift}(\sim 3kV/cm)$ to assure good photo-electron extraction. The field between MW1 and E_{nor} was ~6kV/cm to assure full e^- transfer and ΔV applied across the THGEM was 0 to have the $ETE \approx 1$.

2. The ETE of the THGEM which was measured by keeping the total gain of the cascaded THGEMs fixed along with the same gain value of MW_{trans} which MW_{nor} had previously, with a condition that $E_{drift} = 0 kV cm^{-1}$. The measurement of ratio of the number of event rate (n_{trans}/n_{nor}) gives the ETE of

the THGEM. Here it is assumed that the single photon spectra are exponential, which can be confirmed by looking into a typical spectrum as shown in Fig.4.5b.

The measurement of ETE as function of ΔV_{THGEM} was performed for four different gas mixtures and the results are shown in Fig.4.6a, where E_{drift} was 0 kV/cm. A study of ETE vs E_{drift} for the same detector is shown in Fig.4.6b.

The ETE measurements need to be complemented by the measurement of the photo-electron extraction efficiency, ϵ_{E_x} defined as:

$$\epsilon_{E_x} = \frac{I_{gas}(E_{drift})}{I_{vac}} \tag{4.1}$$

where I_{vac} is the extraction efficiency in vacuum, I_{gas} is the extraction efficiency in the gas and E_{drift} is the field at the photo-cathode; Fig.4.7a and 4.7b shows ϵ_{E_x} as function of drift field for several gases. The measurement was performed in parallel plate mode (no ΔV applied across the THGEM) and the data were normalized to the extraction in vacuum. The results show the importance of choosing the right gas and right field values for PD with solid state photo-cathode.

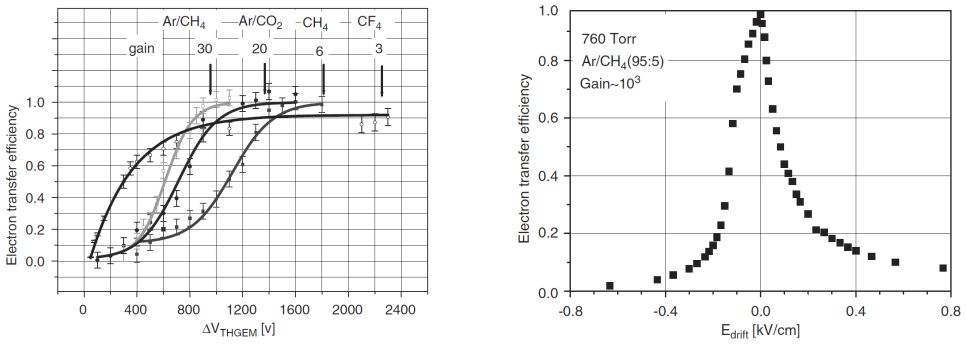

(A) (B)

FIGURE 4.6: (A) electron Transfer Efficiency versus ΔV_{THGEM} in a Ref photo-cathode detector, in several gases (Ar/CH_4 95/5, Ar/CO_2 70/30, CH_4 and CF_4) for a THGEM with geometrical parameters: d= 0.3 mm, p=0.7 mm, t=0.4 mm and rim=0.1 mm [140]. (B) ETE measurement for a single THGEM detector with geometrical. parameters: d= 0.3 mm, p=0.7 mm, t=0.4 mm and rim=0.1 mm, at gain $\sim 10^3$ in Ar/CH_4 (95:5) as a function of the drift field, E_{drift} [140].

THGEM characterization with different gas pressures [143] [141] and measurements of time resolution of THGEM based detectors [145] were performed by our group too. In the Ph.D. thesis of Elena Rocco [146], one can find a complete introduction on THGEMs, followed by a detailed description of the full set of the first measurements performed by our group along with the discussion of the results.

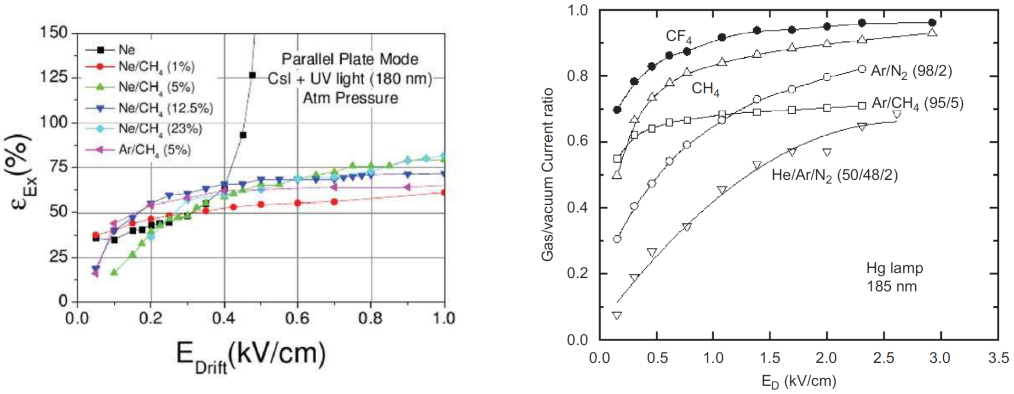

(A) (B)

FIGURE 4.7: (A) Photoelectron extraction efficiency, $\epsilon_{E_x}(E_{drift})$, from the CsI PC, as a function of the drift field [142]. (B) Photoelectron collection efficiency measurement for different gasses as a function of drift field, E_{drift} [144].

The THGEM photo-electron extraction and collection efficiencies are discussed in the next section.

4.4 THGEM characterization in INFN Trieste lab

4.4.1 Production of THGEMs for INFN Trieste lab

Before presenting the measurements performed in the INFN Trieste lab and at CERN, a short discussion is dedicated to the THGEM production methods.

THGEM detectors can be produced by drilling standard Printed Circuit Boards (PCBs) in industries and don't require any custom procedure or very special tools for productions. Nevertheless, the production procedure, even if industrial, needs to be optimized and needs to satisfy the requirements of THGEM based PDs. The first prototypes tested by the INFN Trieste THGEM group, were either provided by our Weizmann colleagues or produced at CERN by Rui de Oliveira. The systematic studies needed a large set of samples with different geometrical parameters and production procedures. The industrial partner able to provide us with all the required pieces was the ELTOS S.p.A. company from Arezzo, Italy. This company, thanks to the acquired expertise, later produced for us the medium size THGEM prototypes and the whole set of final THGEMs for the COMPASS RICH-1 upgrade.

The holes of a THGEM are obtained by mechanical drilling the fiberglass, using a milling tool mounted on a Computer Numerical Control (CNC) machine. The quality of the hole shape strongly depends on the characteristic of the CNC machine, the quality of the tool, the rotation and advancement speeds and on the frequency of the tool replacement: this last parameter turned out to be essential, since only changing the tool every 1000 holes, a satisfactory hole quality could be achieved. The cleaning procedure applied after drilling is essential too.

A detailed discussion on different THGEM production techniques and on the role played by each geometrical parameter can be found in the Ph.D. Thesis of Elena

Rocco [146]. In Fig.4.8 a summary of different THGEM production procedures is sketched. The procedure called "Global Etching" was chosen for our production. The procedure starts with a preliminary chemical etching to obtain the final THGEM electrode borders and then drilling of the PCB sandwiched between Al foils, followed by a chemical (micro-)etching without any masking of the whole Cu-clad surface. This procedure provides well centered and uniform rim with small width ($\leq$10 μm). Several different geometries as shown in Table4.2 have been produced and characterized during the early $R\&D$ phase.

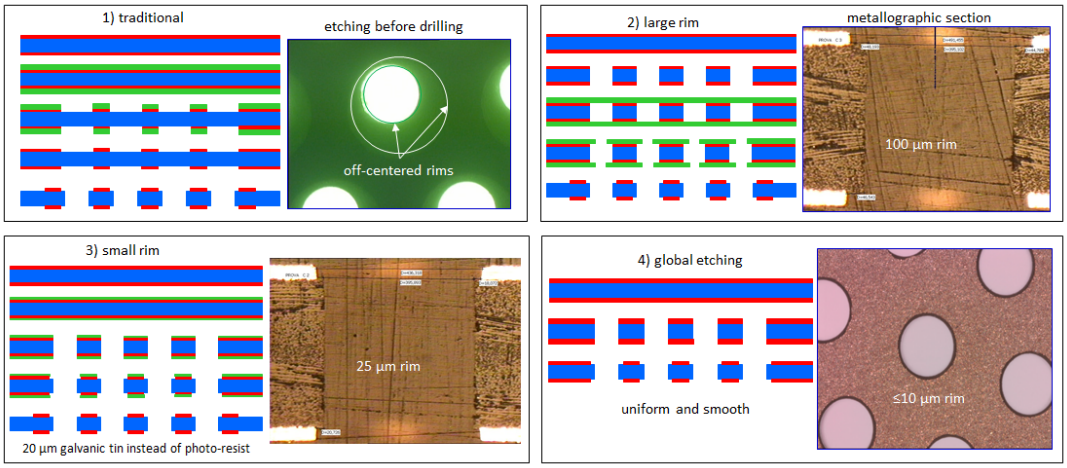

FIGURE 4.8: 1.Left: Sketch of ELTOS Chemical Etching Procedure; Right: Microscopic Picture of a THGEM holes produced by Chemical Etching procedure; 2. ; 3. Left: Sketch of ELTOS Chemical Etching Procedure; Right: Microscopic Picture of a THGEM holes produced by Chemical Etching procedure; 4. Left: Sketch of ELTOS Global Etching Procedure; Right: Picture of the cross section of a THGEM obtained by Global Etching procedure

4.4.2 THGEM characterization setup

The precondition for a detailed characterization of a detector is the reproducibility of its response. The first studies of the THGEM showed it was difficult to accurately reproduce previous results and this was related to significant variations of the gain response in time. In particular the sample with large rim (as shown in Fig.4.9-Left) shows a large increase in the signal amplitude over time while the prototype with smaller rim (as shown in Fig.4.9-Right) presents a sharp decreasing trend of the signal amplitude.

TABLE 4.2: Details of THGEMs produced with different technologies

Name	Diameter (mm)	Pitch (mm)	Thickness (mm)	Rim (mm)	Treatment	Material/Producer
F 0 rim	0.3	0.7	0.4	0	none	Isola
F 10 rim	0.3	0.7	0.4	10	chemical	Isola
F 100 rim	0.3	0.7	0.4	100	none	Isola
F 0/100 rim	0.3	0.7	0.4	0 & 100	none	Isola
K 10 rim	0.3	0.7	0.4	10	none	kapton
F plate 1	0.3	0.7	0.6	0	none	Isola
F plate 2	0.3	0.6	0.6	0	none	Isola
F plate 3	0.3	0.5	0.6	0	none	Isola
F plate 5	0.4	0.7	0.6	0	none	Isola
F plate 9	0.5	0.7	0.6	0	none	Isola
M1	0.4	0.8	0.4	0	none	Panasonic
M2	0.4	0.8	0.4	0/25	mech. drilling	Panasonic
M3	0.4	0.8	0.4	0/50	mech. drilling	Panasonic
M4	0.4	0.8	0.4	0/100	mech. drilling	Panasonic
M5	0.4	0.8	0.4	50	mech. drilling	Panasonic
C1	0.4	0.8	0.4	10	chem. etching	Panasonic
C2	0.4	0.8	0.4	25	chem. etching	Panasonic
C3	0.4	0.8	0.4	50	chem. etching	Panasonic
C3I	0.4	0.8	0.4	50	chem. etching	Isola
C4	0.4	0.8	0.4	100	chem. etching	Panasonic
C5	0.4	0.8	0.4	10	laser + chem. etching	Panasonic
C6	0.4	0.8	0.4	50	laser + chem. etching	Panasonic
C7	0.4	0.8	0.4	10	global etching	Panasonic
M2.6	0.4	1	0.6	0	global etching	Panasonic
M2.7	0.3	1	0.6	0	global etching	Panasonic
M2.10	0.4	0.8	0.8	0	global etching	Panasonic
M2.11	0.3	0.8	0.8	0	global etching	Panasonic
M2.12	0.4	1	0.8	0	global etching	Panasonic
M2.13	0.3	1	0.8	0	global etching	Panasonic
C2.1	0.3	1	0.6	2	global etching	Panasonic
C2.2	0.3	1	0.6	5	global etching	Panasonic

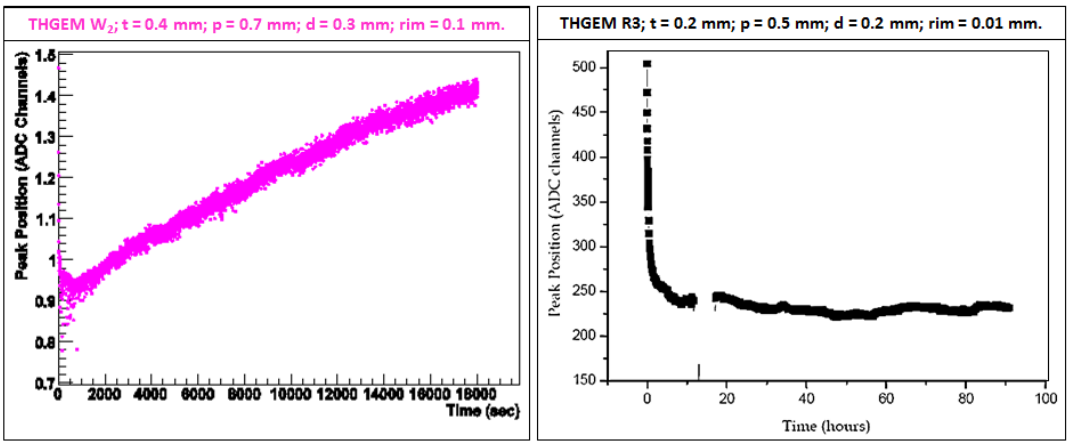

FIGURE 4.9: Signal amplitude variation in time. Left: THGEM with 100 μm rim; Right: THGEM with 10 μm rim.

In order to systematically reproduce previous results a complex protocol including the HV switching on procedure, the time and intensity of illumination and all details of the test conditions had to be followed. In particular the signal amplitude dependence on the value of the drift field (E_D), shows different and opposite trends for THGEMs with large and small rims respectively (Fig.4.10) [147]: for 100 μm rims (blue dots) the signal amplitude increases linearly with the E_{drift}, for a piece with electro-chemically produced rim $\leq$10 μm, the signal amplitude reaches a plateau at E_{drift} values depending on ΔV applied (1.45 kV for black dots and 1.35 kV for the empty dots) to the THGEM and decreases for higher E_{drift}. The choice of the optimal E_{drift} thus depends on the THGEM geometry and the applied ΔV_{THGEM}.

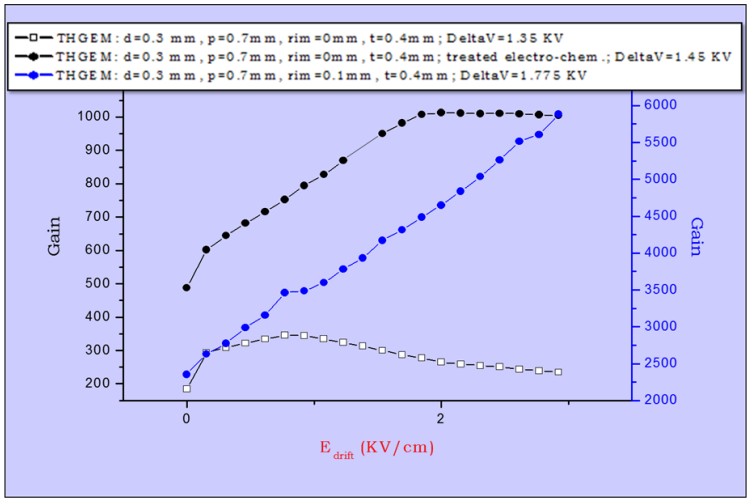

FIGURE 4.10: signal amplitude vs. E_D for THGEMs with different rims. [147]

The setup used to perform the characterization of single THGEM pieces is sketched in Fig.4.11.

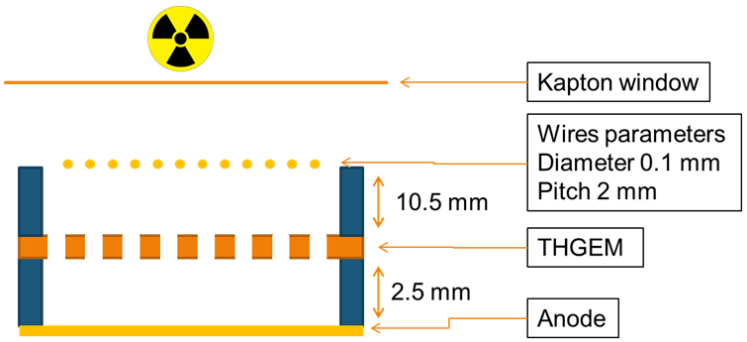

FIGURE 4.11: schematic of the setup used for the characterization of single THGEMs

To read the signal from the anode, a standard readout chain was used: it included a CREMAT CR-110/111 preamplifier connected to an Ortec research amplifier (or a Canberra spectroscopy amplifier) coupled to an AMPTEK 8000A Multi Channel Analyzer. To calibrate the readout chain test pulses were provided by an Agilent digital waveform generator. The scheme of the readout chain is presented in Fig.4.12.

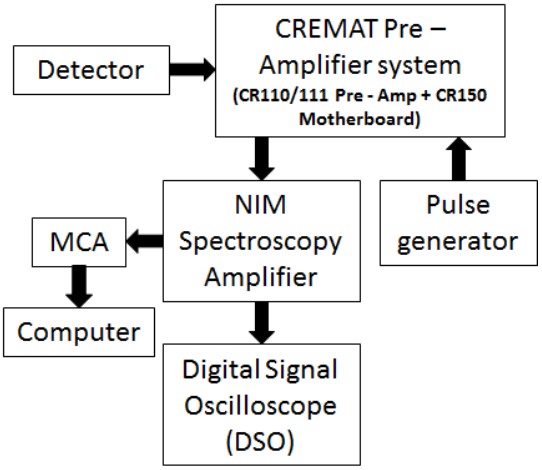

FIGURE 4.12: Schematic of the signal readout chain used for characterization.

4.4.3 Characterization of single layer THGEMs in INFN Trieste Lab

To clarify the reproducibility problem, systematic THGEM stability studies were performed [146] [148]. Two THGEM pieces with common parameters (t = 0.4 mm; d = 0.4 mm; p = 0.8 mm.), one with 0.1 mm rim and the other with no rim were tested using a ^{55}Fe source, Ar:CO_2 70:30 gas mixture and the standard readout chain.

The two THGEMs were kept at nominal condition (ΔV = 1750 V for THGEM with 0.1 mm rim (a); ΔV = 1330 V for THGEM with no rim (b), corresponding to an effective gain $\sim$ 500) under continuous irradiation for 20 hours. Fig.4.13a shows the evolution of the effective gain: $\sim \times 5$ increase for (a), $\sim \times 0.8$ for (b).

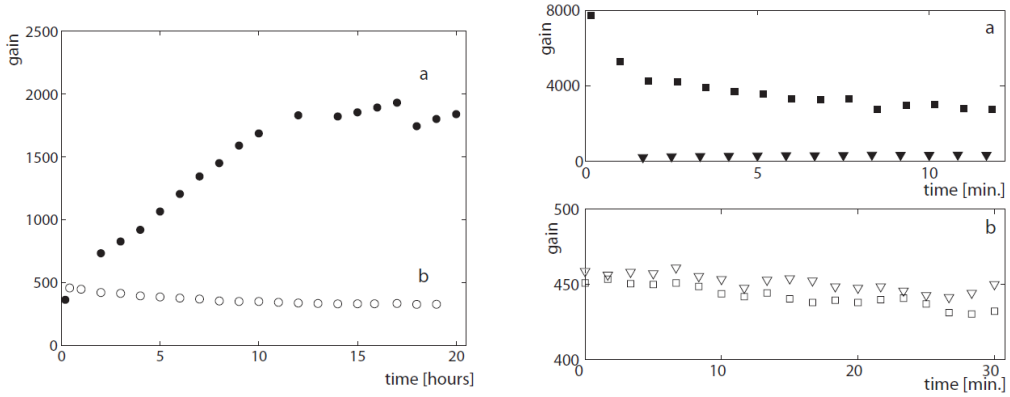

(A) (B)

FIGURE 4.13: (A) gain versus time for two THGEMs with the following geometry: thickness 0.4 mm, pitch 0.8 mm and hole diameter 0.4 mm (common parameters); different parameter: 0.1 mm rim for (a), no rim for (b). Continuous detector irradiation; DV: 1750 V for (a) and 1330 V for (b). (B) gain versus time for the THGEMs with large rim and without the rim.. Full (empty) square points represent the gain measured irradiating the THGEM with large (no) rim after it has been for 10h at nominal voltage without irradiation. Full (empty) triangle points represent the gain measured irradiating the THGEM with large (no) rim immediately after switching on the high voltage, after it has been switched off for 1 day. [148]

The evolution of effective gain for few minutes was studied under two extreme conditions: the square points for both (a) and (b) in Fig.4.13b show the response after keeping the piece off for one day and then at nominal voltage for 10 hours without irradiation before the measurement; for (a) the initial signal amplitude is larger than ten times the nominal value and shows a fast decrease ($\times 2$ in the first two minutes), whereas for (b) the value varies $< 10\%$. The triangular points represents the response after 1 day of turned off state, applying both HV and irradiation from time = 0: for (a) the signal amplitude is significantly smaller than the nominal, while for (b) the response is comparable with the square points.

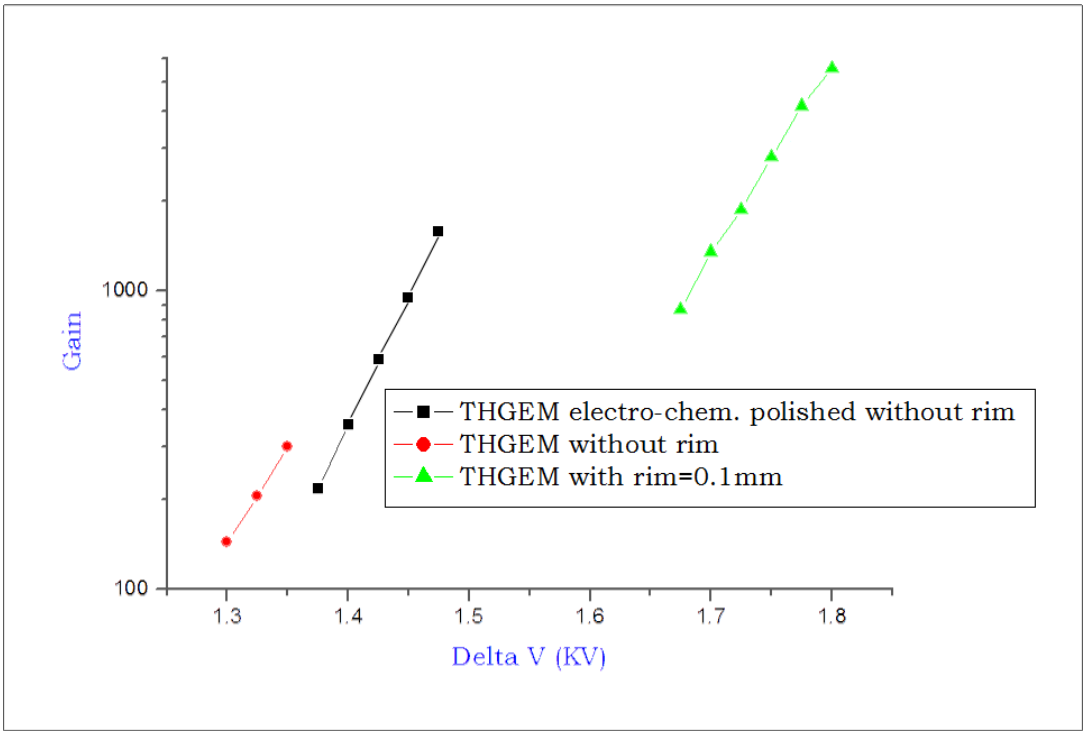

FIGURE 4.14: effective gain versus applied ΔV for THGEMs with holes of 0.3 mm diameter and 0.7 mm pitch, having different rim widths.

The choice of THGEMs with large rim is not compatible with the requirement of stable gain response needed by detectors of single photons. On the other hand the use of large rim allows to achieve higher gain values as can be clearly seen in Fig.4.14 (for red points: rim = 0 mm and G_{max} ~300; for black points: rim = 10 mm and G_{max} ~1500; for green points: rim = 100 mm and G_{max} ~6000). The data were taken in Ar:CO_2 70:30 gas mixture using a Cu X-Ray source.

The large gains ensured by sizable rims can be recovered by increasing the THGEM thickness. This is demonstrated in Fig.4.15, where, for various gas mixtures and a SetLED@5.52V UV source, the gains obtained using two different THGEMs are presented. Gains as large as those provided by 20 μm rim THGEMs (Fig.4.15-Top) can be obtained by doubling the thickness from 0.4 mm to 0.8 mm and using THGEMs without rim (Fig.4.15-Bottom).

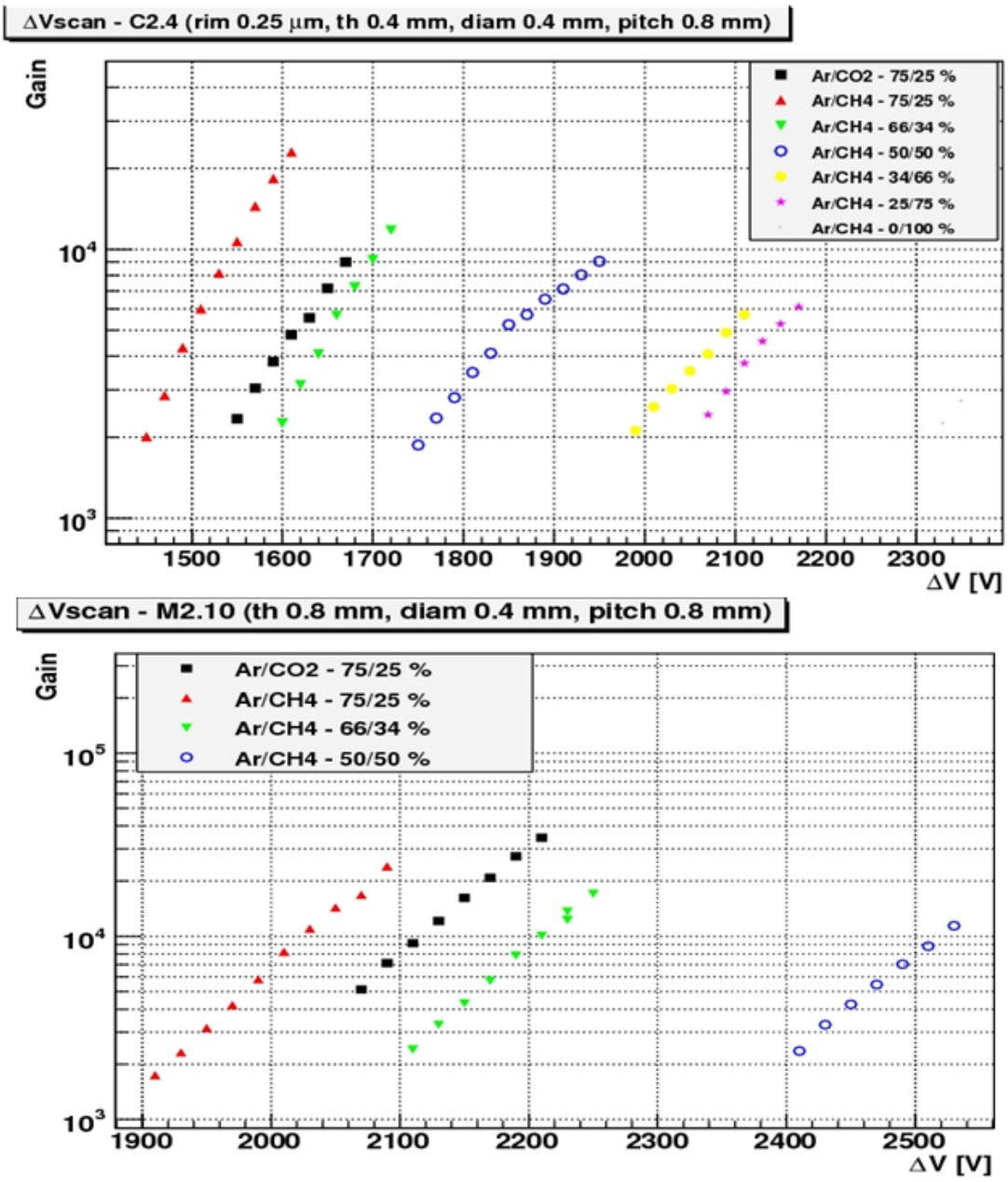

FIGURE 4.15: Effective gain vs. ΔV for different gas mixtures and different THGEM thickness. In the Top: THGEM C2.4 (details are shown in Table-4.2), maximum gain $\sim 2\times10^4$. Bottom: THGEM M2.10 (details are shown in Table-4.2), maximum gain $\sim 2 \times 10^4$.

Another way to achieve higher values of effective gain is by decreasing the hole diameter as shown in Fig.4.16 an effective gain of 5000 can be reached with a piece with 0.3 mm hole diameter and 0.7 mm pitch (t = 0.6 mm and rim = 0.1 mm) using a Cu soft X-Ray source and Ar:CO_2 70:30 gas mixture. This geometry turned out not to be suited for high photo-electron extraction and collection efficiency.

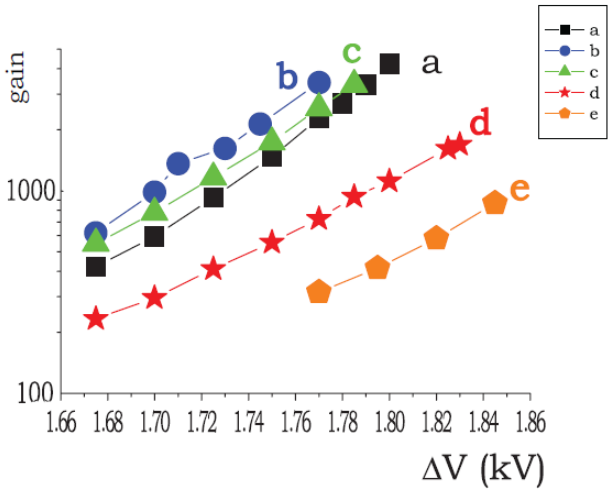

THGEM	Diameter (mm)	Pitch (mm)
a	0.3	0.7
b	0.3	0.6
c	0.3	0.5
d	0.4	0.7
e	0.5	0.7

FIGURE 4.16: Effective gain versus applied ΔV for THGEMs with 0.6 mm thickness and no rim, having different hole diameters and pitches.

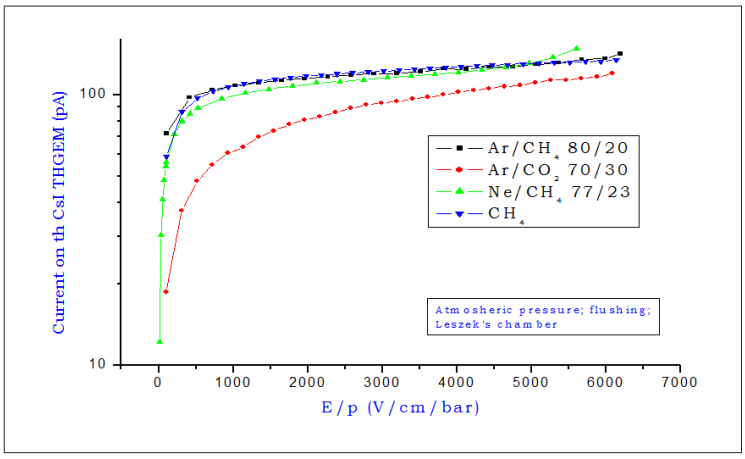

FIGURE 4.17: CsI photocurrent from a reflective photo-cathode of a THGEM versus applied electric field in various gases and gas mixtures at atmospheric pressure;

Thicker THGEMs and narrower holes seems favoured but the optical transparency should be small enough (not larger than ∼25%) to have sufficient photo-conversion efficiency. The third essential ingredient for efficient photo-electron extraction is an electric field large enough at the surface of the photo converter (∼ 1kV.cm^{-1} as shown in Chapter-1 in Fig.7.43).

The photo-electron extraction efficiency has been studied in detail (see fig.4.17). The curves can be easily interpreted with the help of electric field configurations shown in Fig.4.19.

For a THGEM to be used as an efficient reflective photo-cathode, two characteristics have to be provided: The photo-electron extraction efficiency (see Fig.4.17), which is guaranteed by a field value at the surface ≤ 1 kV.cm^{-1} and the photo-electron collection efficiency namely the fact that the extracted photo-electrons are guided to the THGEM holes and multiplied. The product of this two factors defines the THGEM photo-cathode efficiency.

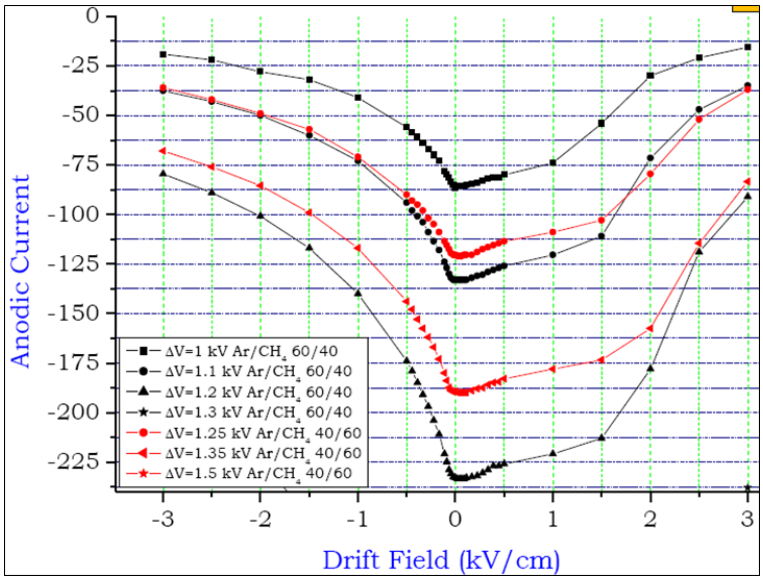

FIGURE 4.18: Anodic current versus drift field for different values of the dipole voltage ΔV; two gas mixtures have been used: Ar:CH_4 (60:40) (black) and Ar/CH_4 (40:60) (red)

The THGEM photo-cathode efficiency had been studied using a single THGEM coated with CsI to form a reflective photo-cathode, irradiated with an UV source. The anodic current was measured using a Keithley picoammeter, which is directly proportional to the product of "THGEM photo-cathode efficiency" and "THGEM gain". In Fig.4.18

The electron trajectories from the top THGEM surface (photo-cathode) for three different drift field configurations have been simulated using GARFIELD and making use of the field calculated using ANSYS

For zero drift field, all electrons are driven into the holes in both cross section of x and y as shown in Fig.4.19-Top. When the drift field is negative (reversed bias), the electrode at the lowest potential is the THGEM top one. For -0.5 kV/cm drift field (field pointing towards the drift electrode), part of the electrons are collected at the drift electrode and, thus, lost from the point of view of the detection as shown in Fig.4.19-Middle. When the drift field is positive, the electrode at the lowest potential is the drift one. This is the fields configuration used to detect ionizing particles. For 0.5 kV/cm drift field (field pointing towards the top THGEM electrode), the sum of the drift field and the dipole field results, in certain regions of the THGEM surface, either in a field pointing inside the THGEM or very feeble; in both cases the electrons are not guided to the holes and are lost as shown in Fig.4.19-Bottom.

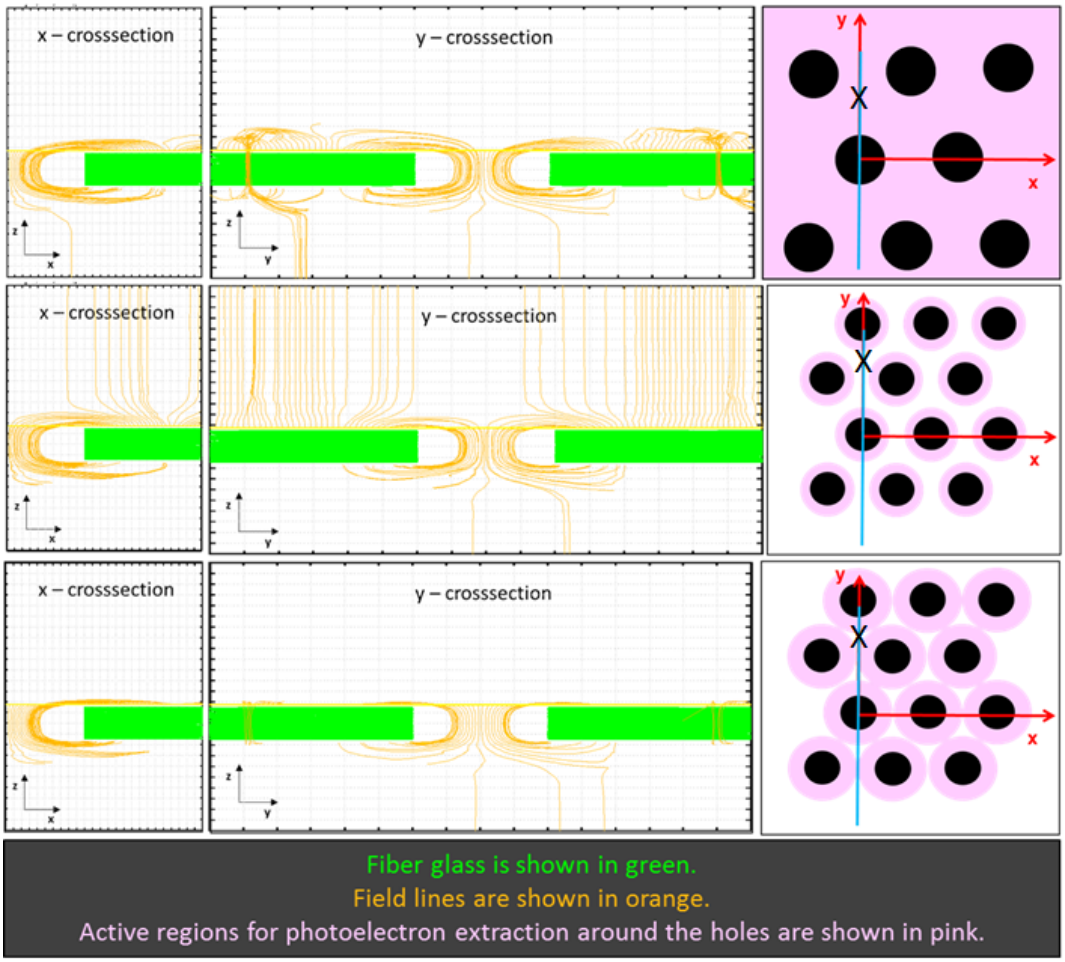

FIGURE 4.19: The effect of the interplay between the E_{drift} and the Dipole Field of the THGEM on the photo-electron extraction efficiency. The filed lines are projected on cross-sections along x and y axis for three different E_{drift} values. A sketch of the TOP view of the THGEM for each case shows in pink the region of efficient photo-electron extraction and collection.

The curves in Fig.4.18 clearly indicate a sharp current decrease when the additional field points towards the drift electrode (negative field values), a rough plateau for moderate values of the additional field oriented towards the photo-cathode (positive field values), followed by a drop when the total field (sum of the dipole and drift fields) becomes too low. In particular, the current drops at lower values of the drift field when the dipole voltage is smaller, namely for lower dipole field. The sketch of the THGEM top view presented in the right part of Fig.4.19, illustrates the regions of efficient photo-electron extraction and collection, colored in pink. The black "X" marks indicate the point at the THGEM photo-cathode surface in which the absolute value of the electric dipole field is minimum. This points are called "critical points".

The interplay between dipole field and drift field poses conditions on the geometrical parameters of the THGEM which could allow the optimization of the THGEM photo-cathode efficiency. The inefficiency due to the optical transparency of the THGEM is shown in Eqn.4.2.

$$T_{Optical} = \frac{\pi}{2\sqrt{3}}\left(\frac{d}{p}\right)^2 \tag{4.2}$$

Where d is the hole diameter and p is the pitch of the THGEM: this suggests $\frac{d}{p} \leq 0.5$. The ΔV_{THGEM} has to provide a large enough dipole field to guarantee the $|E| \geq$ 1 kV.cm^{-1} even at the critical points, but the THGEM should be operated at low enough bias to avoid electrical instabilities.

In CH_4 rich gas mixtures (imposed by the photo-electron back-scattering reduction) the optimal configuration of THGEM parameters turned out to be t = 0.4 mm; d = 0.4 mm; p = 0.8 mm and no rim.

The limitation of this geometry is the moderate value of the effective gain in the optimal configuration. This imposes the use of a multi-layer architecture to achieve the desired detector effective gain (schematic shown in Fig.4.20).

4.4.4 Triple THGEM configuration

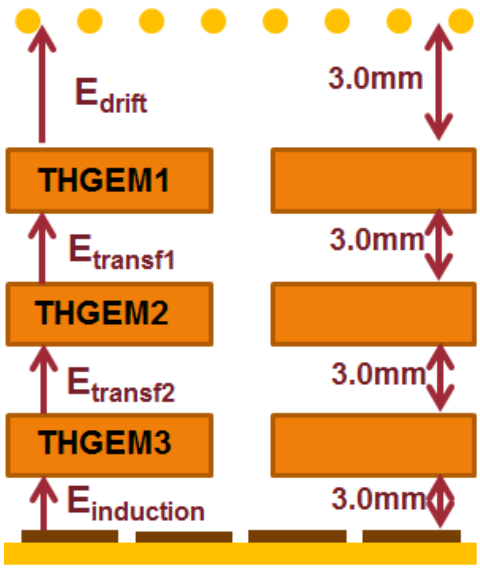

FIGURE 4.20: schematic of a multilayer THGEM setup.

Several chambers with triple layers of 30×30 mm^2 THGEMs have been built (sceme shown in Fig.4.20) and characterized using an UV LED source. The wavelength of the UV source was adequate to extract photo-electrons from copper of the TOP of the first THGEM layer. The effective gain of the system was measured for different gas mixtures and for different ΔV on different layers. When single photons are detected, the corresponding single photon–electron amplitude spectrum (Fig.4.21b)is exponentially distributed. Good signal to background ratio and a good gain stability of the detector are mandatory requirements in order that the threshold setting does not result in a critical issue. In (Fig.4.21a) the signal amplitude spectrum for a triple-layer configuration with identical THGEMs having 0.4 mm, thickness, 0.8 mm pitch, 0.4 mm hole diameter and 10 μm rim in Ar:CH_4 50:50 gas mixture, using a pulsed UV LED (model PLS 265-10 by PicoQuant GmbH, Berlin, generating 600 ps pulses) is presented. The biasing of the THGEMs was ΔV_1 = 1600 V; ΔV_2 = 1600 V; ΔV_3 = 1500 V; with E_{drift} = 0 kV.cm^{-1}; E_{tr1} = E_{tr2} = 1 kV.cm^{-1} and E_{ind} = 3 kV.cm^{-1}. The observed rate from the MCA was 4 kHz. The spectrum shows no deviation from a pure exponential distribution over a dynamic range of two orders of magnitude. The estimated effective gain $\sim 9.61 \times 10^5$[148].

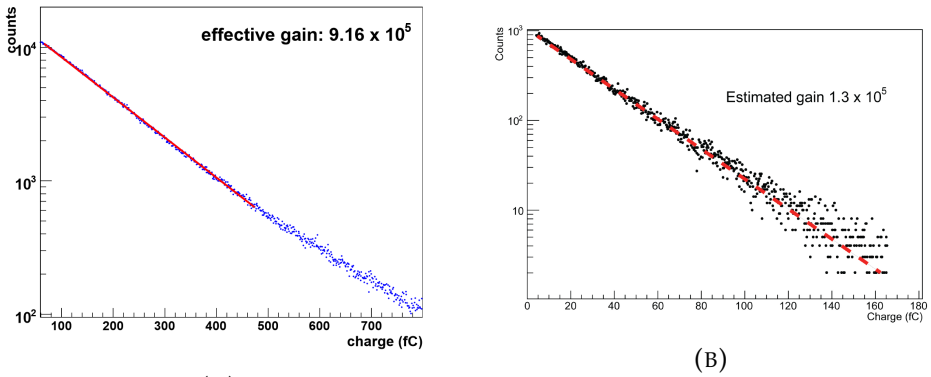

(A) (B)

FIGURE 4.21: A. Single photo-electron amplitude spectra measured with the THGEM detector described in the text. B. Example of single photon amplitude spectrum from typical triple THGEm configurations; in particular, E_{TR1} = 2 kV/cm and E_{TR2} = 4 kV/cm.

To ensure a higher reproducibility of the results THGEMs with no rim were used in the same setup and the signal amplitude spectrum can be seen in Fig.4.21b. The distribution is a pure exponential also for this case with an estimated effective gain of 1.3 $\times$ 10^5. Various sets of measurements were performed to understand the response with different sources, rates, gas mixtures, gain sharing between three pieces. Effective gain, time resolution, energy resolution and IBFR were compared. Triple THGEM detector with increased thickness (0.8 mm) of THGEM2 and THGEM3 allowed to stably operate at high gain in different gain sharing and gas conditions (see Fig.4.22). However the thickness of THGEM1 cannot be increased without compromising the photo-electron extraction and collection efficiency.

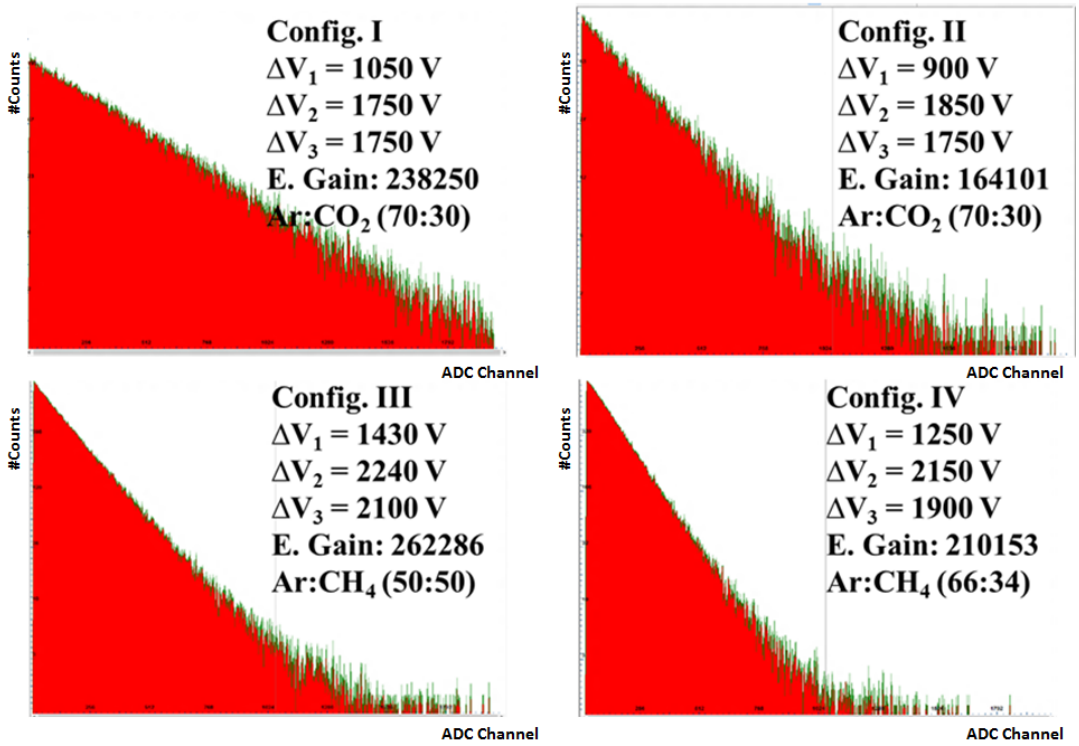

FIGURE 4.22: Spectra obtained for different applied Δv and different gas mixtures.

4.5 Ion Back Flow Study

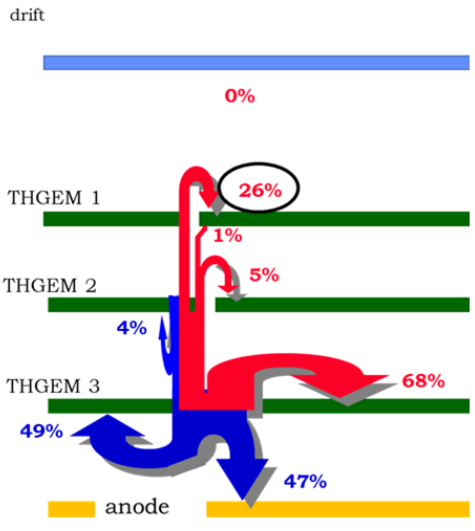

FIGURE 4.23: Schematic shows the sharing of ions and e^-s between the electrodes of a triple layer THGEM detector

High gain PDs, operating at high rate, produce a large amount of ions: a good control over their flow and reduction of IBF to the photo-cathode is thus essential. A precise measurement of the currents of all electrodes is needed to study the IBF in detail. A fundamental tool to achieve accurate measurement of the currents at a high voltage (up to 8 kV) with a resolution $\sim$ 1 pA was developed: the first versions of this pA meters are discussed in E. Rocco's Ph.D. thesis [146]. A new version, fully computer controlled and with wireless connection capabilities, was developed recently. In Fig.4.24 A wireless pico-ammeter and its corresponding Vixel wireless connectors can be seen. In Fig.4.25 the schematic of the circuit diagram for the wireless pico-ammeter is shown. The computer based custom built Graphical User Interface (GUI) is presented in fig.4.26. These pico-ammeters are used to measure the IBF ratio for the triple THGEM configuration.

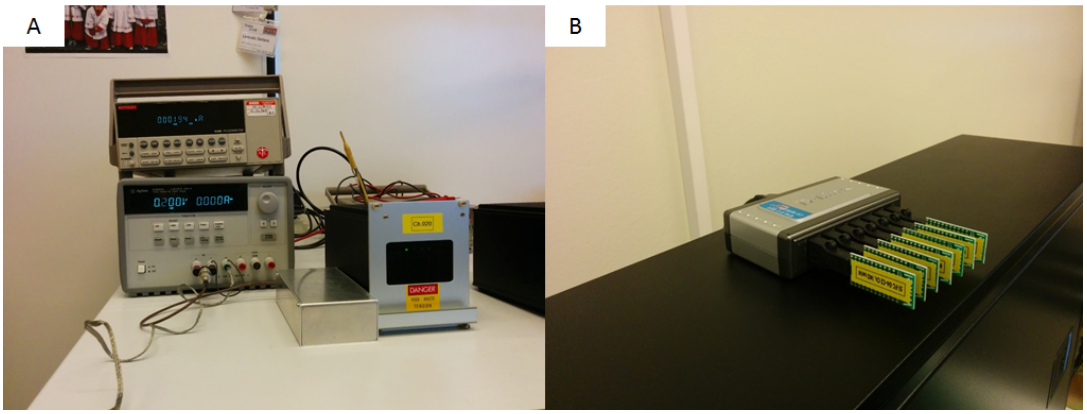

FIGURE 4.24: A. As wireless piccoammeter under tests. B. the Vixel WiFi USB data receiver/transmitter(s); connected to a USB hub to the computer

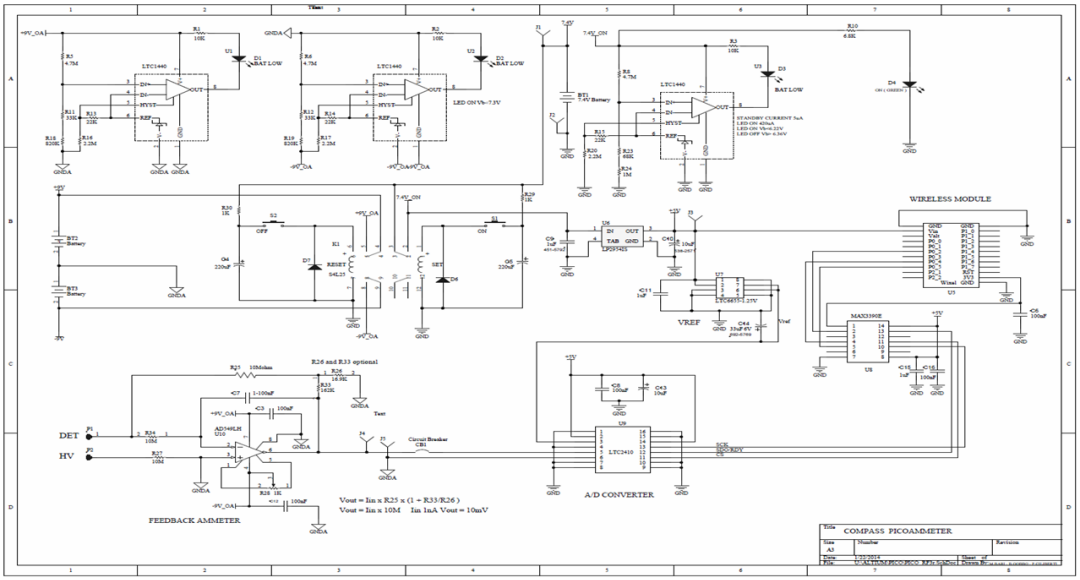

FIGURE 4.25: Circuit diagram of the Picoameter module

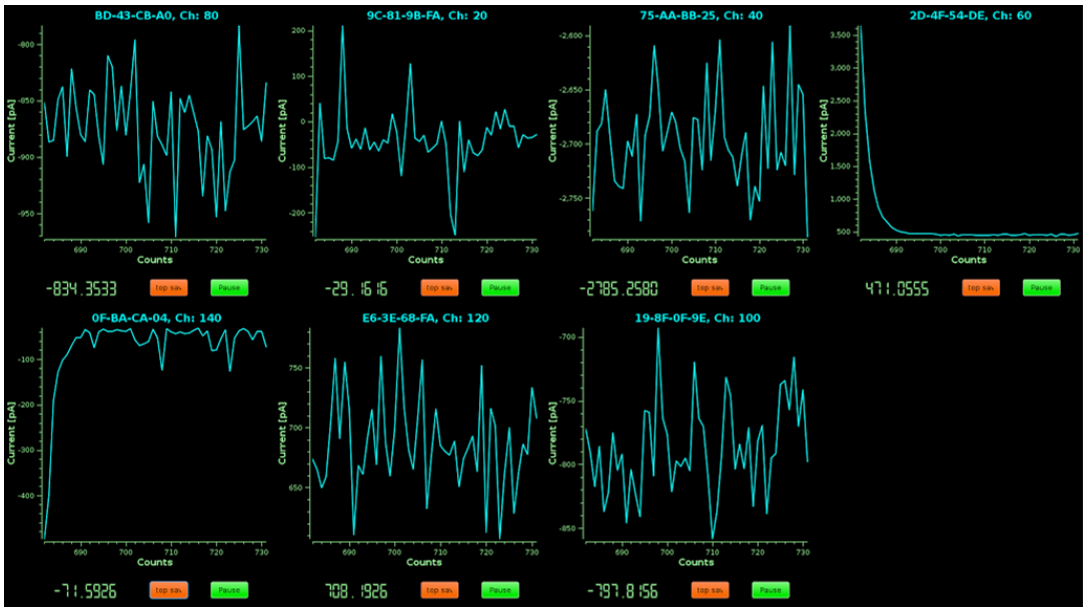

FIGURE 4.26: Graphical User Interface (GUI) of the pA meter control program

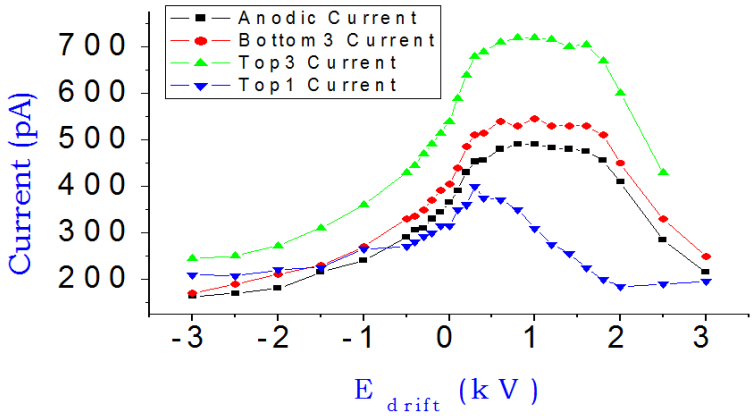

FIGURE 4.27: Measurement of anodic currents vs. E_{drift}

A typical measurement of the currents on different electrodes for a triple THGEM chamber vs. E_{drift}, performed in Ar:CH_4 50:50 gas mixture using an UV LED-255 (Seoul Optodevice Co., Ltd, Seoul, Korea (South)) and our picoammeters, is shown in Fig.4.27, where the currents of anode and bottom 3 are plotted with the reversed sign. Using standard readout chain, a good exponential amplitude spectrum for an estimated gain $\sim 10^5$ and a converted UV photon rate of $\sim$ 4 kHz was observed. The shape of the anodic current is similar to the one obtained in the analogous single THGEM current measurement despite the larger gain and the different detector architecture. From similar measurements, the sharing of ions and electrons produced in the multiplication process between the various electrodes have been computed. A typical example is presented in Fig.4.23. About 26% of the total positive ions collected in all the electrodes are detected at the photo-cathode. The total no. of ions produced in the chamber is not easily accessible experimentally.

In literature the definition of the Ion Back Flow Ratio (IBFR) is not unique. In particular, in the field of gas photon detectors, the various definitions mainly differ because

the rate of the positive ions reaching the photo-cathode is normalized either to the effective gain or to the total amount of ions produced in the multiplication process. In this thesis we normalize it to the total amount of ions produced. It has been wisely proposed by Leszek Ropelewski, to use a different parameter for a quantitative comparison of the ion back flow properties, namely the mean number of ions (N_i) reaching the photo-cathode per electron entering the multiplication process. IBFR and N_i alone do not provide enough information to access the performance of a detector: they must be complemented by the gain information.

A relevant question is the adequateness of the IBFR that can be obtained and, correspondingly, of the N_i-value. The answer depends on the specific application. Several parameters must be taken into account: (a) the expected photo-electron rate, (b) the rate of the MIPs crossing the photon detector, (i) the total charge per electron produced in the multiplication process, (ii) the number of electrons entering the multiplication chain per crossing MIP, and (iii) the ion back flow rate at the photo-cathode per multiplied electron. Parameters (a) and (b) are related to the environment; The COMPASS experiment, the rates experienced by the gas photon detectors, used in COMPASS RICH-1. The novel photon detectors are developed to replace these MWPCs (Section-3.3.1). Parameters (i), (ii) and (iii) are specific to the detector type: we compare two detectors, namely the novel THGEM-based counters, for which we quote the figures obtained in our R&D development, and the MWPCs in use in COMPASS RICH-1 (as shown in Table-4.3):

TABLE 4.3: IBF comparison between MWPCs and THGEM based PDs

	MWPC	THGEM
Photoelectron rate	$\simeq$10 Hz.cm^{-2}	$\simeq$10 Hz.cm^{-2}
MIP rate	$\simeq$10 Hz.cm^{-2}	$\simeq$10 Hz.cm^{-2}
gain i.e. number of ion-electron pairs generated per multiplied electron	4×10^4	4×10^5
collected electrons per MIP	20	$\simeq$5
IBFR	$\simeq$50%	$\simeq$5%
N_i	2×10^4	2×10^4
ion bombardment rate at the photo-cathode (from MIP and photo-electrons)	4.2×10^6 Hz.cm$_{-2}$	4.2×10^6 Hz.cm$_{-2}$

In the gaseous photon detectors in use at COMPASS RICH-1 the photo-electron rate is everywhere lower than 10 Hz/cm^2 and the ionizing particles rate is $\leq$ 10 Hz/cm^2.

Detector-dependent parameters, estimation for the novel THGEM-based counters

- THGEM-based photon detectors can exhibit a stable operation with an effective gain of a few times 10^5, while the total charge produced in the multiplication process is about twice larger.
- Applying the optimized reverse bias, the thickness of the effective volume for electron collection is reduced to <0.5 mm; therefore, using a methane-argon mixture with a methane fraction in the range 0.3-0.5, it is expected to collect, on average, <5 electrons per MIP.
- We demonstrate that an IBFR $\leq$5% can be obtained.

The total current I_{tot} is defined as the mean value of the absolute values of I_+ and I_-, while the absolute value of their algebraic sum DI, expected to be zero, is checked: the ratio RI=DI/$I_{tot}$is always smaller than 2%. I_{tot} is the denominator we use to calculate the IBFR. The current IIBF measured at the photo-cathode, is the numerator in use. DIIBF, namely the limit of the absolute error on IIBF is registered. The fractional error associated to IBFR is the larger between RI and DIIBF/IIBF: the resulting fractional error is always smaller than 2%. In a multilayer-THGEM detector, part of the electrodes collects both ions and electrons and the measured currents are the algebraic sum of the currents generated by the two species of charged carriers: the IBFR determined as described above is an approximated estimation, nevertheless adequate for our purpose. Due to the mild reverse bias applied between the drift anode and the photo-cathode, no electrons are collected at the photo-cathode, making the measurement of the current at this electrode a good estimate of the ion bombardment current. Concerning the current corresponding to the total amount of charge generated in the multiplication process, I_- is typically generated by the currents measured at the anode and at the bottom face of the third THGEM: no ion collection is expected there. Part of the electrons generated at the first and second multiplication stages does not reach the third THGEM layer and they are collected elsewhere without disentanglement from the ions collected at the same electrodes. I_- does not include their contribution. Nevertheless, these losses represent a fraction of the electrons that do not experience the last multiplication stage and, thus, these corrections are small and they can be neglected.

It has been demonstrated that dedicated measurements in single layer and multiple layer configuration can result in disentangling the two components, as it has been done for systematic studies of the GEMs [149] [150]. Nevertheless, a multiple measurement approach prevents extended campaigns when various geometrical and electrical configurations are investigated: we have adopted the approximate IBFR estimation and we present results obtained by this approach. The amplitude spectra collected with the THGEM-based photon detectors are always exponential, even at the largest gain. The effective gain is estimated from the slope of the exponential spectra, which are collected by making use of the standard readout chain mentioned before. An example of an amplitude spectrum is provided in Fig.4.21b

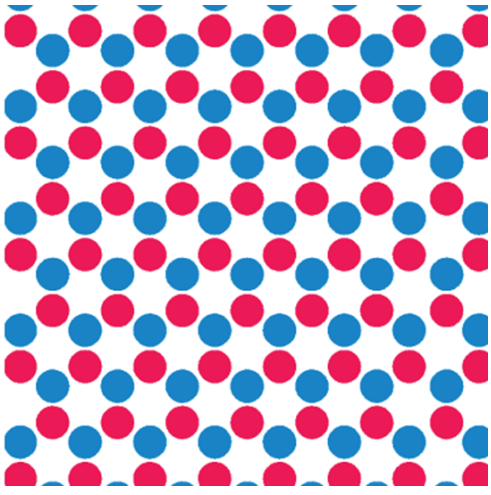

FIGURE 4.28: Misaligned Configuration of THGEM holes between two stages

The gas mixture used is Ar:CO_2 =70:30. This gas mixture, which is not optimized concerning photo-electron extraction, is chosen on the basis of practical considerations related to the procurement and use of flammable gases. The photo-electron extraction is not an issue, while the different diffusion properties of electrons and ions in the optimized gas mixture and in one which was used , do not influence the conclusions of the investigation. In fact, in the THGEMs, the scale of the geometrical parameters is such that the ion and electron motion is largely driven by the electric field, while the diffusion plays a minor role.

The IBFR has been measured for both

aligned hole configuration between two steps and with a misaligned hole configuration(Fig.4.28) between two stages.

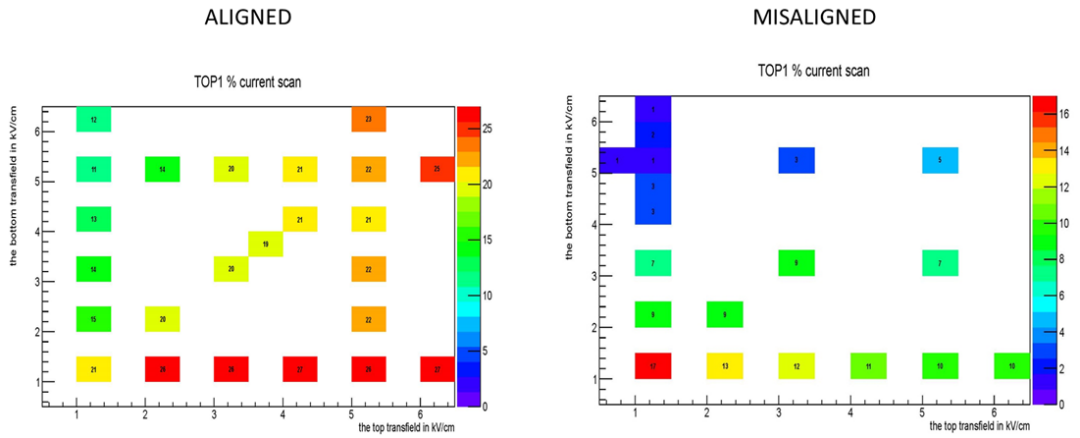

FIGURE 4.29: Ion Back Flow Ration measurement of TOP1 in Aligned and Misaligned condition

A clear indication of IBFR ∼few% has been observed for lower(∼1kV/cm) $E_{Transfer-top}$ and higher value of $E_{Transfer-bottom}$ as shown in Fig.4.29.

We have seen that $\sim$ 26% of IBF is obtained in normal multilayer configuration, where as a staggered configuration of holes between different layers and with unbalanced transfer electrical field configuration between layers ∼few% of IBF can be achieved.

Even though the possibility to operate a PD with triple THGEM misaligned configuration with a IBF of $\leq$5% has been demonstrated, the constrains on the electric field to obtain a very unbalanced configuration are conflicting with the optimization of the photo-electron detection efficiency. A better solution to this challenge will be discussed in the next chapter.

4.6 Summary

The dedicated R&D to develop novel PDs for the upgrade of COMPASS RICH-1 examined various technologies and THGEM based PDs has been selected as the best choice: they are robust and able to provide high stable effective gain in high rate environment as previosely shown by the systematic studies performed at Weizman Institute.

Many (∼50) different 30×30 mm^2 prototypes have been characterized and the role of THGEM geometrical parameters and electrical conditions has been investigated: THGEMs with large rim have being discarded despite the large gain they provide as they cannot guarantee a stable response. Thicker THGEMs allow achieving larger gains but they are not suited as reflective photo-cathodes. The optimal geometry has been found to be d = 0.4 mm, t = 0.4 mm, p = 0.8 mm and no rim. CH_4 rich gas mixtures have to be use to minimize the photo-electron back-scattering. Snmall area detectors with triple THGEMs provide stable effective gain $\sim$ 10^5 in high rate conditions.

The ion flow in triple THGEM configuration, to all the electrodes, was measured using custom built sensitive picoammeters. The IBFR to the photo-cathode, which in standard configuration is closed to 30% was reduced to ∼few% using misalignment of the THGEM holes between different layers and very unbalanced transfer field configurations.

The challenge of building and operating larger size prototypes was the next step in the R&D. I tested and characterized many prototypes, in the laboratory and at the CERN test beam facilities (described in Chapter-5). I contributed in developing several tools and methods for quality control and characterization of the components as will be discussed in Chapter-6.

Chapter 5

Towards the large size PDs

5.1 THGEM Performance Studies

After the intensive studies with small size (30×30 mm^2) THGEM prototypes (as described in Chapter4), larger active area (300×300 mm^2) THGEMs with no rim have been produced by ELTOS and tested. The capacitance of these THGEMs is $\sim$100 times larger than that of the small ones and, if the electrodes are not segmented, the average energy release from a discharge could easily damage the readout or even the THGEM surface. Intermediate size pieces have been tested before and the largest size pieces with no segmentation, which could be successfully operated

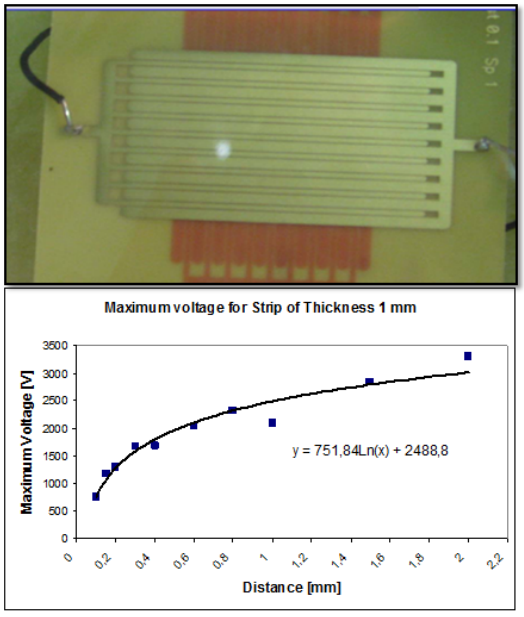

FIGURE 5.1: TOP: Picture of a discharge occurring during a study of the optimization of the THGEM segmentation performed with the special PCBs; BOTTOM: Measured breakdown voltage as function of the distance between electrode segments.

were 100×100 mm^2 THGEMs which had a capacitance of $\sim$ 1 nF. The segment size for large THGEMs was thus chosen to be 288×48 mm^2 to have a similar capacitance resulting in six sectors per 300×300 mm^2 THGEMs.

The electrode segmentation study was performed using dedicated PBCs and with a spark test setup (see Fig.5.1-TOP). A clearance between sectors of 0.7 mm was finally

decided based on the results shown in Fig.5.1-BOTTOM, to prevent discharge cross-talk between sectors for voltage differences up to 2 kV.

The first problem to be faced with large area THGEM pieces was the fact that they did not meet the expectations extrapolating from the small size, in terms of performance and discharge rates. Several tools were employed to study this problem.

The full characterization of a large THGEM includes usually takes several days while a simpler test of the breakdown voltage in air is much faster. The expected breakdown voltages in dry air can be extracted from the Pashchen curve which follows the equation-5.1:

$$V_{BreakDown} = \frac{Apd}{ln(pd + B)} \tag{5.1}$$

Where p is the gas pressure, d is the distance between two electrodes and A and B are constants specific of the gas used. V_{BD} depends on p and d only via the product pd.

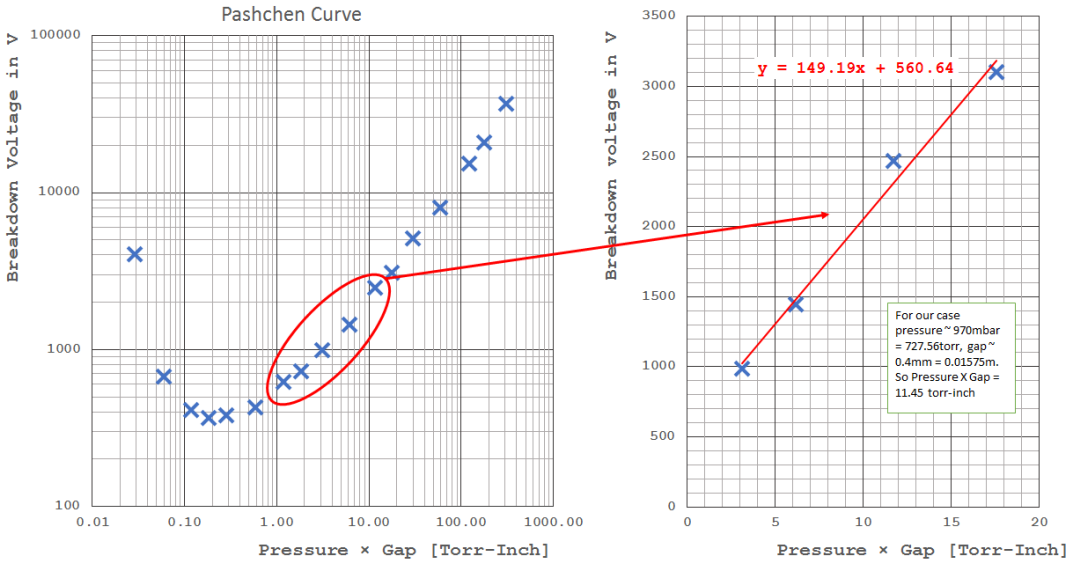

FIGURE 5.2: Left: Result of Pashchen measurement done in air; Right: The linearized portion of the curve which belongs to the distance of our interest

In Fig.5.2-a one can see the Pashchen curve: breakdown voltage vs. "gas pressure"×"electrode gap" and in Fig.5.2-b the linearized portion of the Pashchen curve in our region of interests. A dedicated system was built to check the breakdown voltage by providing voltage on electrodes in a dust free environment. A typical outcome of the "Pashchen Test" (nickname given by us to this dry air breakdown voltage measurement) is presented in Table-5.1. The spread in the measured values of the breakdown voltage is extremely large indicating the presence of a local problem in many sectors of the newly produced large size THGEMs, which were absent in the small size prototypes.

TABLE 5.1: Sector wise Pashchen Test results for $300 \times 300 mm^2$ THGEMs. Numbers are in Volts

THGEM	Sect1	Sect2	Sect3	Sect4	Sect5	Sect6
#18	1820	1650	1660	1630	1570	1330
#19	2270	2380	2370	2080	2050	1470
#23	2400	2360	2300	2130	2030	2100

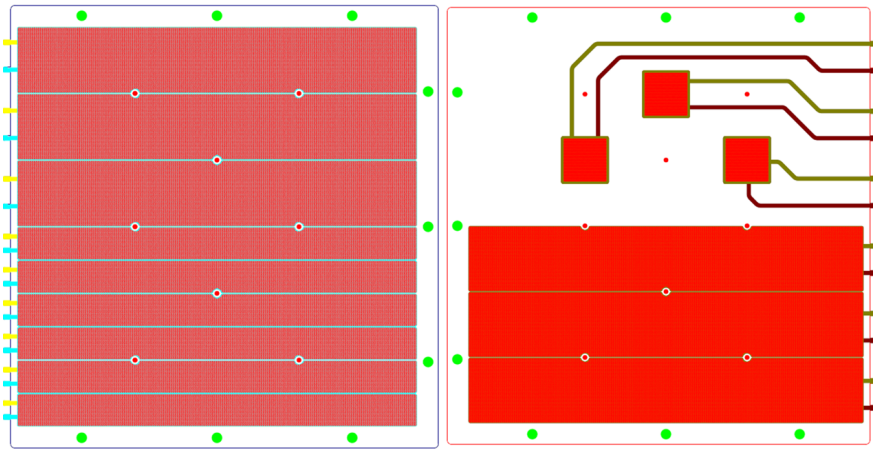

FIGURE 5.3: THGEM foils with sectors having different active area to compare the response

Special pieces were produced and used to study the spark rates as a function of the maximum effective gain for different active areas as shown in Fig.5.3. The measurements were performed in a special test chamber with Ar:CO_2 70:30 and using an ^{55}Fe X-Ray source. Table5.4 shows the result obtained: The 30 $\times$30 mm^2 sectors achieved stable maximum effective gains larger than 1000 while 288$\times$48 mm^2 sectors could only achieve a maximum effective gains between 300 and 600 for the same measurements.

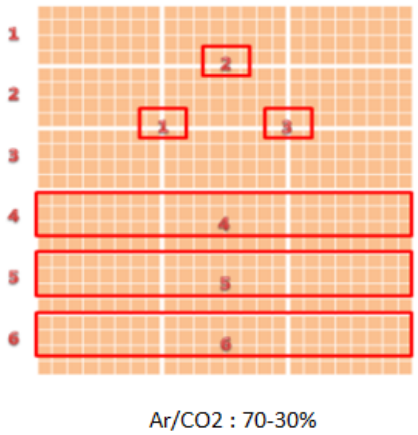

Gain measurement @ highest ΔV of the sectors

	A	B	C
1		~1100	
2	~1050		~1000
3			
4			
5	~300	~330	~350
6	~581	~474	

FIGURE 5.4: Table of gains obtained from different sectors with different area

Two sparks categories were occurring: sporadic sparks with random locations, which did not prevent further increase of the THGEM bias and systematic persistent sparks, which regularly occurred at the same hole for the same voltage bias, preventing the

application of higher bias. The setup allowed to locate the persistent sparks. The optical investigation of the regions where the spark was occurring was performed using "Dino Lite Digital microscope"[1] and revealed a set of problems linked to the drilling of the holes and handling of the pieces. defects were categorized:

- Type 1 and 2: The border of the holes are not smooth probably due to the quality of the drilling tools,
- Type 3: A part of the copper around the hole is detached probably because the drilling tool is not sharp enough and is breaking the Cu and fiberglass instead of cutting it!
- Type 4: Remnants of fiberglass are present inside the hole.
- Type 5: Dirt (mainly remnants of dust etc.) is stuck inside the hole.

Fig-5.5 shows typical examples of these pathologies. In several cases despite investigation no evident pathologies were found.A solution, proposed by Rui de Oliviera was attempted: the THGEM surface, including the inner part of the holes, was coated by sprayed polyurethane (Fig.5.6), later removed from the Cu surface leaving the polyurethane film inside the holes. Good performance of the treated pieces were indeed obtained but a better solution more compatible with the further treatment on the THGEM was later found to be more appropriate.

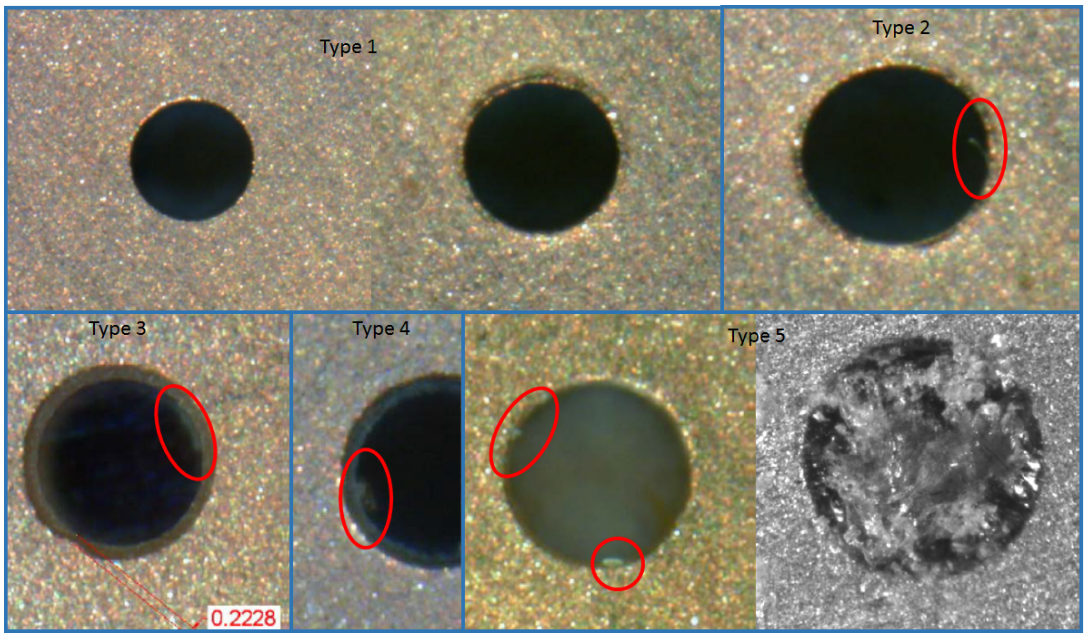

FIGURE 5.5: Several irregularities were found in larger THGEM foils after production

[1]AnMo Electronics Corporation, Hsinchu Headquarters: 5F-1, No.76, Sec. 2, Dung-Da Road, Hsinchu 300, Taiwan; web: http://www.dino-lite.com/

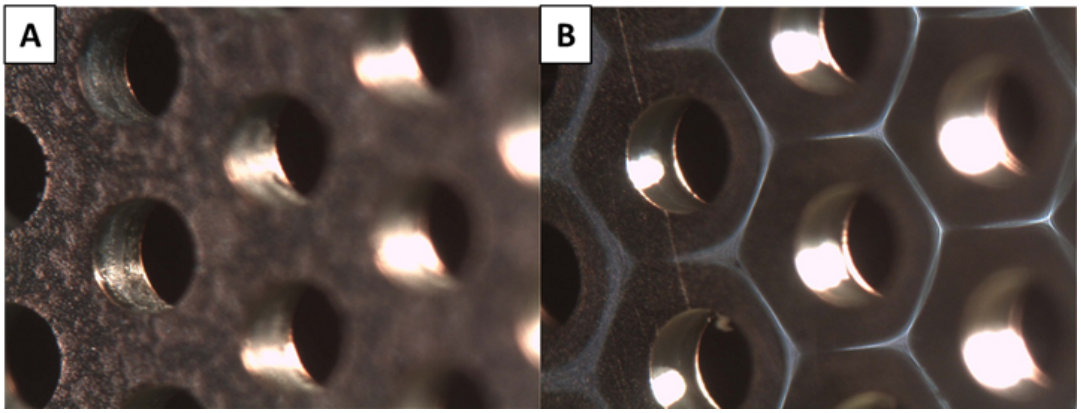

FIGURE 5.6: Left: Microscopic picture of THGEM holes without PU coating. Right: Microscopic picture of THGEM holes after PU coating.

- Polish THGEMs with fine grain pumice powder ($60 - 100mu$m) to enhance the surface quality.
- Cleaning that piece with high pressurized water to get rid of the pumice powder even within the holes.
- Cleaning it inside an "Ultrasonic Bath"at 60^0C temperature with a high PH solution (SONICA PCB Cleaner PH $\sim$11) for two hours.
- Drying it in the oven for 24 hours at 120^0C.

TABLE 5.2: Different $300 \times 300mm^2$ THGEMs sector wise Pashchen test results showing the improvement of the breakdown voltage. Numbers are in Volts

Situation	Sect1	Sect2	Sect3	Sect4	Sect5	Sect6
Out of the box	1820	1650	1660	1630	1570	1330
After first treatment	2270	2380	2370	2080	2050	1470
After Second treatment	2400	2360	2300	2130	2030	2100

The polishing was performed using a BOSCH orbital polishing machine with soft head (without abrasive paper etc) attached to it (See Fig.5.7-A and B.). Comparative studies of the effects and the efficiency of the polishing procedure with different "head materials" were performed. Using a sponge head takes longer than using a faelt head but the faelt may leave remnants inside the holes, which can cause irregularities of type Type 4 and 5. The optimal procedure for this special treatment has been finalized and a typical result is shown in Table5.2 for one THGEM.

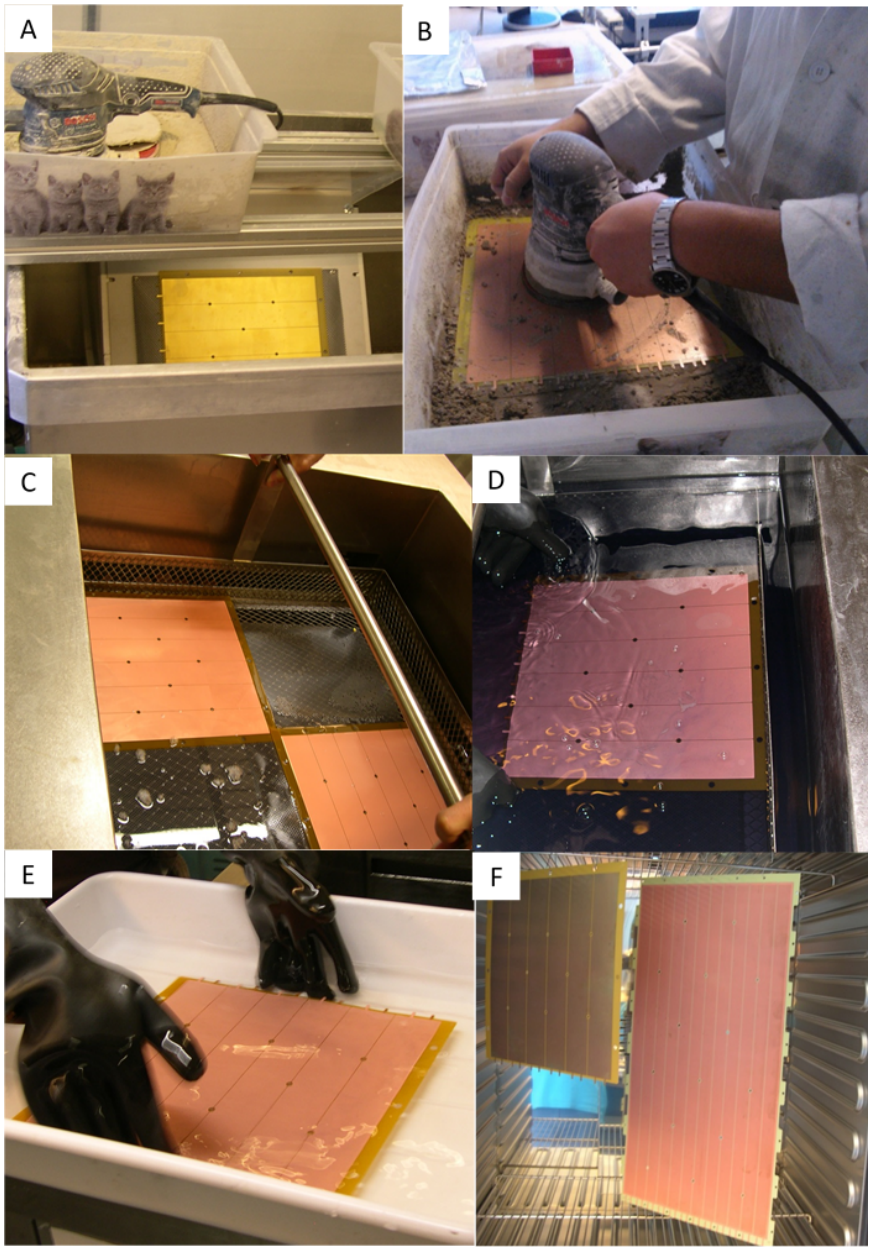

FIGURE 5.7: A. The BOSCH polishing machine; B. Performing polishing operation; C. Two THGEM foils inside the ultrasonic bath after polishing; D. After the operation of the ultra sonic bath; E. cleaning THGEM foil with deminaralized water to remove the high ph solution came from the bath; F. THGEM foils inside the oven.

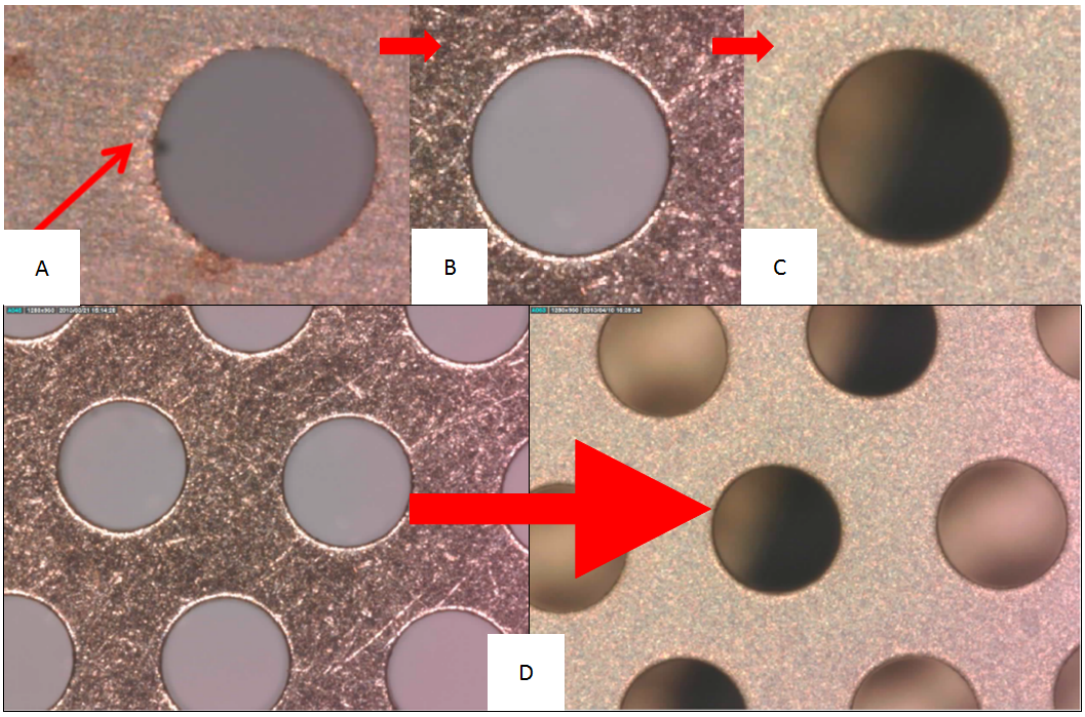

FIGURE 5.8: A. Microscopic picture of a hole after production showing Type1 irregularities; B. Microscopic picture of the same hole after polishing showing surface and border defects; C. Microscopic picture of the same hole after treatment done at ultrasonic bath, no more surface or border deffect; D. Microscopic picture of a THGEM foil to compare the surface quality before and after the treatment done in Ultrasonic bath.

The treatment can be repeated to achieve a more homogeneous distribution of measured breakdown voltages (see Table-5.2). In total more than 36 pieces of 300×300 mm^2 were treated and the large majority showed significant improvement in the "Pashchen Test" results.

5.2 Characterization of 300×300 mm^2 THGEM pieces

A detailed characterization of the large THGEM prototypes was performed at INFN Trieste THGEM lab. The setup used for the characterization is sketched in Fig.5.9. The anode was segmented in 572 (24×24), $12\times12 mm^2$ pads. Each group of 4×8 pads was connected to a switch system which allowed selecting the group to be read by the standard read out chain. A soft X-Ray source (^{55}Fe) was used for characterization. To put the source in position at the center of readout pads, a Cu plate with holes drilled according to the position of the readout pads was mounted over the kapton window (Fig5.9D).

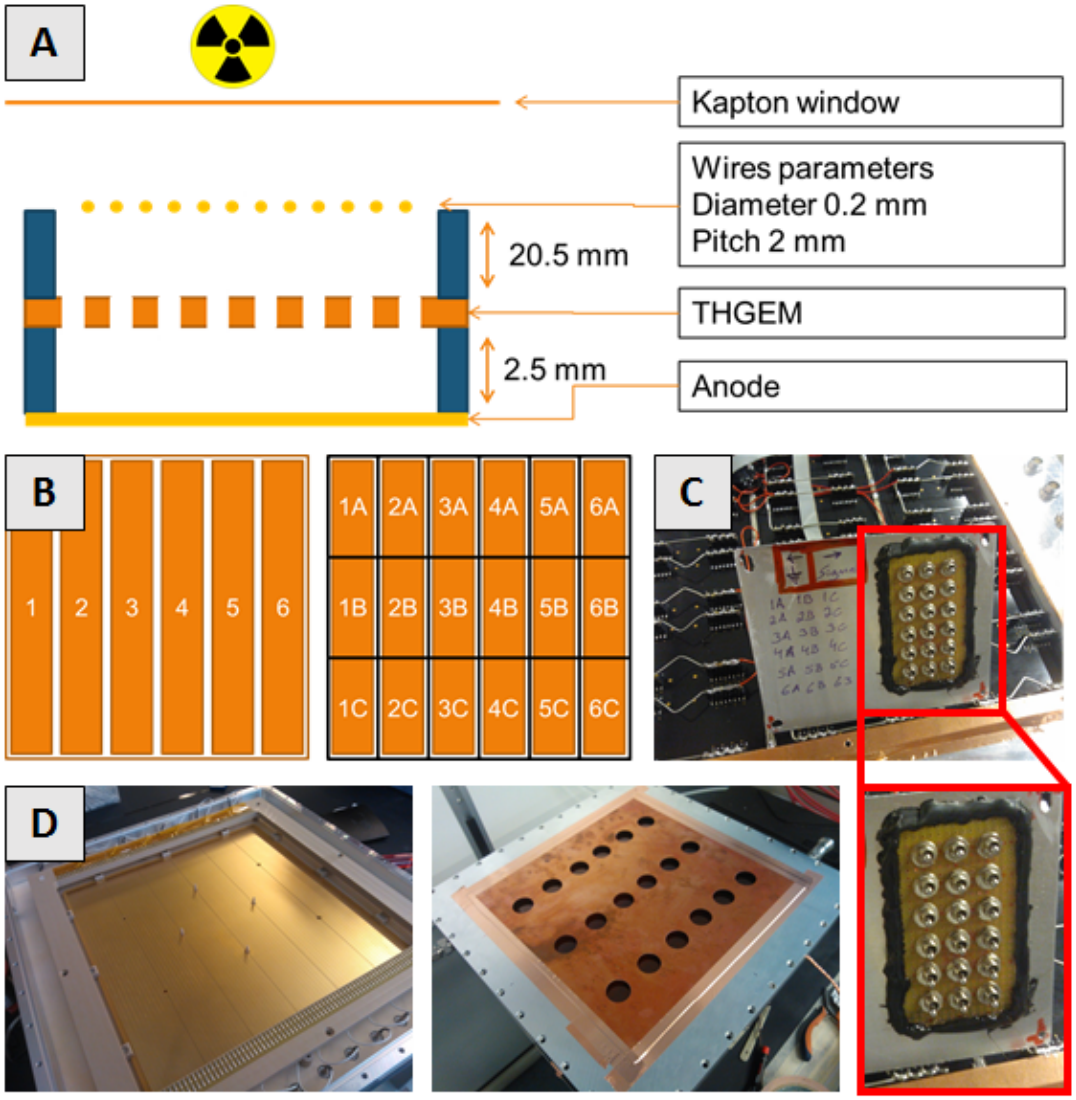

FIGURE 5.9: A. Schematic of the single THGEM characterization setup. B. Scheme of the 6 sectors of a $300 \times 300 mm^2$ pieces (left) and 18 (3×6 sets of 32 pads) readout sectors (right). C. The switching system to read only one sector at a time (top) and zoom of the switching system (bottom) D. An Au coated THGEM mounted on the chamber (left) and closed chamber with the Cu cover with holes to position the ^{55}Fe source in center of the readout sectors (right).

The measurement of the effective gain uniformity has been performed for several pieces. A typical result for a good THGEM is shown in Fig.5.10. More than half of the THGEMs were showing large gain non-uniformity.

An example is shown in Fig.5.11, where a THGEM (t = 0.8 mm; d = 0.4 mm; p = 0.8 mm; rim = 0 mm) was characterized using the previous setup with ΔV_{THGEM} = 1825 V. The signal distribution for each readout sector is fitted with a Gaussian (left) and the calculated effective gain is shown in the color plot (right). The ratio of the maximum and minimum effective gain values is $\sim$ 2.3 and a clear gradient can be observed. A corresponding gradient with opposite sign is present in the map of the values of the THGEM thickness. The measured average thickness values for the four corners of the THGEM PCB are shown inside the blue boxes.

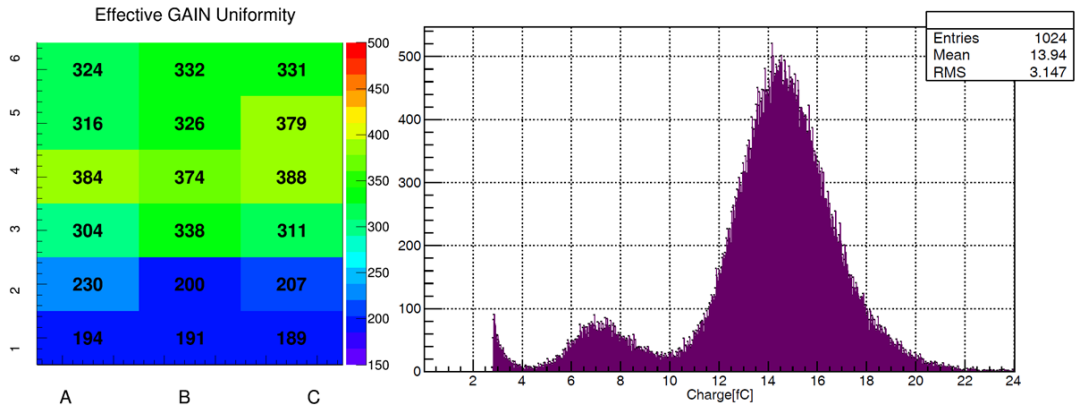

FIGURE 5.10: Left. Measured gain uniformity for applied ΔV of 1400V on all sectors; Gas used $Ar : CH_4 50 : 50$; Source used: ^{55}Fe X-Ray source. THGEM used #19 d = 0.4mm, t = 0.4mm, p = 0.8mm, rim $\leq 5\mu$m; Right. Amplitude spectra obtained for sector 3B.

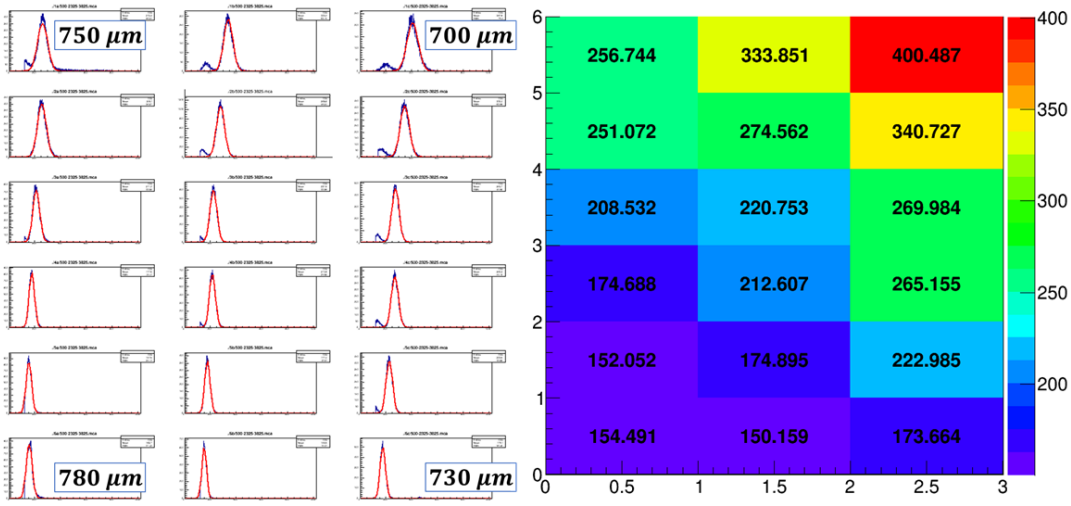

FIGURE 5.11: ^{55}Fe Signal amplitude spectra for all 18 readout sectors with gaussian fit (left), calculated effective gain values from the fits (right). The values inside blue boxes (left) are the measured average thickness of the PCB corner regions.

Only those THGEMs, which provided good electrical stability and good gain uniformity were used in the following studies and tests.

Different PDs based on triple 300×300 mm^2 THGEMs were built and operated in laboratory and at CERN Test Beams. Satisfactory results including the collection of Cherenkov rings for single events were obtained as reported later in this chapter. After several years of R&D on triple THGEMs and other architectures an alternative one based on hybrid configuration using THGEMs and MM provided more convincing results: the superior IBF intrinsic suppression property of the MM and the evidence of a higher electrical stability of the hybrid large area detector with respect to the triple THGEM when operated at large gain in high irradiation environment, lead to the decision to perform the upgrade of COMPASS RICH-1 with Hybrid PDs.

5.3 Micromegas for the Hybrid PDs

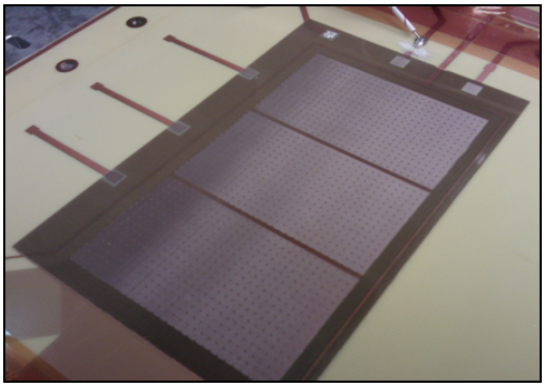

FIGURE 5.12: Micromegas borrowed from Sacley

Micromegas detector technology is mature and widely used (as described in Chapter-1). In HEP experiments MM detectors are mostly used as trackers. Our first ever prototype to validate the novel idea of coupling THGEMs and Micromegas was built, borrowing a $60 \times 100mm^2$ active area MM (Fig.5.12) from CEA, Saclay COMPASS colleagues and we characterized the hybrid detector, (see Fig.5.13) obtained by coupling it to a $30 \times 30mm^2$ active area THGEM. A very promising result was observed from the first measurements. High gains ($\sim 10^6$) were observed using a THGEM with 20 μm rim, a UV LED 255 source in Ar:CO_2 70:30 gas mixture (see Fig.5.14-A).

For ^{55}Fe X - Ray source a gain of 10^5 was reached as shown in Fig.5.14-B. A study of the electrical stability for different gain sharing configurations was performed. Gain scans were obtained using an ^{55}Fe X-Ray source in Ar:$CH_4$0 30:70 gas mixture, first keeping the THGEM at a ΔV of 1850 V varying the V_{MESH} is shown in Fig.5.15. Later the same measurement was performed, keeping the MM at a constant voltage of V_{MESH} =680 V and by varying ΔV_{THGEM} is shown in Fig.5.16. A maximum effective gain of 2.1$\times 10^5$ (with a gain of the MM around 500) was obtained.

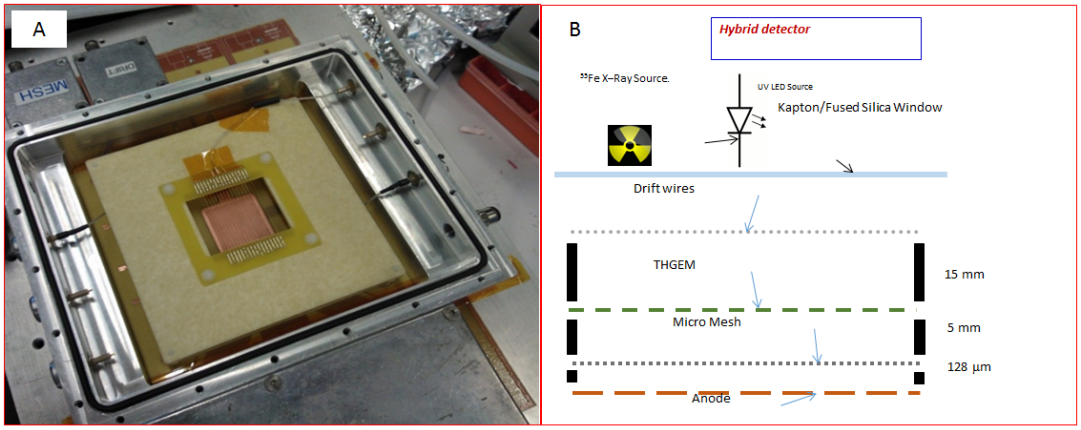

FIGURE 5.13: A. The first ever hybrid prototype built; B. Schematic of the prototype showed in A.

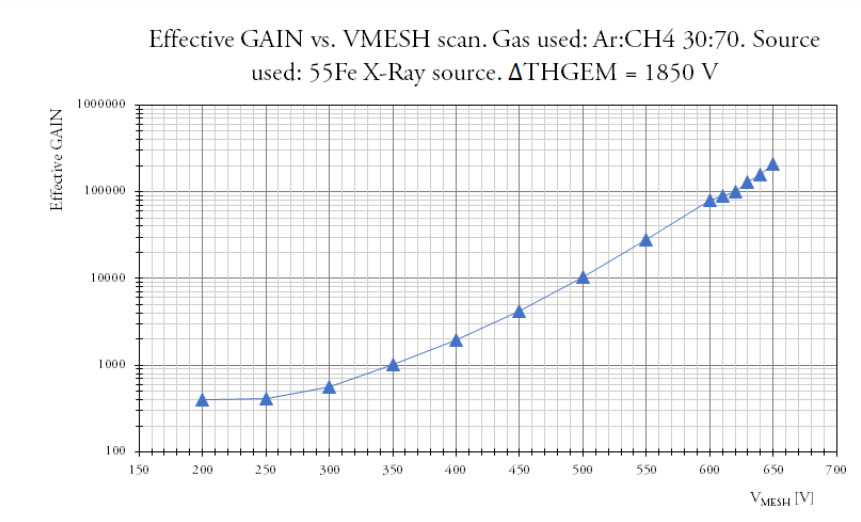

FIGURE 5.15: Effective gain of the hybrid detector as function of V_{MESH}. ΔV_{THGEM} = 1850 V.

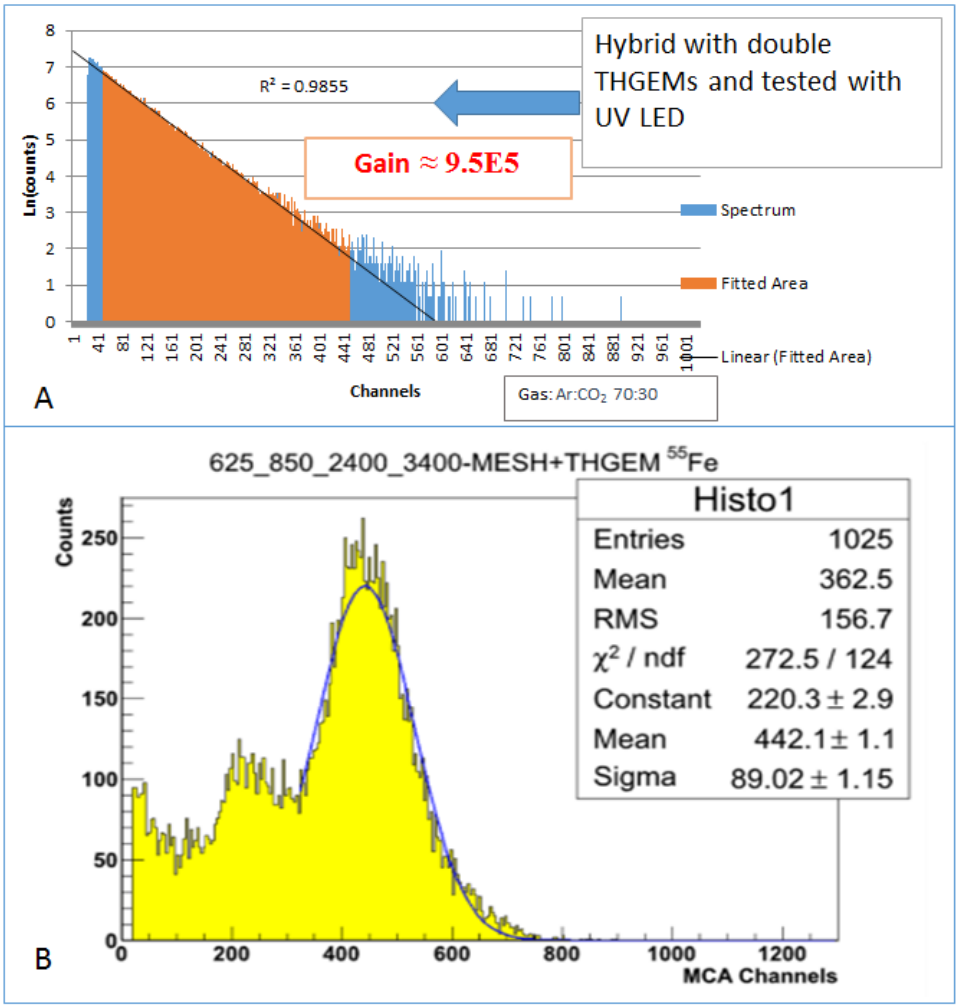

FIGURE 5.14: A. Spectra taken by focusing an UV LED to the top copper surface of the first THGEM in the Hybrid structure; B. A spectra taken by illuminating the setup by ^{55}Fe X-Ray source

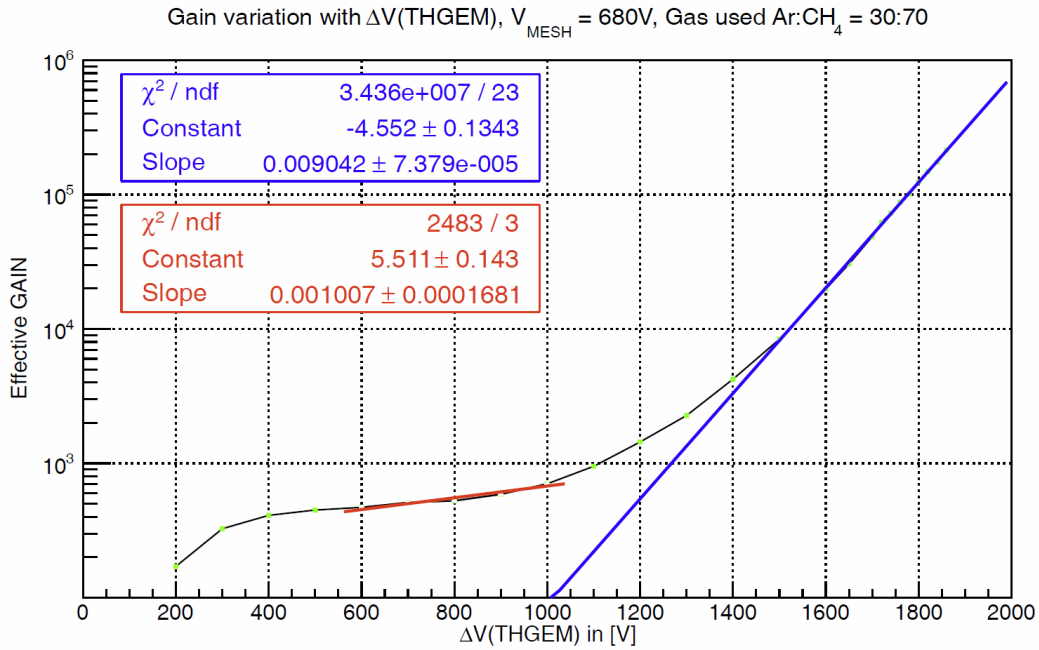

FIGURE 5.16: Hybrid effective gain vs ΔV_{THGEM} for MM at 680V. Gas used Ar:CH_4 30:70. Source: ^{55}Fe

The electrical stability with different gain sharing between the Micromegas and the THGEM was studied with the same setup. In Fig.5.17 the effective gain as function of both ΔV_{THGEM} and V_{MM} is plotted.. The red boxes are introduced to indicate that the chamber was not electrically stable for that voltage combination.

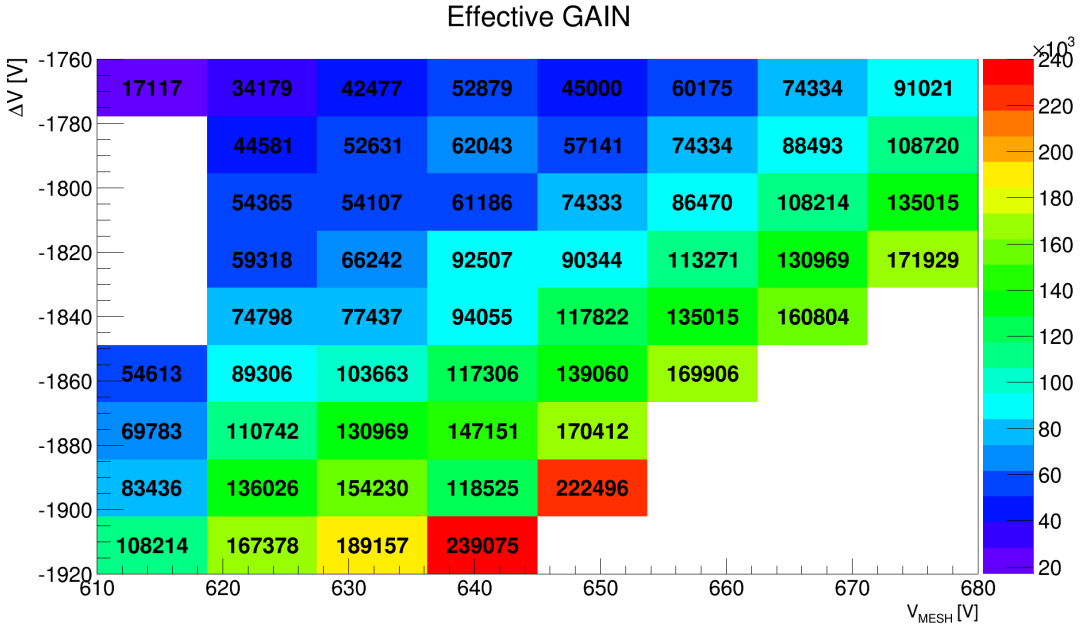

FIGURE 5.17: Hybrid effective gain as fuction of ΔV_{THGEM} and V_{MM}. Gas used Ar:CH_4 30:70. Source: ^{55}Fe. Red boxes defines start of limited stability conditions.

5.4 300×300 mm^2 Hybrid PDs

5.4.1 Bulk Micromegas

Two 300×300 mm^2 MM were produced by Rui de Olivera at CERN using the standard bulk technology with a gap of 128 μm (Fig.5.18-A). They were fabricated on special PCBs, designed in Trieste and produced by TVR Srl, with the anode segmented in readout pads of 12×12 mm^2. In Fig.5.18-B a test chamber with one MM is shown. The first measurement was dedicated to test gain uniformity of the MM using an ^{55}Fe source in Ar:CO_2 gas mixture. Fig.5.19 shows the measured effective gain values normalized to the effective gain value of 594 corresponding to the highest signal amplitude region.

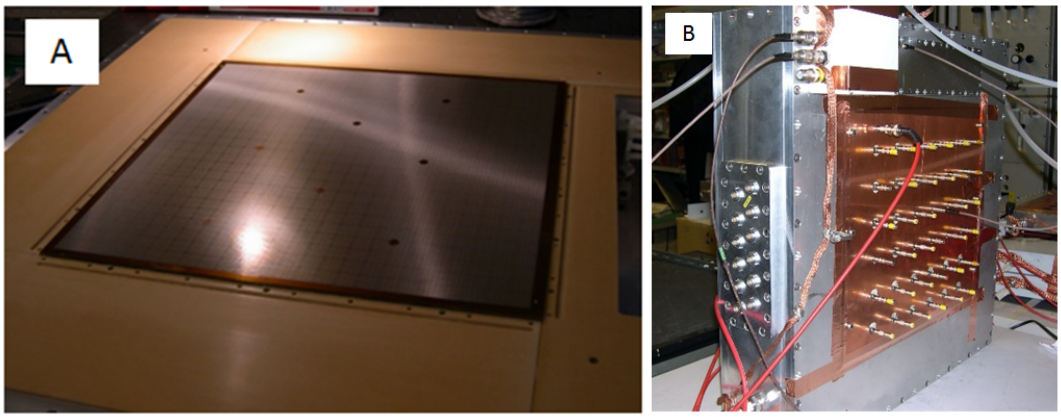

FIGURE 5.18: A. The anodic PCB with the Micromegas; B. Assembled chamber ready to take data;

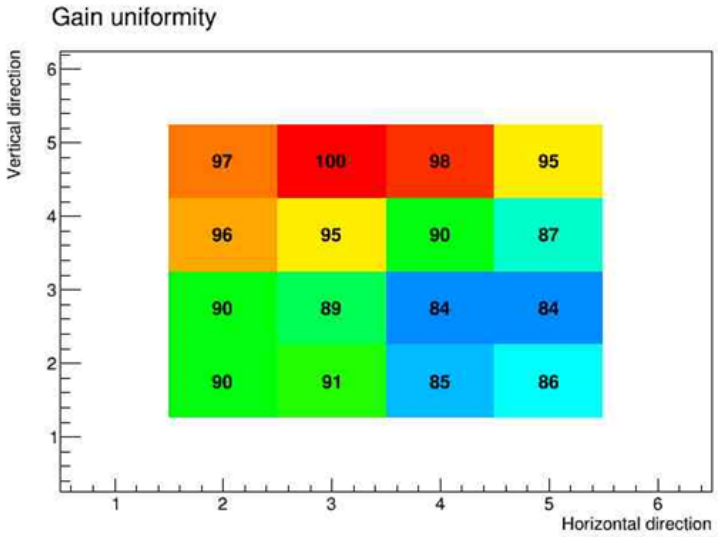

FIGURE 5.19: Gain uniformity study. The uniformity is presented in % of the normalizer cell gain (taken as 100%)

A full characterization of the MM was performed and a maximum gain of 2247 in the same setup was obtained.

5.4.2 Test of THGEM+Micromegas based PDs

A good 300×300 mm^2 THGEM with final parameters (t = 0.4 mm; d = 0.4 mm; p = 0.8 mm; rim = 0 mm) was mounted over the MM and an effective gain scan for each sector of the THGEM was performed. The results are shown in Fig.5.20. It can be seen that all the sectors of the THGEM provided a hybrid maximum effective gain $\sim 10^5$; apart sector 4 which provides a systematically lower response, all sectors have identical behavior.

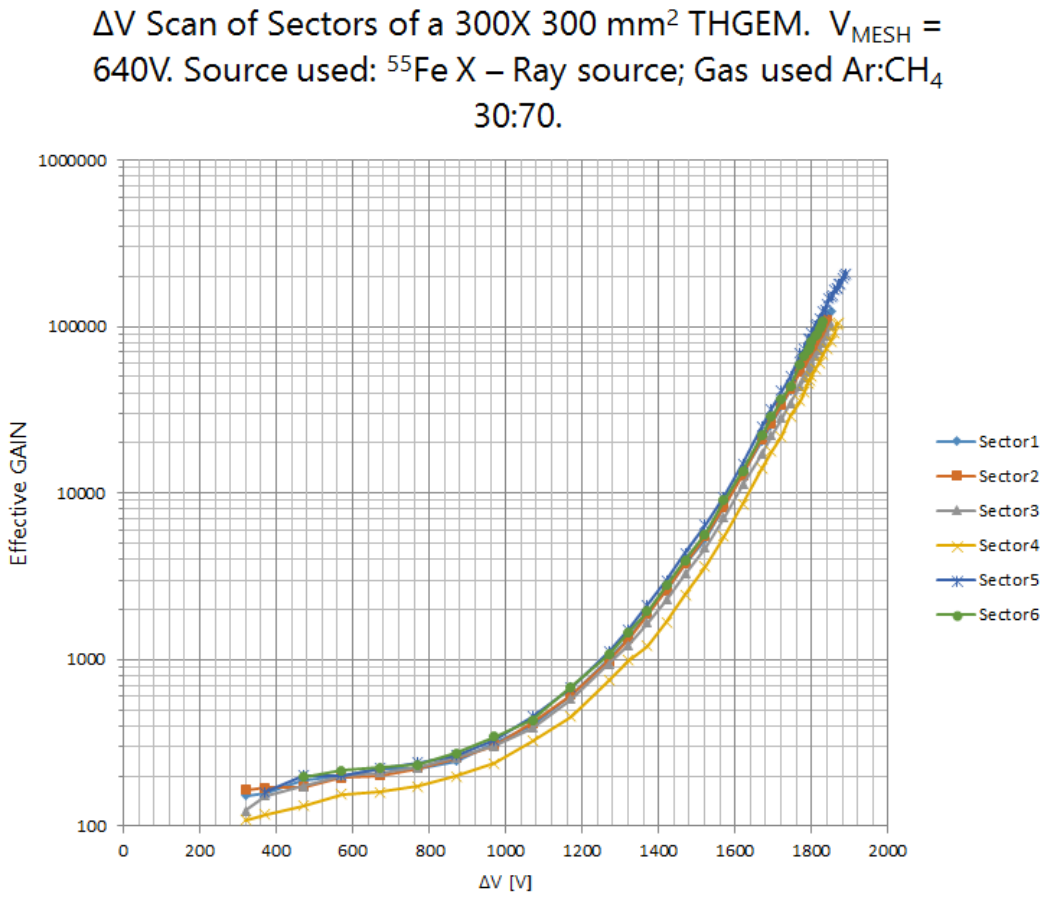

FIGURE 5.20: Effective gain as function of voltage for THGEM sectors separately

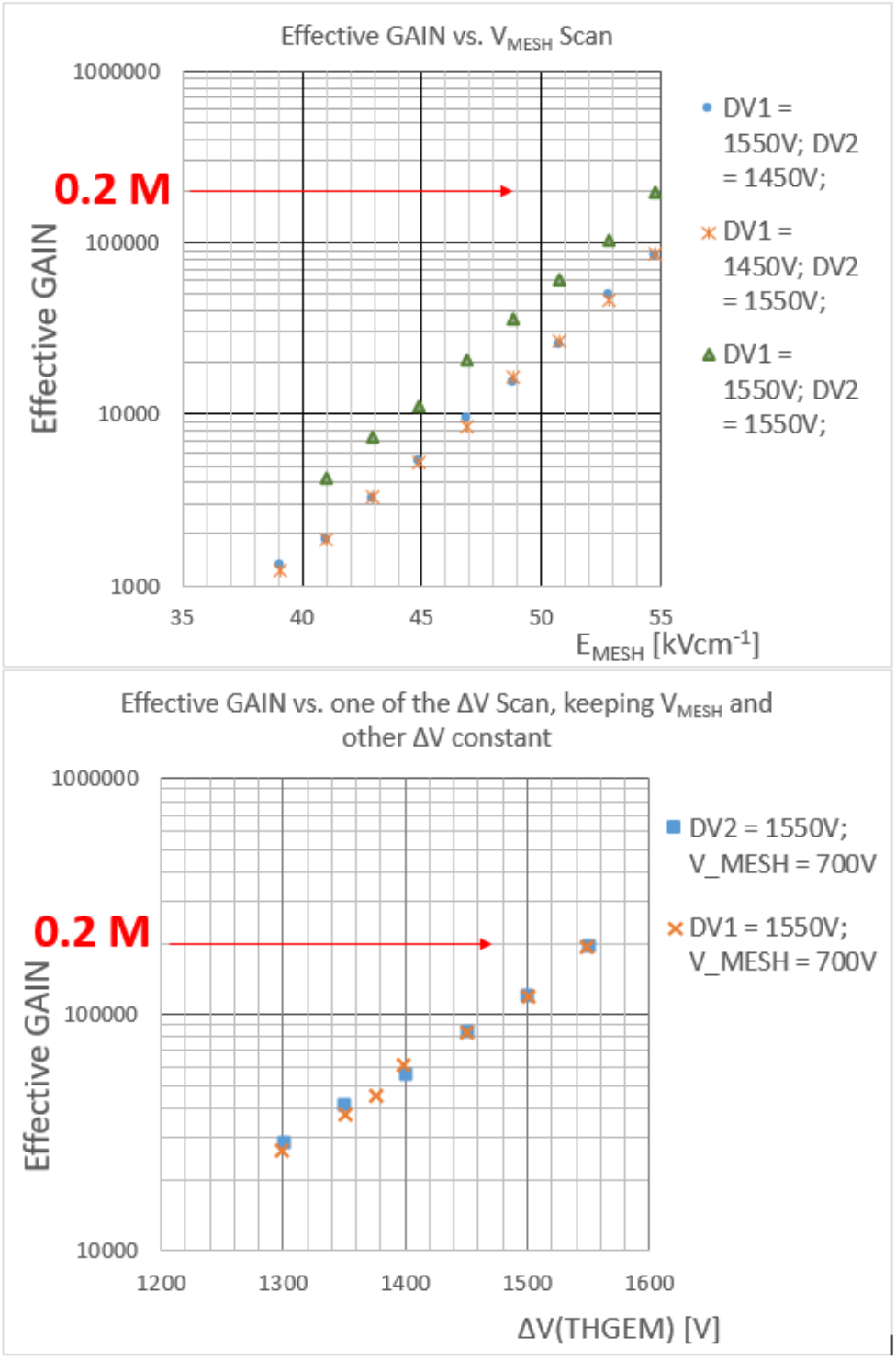

FIGURE 5.21: Study of gain sharing between THGEMs and Micromegas

After mounting a second THGEM on the chamber a detailed characterization of the system was performed also in Ar:CH_4 40:60 using an ^{55}Fe X-Ray source: In Fig.5.21-Top the effective gain as function of the V_{MESH} is presented for three different conditions of ΔV_{THGEM1} and ΔV_{THGEM2}. The gain response of the hybrid for ΔV_{THGEM1} = 1550 V and ΔV_{THGEM2} = 1450 V is the same as for ΔV_{THGEM1} = 1450

V and ΔV_{THGEM2} = 1550 V. When ΔV_{THGEM1} and ΔV_{THGEM2} both are 1550 V, the expected increase of effective gain $\sim \times 2$ can be seen (green triangles). In Fig.5.21-Bottom, the identical behavior of the two THGEMs is shown by keeping the V_{MESH} fixed at 700 V and one of the two THGEMs at 1550 V, varying the ΔV of the other THGEM.

5.4.3 MM with "Capacitive Anodes"

The response of the bulk MM compared to that of the small MM was only partially satisfactory: the maximum stable gain was smaller and the spark rate was definitely larger. Furthermore, whenever a spark occurred the micromesh voltage moved to very low values and the recharge of the whole MM was long. The micromesh cannot be segmented but it can be kept at ground voltage if a positive bias is applied to the anodic pads. This configuration is superior to the standard one, since in case of a spark, The micromesh voltage will not move, while only a small region in case of anodic HV segmentation is affected by the discharge. other advantages are:

- The electrical instabilities in the THGEM region and in the MM are decoupled by providing a good grounding to the micromesh.
- The front-end electronics is protected from the discharges occurring in the MM by the capacitive decoupling.
- The effect of discharges on the detector operation can be limited to the involved pad only.

To test the concept of the hybrid detector and the "Capacive Anode" two 300×300 mm^2 prototype chambers have been built. Both had two layers of THGEMs coupled to a Micromegas layer. The anodic PCBs of both were segmented to 572 $(24 \times 24), 12 \times 12 mm^2$ readout pads hosting the BULK Micromegas produced at CERN. The only difference between the two anodes was the architecture of the readout. One had a standard anode and the other used a new technology based on capacitive/resistive readout techniques, developed in INFN Trieste lab and consisting in applying the HV to the anode PADs via individual large resistors. Each anodic pad induces the signal from the MM to an embedded pad buried inside the PCB, which is connected to the front-end readout (Fig.5.22). This scheme has been designed by Stefano Levorato.

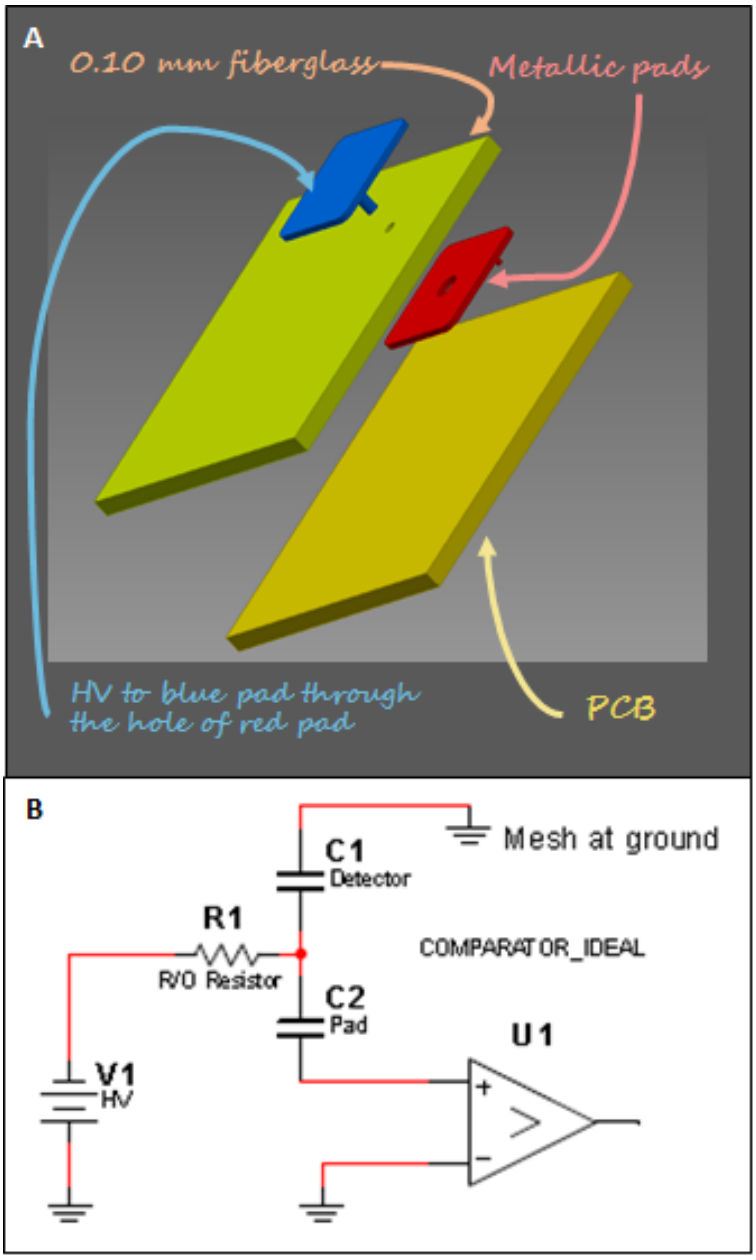

FIGURE 5.22: A: Exploded view of one single readout pad structure. The red pad facing the MM is connected to HV through a resistance and the blue embedded pad 100 μm below is reading the induced signal from the red pad through RC coupling and connected to the Front End Electronics. B: The schematic of the circuit diagram of the "capacitive anode" idea

5.4.4 Test of hybrid PD prototypes at CERN T10 Beam Line

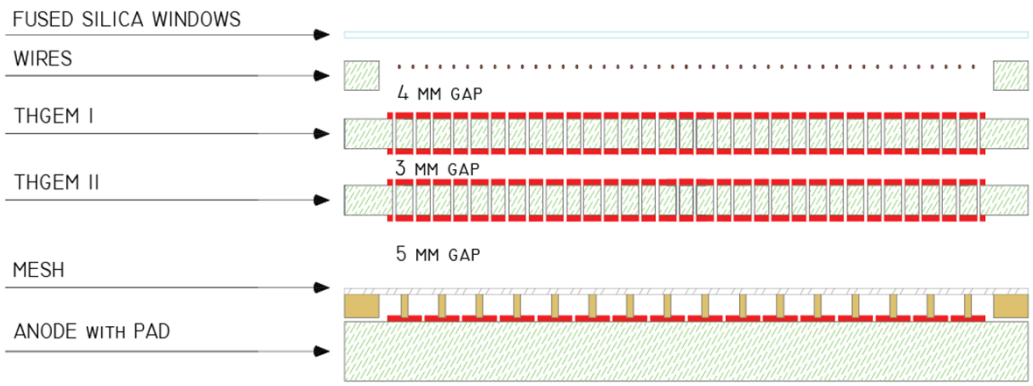

FIGURE 5.23: Scheme of a THGEM+Micromegas-based photon detector

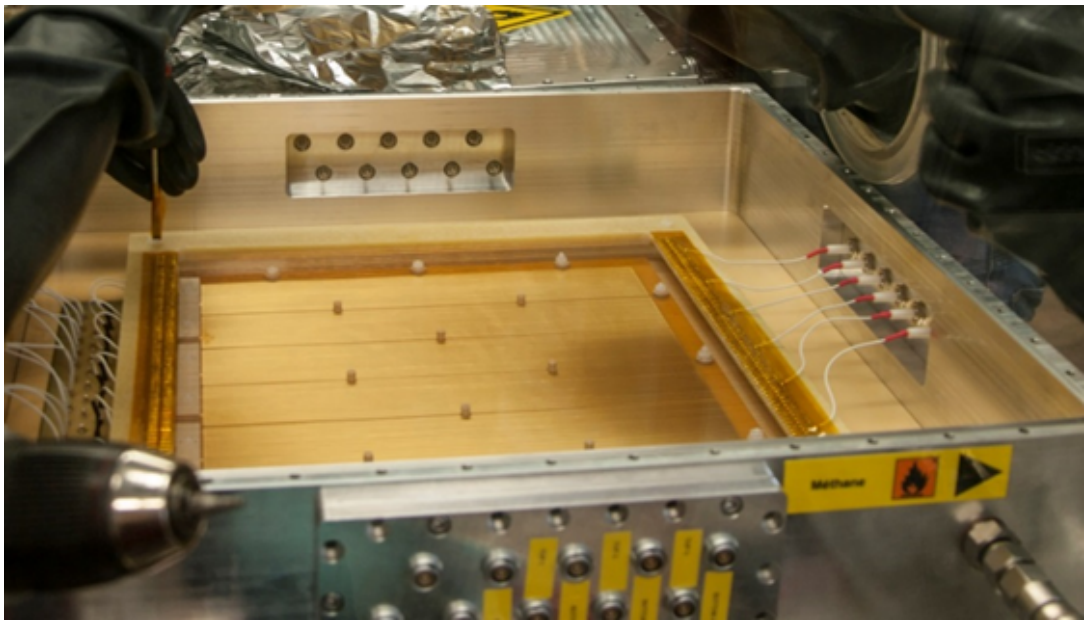

FIGURE 5.24: Picture of a 300×300 mm^2 THGEM mounted in a PD

The PD Prototype (Fig.5.23 and Figs. 5.24) consists of a chamber hosting two planes of wires (needed to define a uniform electric field in the region above the photocathode), two THGEMs, all having a hole diameter = 0.40 mm, hole pitch = 0.80 mm and a rim of $\leq$ 5 μm; and thickness of = 0.40 mm and a bulk MicroMegas on an anodic PCB segmented in 12 $\times$ 12 mm^2 pads.

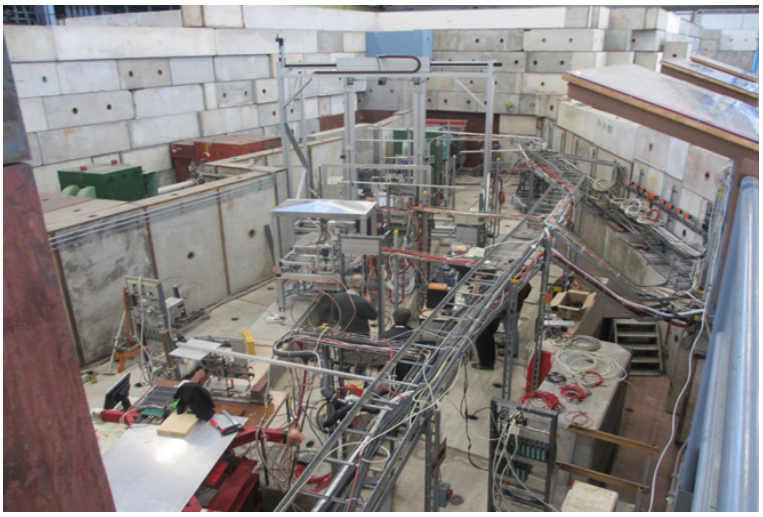

FIGURE 5.25: Test Beam setup at CERN PS T10 beam line with two Micromegas chamber

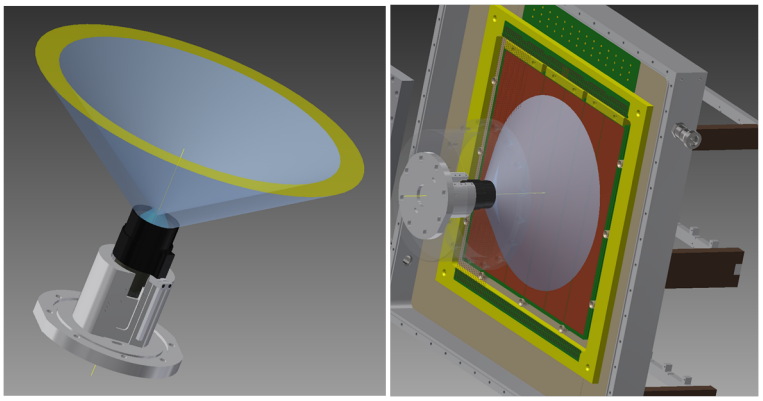

FIGURE 5.26: CAD images of the movable interceptor, including the corona of the Cherenkov photons

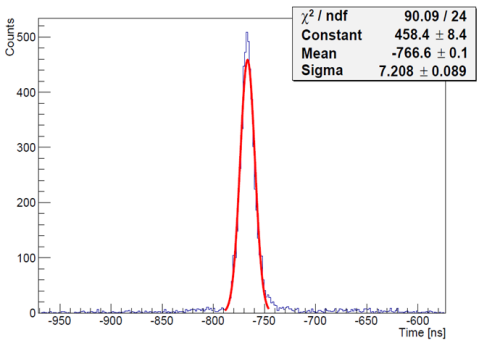

FIGURE 5.27: Time resolution of the chamber with "Capacitive Anode".

A set of inner columns, border blocks and spacers, made of PEEK (Polyether-ether-ketone) provides precise positioning and the THGEM planarity and allows easy mounting operations. The spacings between the electrodes are: 128 μm between the anode and Mesh, 3.0 mm between Mesh to the THGEM2 and between the THGEMs, 5.2 mm between CsI and the drift wire plane, 30.0 mm between wire planes. The two chambers had identical parameters apart from the anode readout concept.

In October 2014 the two 300x300 mm^2 Hybrid PD prototypes have been installed (see Fig.5.25) and operated at the CERN PS T10 test beam of 6 Gev/c π^+.

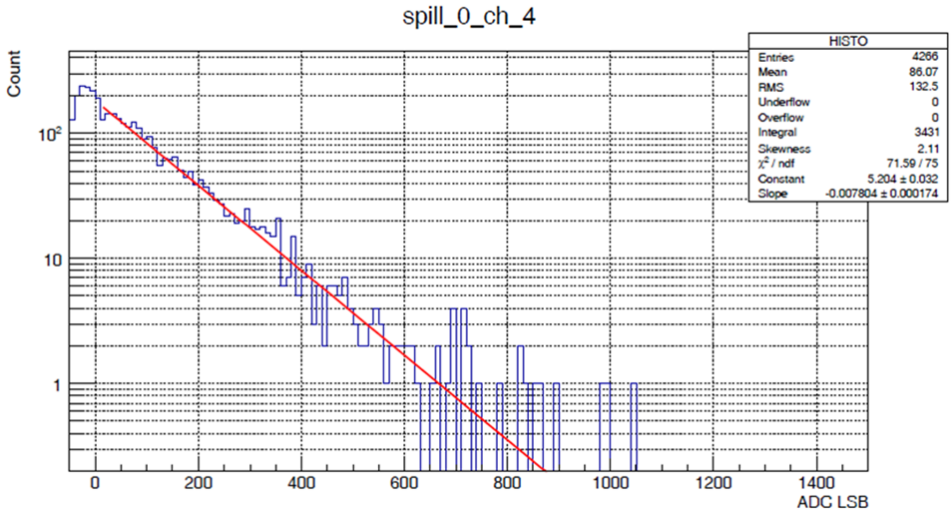

FIGURE 5.28: Signal Amplitude spectrum for single photon event read by the "Capacitive Anode". Estd. effective gain $\approx 1.3 \times 10^5$.

A truncated cone fused silica radiator (Fig. 5.26) was placed on the beam axis and equipped with a cylindrical interceptor having a remotely controlled movement. A trigger system based on a 5-fold scintillator coincidence allowed selecting beam particles traveling along the radiator axis.

An Ar/CH_4 (60/40) gas mixture was used, and the high voltage was provided to each sector via individual resistive dividers (6 channels from a CAEN A1526N board on an SY1527 mainframe were used).

The detector was equipped with the digital electronic readout, already mentioned in Chapter-3, based on the CMAD [129] front-end chip and on the F1 TDC [131] during half the period of the run. The time resolution from the "Capacitive Anode" is shown in fig.5.27. The distribution is a Gaussian with a sigma of 7.2 ns. During the rest of the period it was equipped with a FPGA based analogue readout system developed by Frieburg group, named GANDALF. Except for an initial test where the anode pads had been grouped and connected to an analog readout for signal amplitude studies. A typical signal amplitude spectrum obtained with GANDALF readout for single photoelectrons is shown in Fig.5.28. The distribution is a pure exponential with an estimated effective gain of 1.3×10^5.

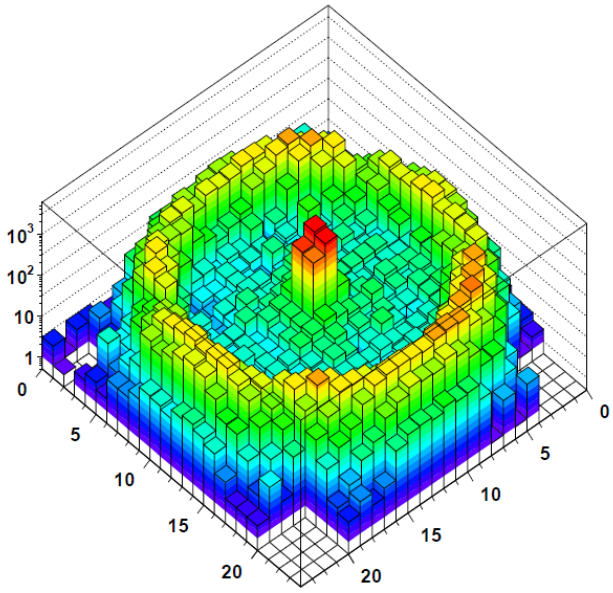

FIGURE 5.29: Superimposed events including the beam region

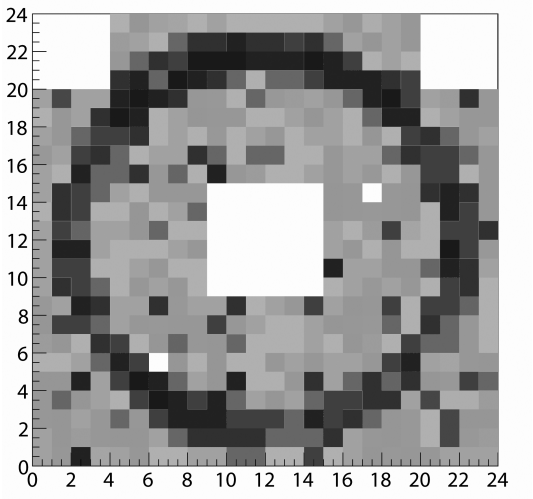

FIGURE 5.30: Superimposed events, beam region excluded

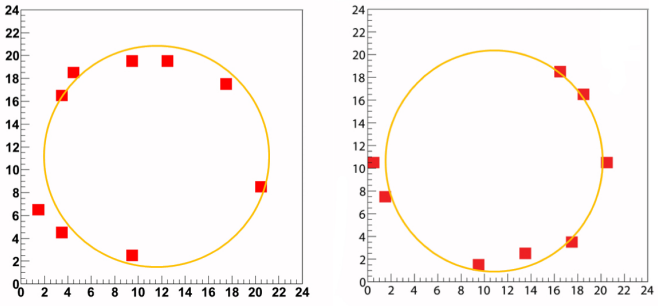

FIGURE 5.31: Single events

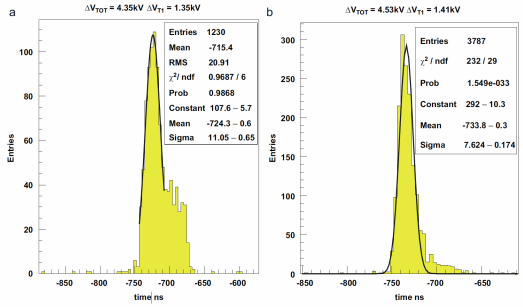

FIGURE 5.32: Left: time distribution of events for a gain of 0.9×10^5, corresponding to a sum of the voltage drops across all the three THGEM layers of 4.35 kV and a ΔV on the first layer of 1.35 kV; a secondary distribution of events outside the Gaussian peak is due to photo-electrons arriving late because they were extracted in a low field region: The absence of this tail is a guarantee of full PE collection. Center: time distribution of events for a gain of 2×10^5, corresponding to a sum of the voltage drops across all the three THGEM layers of 4.53 kV; the secondary peak is reduced.

The response of the two detectors to charged particles and to Cherenkov photons has been studied at different voltages, corresponding to gains between 10^4 and 10^5, keeping the drift wires and the photo-cathode at the same potential.

Typical images of superimposed events and of single events as well as time distribution from previous exercises are shown in Figs. 5.29, 5.30, 5.31 and 5.32.

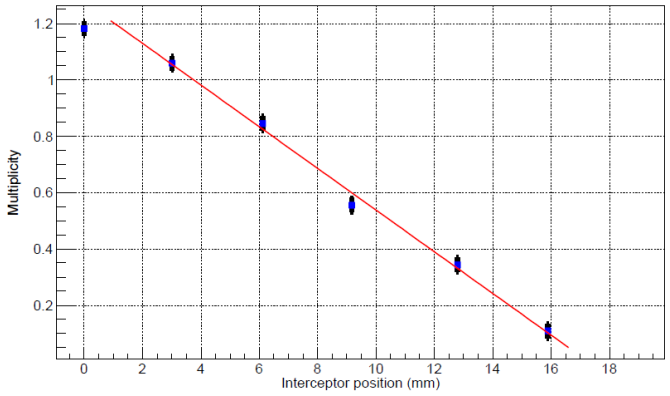

FIGURE 5.33: The average number of detected photons per event in one sector of the PD as a function of the photon interceptor position

A set of measurements were performed at various interceptor positions: the measured multiplicity decreases linearly with the closing of the interceptor (corresponding to a shorter unscreened radiator thickness) as can be seen in Fig. 5.33, where the measured number of hits per event in one sector of the detector is presented as a function of the interceptor position.

A detailed study has been dedicated for the understanding of the response of both chambers with ionizing particles. The relation between V_{MESH} and the signals from charged particles is shown in Fig.5.34. A very interesting measurement was performed by changing the E_{drift}. The photon yield vs. E_{drift} is shown in Fig.5.35. The ionizing particle signal amplitude vs.

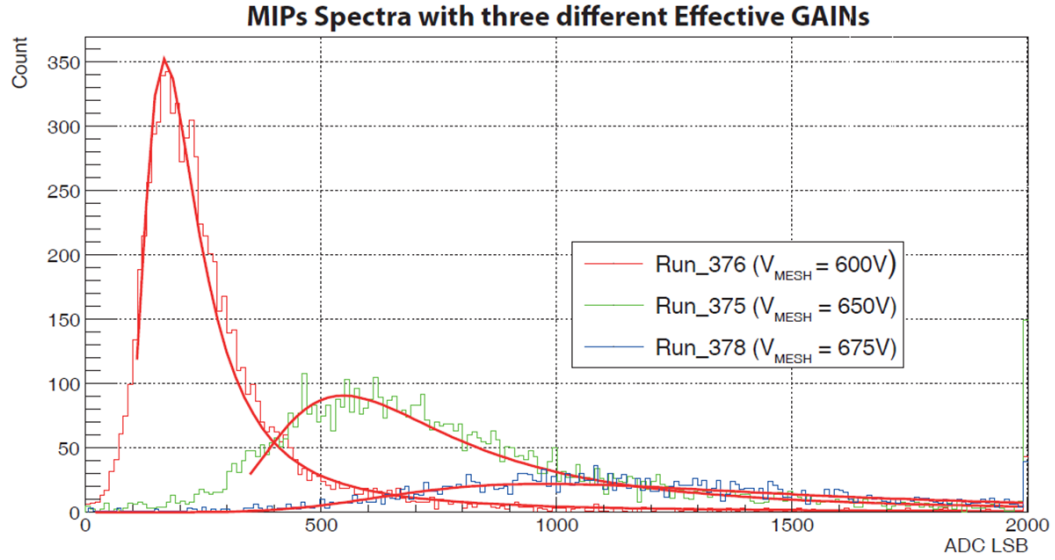

FIGURE 5.34: The curves represent the fit with a Landau of the charged distribution at different V_{MESH}.

E_{drift} is shown in Fig.5.36. It can be seen that operating with E_{drift} between 0 and 100 V.cm^{-1}, a good suppression of the charged particle ionization can be achieved with a moderate loss in the photon yield.

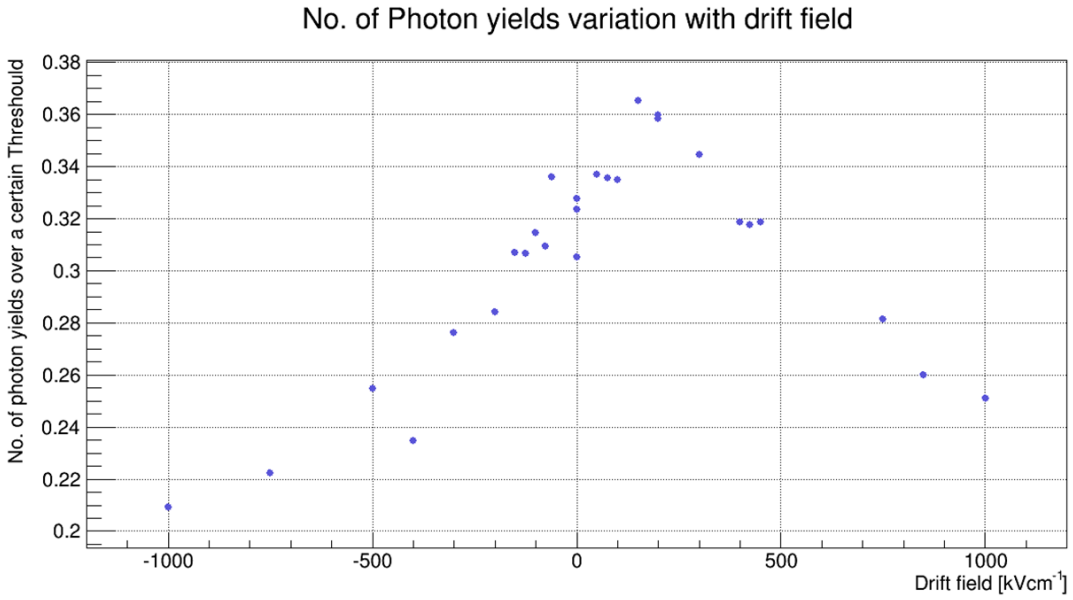

FIGURE 5.35: Drift field scan of photo-collection efficiency

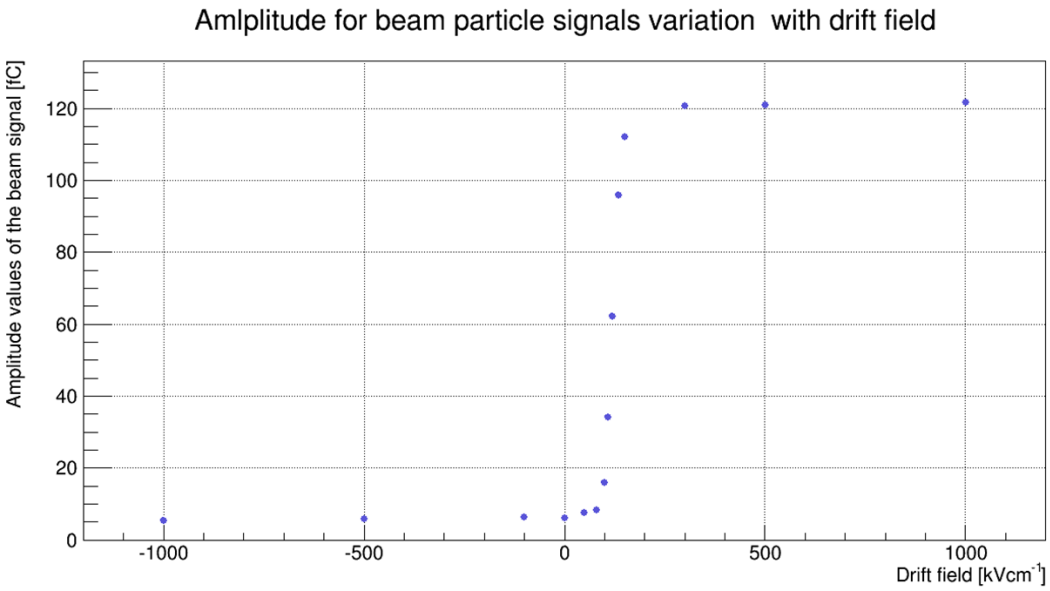

FIGURE 5.36: Drift field scan of ionizing particles collection efficiency

5.5 The hybrid detector architecture for COMPASS RICH-1 upgrade.

Each of the four large hybrid $600 \times 600\ mm^2$ single photon detectors for COMPASS RICH-1 upgrade is built using a modular architecture and consists of two identical modules $600 \times 300\ mm^2$, arranged side by side.

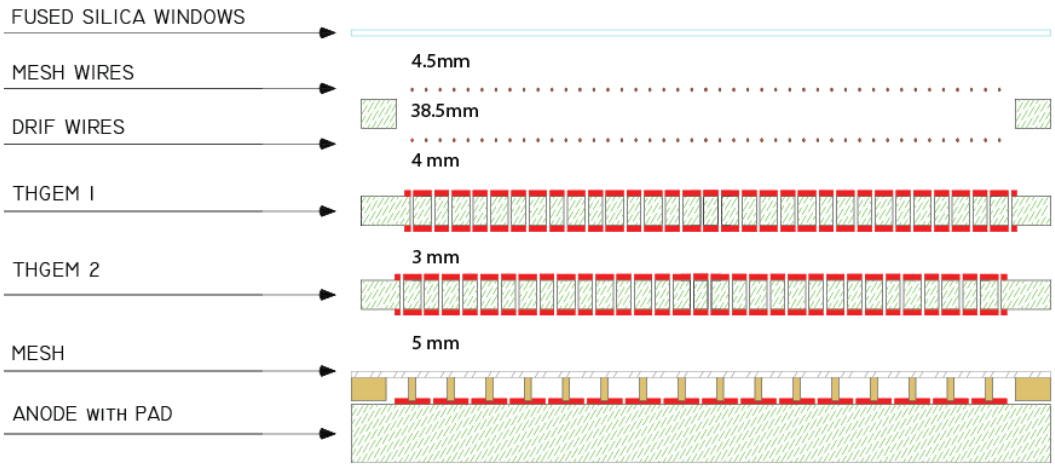

FIGURE 5.37: Basic scheme of the final hybrid PD.

The basic structure of the hybrid module (fig. 5.37) consists of two layers of THick Gas Electron Multipliers (THGEM), one MicroMegas[13], and two planes of wires. UV light sensitivity is obtained via the deposit of a thin (few hundred nm) CsI layer on the first THGEM electrode which acts as a reflective photo-cathode for VUV photons. The THGEM geometrical parameters are the same for all the THGEM layers: thickness of 470 μm, total length of 581 mm and with of 287 mm (Fig.5.38). The hole

diameter is 400 μm and the pitch 800 μm. Holes are produced by mechanical drilling and have no rim. To obtain a symmetric field line configuration near the edges of the THGEM, the diameter of the holes located along the external borders have been enlarged to 500 μm.

This solution results in an improved electrical stability of the whole system. Other constrains imposed by minimizing the border dead areas will be described together with the challenges related to the integration of hybrid PDs in RICH-1 in Chapter-7. The top and bottom electrodes of each THGEM are segmented in 12 sectors: 10 are 564 mm long and 23.3 mm wide, the most external ones are 17.9 mm wide; all sectors are separated by 0.7 mm clearance area. The biasing voltage is individually provided to each sector of the THGEM.

The Drift wire plane is installed 4 mm from the CsI coated THGEM and is biased to a suitable voltage in order to maximize the extraction and collection efficiency of the converted photo-electron. The other wire plane is positioned 4.5 mm away from the quartz window which separates the radiator gas volume from the $Ar/CH4$ 50/50 gas mixture and guarantees the correct closure of the drift field lines. The details of the wire planes will be described together with their frames in Chapter-7.

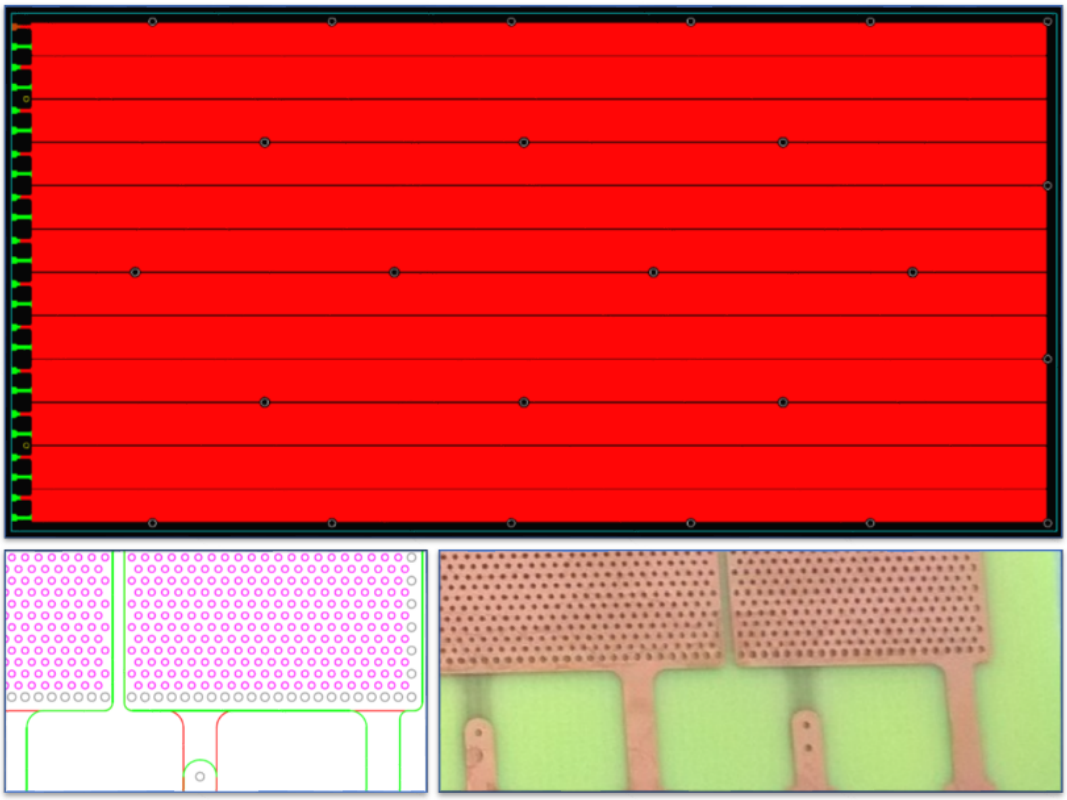

FIGURE 5.38: Top: Cad drawing of a 287×581 mm^2 THGEMs with 12 sectors; Bottom left: Zoom of a corner of the CAD drawing showing the holes with 500 μm diameter; Bottom right: Picture of the corner for a real THGEM

The photo-electron is guided into one of the first THGEM holes where the avalanche process is started due to the electric field generated by the biasing voltage applied between the top and bottom THGEM electrodes. The electron cloud generated in the first multiplication stage is then driven by the 1.5 kV/cm Electric field across the 3

mm transfer region to the second THGEM, where thanks to the complete misalignment of the holes with respect to the first THGEM layer ($\approx 462\mu m$ displacement along the THGEM length coordinate), the charge is separated and undergoes a second independent multiplication process.

Finally the charge is guided by the 0.8 kV/cm field across the 5 mm gap to the bulk MicroMegas where the last multiplication occurs. The charge is collected by the anodic pads biased at positive voltage (powered through a independent resistor) facing the grounded micromesh, and the signal induced on the buried pad is read out by the Front End APV 25 chip[151]. The intrinsic ion blocking capabilities of the MicroMegas as well as the arrangements of the THGEM geometry and fields grants an ion back flow on the photo-cathode surface lower or equal to 4 % [152].

5.6 Summary

Large area THGEMs need electrode segmentation as sectors with capacitance > 1 nf can generate discharges which can be dangerous for the front-end electronics and for the detector itself. The optimal segmentation was studied and defined. To achieve with large THGEM prototypes the same performance as for the small ones, turned out to be difficult. Microscopic defects on the Cu surface and inside the hole have been studied in details and a specific procedure to avoid their presence was developed. Several 300 $\times$ 300 mm^2 prototypes were built and characterized. Good results were obtained but in terms of the discharge rate, the gain uniformity and the highest stable effective gain they were not as good as for the small (30 $\times$ 300 mm^2) prototypes, despite the large effort to optimize the large area triple THGEM PDs.

An alternative hybrid architecture, based on the use of the double THGEMs coupled with a MicroMegas layer, provides superior performance: a higher electrical stability at high gain in a high irradiation condition was clearly observed. The intrinsic IBF suppression of the MM increases the electrical stability in that condition.

A novel scheme for the anode based on capacitive/resistive pad architecture was developed in our lab to protect the front-end electronics from discharges and allow maintaining the micromesh (the only non segmented electrode in the hybrid architecture) at the ground potential.

The hybrid architecture with capacitive/resistive pads was validated in the laboratory and at the CERN PS T10 Test Beam facility. The response of the detector to Cherenkov photons and to ionizing particles was studied in details and an optimal value of the drift field was identified.

As a result of the previous tests the final design of the hybrid PDs for the COMPASS RICH-1 upgrade has been defined. The final components, their quality control and tests are the subject of the next chapter.

Chapter 6

The Main Components of the Final Hybrid PDs

6.1 The Final THGEMs

The THGEM gain non-uniformity related to the PCB thickness variation observed with the 300×300 mm^2 prototypes (as described in Chapter-5), could not be accepted for the final THGEMs. To assure an uniform gain response a strict tolerance in the PCB thickness (∼2-3%) had to be imposed. Industrial PCB suppliers only offer relaxed tolerances in PCB thickness (∼5-10%): a selection of PCBs with uniform thickness had to be applied. To avoid waisting produced THGEMs, the selection had to be performed on the raw material before drilling.

The simple operation of mapping of a foil thickness turned out to be challenging:

- The needed measurement accuracy was at the micron level.
- Thickness uniformity for raw PCB foils of $\sim$ 1.3 m^2 needed to be measured.
- The measurement needed to have high granularity.
- The 400 μm thick fiberglass foil is flexible but not stretchable.
- Many techniques had been proposed and none apart from the one described was realistic.

A special setup was prepared using a MITUTOYO EURO CA776 coordinate measuring machine (Fig6.1), in the INFN mechanical workshop at the Department of Physics, University of Trieste. We measured thickness over $0.7 \times 0.7m^2$ surface with a pitch of 2 cm along x and y axis: with a precision of ± 1 mum. The MITUTOYO machine uses a ruby tip (Fig.6.2) to touch an object and provide the corresponding coordinates. A reference marble table with high flatness is used as a base for the object. The measured thickness at a point (x, y) is calculated by subtracting the z-coordinate of ruby tip touching the marble from the z coordinate of the tip touching the PCB at that (x, y).

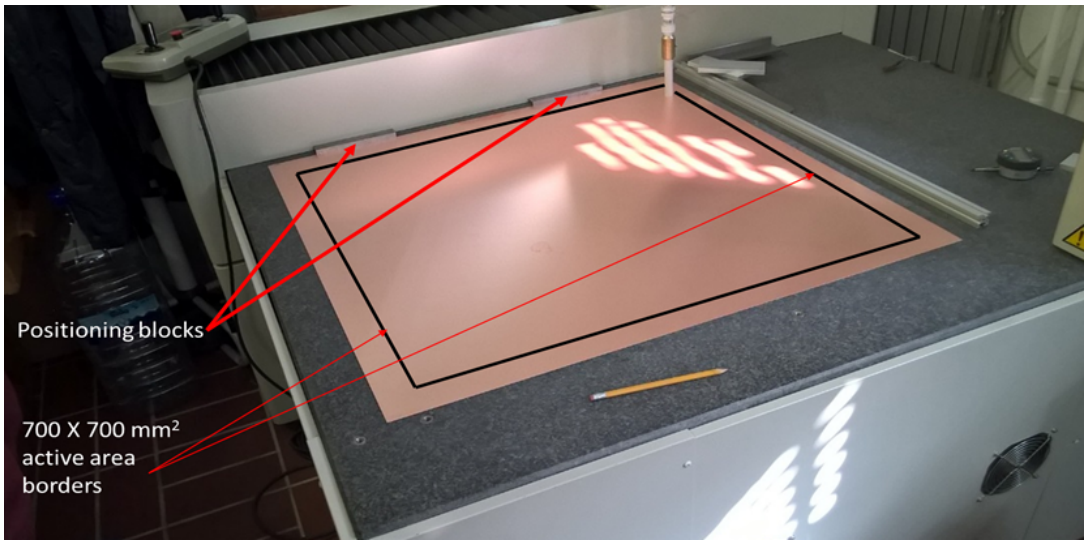

FIGURE 6.1: Mitotoyo Setup for thickness measurement

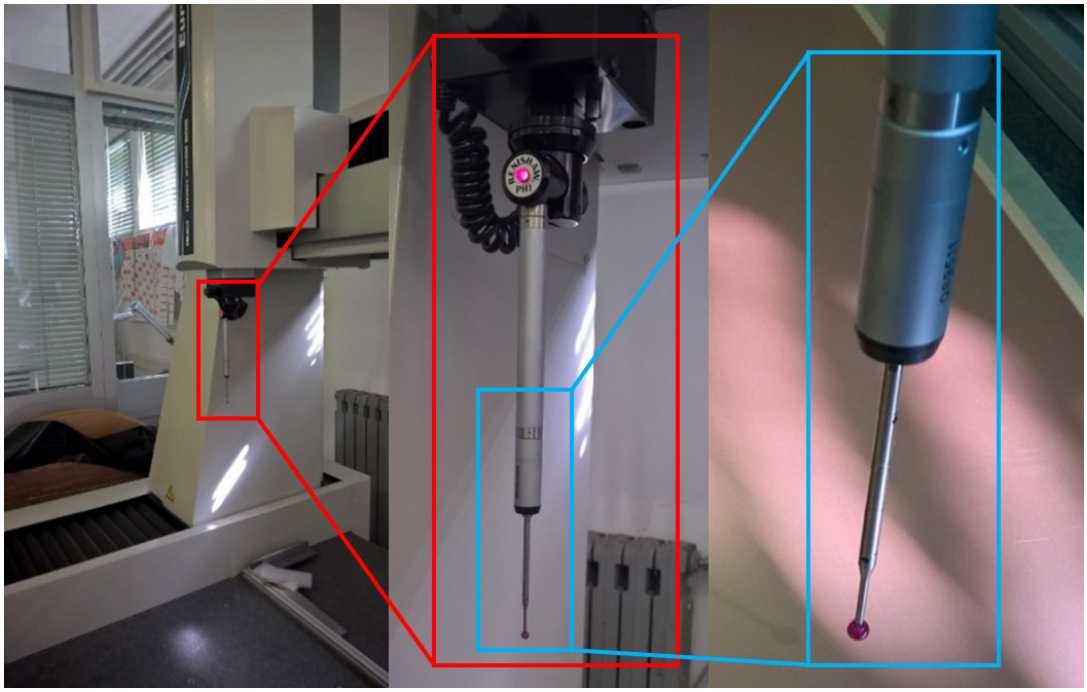

FIGURE 6.2: Ruby TIP of the thickness measurement machine

To assure the contact between the PCB and the marble reference table, a vacuum pump and a tight frame around the PCB foil were used (as shown in Fig.6.3). 50 foils of 1245 $\times$ 1092 mm^2 surface area of EM 370-5 lead free, halogen free PCB material were bought from Elite Material Co. Ltd. The foil borders turned out to have larger thickness variations so the central part of 800$\times$800 mm^2 each foil was extracted. The measurable area ($0.7 \times 0.7m^2$) was centered on the extracted foil.

FIGURE 6.3: A. The frame by which the PCB foil had been pressed onto the marble top of the thickness measuring machine. B. The vacuum pump

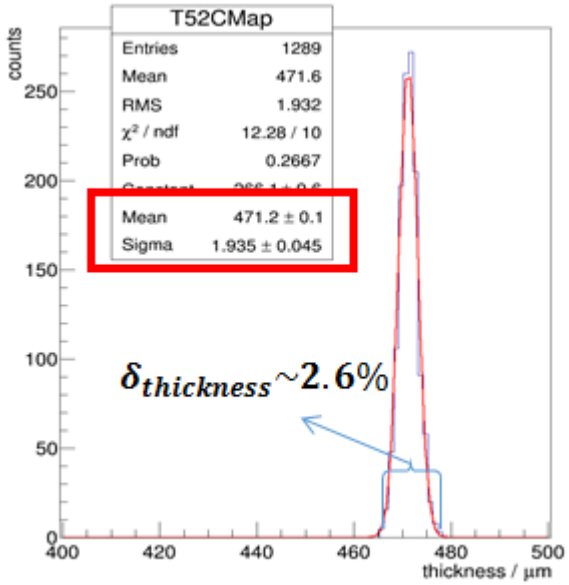

FIGURE 6.4: Thickness distribution of an uniform PCB foil

A ± 1 μm accuracy can only be achived with multiple measurement of the same point. A high granularity was needed in order to check for local thickness problems. A measurement with 1 cm pitch along x and y coordinates and 3 consecutive measurements per point takes $\sim$7 hours. At least four measurements (Marble, Marble + PCB, MARBLE + reversed PCB, Marble) are needed to check the thickness consistency. The first long measurements revealed a gradient in the measured thickness, even for the reference marble alone (see Fig.6.5).

The origin of the observed gradient was investigated and correlated to temperature variations. Thermalizing the room and reducing the time of the measurements by doubling the pitch, fixed the problem and allowed for a reasonable duration of the operation. All 50 pieces were measured. The distribution of the measured local thickness values is presented in Fig.6.4 for a typical good piece. The average thickness of that piece is 471.6 μm (to be compared with the nominal 400 μm fiberglass + 2$\times$35 μm Cu), and the sigma of the gaussian fit is 1.935 μm. The 2D thickness distribution is shown in Fig.6.6. Two THGEMs can be produced from each foil: the proposed area for the two THGEMs of this foil are marked with red boxes.

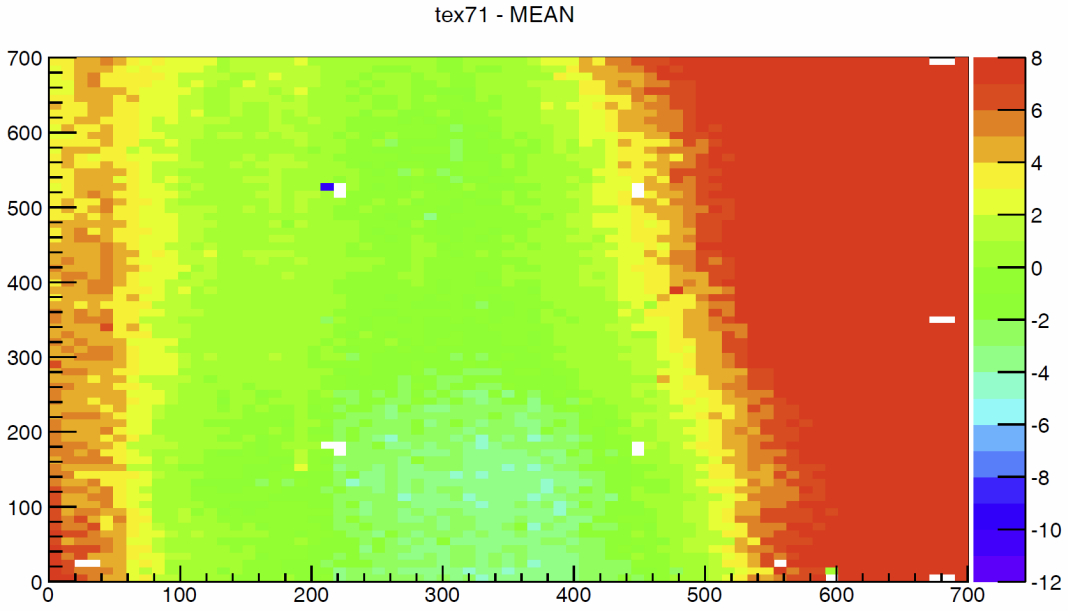

FIGURE 6.5: Measured z-coordinate of the marble reference table (before thermalization).

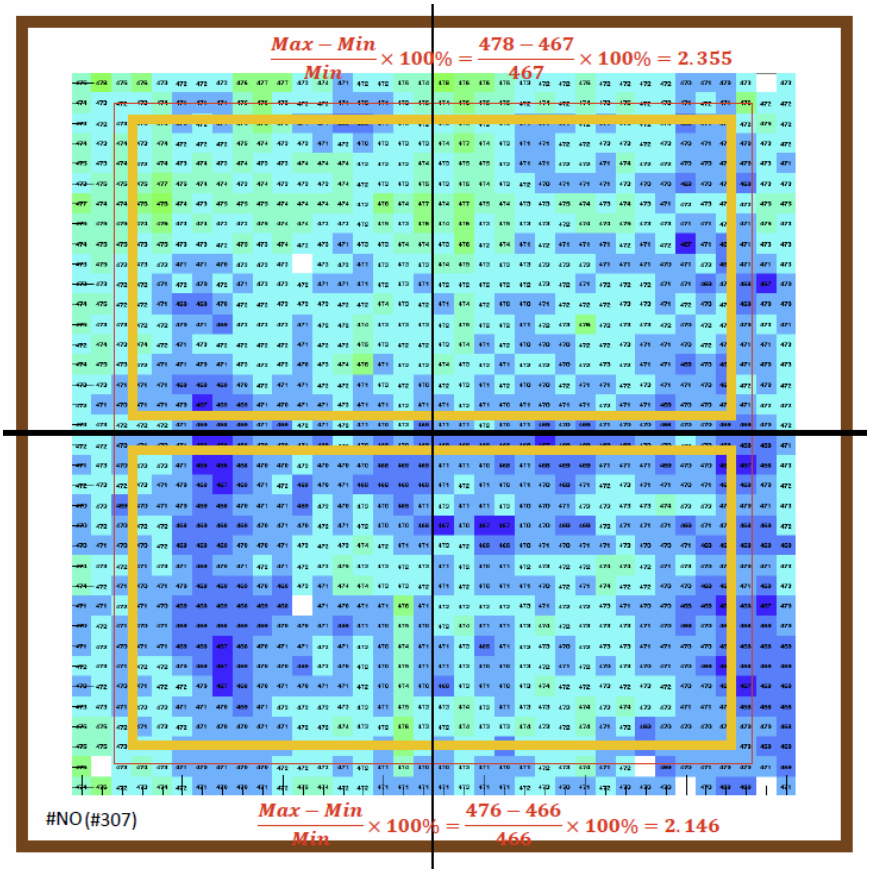

FIGURE 6.6: 2D map of local thicknesses measured for PCB no. 313. Two possible THGEM area are marked with red bixes. The yellow boxes are showing the THEGM active areas and the brown box defines the PCB foil borders: the unit is μm

In Fig.6.7 for each measured point, the difference between the local thickness and the average foil thickness is shown.

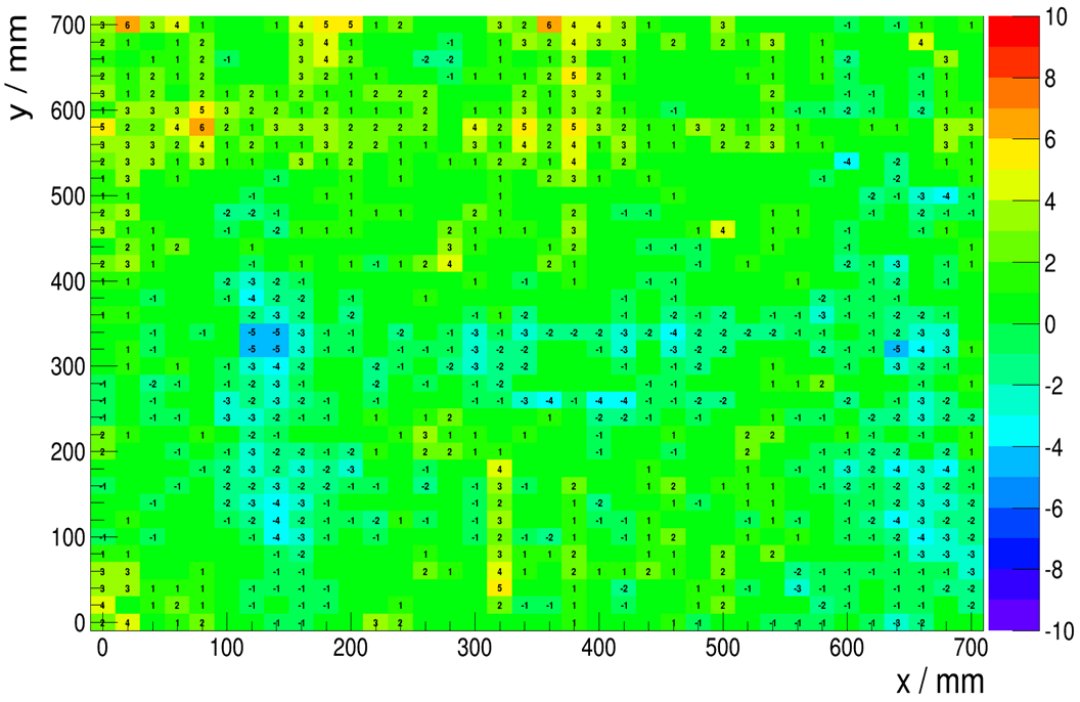

FIGURE 6.7: 2D plot of the difference between the local thickness and the average foil thickness

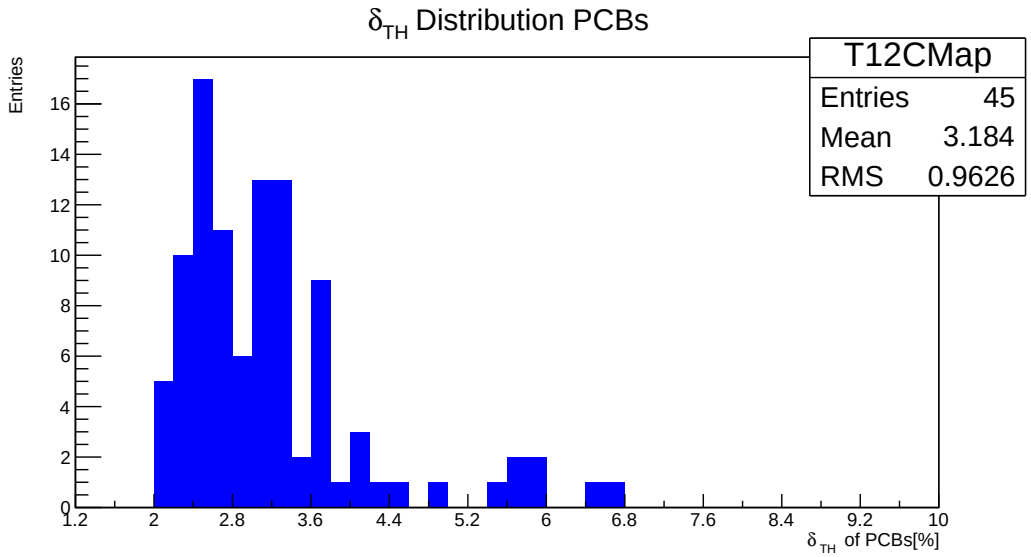

FIGURE 6.8: Distribution of measured $\delta_{thickness}$ for all 45 pieces

To asses the foil thickness uniformity quality of a PCB, an indicator called $\delta_{thickness}$ was defined by: $\delta_{thickness}$ = (Max$_{thickness}$ - Min$_{thickness}$)/Min$_{thicknes}$. A similar indicator for each proposed THGEM area had also been calculated. Out of the 100 measured THGEM areas, 50 were found to be within a $2\% \geq \delta_{thickness} \leq 3\%$ whereas 38 pieces were found to be within $3\% \geq \delta_{thickness} \leq 4\%$. A complete database of local thickness values for all 100 THGEM foils has been produced and a complete

traceability of all the final THGEMs is possible: THGEMs are labelled and their orientation has been strictly maintained. In total 60 THGEMs were produced by ELTOS SpA, from the pieces, according to the procedure mentioned in Chapter-4 and illustrated in Fig.6.9.

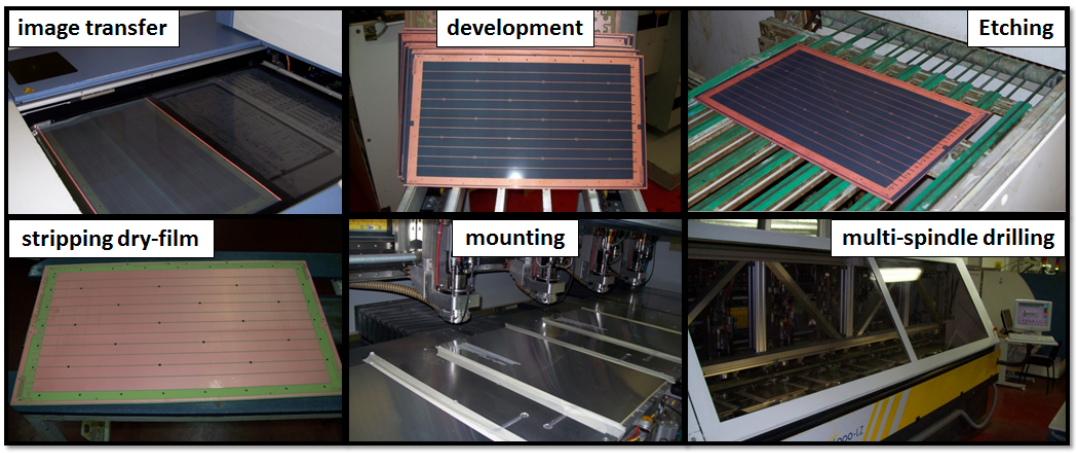

FIGURE 6.9: Production procedure in ELTOS SpA.

6.1.1 THGEM Selection and Quality Assessment

After receiving the newly produced THGEMs, the treatment procedure described in Chapter-5 was strictly followed. A dedicated special setup was built for the serial treatment to be applied. A specialized person was required to perform the serial polishing and cleaning procedure which previously was my specialty. All of the 60 produced THGEMs were treated. 8 of them needed to be re-treated.

The THGEM quality control protocol was then applied, consisting in electrical stability tests and gain response uniformity measurements.

The electrical stability test consists of two parts: the "Paschen test", performed in a special box flushed with N_2 and a discharge study applied only to the THGEMs validated by the Paschen test.

About 60% of the THGEMs were passing the validation requirement of the "Paschen test": $V_{Breakdown} \geq 90\%$ of the expected Paschen breakdown voltage on all sectors.

The study of the THGEM discharge rate was performed inside the chamber also used for THGEM gain uniformity measurement flushed with Ar:CO_2 70:30, placed inside an irradiation test facility (MINIX Setup) (see Fig.6.10) hosting an AMPTEK inc.[1] MINI-X Au X-Ray source.

[1] AMPTEK inc. USA; www.apmtek.com

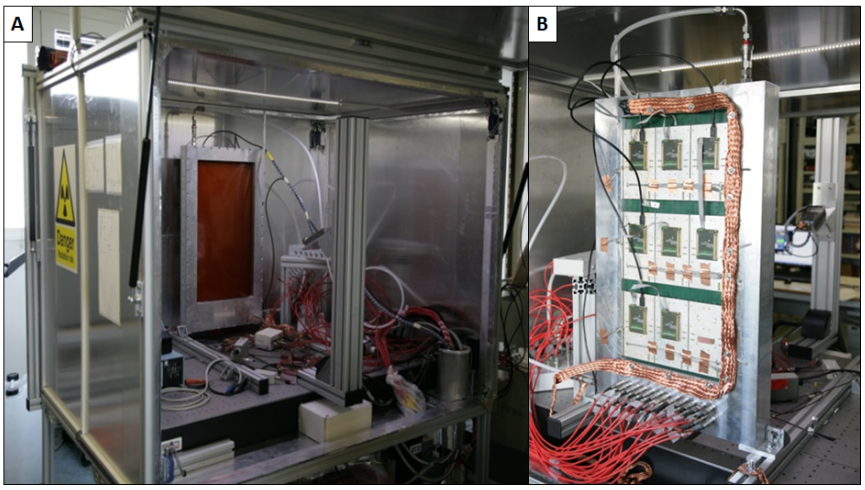

FIGURE 6.10: A. MINIX setup from the front. B. MINIX setup from back.

As shown in Fig6.10a and 6.10b a special large safe housing for the test had been built with $\sim 2mm$ of Pb sheets covered with aluminum foils and movable doors in the front and in the back side. The chamber which was used for this characterization had an anode plane segmented in $12 \times 12mm^2$ pads and hosted the THGEM at 3 mm from the anode. A wire frame mounted on the cover of the chamber in front of a big Kapton window provided the required drift field.

6.1.2 Discharge rate measuremnet

A CAEN mainframe based HV PS was used to provide individual bias to each THGEM sector: the bottom electrodes were connected to a single HV channel, while the 12 top sectors were connected to 12 high voltage channels. The High Voltage power supply was controlled by a computer program to test in parallel 12 sectors with the following algorithm:

- HV on with standard E_{drift} and E_{ind}, ΔV_{THGEM} = 1000V.
- Automatic increase of ΔV_{THGEM} in 10V steps every 30 minutes.
- Reading of currents (I_{Sector}) every second and registering discharges (defined as I_{Sector} > 50 nA)

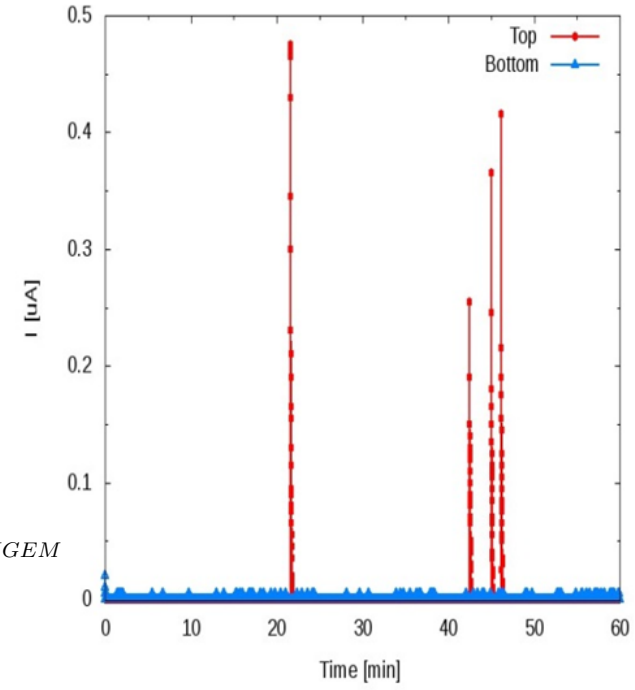

FIGURE 6.11: Moniterring the current to count discharges

- Tag the sector as unstable for a voltage value if the number of discharges is ≥ 10 and lower its bias by 50 V.
- Continue the test and collect the discharge distribution.

in Fig.6.11 one can see an example of current monitoring for one sector and one hour showing four discharges.

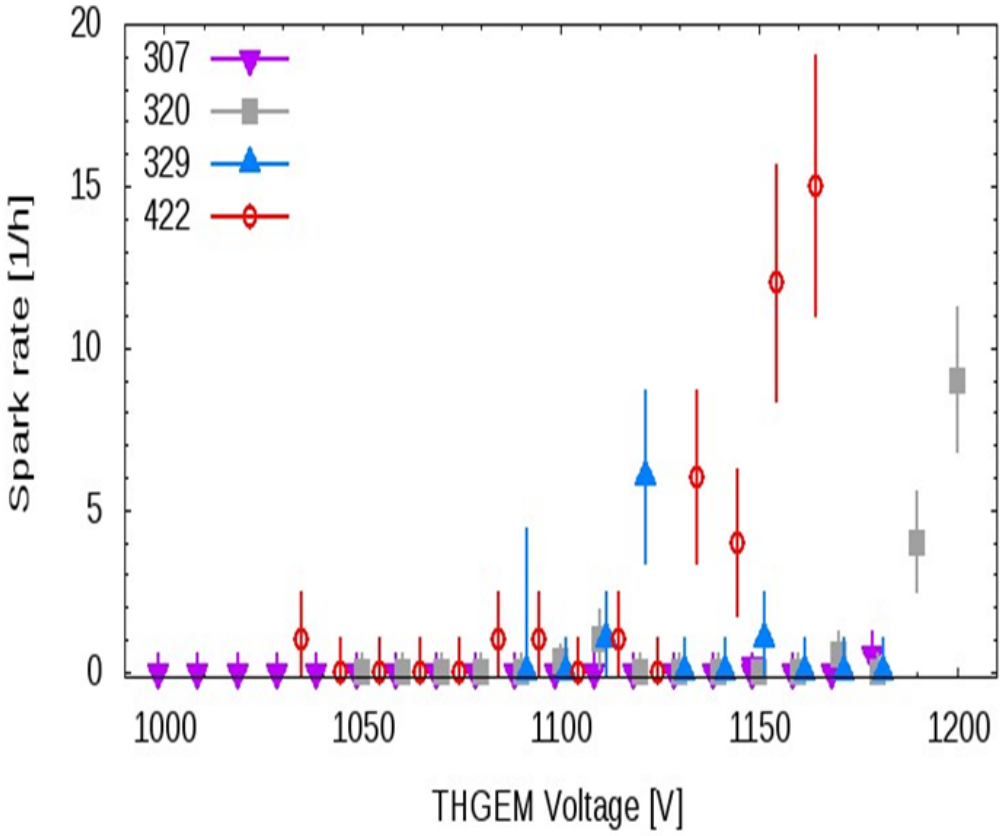

FIGURE 6.12: Spark rate distribution of several THGEMs

In Fig.6.12 the discharge rate as function of ΔV_{THGEM} is presented for four THGEMs: THGEM #422 was discarded because of its large discharge rate.

6.1.3 Gain Uniformity studies

The THGEMs validated by the discharge studies were subject to the gain uniformity measurement. The MINI-X Au X-Ray source was illuminating a 300 μm Cu foil to produce X - Rays generating ~300 primary ionization electrons in Ar. This condition was confirmed by a calibration using an ^{55}Fe X-Ray source. Along with the standard readout chain, a multichannel APV-25-S1 based on Scalable Readout System was used. In Fig.6.13a) the two schemes are shown.

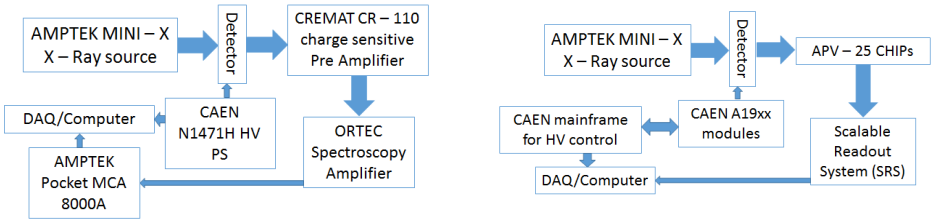

(A) (B)

FIGURE 6.13: A. Sceme for Cremat based standard readout; B. Sceme for APV based SRS readout

A typical measurement of the gain uniformity using the standard electronics chain, is shown in Fig.6.14a. With the APV-25 based electronic system we could read the gain values over a large surface area $\sim 90\%$ (since only 8 APV chips were available for our SRS system).

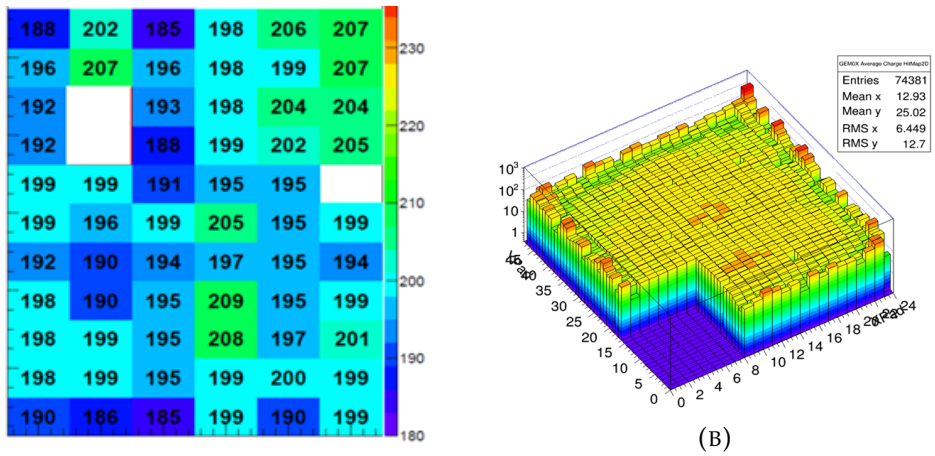

(A) (B)

FIGURE 6.14: a: gain uniformity obtained by MINIX X-Ray source and CREMAT based electronics b: gain uniformity obtained by MINIX X-Ray source and APV-25 based electronics

The result obtained is shown in the plot in Fig.6.14b: one can see the high granularity of the plot and the confirmation of good uniformity. The work which has been done for selecting uniform PCB foils in terms of thickness has paid off allowing to reach a uniform response in gain.

6.1.4 THGEM Storage and Transport

To store and transport the final THGEM pieces, dedicated boxes and special aluminum frames to hold THGEMs have been built (Fig.6.15). The THGEMs are fixed on six points by nylon clips holding them on the fiberglass only, not touching the Cu or Au surface. Each frame can hosts two THGEMs (one on each side) and each box can accommodate six frames: twelve THGEMs in total. Channels on the top and the bottom of the box secure six frames in place to avoid contacts which could damage the THGEM surfaces during transportation. The box is made by plexi-glass plates. To close the box a plexi-glass cover is secured in place by screws and with an O-ring

to assure gas tightness. Gas connections allow flushing the stored THGEMs with clean gas. The Al frames can be used to handle the THGEM pieces without touching them. These boxes turned out to be essential elements in hybrid PD project.

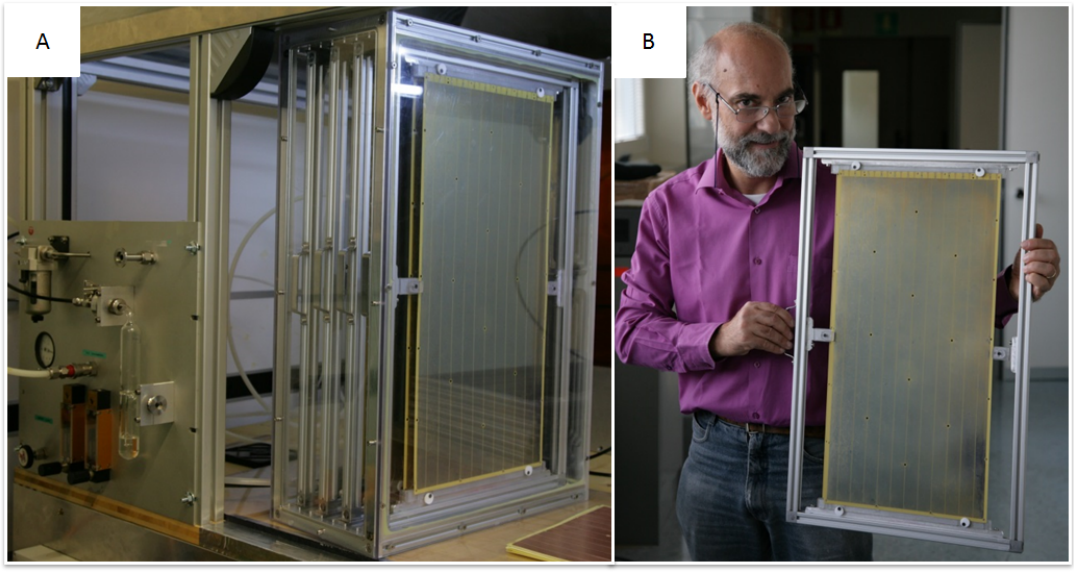

FIGURE 6.15: A. Transparent fiber-glass box with special aluminum frames inside. B. My supervisor Dr. F. Tessarotto with a THGEM holding frame with one THGEM mounted on the frame.

6.2 The large MM prototype

Unlike the THGEMs which are re-usable active elements of the hybrid PDs and can be tested independently before the final assembly, the MicroMegas are fused to the anodic PCBs which are also glued to the detector frame: they cannot be reused or tested independently. A quality control procedure analogous to the THGEM one, cannot be adopted for the MicroMegas:

- Producing Micromegas (which includes producing very expensive anodic-PCBs with soldering of the large no. of readout connectors) in such a large quantity like THGEMs, to allow for selections, is a luxury which we couldn't afford.
- Since they need to be glued to a frame to be characterized, a temporary frame cannot be an option and the final frame contains two of them and is very complex, delicate and expensive (as will be described in Chapter-7).
- It was not reasonable to use for Micromegas characterization the other elements of the final chambers (Drift wire plain is $\sim$1.7 m long, The R/O electronics available in the laboratory is not the same as the final one etc.)

We decided to characterize two MicroMegas as similar as possible to the final ones in a special chamber of 800×800 mm^2 area, where the two MMs were attached side by side (Fig.6.16). These two $\mu-$mesh were called as MESH α and MESH β. They were produced at CERN by Rui de Oliviera using the bulk technology, on PCBs of about 300×600 mm^2.

These two PCBs were similar to the final PCBs for the hybrid PDs apart from the pad size (12×12 mm^2 instead of the final 8×8 mm^2), the readout connectors on the back side of the PCBs (standard 16-pin connectors instead of the Robinson Nugent 50-pin connectors used in the final PCB) and the standard readout scheme (not the resistive/capacitive one). On the other hand the MicroMegas production was identical to the final production.

FIGURE 6.16: 600×600 mm^2 MM prototype: made by gluing two ∼300×600 mm^2 MicroMegas PCBs (α and β) side by side.

A stretched myler foil[2] of 750×750 mm^2, coated with 300 nm Al was used as drift plane.

The chamber was closed with a large kapton window to allow illuminating the entire surface of both MMs with an ^{55}Fe X-Ray source. To understand the effective gain uniformity of the MMs, the readout was segmented in groups of 16 pads (4×4). Each MM had 66 readout sectors. The standard readout chain consisting of a CREMAT preamplifier and an Amptek MCA 8000A (as mentioned in Chapter-5) was used.

[2]BoPET (Biaxially-oriented polyethylene terephthalate) is a polyester film made from stretched polyethylene terephthalate (PET) and is used for its high tensile strength, chemical and dimensional stability, transparency, reflectivity, gas and aroma barrier properties and electrical insulation. Metalized BoPET foils are called Mylar.

(A)

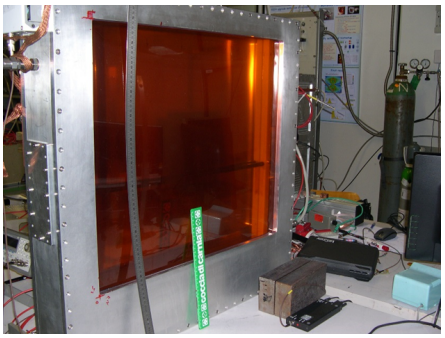

(B)

FIGURE 6.17: A. Assembled drift plane made with 300nm Al coated mylar foil. The reflected image of me and my supervisor can be seen. B. The large Kapton window of the 800×800 mm^2 allows to test the whole surface of the two MMs using the ^{55}Fe X-Ray source.

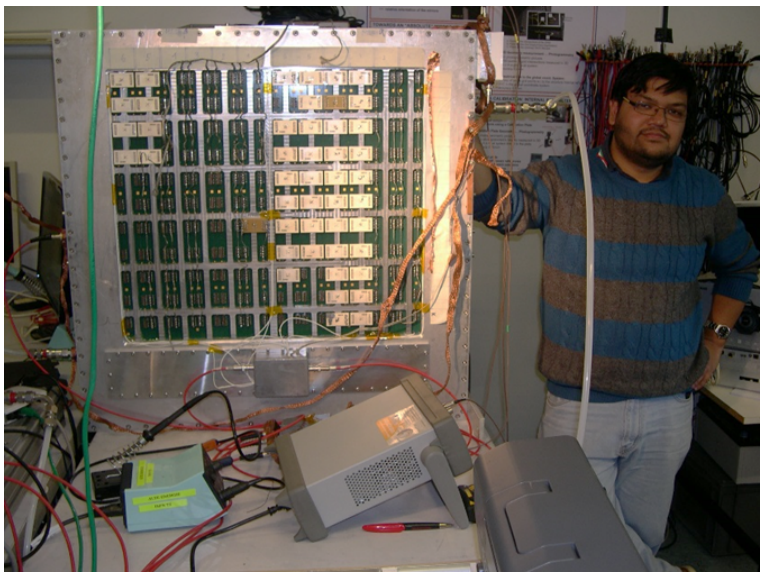

FIGURE 6.18: Assembled chamber from the back.

The mapping of effective gain uniformity for all sectors of both MMs is shown in Fig.6.19. The distribution of the effective gain values for the 132 readout sectors is shown in Fig.6.20: the distribution has an RMS of 5.4%.

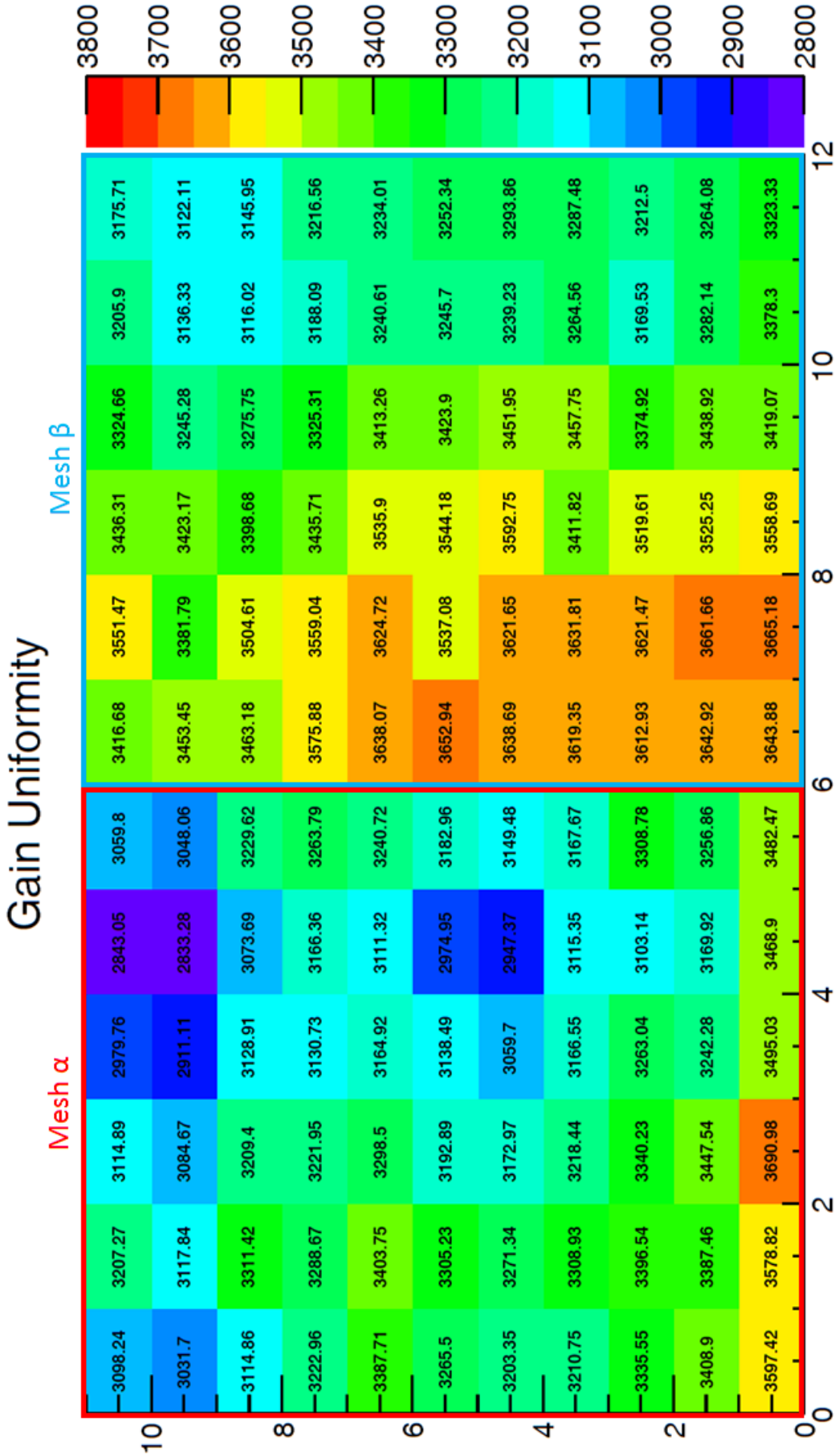

FIGURE 6.19: Gain uniformity of MESHα and MESHβ

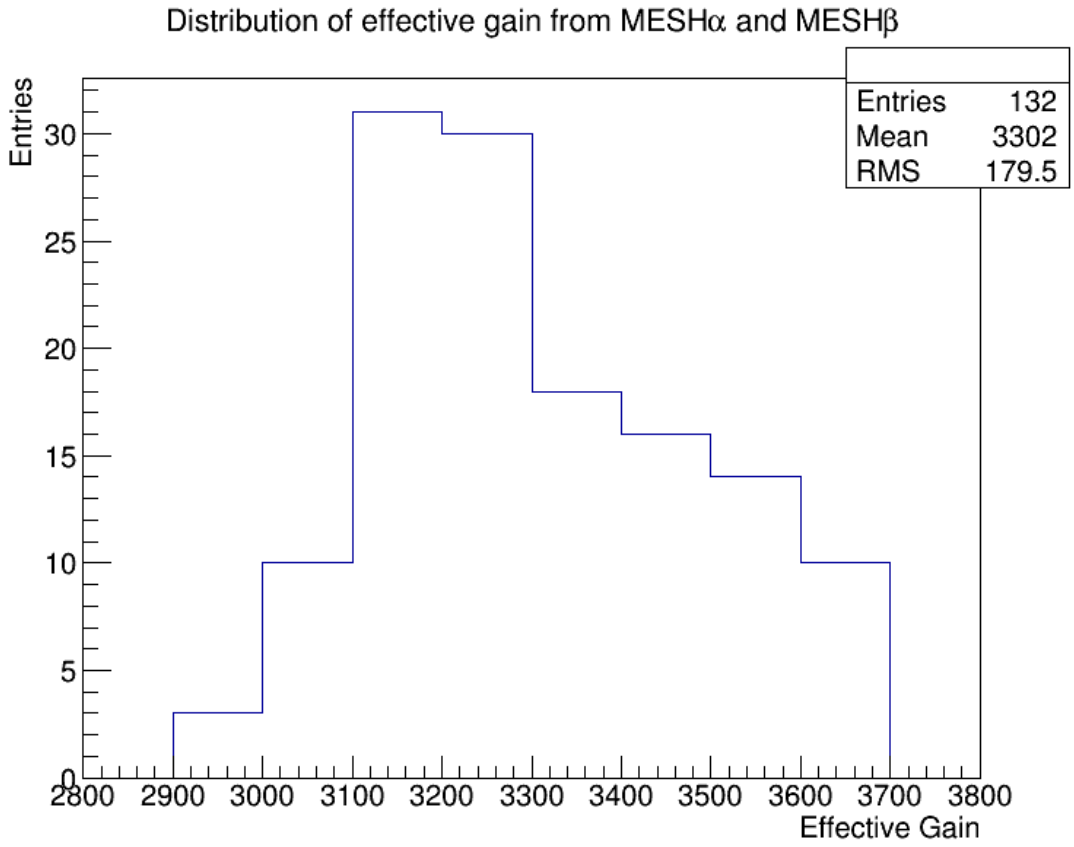

FIGURE 6.20: 1D distribution of measured effective gain for MESHα and MESHβ for the gain uniformity study

The effective gain variation with mesh voltage V_{MESH} was studied for several different readout sectors in Ar:CH_4 40:60 gas mixture with an ^{55}Fe X-Ray source, using the 300×300 mm^2 MM prototype with "Capacitive anode" used in the beam test at CERN (mentioned in Chapter-5). A maximum effective gain of $\sim 10^4$ in stable conditions with a good energy resolution ($\sim 15\%$ FWHM) was observed (see Fig.6.21). The corresponding effective gain scan is shown in Fig.6.22.

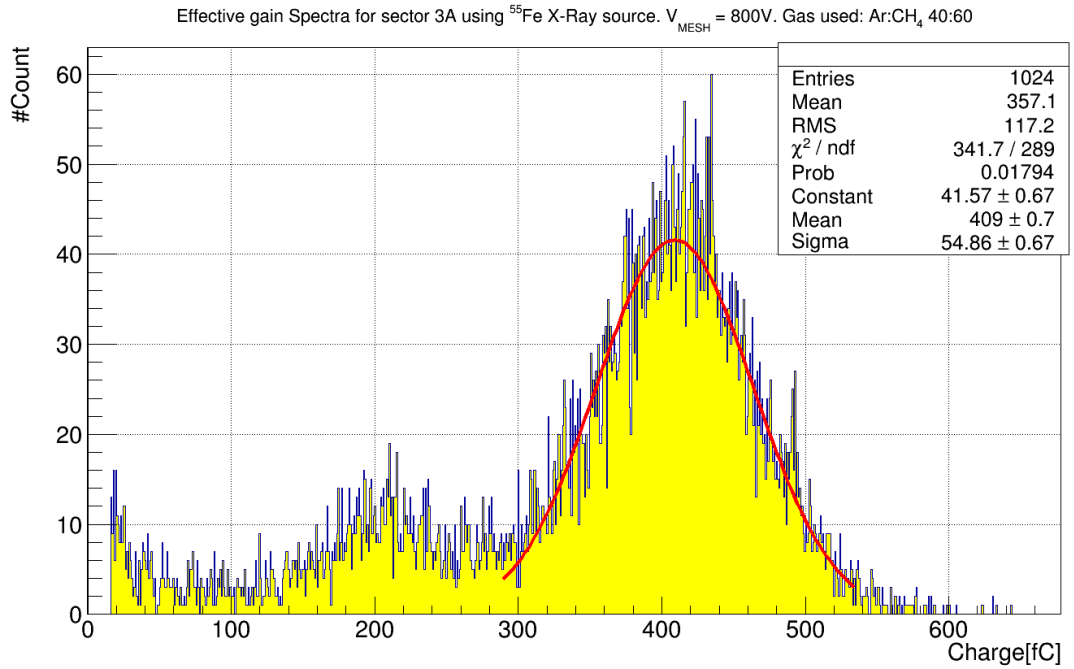

FIGURE 6.21: Efefctive gain spectra of sector 3A obtained with ^{55}Fe X-Ray source; V_{MESH} = 800V; Gas used Ar:CH_4 40:60; Calculated effective gain from the Gaussian fit ∼11600 with an energy resolution (obtained by calculating from the fit: sigma/mean×100%) ∼13%

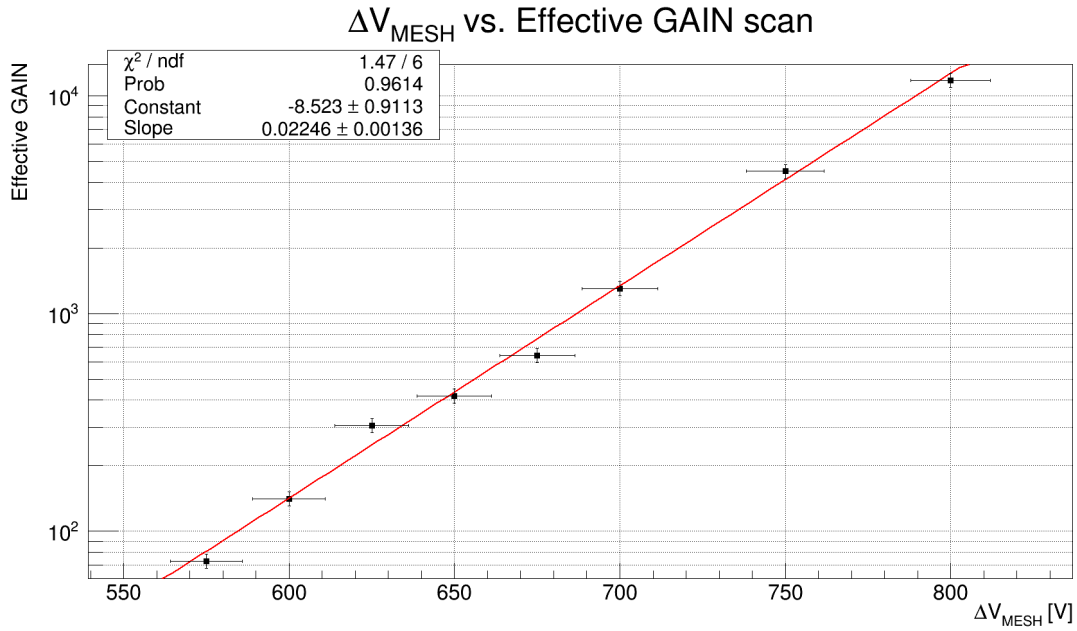

FIGURE 6.22: Scan of effective gain for different MESH voltages at sector 3A done using ^{55}Fe X-Ray source; V_{MESH} = 800V; Gas used Ar:CH_4 40:60. An exponential fit to the distribution is also shown.

6.3 Discharge Studies

A clear advantage of the capacitive/resistive anode architecture is the localization of discharge effects in a single pad. The effect of a discharge on a pad to the adjacent pads was studied using a special configuration: two neighboring pads (PAD A and PAD B in Fig.6.23) were biased and monitored by two independent high voltage channels and connected to oscilloscopes or to analogue readout chains (Fig.6.23).

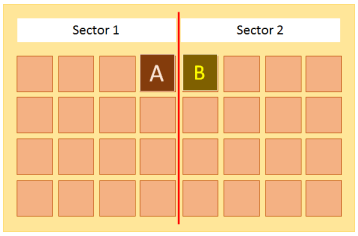

FIGURE 6.23: Schematic of pads to test the discharge corellation

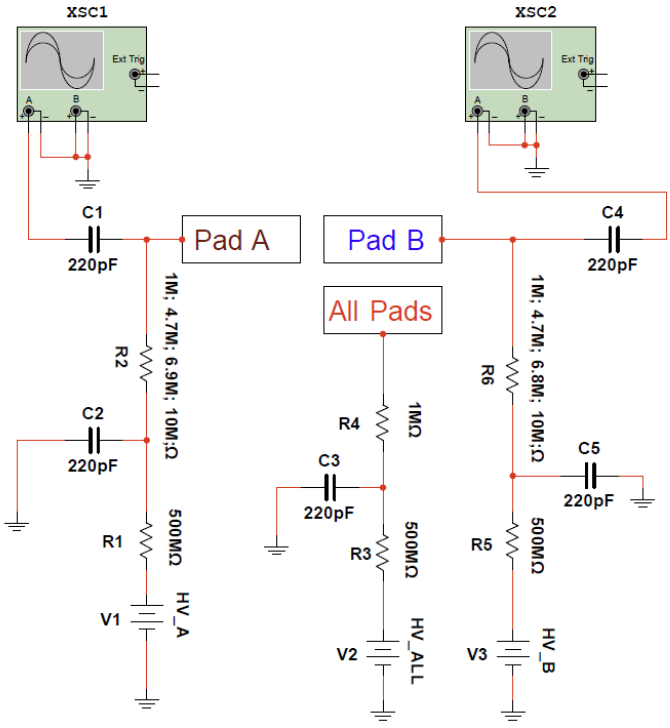

FIGURE 6.24: circuite schematic for measuring the effect of a discharge on a neighboring pad.

Various configuration were investigated, in particular, either PAD A and PAD B or both were kept at an anomalously high voltage of 720V - 735V to induce frequent discharges (∼0.1-0.2 Hz), and the correlation between the discharge times, shown in Fig.6.25a was studied.

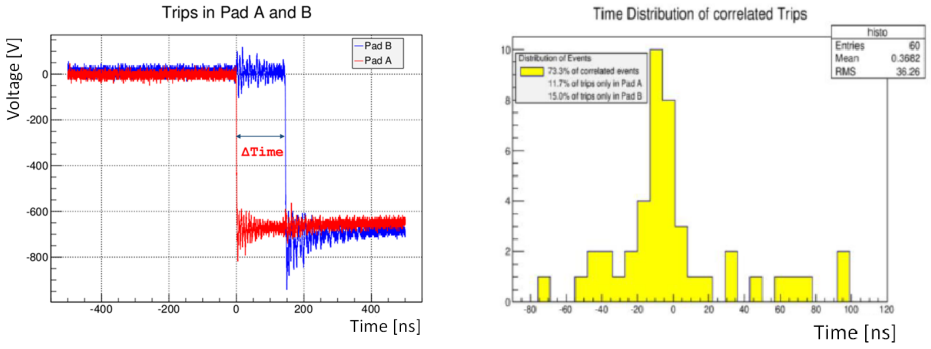

(A) (B)

FIGURE 6.25: A. The time distribution of a discharge; B. Time correlation of discharges between two neighboring pads.

The distribution of the time correlation (Fig.6.25b)shows a clear peak around 10 ns with large tails ($\sim \pm 100$ ns).

When only one of the PADs A and B is kept at an anomalous voltage (720 V) to induce continuous discharges, and the other was at nominal voltage of 600V, The probability of correlated discharges drops to zero from the high (70% - 90%) values observed when both pads are at anomalous voltage (shown in Table-6.1).

TABLE 6.1: Correlation studies of discharges between 'PAD A' and 'PAD B'

Position of pads	PAD A voltage $[V]$	PAD B voltage $[V]$	% correlated events	% only for PAD A	% only for PAD B
AB	720	720	73.5	11.7	15
AB	735	720	90	8.3	1.7
AB	720	735	70.5	1.6	27.9
AB	**730**	**600**	**0**	**100**	**0**
AB	**600**	**730**	**0**	**0**	**100**

In Fig.6.26 the effect of a discharge occurring on PAD A (left: 650V drop) can be seen in PAD B, with various amplitudes and time constants, depending on the value of the resistor providing HV. Many resistance values have been tried (1MΩ, 4.7MΩ, 6.8MΩ, 10MΩ etc) and the optimal value turned out to be around 500 MΩs. In this case the voltage drop induced in PAD B is ∼2 V only (Fig.6.26-Right), corresponding to an effective gain drop of ∼4%.

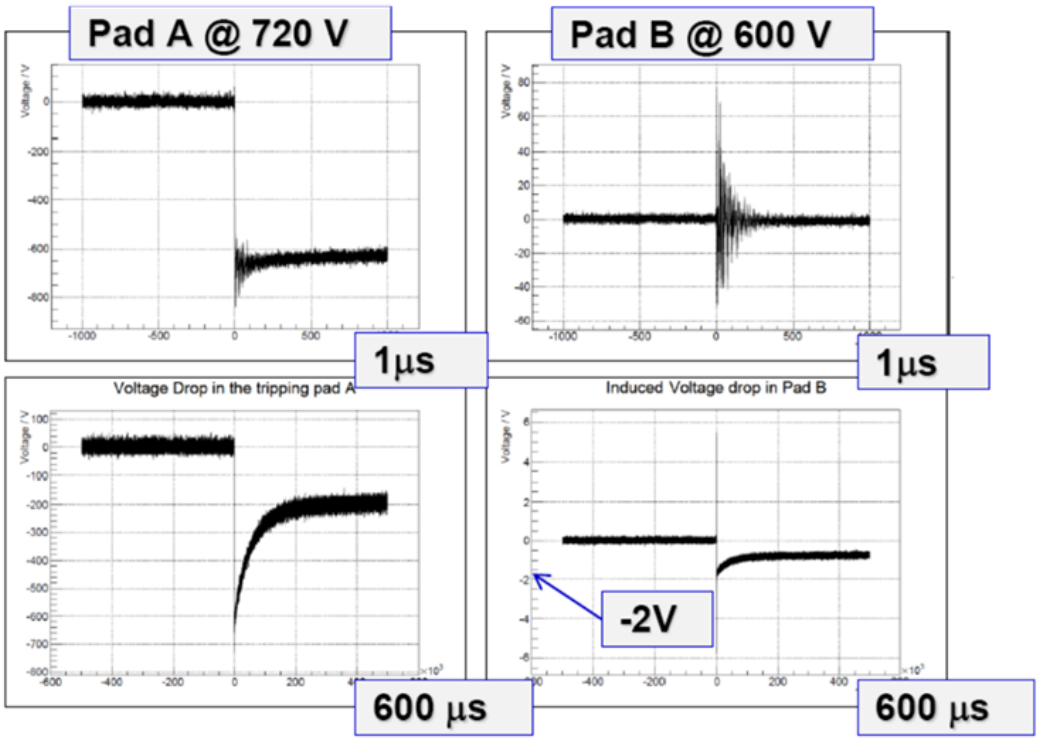

FIGURE 6.26: Discharge study for to adjecent pads

6.4 Gain Variations of Hybrid PDs

To assure a stable detector response, not only the electrical stability but also the effective gain stability has to be guaranteed. It is well known that variations in temperature (T) and pressure (P) of the multiplication gas affect the ionization mean free path of the gas, thus the gas gain. RICH-1 hybrid PDs cannot be fully thermalized and pressurized, thus changes in environmental P and T will reflect in similar changes in internal gas P and T: their effective gas gain will be affected accordingly. Also P and T variations due to local effects (e.g. change in gas flow, change in T due to front end heating etc.) are contributing to the variation of the gas gain. A recipe to stabilize the gain response of our hybrid PDs had been provided by performing a group of systematic studies using the 300×300 mm^2 hybrid PD prototype discussed in Chapter-5.

The gas gain response over long periods ($\sim$weeks) was measured and large variations in the effective gain were observed (Fig.6.27).

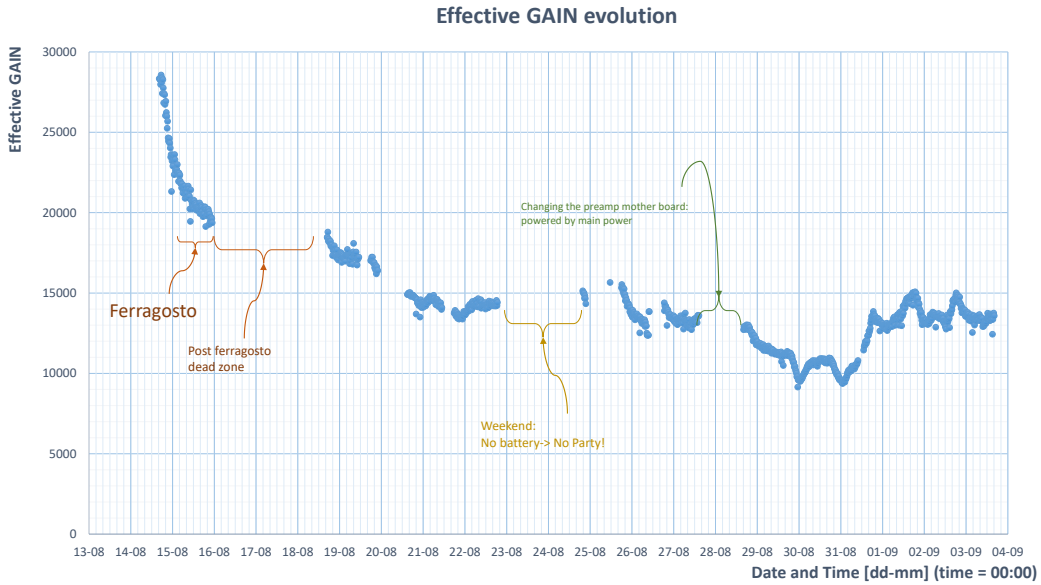

FIGURE 6.27: Gain variation with Temperature and pressure

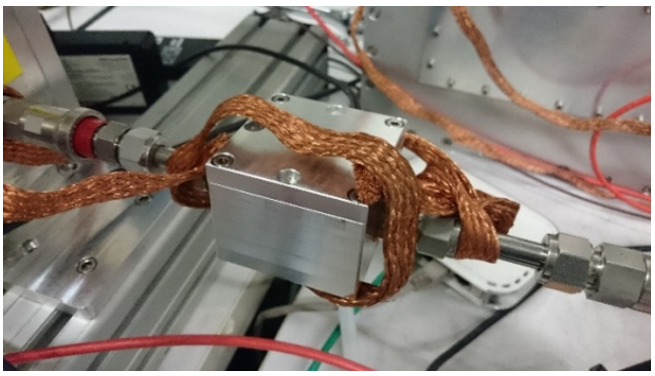

FIGURE 6.28: Temperature and pressure sensor box used in gas input and in gas output

To investigate the possible correlation of effective gain variation with P and T a special setup was built in our lab. Automatic registration of effective gain spectra, for every minute over long time periods, was realized by modifying AMPTEK 8000A MCA internal settings. The P and T for both the PD gas and the environment, were measured with the same time frequency, using special sensors (for P: MS5611-01BA; for T: ADT7420), soldered over a custom built board with a commercial ADC and an I^2C module to record the data into a PC via an USB connection. To measure P and T at gas input and output special sealed aluminum boxes equipped with PT boards were built (Fig.6.28). Dedicated measurements of effective gain variation over long period along with P and T measurements were performed (Fig.6.29): a clear correlation between T/P and effective gain variation was observed.

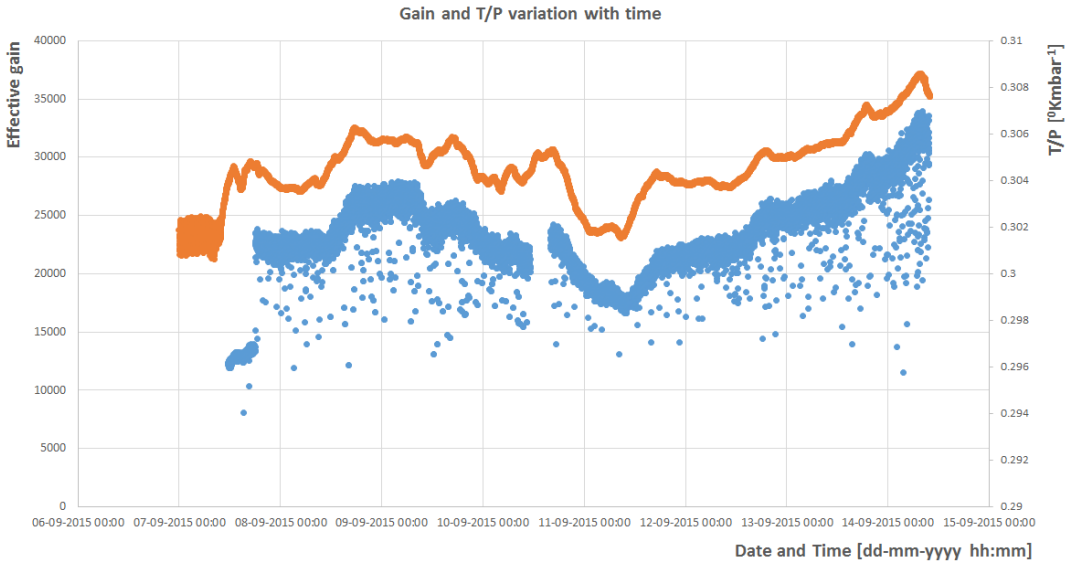

FIGURE 6.29: Gain and T/P variation in Time

To formulate the correlation between T/P and the effective gain a detailed analysis of the collected data was performed.

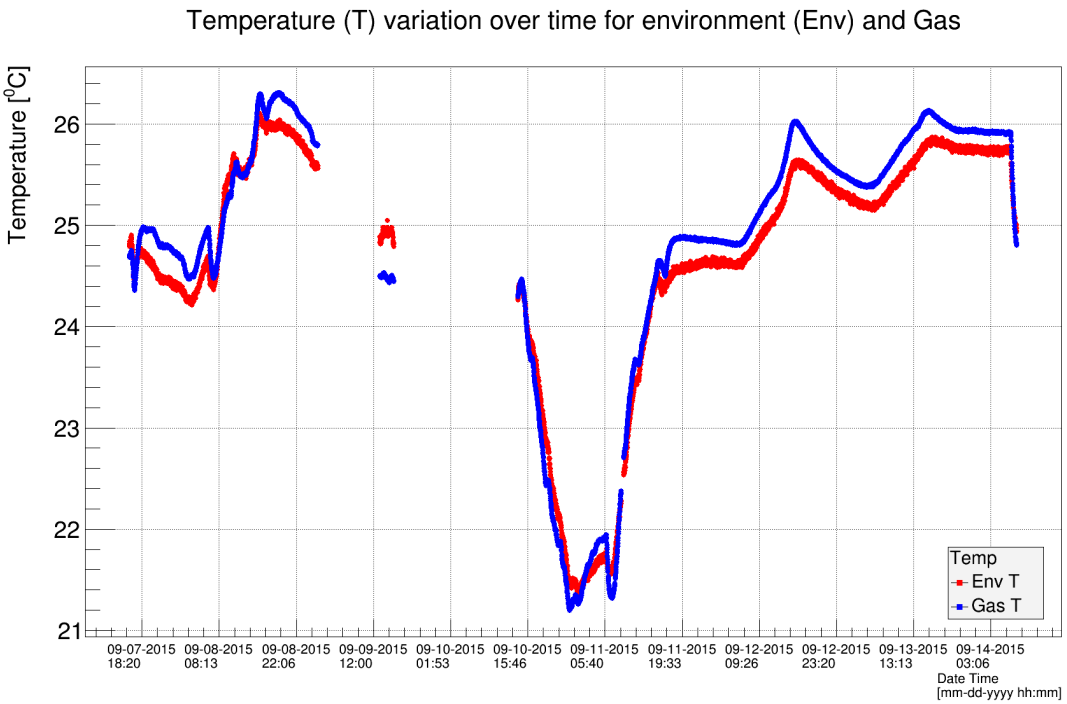

FIGURE 6.30: Environmental and gas temperature variation over time

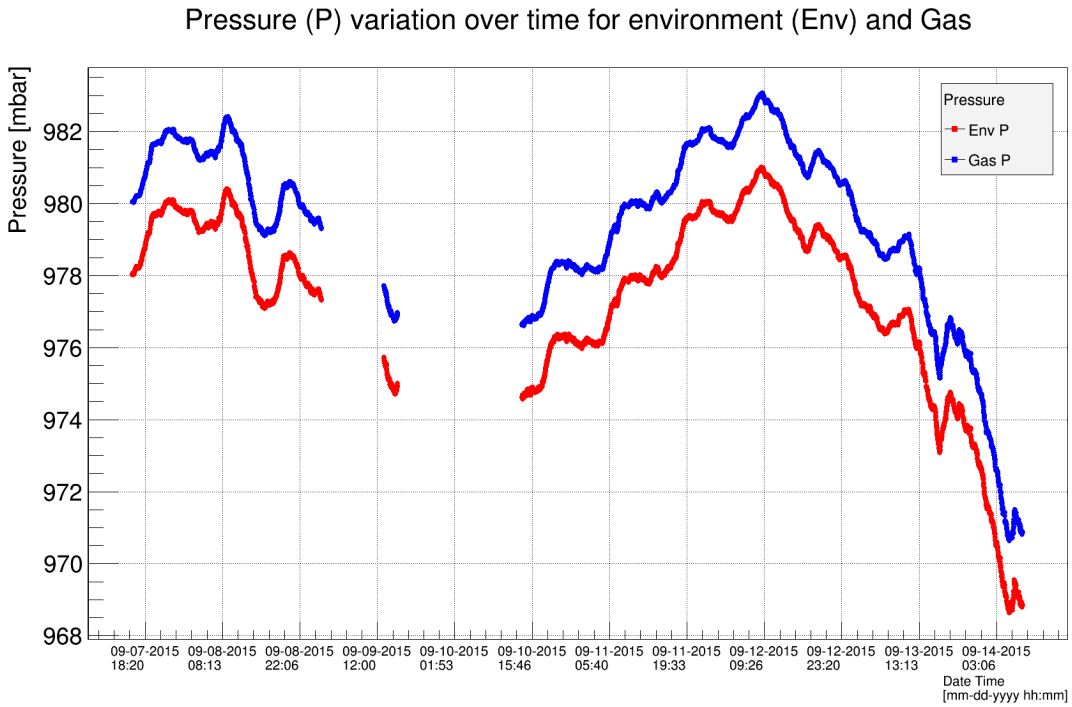

FIGURE 6.31: Environmental and gas pressure variation over time

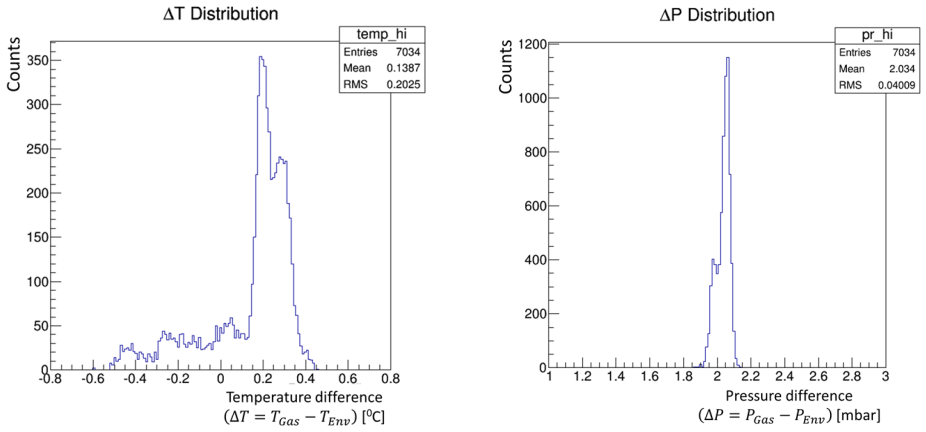

(A) (B)

FIGURE 6.32: (A) Distribution of Env and Gas temperature difference. (B) Distribution of Env and Gas pressure difference.

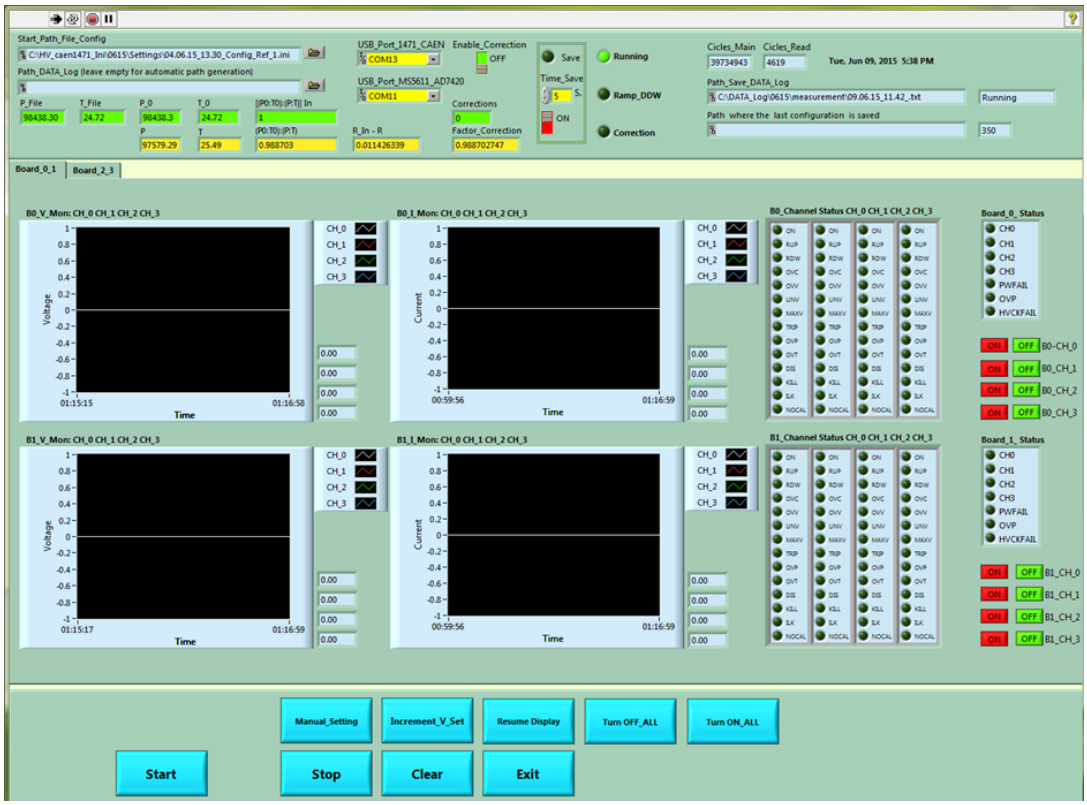

FIGURE 6.33: Custom build LabVIEW based control interface to control effective gain of the chamber with PT variation

To study gain variation a system dedicated to measure the gain over longer period (∼days) and a custom built software based on LabView[3] (screenshot of the GUI can be seen in Fig.6.33) were used to read the temperature and pressure from those sensors (Fig.6.28) and to control CAEN N1471H class HV PSs (Fig.6.34). A detailed study of these variables helped in extracting the equation to relate the effective gain, Voltages and Temperature and pressure as

FIGURE 6.34: CAEN HV PSs used for automatic control over HV to be implemented

$$V_{calc} = V_0(1 + \alpha\frac{P - P_0}{P_0} - \beta\frac{T - T_0}{T_0}) \tag{6.1}$$

[3]A Data Aquisition and control software from National Instrument, www.ni.com

Where α and β are two constant calculated from slope of the P, T curve. P_0 and T_0 are the initial pressure and temperature respectively.

The result with and without corrections by this home made software is shown in Fig.6.35, where one can see that the effective gain variation with correction applied ($\sim$10%) is smaller compared to without the correction ($\sim$40%).

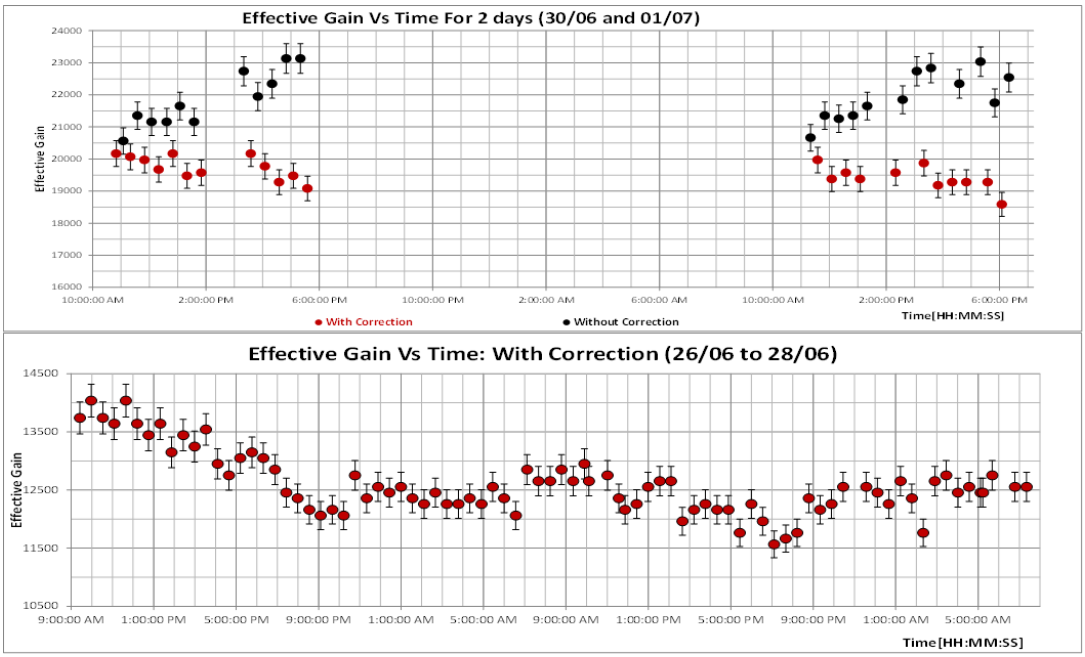

FIGURE 6.35: gain variation with (top) and without (bootom) PT corrections over time.

Similar systems have been implemented in the final setup in COMPASS RICH-1 and the results obtained from these corrections have been shown in chapter-8 along with a final validation of the discharge rate studies from the final pieces.

6.5 Summary

The final THGEMs for the RICH-1 upgrade were prepared: specific procedures (result of intense studies) for raw material selection, THGEM production, quality assessment, characterization and for storage were developed and applied.

MicroMegas with the final characteristics were studied and validated. The response of the detector in case of a discharge was studied in detail. The effects of the variation of environmental conditions (pressure and temperature) were studied and an automated high voltage correction system was built to stabilize the PD gain response.

The story of building and installation of the final hybrid PDs on RICH-1 is presented in a temporal sequence in the next chapter.

Chapter-8 will then describe the preliminary commissioning of the novel hybrid PDs and conclude by presenting some of the promising first results obtained before the writing of this thesis.

Chapter 7

Construction and Installation of the new Hybrid PDs

7.1 Constrains on the final mechanical design

In the MWPC based PD case the field region is properly contained between the photo-cathode and the cathode wires; in the hybrid PD case the drift wires are the most negative biased electrodes and the field region needs to be properly closed. The electrode which closes the field needs to be optically transparent (the wire diameter should be as small as possible) and cannot be put too near to the drift electrode as the field values at the wire surface should be small enough to avoid electron extraction (for drift wires) or electron multiplication (for field wires): dedicated field calculations were performed to optimize the geometry of the wire planes used in the final hybrid PDs. The minimization of border dead areas imposes the introduction of extra electrodes for field shaping, which were also optimized using dedicated field calculations.

Further constrains on the new PD geometry, linked to the compatibility with the other elements of RICH-1 were:

1. Fixation of the hybrid PDs on the existing RICH-1 quartz window frames.
2. Com-penetration of the MAPMTs + lenses & R/O with the hybrid PDs in the new frames.
3. Use of existing APV-25 based R/O: 48 large motherboards with 512 channels each.

7.2 Field calculations and design optimization

COMSOL[1] software has been used to calculate the electric fields for the optimization of the final Hybrid PD structure. To assure the validity of the calculation, first a dedicated exercise to reproduce the MWPC field configuration was performed: the schematic of the COMPASS RICH-1 MWPC (Fig.7.1) has been incorporated in the COMSOL framework (Fig.7.2).

[1]COMSOL inc. www.comsol.com

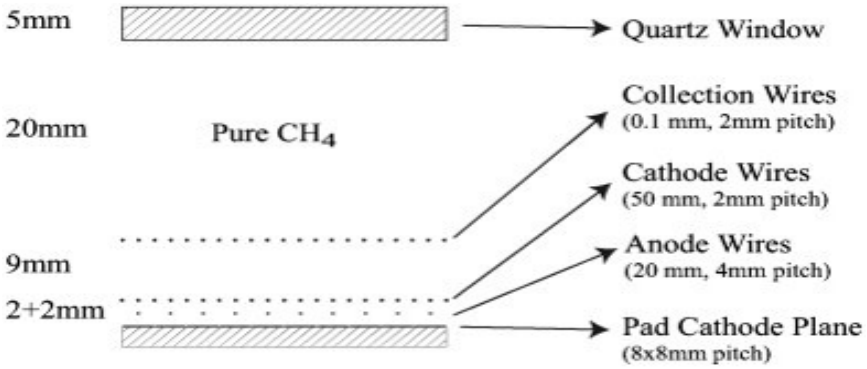

FIGURE 7.1: Scheme of COMPASS RICH-1 MWPC based PD

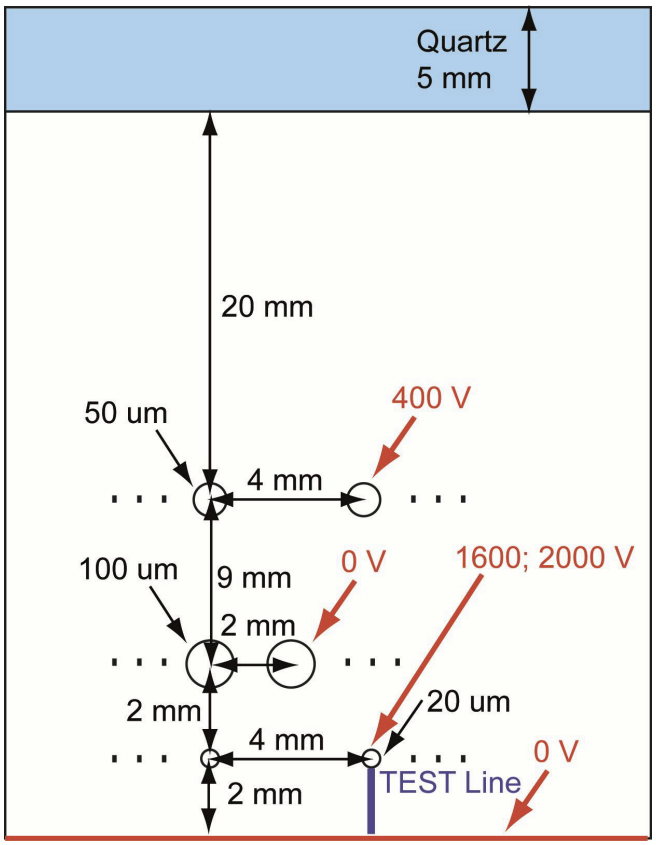

FIGURE 7.2: Schematic of COMPASS RICH-1 MWPC used for COMSOL field calculation

The electric field has been computed for ΔV of 1600V and 2000V respectively: the streamlines of the calculated electric field can be seen in Fig.7.3 and the average value of the electric field near the anodic wires has been computed in steps of 1 μm from the wire surface as shown in Fig.7.4. The corresponding Townsend coefficients α_k (Fig.7.5) have been calculated using these values of the field and the equation-7.1 where A = 1.5933 and B = -35.98 are the two constants for pure CH_4.

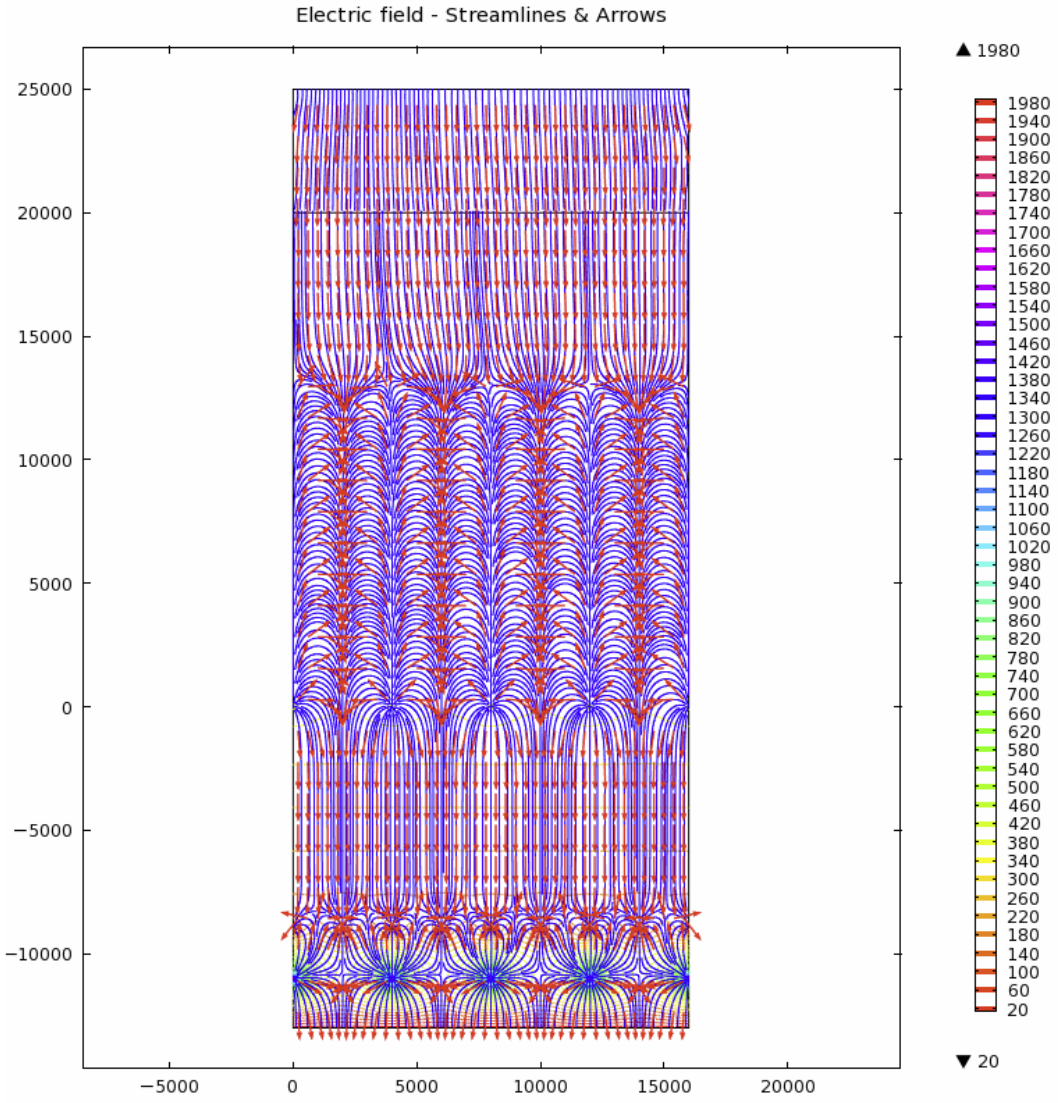

FIGURE 7.3: Calculated electric field streamlines for COMPASS RICH-1 MWPC by COMSOL

$$\alpha_k = \frac{(A|\vec{E_k}| + B)^{1.5}}{10^4} \, [\mu m^{-1}] \tag{7.1}$$

$$g = e^{\sum_{k=0}^{99} \alpha_k} \tag{7.2}$$

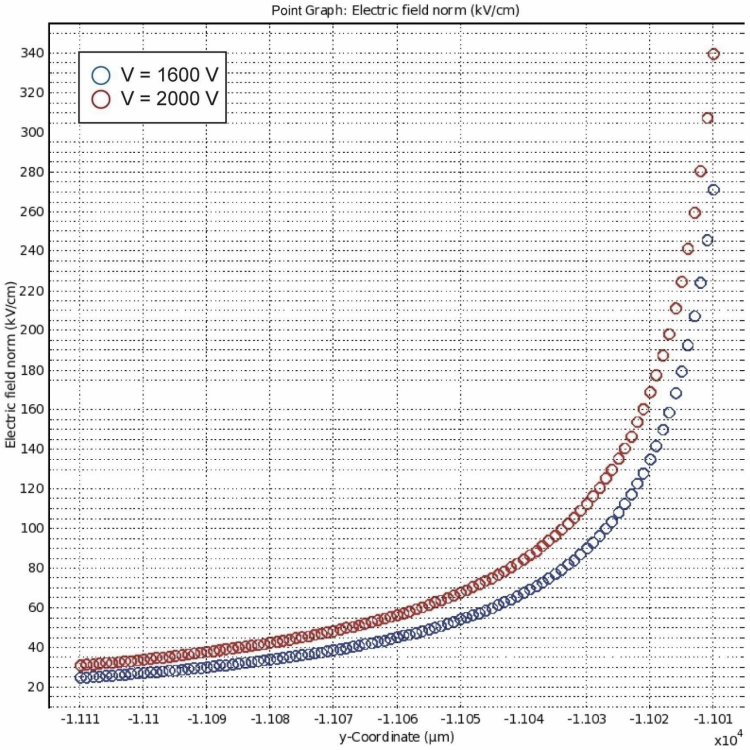

FIGURE 7.4: Calculated average electric field values in 1 μm steps from the COMPASS RICH-1 MWPCs anodic wires.

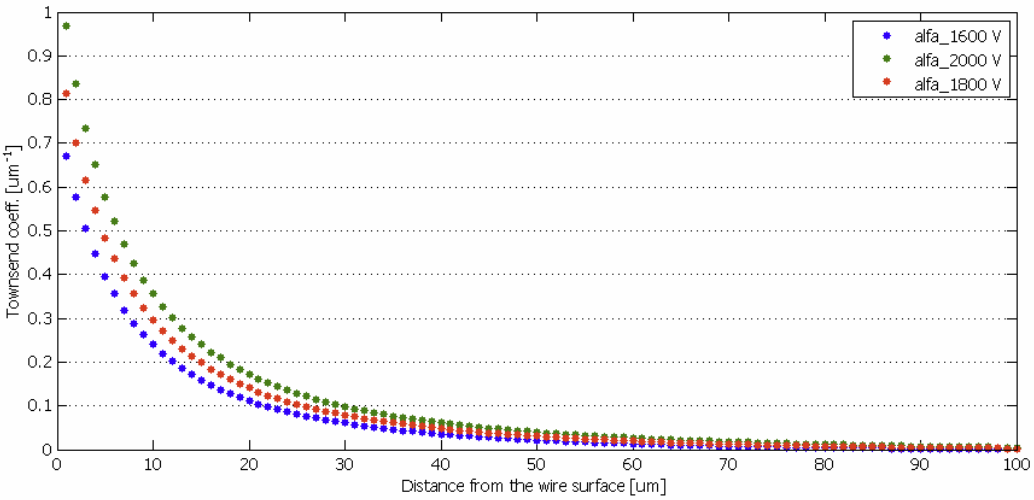

FIGURE 7.5: Calculated Townsend coefficient for COMPASS RICH-1 MWPC using COMSOL.

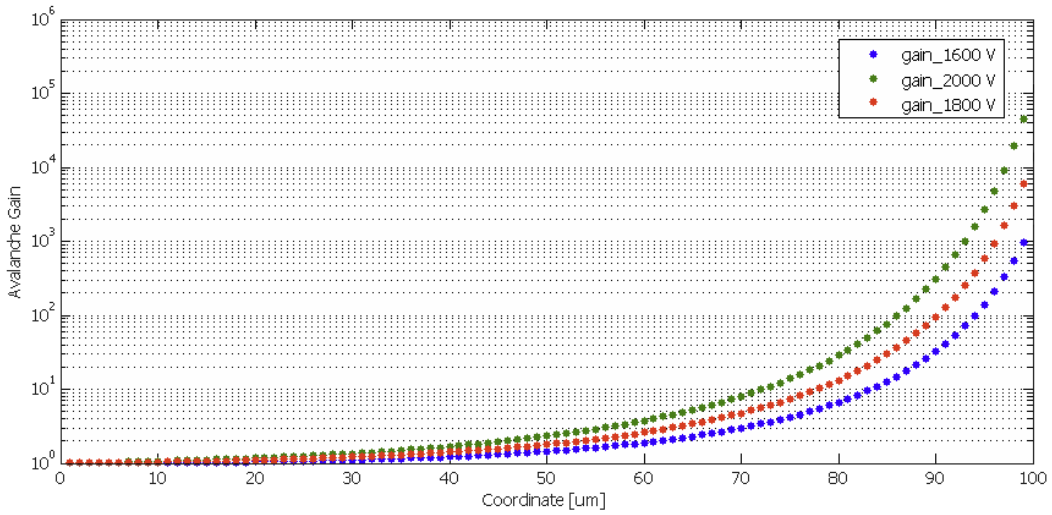

FIGURE 7.6: Calculated gain for COMPASS RICH-1 MWPC using COMSOL

Integrating the calculated Townsend coefficients (equation-7.2) starting from 100 μm from the surface of the anodic wire in steps of 1 μm the expected gain has been obtained (Fig.7.6). The calculated values are in good agreement with the gain values measured long ago by using a ^{106}Ru β-source on the COMPASS RICH-1 MWPCs (Fig.7.7).

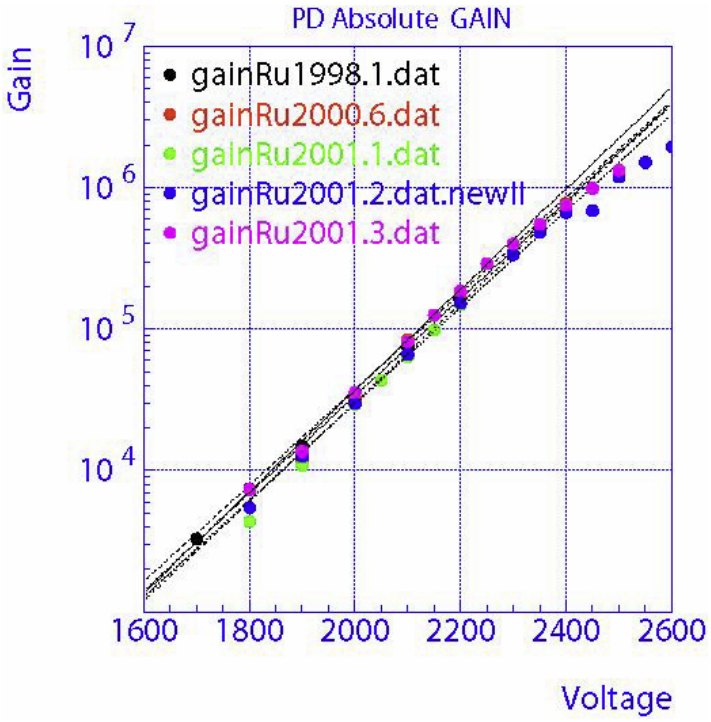

FIGURE 7.7: Gain scan of COMPASS RICH-1 MWPCs

A similar exercise has been performed for the optimization of the wire parameters for the COMPASS RICH-1 THGEM-based PDs. In this case: wire diameter, pitch

and distances needed to be tuned. One of the schemes incorporated in COMSOL framework for diameter study is shown in Fig.7.8.

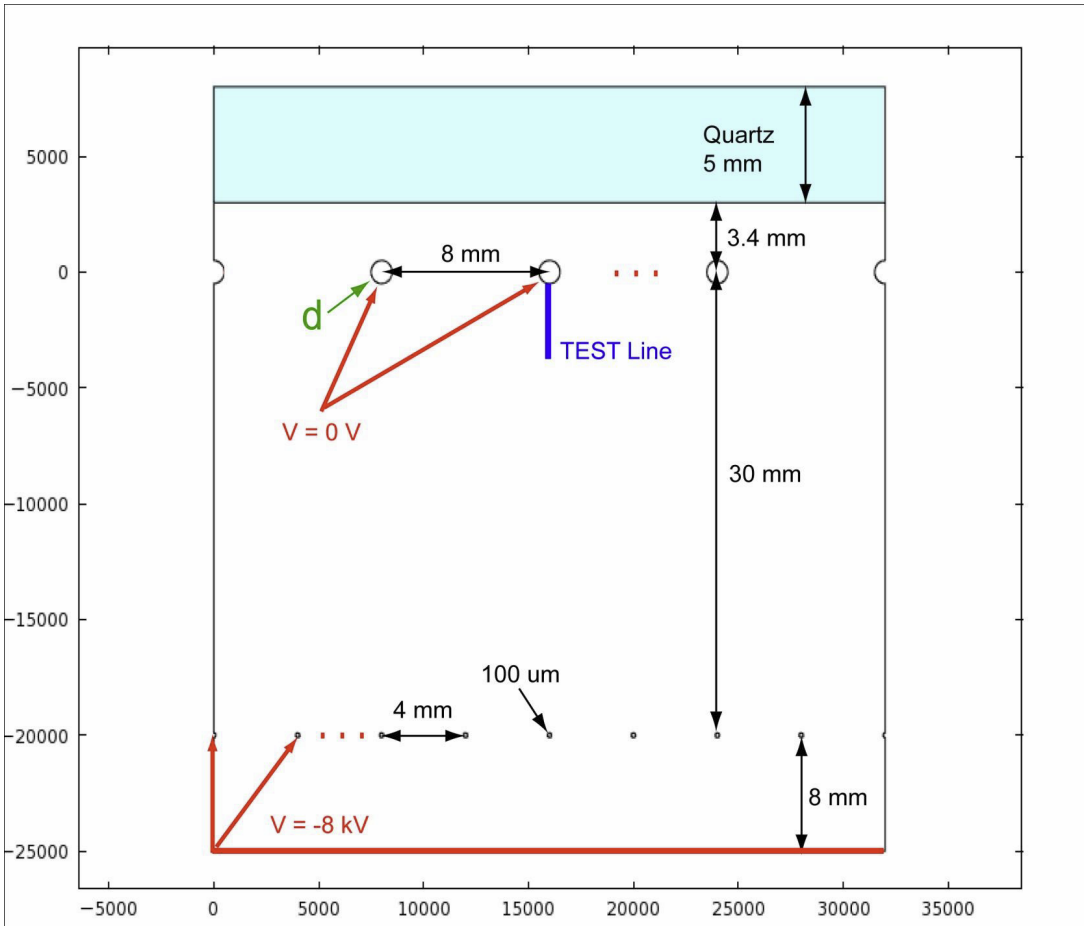

FIGURE 7.8: Schematic of COMPASS RICH-1 THGEM-based PD used for COMSOL field calculation

The calculated stream lines of the electric field for the presented scheme (Drift wires: 100 μm diameter, 4 mm pitch , field wires: 8 mm pitch, tested with different diameter (**d**); with 30 mm distance) for **d**=250 μm is presented in Fig.7.9: for -8 kV drift bias the field at the wire surface approaches $\sim$30 kV.cm^{-1}. Similar values of the field at the wire surface are obtained with a different configuration (100 μm diameter and 4 mm pitch for both drift wires and field wires, 30 mm distance, -8 kV drift bias) as shown in Fig.7.10. This symmetric configuration provides a higher optical transparency and a more uniform field configuration.

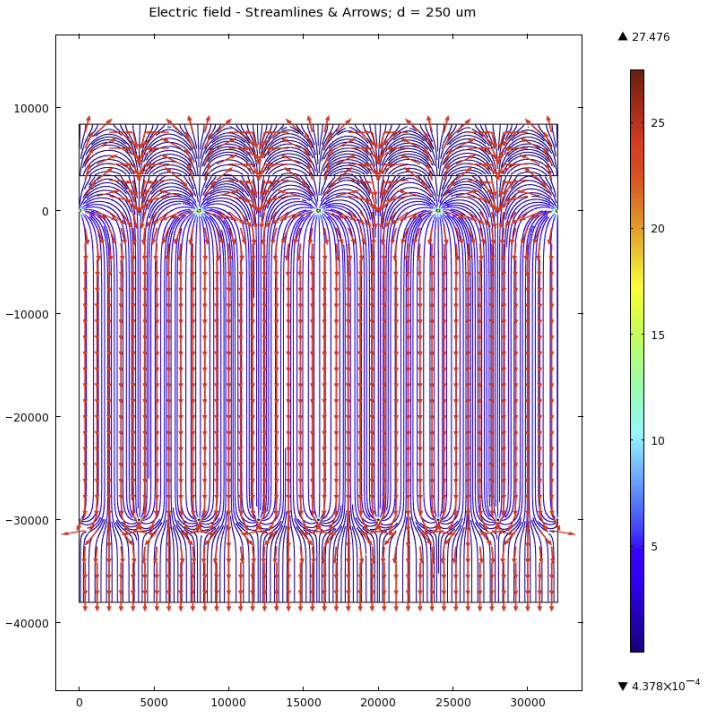

FIGURE 7.9: Calculated electric field streamlines for COMPASS RICH-1 THGEM-based PD with 250 μm diameter wires with 4 mm and 8 mm pitches for the drift and field wire plains respectively.

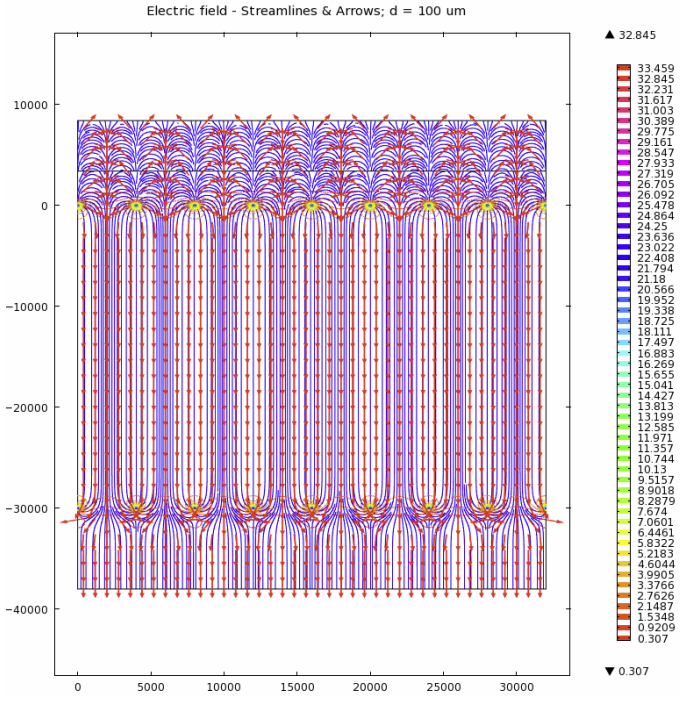

FIGURE 7.10: Calculated electric field streamlines for COMPASS RICH-1 THGEM-based PD with 100 μm diameter wires with 4 mm pitche for the drift and field wire plains respectively.

For the final Hybrid PDs for COMPASS RICH-1 both wire planes were built with 100

μm diameter wires having 4 mm pitch with 38.4 mm distance between them. The field wire plane is placed at 4.5 mm from the fused silica window which separates the radiator gas volume from the multiplication gas ($Ar/CH4$ 50/50 gas mixture). The scheme is shown in Fig.7.11.

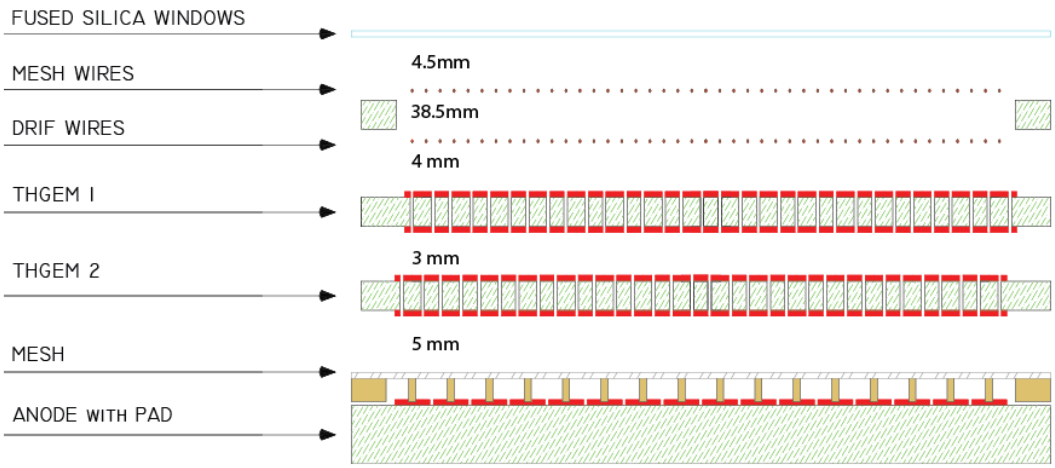

FIGURE 7.11: The final hybrid PD scheme with two wire planes

7.3 Chamber construction

The final PDs are very complex objects. As can be seen in Fig.7.12 each PD is composed of three parts:

1. The hybrid PD.
2. The matrix of 108 MAPMTs with their lens systems, soft iron shielding and the front-end electronics.
3. The common frames which hold both the MAPMT system and the hybrid PD.

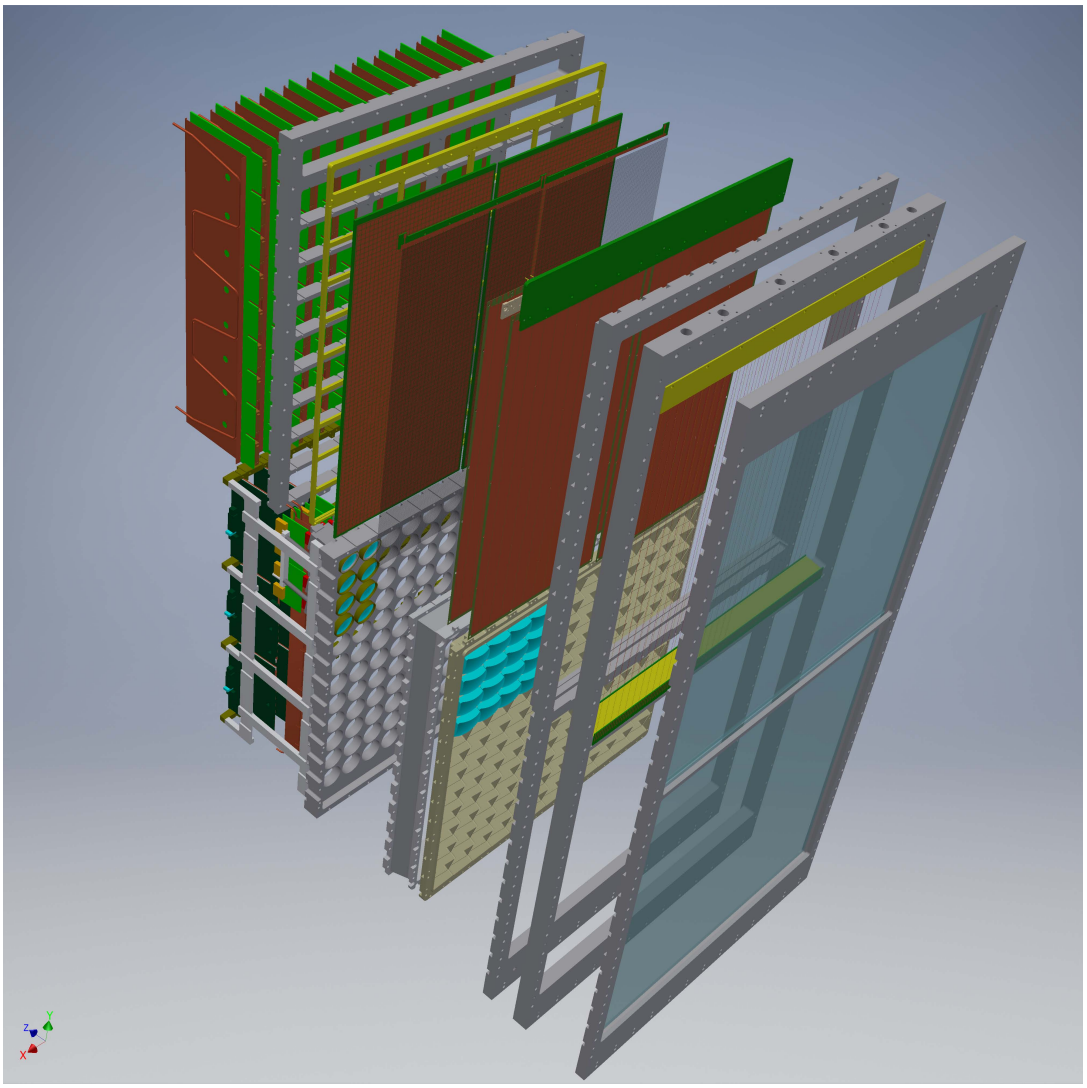

FIGURE 7.12: Exploded view of the final PD with Hybrid detector and MAPMTs

The frames are attached to the RICH-1 vessel via the fused silica windows frame. An exploded view of the frames only can be seen in Fig.7.13. A longitudinal cross-section of the final PD is shown in Fig.7.14 where the com-penetration of the different parts can be appreciated.

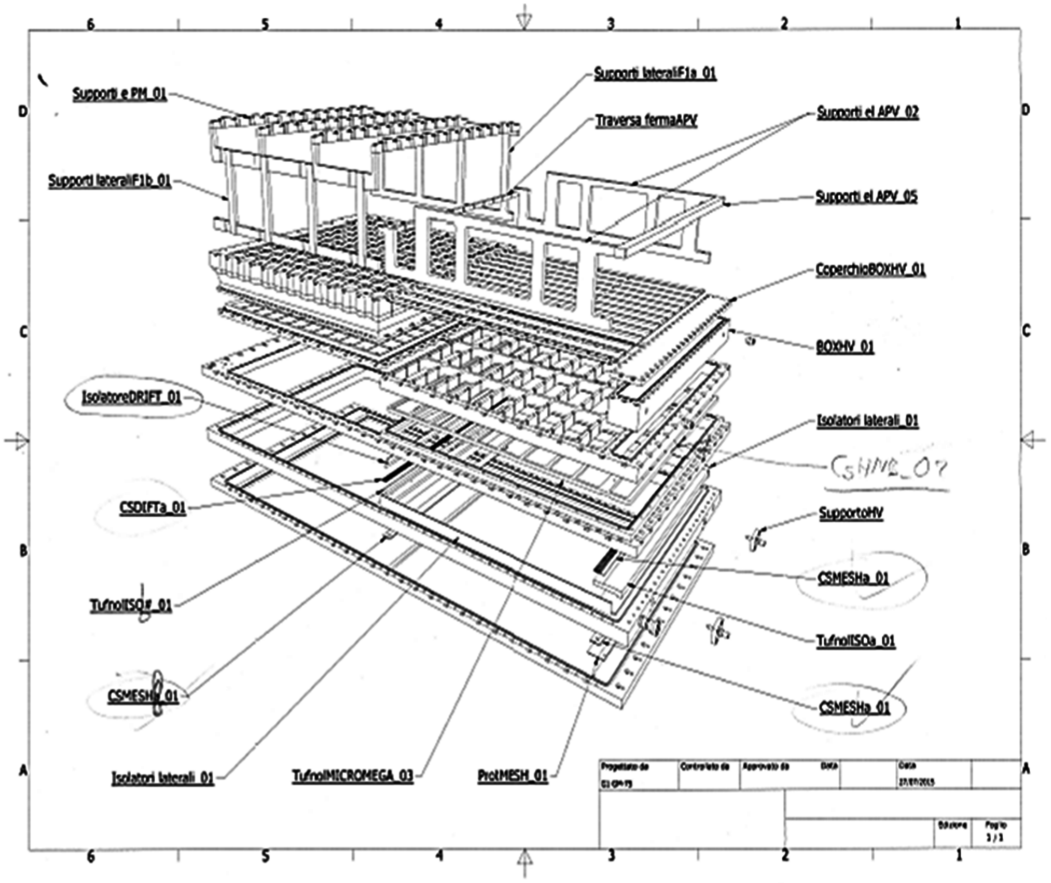

FIGURE 7.13: Exploded view of the frames of the final hybrid PD, from a drawing used in the workshop

7.3.1 Wire and spacer frames

As shown in Fig.7.12 the chamber is mounted on the fused silica window frame (the first frame from the bottom (Fig.7.13)), which is attached to the RICH-1 vessel. The second (wire) and third (spacer) frames from the bottom (Fig7.13) are 634 mm wide and 1372 mm long, machined from a unique plate of aluminum alloy EN AW-5083[2]. The machining was performed by CINEL[3] according to the drawings by Giorgio Menon of INFN Trieste.

The internal sides of these frames were covered with thin layer ($\sim$mm) of an insulating material (Tufnol[4]), which was machined to match the shape of the aluminum frames and glued to the frames using Araldite 2011 epoxy glue.

[2] ©G-Alu25 from HABA; datasheet: http://www.haba.ch/

[3] CINEL Strumenti Scientifici s.r.l.; via dell'Artigianato, 14-14/A, 35010 Vigonza (Padova) - Italy, http://www.cinel.com

[4] Fine weave cotton/Epoxy resin laminated plastic (TUFNOL Grade 6F/45) http://www.tufnol.com/

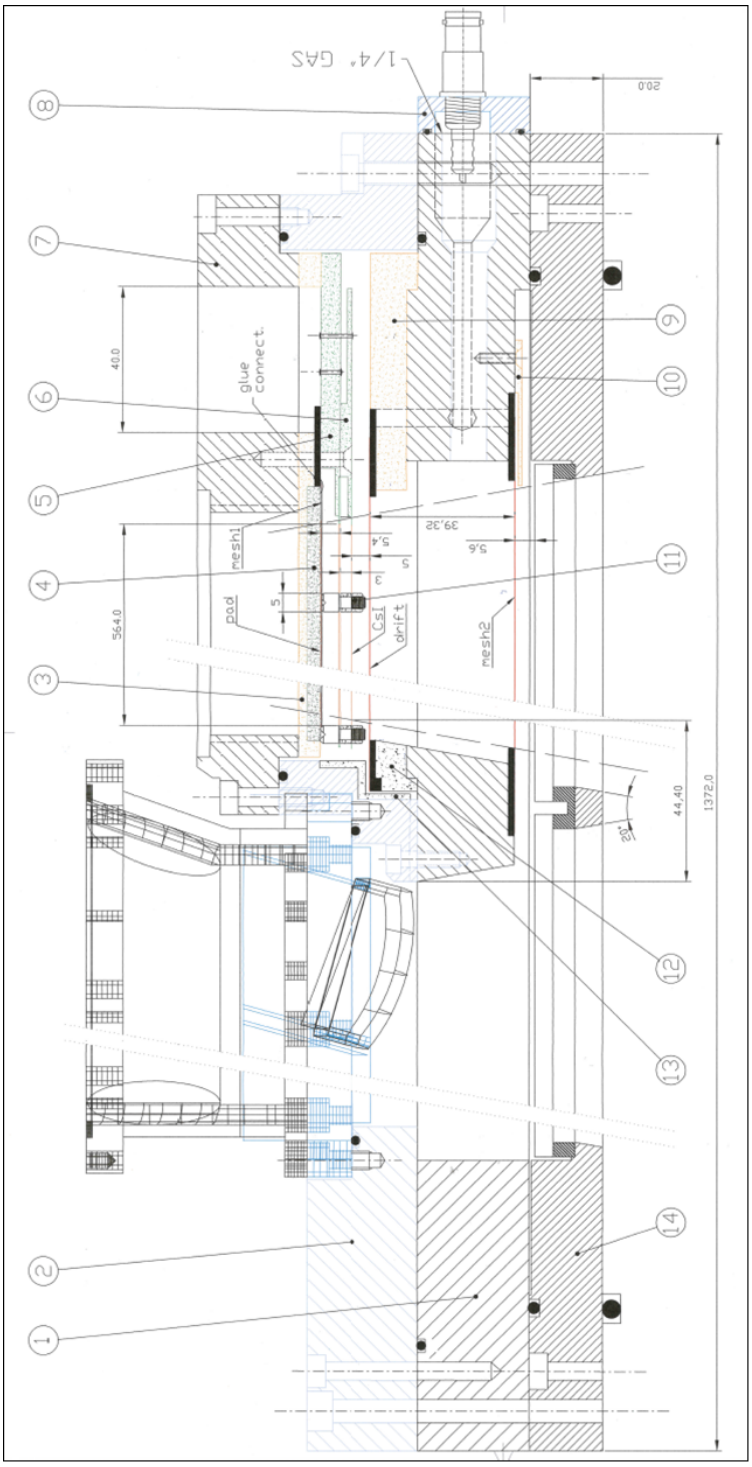

FIGURE 7.14: Section of technical drawing of the final chamber with Hybrid PD and MAPMT frames: 1. Wire frame 2. Spacer frame 3. Anodic TUFNOL 4. Anode PCB 5. HV-THGEM2 PCB 6. HV-THGEM1 PCB 7. Hybrid frame 8. Wire HV cover 9. Drift wire HV TUFNOL 10. Field wire TUFNOL 11.THGEM pillars 12. Drift wires central TUFNOL 13. Central isolation TUFNOL 14. Quartz frame

The wire frames were equipped on both sides with PCBs for wire soldering (for forming the drift and the field wire plains). They were glued over special platforms made

of Tufnol pieces (in Fig.7.14 point 9 and 10), which were machined in the INFN Trieste workshop. To the external PCBs, HV is provided through the aluminum frames from SHV connectors (see Fig.7.36). Also gas circulation is provided through the wire frame via Swagelok Quick Connectors[5].

The two wire plains were formed by soldering Cu-Be 25 alloy wires of diameter 0.1016mm (0.004"$\pm$0.0001") with Ni flash and Au coating (.0000005"-.0000015" respectively). They were soldered one at a time by hand with a tension of 150 g, tuned by a tension meter (Fig.7.15). The soldering operation requires special skills and has been performed by an experienced technician (Mauro Gregori of INFN Trieste) (Fig.7.16). Two guard wires of 200 μm diameter were put on each side of the wire planes.

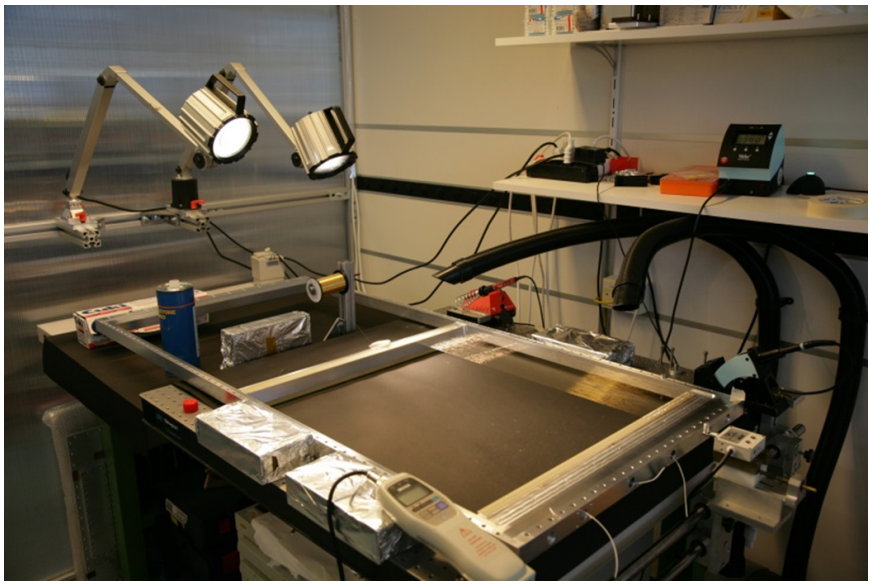

FIGURE 7.15: Setup for soldering of the wires

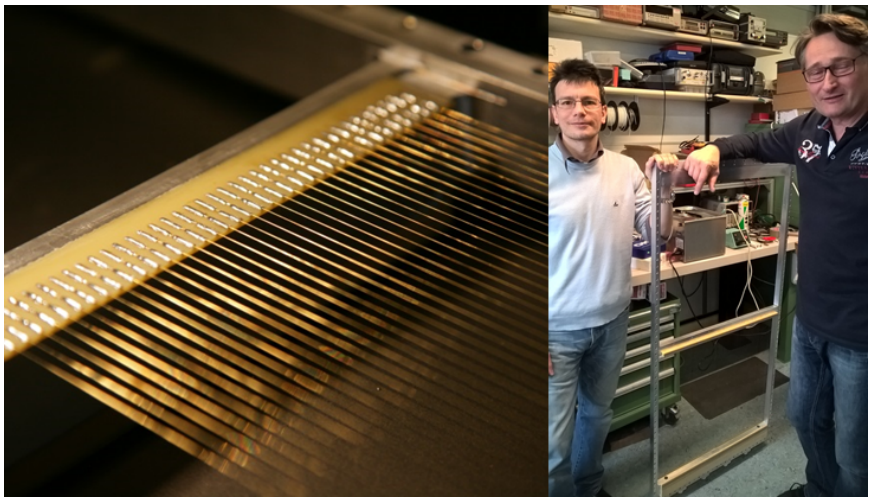

FIGURE 7.16: Left: Zoom on wires being soldered on a wire plain; Right: A finished wireframe in our lab.

To ensure electrical insulation epoxy glue was put over the soldering (Fig.7.17).

[5]https://www.swagelok.com/

FIGURE 7.17: Working with the wire frame inside cleanroom to the lab;

Integration of the new frames in the existing RICH-1 system imposed hard constrains on the frames geometry and in the clearance between the frame borders and the electrodes (wires, detector components, services etc.). Due to the large negative operating voltage of the drift electrode and the photo-cathode, a sufficiently large distance to the metallic frames would be needed to avoid excessive field values. This was the case for the prototypes tested in INFN lab and in test beam exercises. For the final PDs this distance could not be accepted because it translates into dead areas.

The need of introducing two field shaping electrodes in front of drift wires and photo-cathodes respectively was demonstrated by field calculations using COMSOL, as shown in Fig.7.18 and Fig.7.19: without these electrodes, the field values at the guard wires and at the photo-cathode border are too large. The border effects can be reduced and also the distortion of the electric field (large horizontal components) can be suppressed with properly biasing the field shaping electrodes (Fig.7.20).

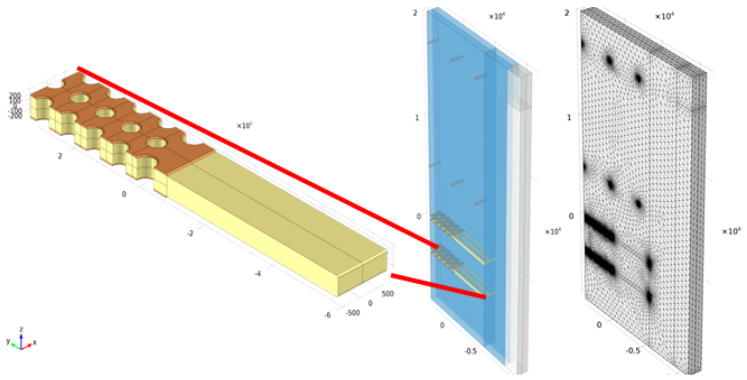

FIGURE 7.18: The unit cell for the field calculation for the effect of the electrodes near the border of the frame

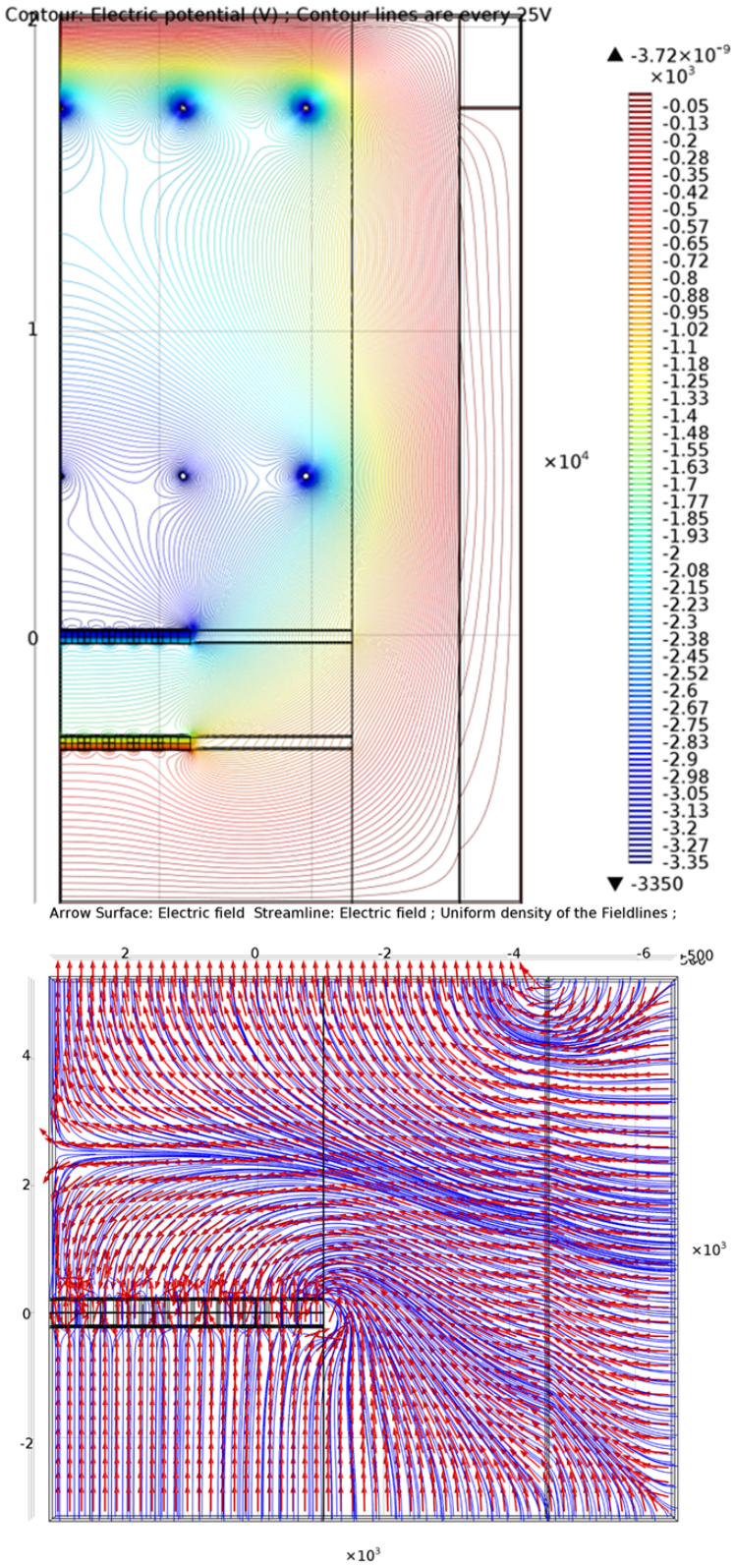

FIGURE 7.19: Top: Electrical potential contour lines for the chamber border region without the field shaping electrodes; Bottom: Calculated electric field stream lines for the THGEM border region without the field shaping electrodes.

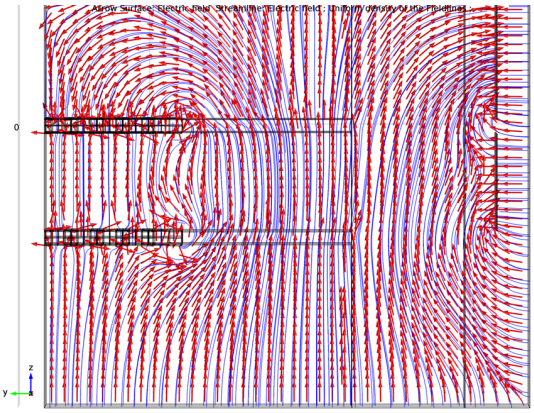

FIGURE 7.20: Calculated Electric field stream lines for the THGEM border region with the field shaping electrodes at suited potential.

7.3.2 Micromegas and Hybrid frames.

The hybrid frame (Fig.7.21) hosts the MM and provides the precision positioning for insertion of the front-end cards via a series of grooves. Due to the special requirements of its mechanical drawing, the hybrid frame was produced by electro-erosion techniques at CINEL. An isolating frame which had been machined from an 11 mm thick tufnol plate was glued to the hybrid frame. After a pre-machining, needed to prepare it for the precise gluing on to the hybrid frame (Fig.7.22). The combined structure was then re-machined to assure planarity of the MM and to guarantee the 4 mm insulator thickness between the anode PCB and the aluminum frame, which reduced the parasitic capacitance coupling between the frame and the readout pads.

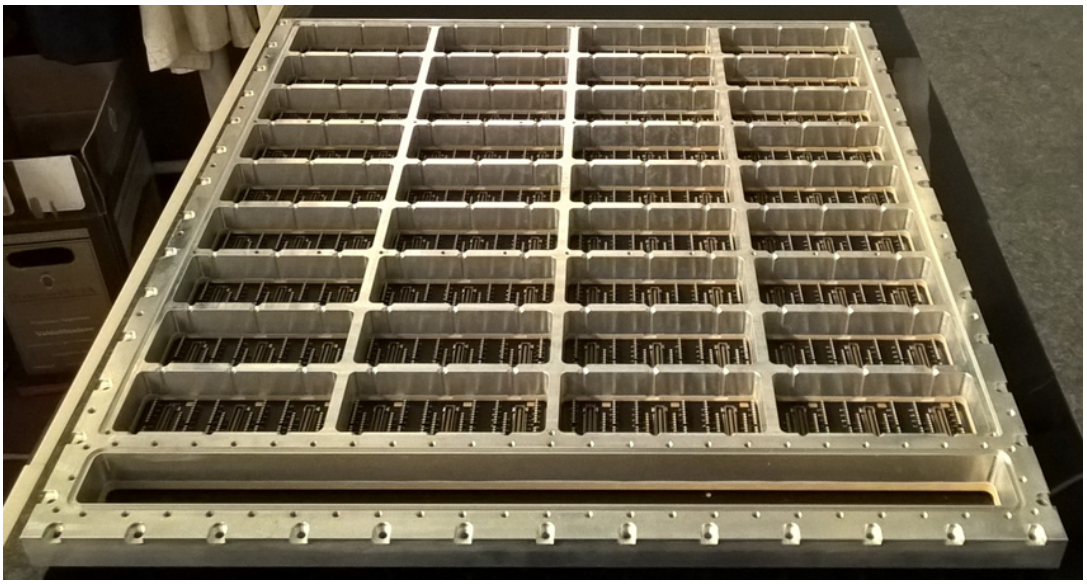

FIGURE 7.21: HybridFrameOnly

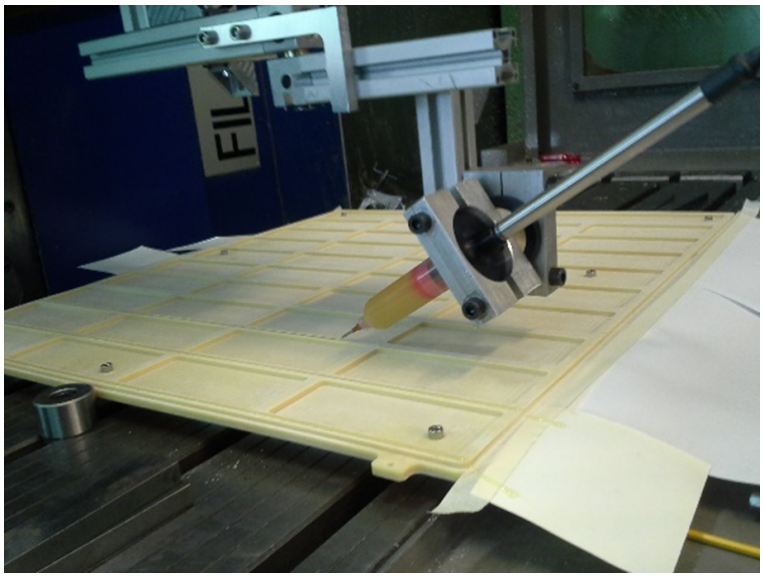

FIGURE 7.22: Depositing glue on the insulator frame with a special volumetric dispenser

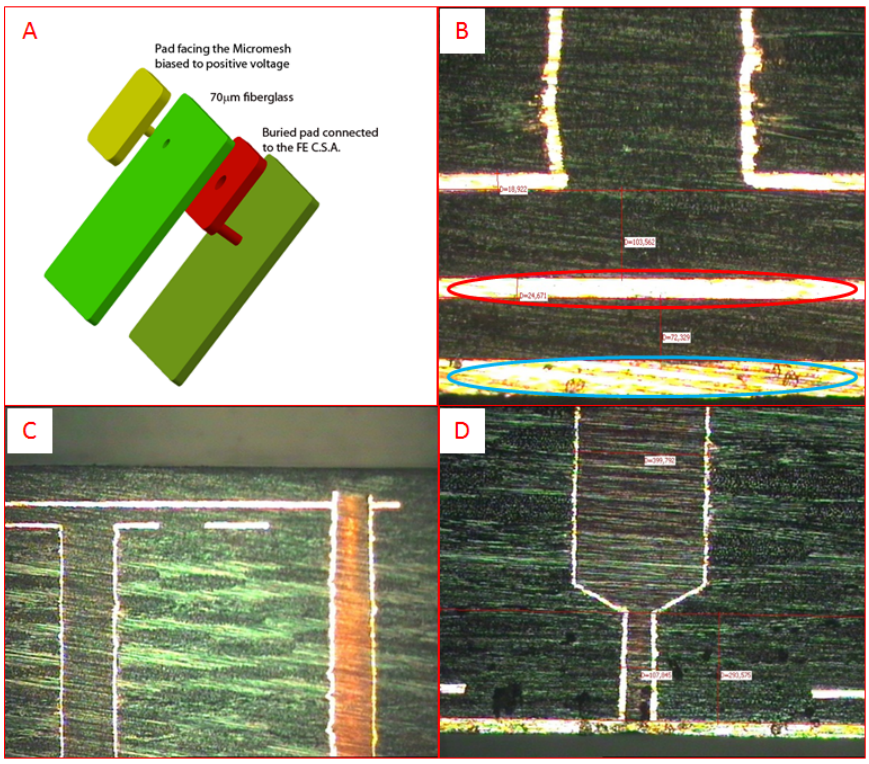

FIGURE 7.23: A. Sketch of the capacitive coupled readout pad. The biasing voltage is distributed via independent 470 $M\Omega$ resistor to the pad facing the micromesh structure. The buried pad is isolated via 70 μm thick fiberglass and connected to the front end chip (schematic is described in Chapter-5 in Fig.5.22) B. Metallographic section of the PCB: blue circle shows the quality of the anodic pads where as the red circle shows the quality of the R/O pad; C and D. Metallographic section of the PCB: the detail of the through-via contacting the external pad via the hole of the buried pad.

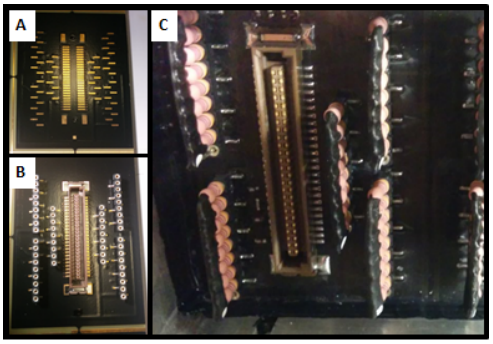

FIGURE 7.24: A. Soldering pads for a set of 48 anodic pads; B. Connectors soldered; C. After mounting of the resistive arrays.

The final MicroMegas PCBs were produced by an industrial company: TVR Srl (Vicenza, Italy) based on the capacitive/resistive concept described in Chapter-5. The distance between the anodic pd and the buried readout pad is 70 μm. Special attention was paid on obtaining a very flat surface for the anodic pad via connections (as shown in Fig.7.23). PCBs were tested for all $\sim$2380 pads: the electrical continuity and the pad capacitance (38-42 pF/pad) were measured. After the PCBs were transported to CERN and the MMs were produced over them using the bulk technology. The final bulk MicroMegas have a square array of 300 μm diameter pillars with a pitch of 2 mm, which keep the micromesh (18 μm woven stainless steel wires, 63 μm pitch) at 128 μm distance from the anodic plane. The $7.5 \times 7.5\ mm^2$ anodic pads are biased at positive voltage and face the grounded micromesh. Each MicroMegas module hosts a set of 24 insulated pads, which are 6 mm wide and 192 μm thick (see Fig.7.28), where PEEK[6] pillars are glued and used as fixation points to guarantee the correct planar positioning of the THGEMs. 108 Robinson Nugent connectors (50pins, 48 pads are connected to each of them) and 648 9-pin connectors for HV resistor arrays were mounted on the back side of the MicroMegas PCB (see Fig.7.24). The external parts of the MicroMegas contain a border ring which is replacing a line of border pads in the MWPC configuration. The channels corresponding to missing pads are terminated with SMD capacitors. All connectors and capacitors were manually soldered at the CERN PCB workshop. Each anodic pad is powered through an individual resistor and the signal, induced on the buried pad (fig 7.23 a),b)), is read out by the Front End APV 25 chip[151].

The MicroMegas PCBs equipped with connectors and capacitors were transported back to Trieste and glued to the hybrid frame with tufnol spacer. The gluing of the PCBs to the modified hybrid frame was very challenging. Distributing the exact amount of glue in the right place with the right pattern could be achieved by using a CNC machine to follow the geometric pattern and an automatic volumetric dispensing machine to ensure the right and equal amount of glue after synchronizing the dispenser speed with the CNC machine speed (Fig.7.25). The glue was put over the back side of the MicroMegas PCB and two MicroMegas were glued side by side, on the same Hybrid frame immediately one after another to avoid surface misalignment due to the different polymerization time of the glue (Fig.7.26).

[6]PEEK: Polyether ether ketone

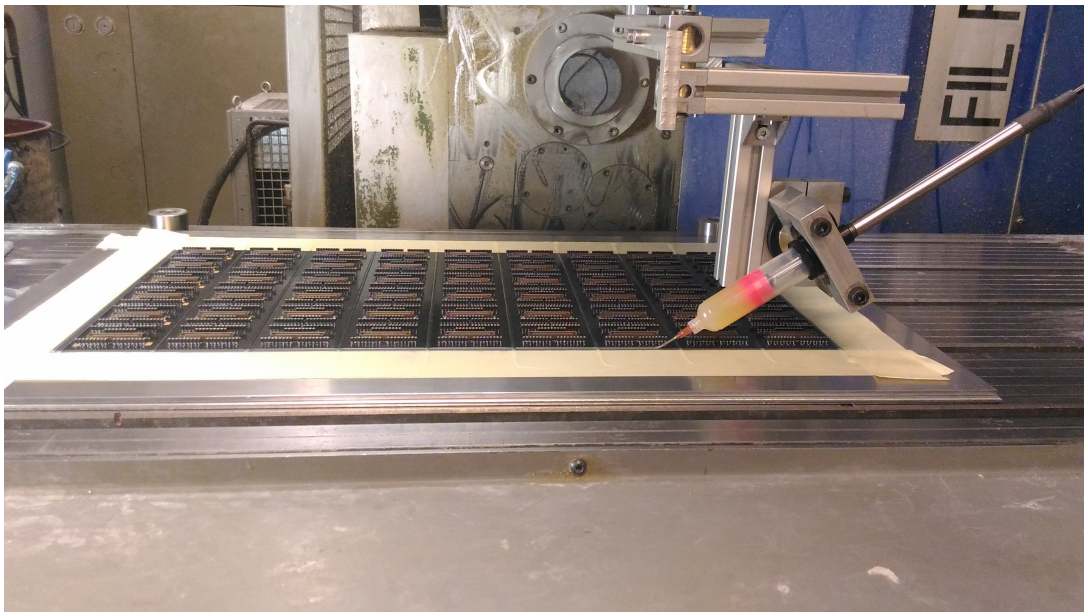

FIGURE 7.25: Putting glue to the Micromegas PCB with special machine;

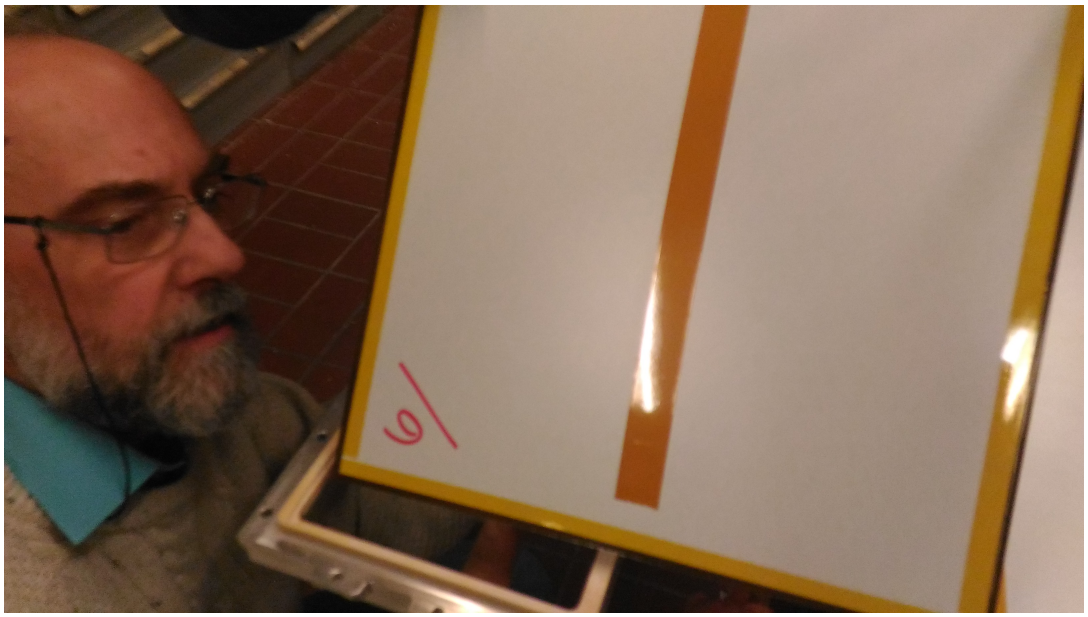

FIGURE 7.26: Attaching the PCB to the mechanical frame;

To ensure the common planarity of the two MicroMegas and the gas tightness of the detector the hybrid frame with the newly glued micromegas was put over a reference marble top table and was pressed by $\sim$ 90 kg weight (Fig.7.27).

FIGURE 7.27: Application of pressure to ensure better gluing.

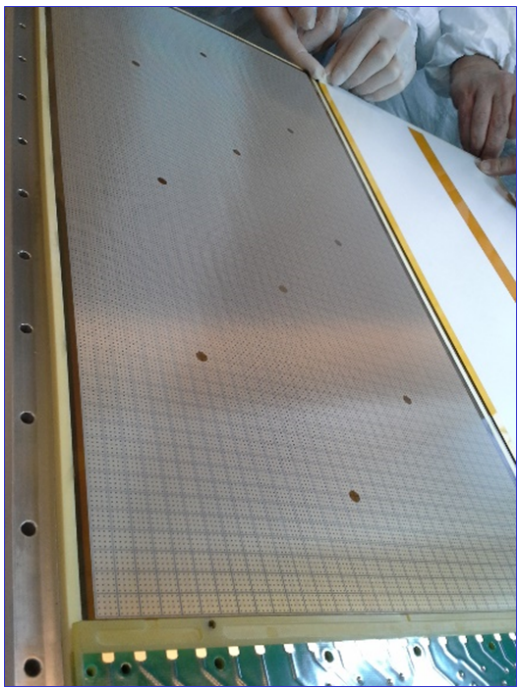

FIGURE 7.28: Stripping of the MicroMegas cover

From the time of production, during all the operations described above, the MicroMegas was protected with a special laminated cover. To proceed with the equipping of the MicroMegas, the removal of the cover (Fig.7.28) and all following operations were performed inside a clean area.

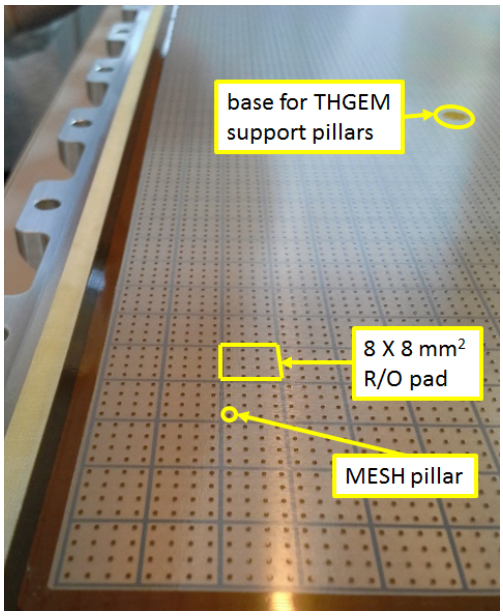

FIGURE 7.29: The structure of the micromegas

In Fig.7.29 one can see 8×8 mm^2 readout pads, Mesh pillars of 0.3 mm diameter and base, for attaching PEEK pillars, of 6 mm diameter, just after removing the cover. To provide a strong micro-mesh grounding, a large surface of the micro-mesh (5×263 mm^2), situated on one side, out of the detector active area was embedded in silver loaded epoxy adhesive. The PCB which distributes the HV to the THGEMs is then screwed and glued on the mesh grounding side of the MicroMegas.

The 48 pillars, to assure THGEM planarity (as mentioned already in Chapter-5), are M3.8 screws made of PEEK. The operation of gluing them over the MM bases is delicate: each pillar has to be very precisely positioned with the right amount of epoxy glue on it, also the pressure to be applied during the epoxy polymerization needs to be well calibrated.

FIGURE 7.30: Mounting of PEEK pillars to the special frame

To overcome these challenges, a special plexiglas frame was designed (Fig.7.30), where the PEEK screws (pillars) are mounted with short metallic springs (taken from ball-point-pens). The frame can be positioned very precisely over the hybrid frame.

The perpendicularity of the pillars is guaranteed as well as the correct pressure provided by the springs (Fig.7.31). A special dispenser provides a calibrated drop of epoxy glue on each screw head and the plexiglas frame with the 48 screws is then positioned over the hybrid-frame and pressed towards it to attach the pillars to the meshes. The curing of the epoxy glue takes ∼24 hours and after the delicate removal of the plexiglas frame the MicroMegas are ready. The fully equipped hybrid-frame with the pillars and the HV distribution PCB is shown in Fig.7.32.

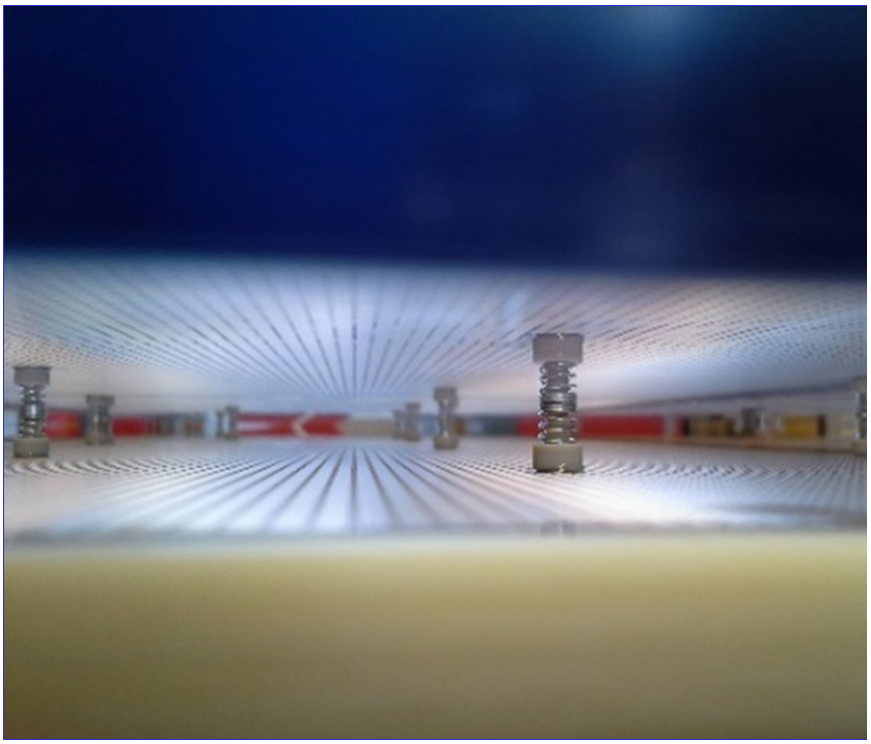

FIGURE 7.31: Spring to assure flexibility while pressing

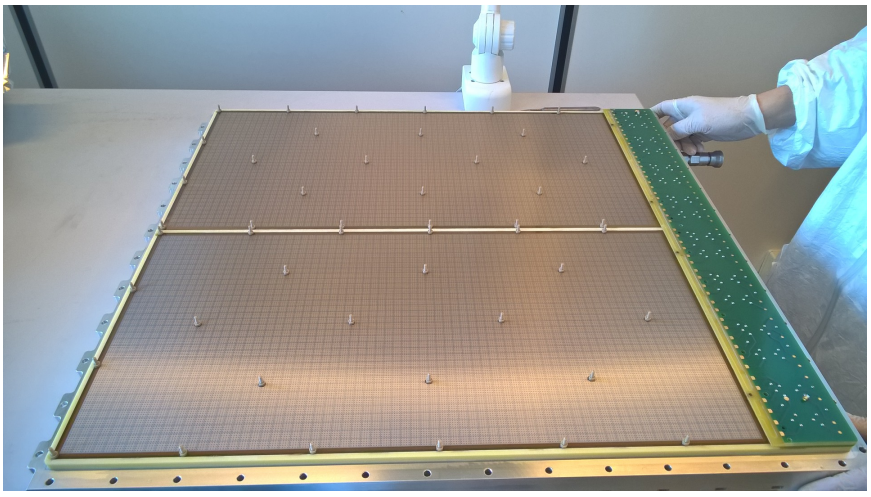

FIGURE 7.32: Glueing of PEEK pillars over the MESH;

A first assembling to test two MicroMegas was performed in the clean-room. A spare quartz frame was used to close the chamber to check the gas tightness and the electrical stability. The wire frame and the spacer frame were mounted over the

quartz frame and the fully equipped hybrid frame was installed on this preliminary assembling. The part of the MAPMTs with lens systems was closed by a special cover plate and transported to the lab as shown in Fig.7.33.

FIGURE 7.33: Bringing back the assembled Deetctor (MM only) from the cleanroom to the lab;

FIGURE 7.34: The Micromegas PCB (back view) after attaching the resistances;

In the lab, the tufnol part was painted with black glue to assure light tightness of the PD (essential for MAPMTs operation). Also the anodic HV connections, grounding and the resistive arrays for providing HV to the pads were provided. The mounted resistor arrays shown in Fig.7.34 are 1MΩ temporary ones, since the final 470 MΩ

arrays suffered delayed delivery and only arrived after the test of the first two MicroMegas.

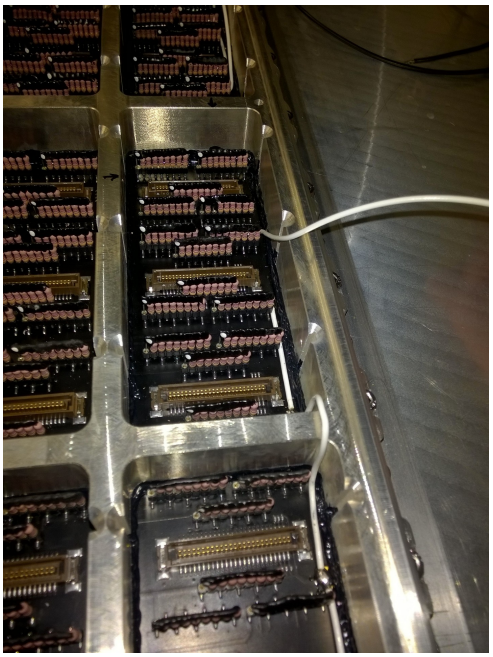

FIGURE 7.35: Particular of the hybrid frame equipped with final resistors and the black epoxy glue

One tedious but important work was to later mount all the final resistor arrays on the anodic PCB (Fig.7.35). The arrays were fragile and putting 9 consecutive misaligned pins of an array in their corresponding aligned sockets was challenging.

To test the MicroMegas response with an ^{55}Fe X-Ray source, a spare quartz frame without fused silica windows was equipped with a kapton foil and replaced the quartz window frame (Fig.7.36 and Fig.7.37).

In the gas tightness test a surprising leak was found from one of the blind holes of the hybrid-frame. After fixing it the desired gas tightness for explosive gas mixtures was achieved. The test of the electrical isolation of the anodic pads towards the mesh and towards the readout pads was then performed. For all 8 MicroMegas used for RICH-1 upgrade, only 3 pads were found short-circuited towards the mesh and 2 pads were connected to their corresponding readout pads with ~ 1 GΩ resistance out of a total of 19040 pads.

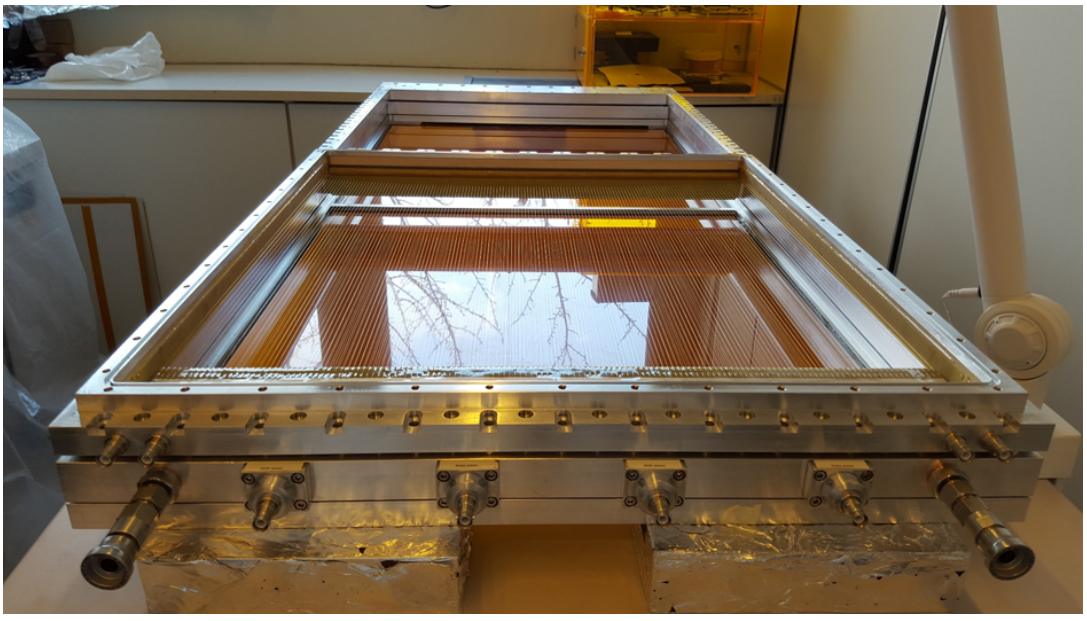

FIGURE 7.36: Assembled wire frame inside the clean room

FIGURE 7.37: The assembled detector in our Trieste lab; ready to be tested

The test with the ^{55}Fe was performed and the first spectra obtained with an effective gain of ∼1800 was observed (Fig.7.38). Due to the lack of time for transporting the chamber to CERN for further operations, only a rough measurement of the effective gain uniformity was performed: it was found to be ∼5% (Fig.7.39).

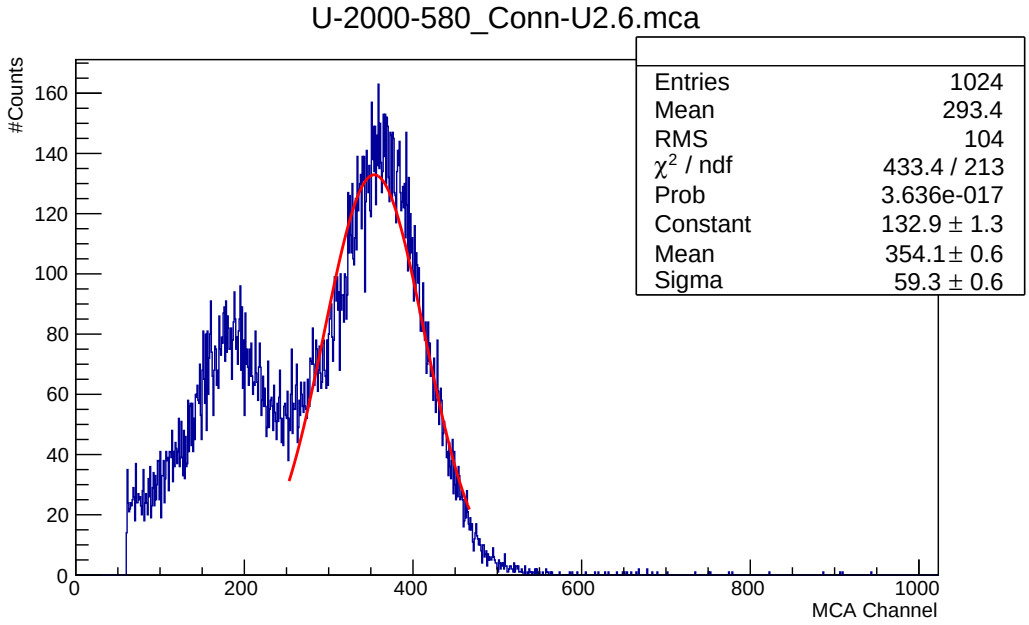

FIGURE 7.38: First amplitude spectra taken at lab; by fitting the main peak with a Gaussian and assuming that the process started with 220 e^-s the calculated effective gain came to be $\sim$ 1835.08 (using measured calibration factor for converting ADC channels to fC).

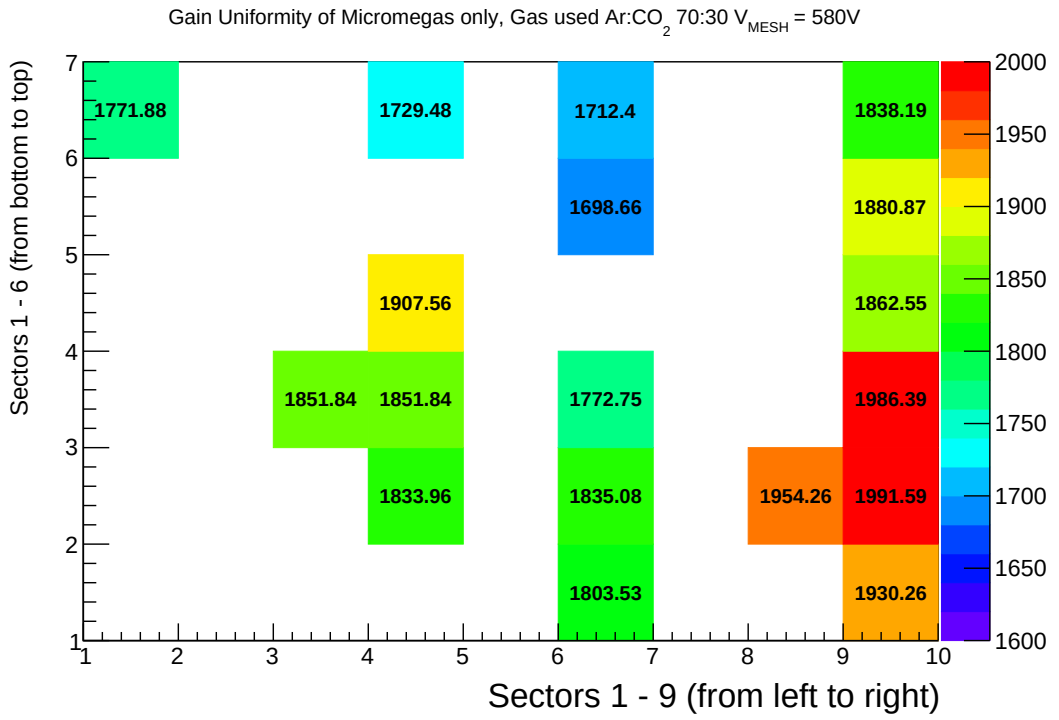

FIGURE 7.39: Gain Uniformity of one of the Micromegas only obtained in INFN Trieste Lab.

7.3.3 CsI coating and PD assembling

Deposition of the solid photo-converter (CsI) to produce new hybrid photo-cathodes was done at the CERN Thin film Laboratory by Thomas Schneider and Miranda Van Stenis, after transporting validated THGEM pieces to CERN inside the special transport box (described in Section-6.1.4) and Ni-Au coating at CERN.

The reason to coat the Cu-clad PCB with Ni-Au is dictated by the fact that CsI directly deposited over Cu shows a significantly reduced Quantum Efficiency. The detailed recipe is a result of the long RD26 R&D, which showed that Au is a good substrate for high QE of a CsI photo-cathode. Depositing Au directly over the Cu surface was not a solution: depositing a thin layer of Au ($\sim$ 0.5-1 μm) over the substrate will produce diffusion of the Cu molecules into the Au layer during the thermal treatment of the CsI photo-cathode after evaporation. Deposition of a thicker layer of Au ($\sim$ 8-10 μm) over the Cu surface was not affordable due to the higher cost of Au. Using a Ni layer of few μm (typically 7 μm) as a barrier between the Cu layer and a thin Au layer ($\sim$ 0.1-0.5 μm), is the standard solution to this problem.

The thermal treatment which needs to be applied to the photo-cathode could also produce diffusion of Cu atoms through the Ni layer to the Au layer and reduce significantly the QE if the temperature is too high. To avoid this, the thermal treatment is done at $\leq$ 60 ^{0}C for 8 h. Before evaporation of the CsI a cleaning of any foreign particles on the Au surface is needed.

The preparation of the photo-cathodes for the new hybrid PDs was done with the procedure described below, adopted accordingly to the new constrains imposed by the THGEM (THGEM surface contains holes whereas MWPC photo-cathodes were pad plains).

The Ni-Au coating of the Cu-clad PCB of THGEMs was done at CERN chemical lab situated at CERN chemical Laboratory.

1. Cleaning the copper with soap (alu7040)
2. Dip the THGEM in hydrochloric acid for 30 seconds.
3. Cleaning with DI Water
4. Dip the THGEM in Palladium (catalyst) for 1 mn
5. Cleaning with DI Water
6. Dip the THGEM in Nickel for 15 mn (a depositing about 5 microns)
7. Cleaning with DI Water
8. Dip the THGEM in Gold for 10 mn (a depositing about 0.1 microns)
9. Cleaning with DI Water
10. Cleaning with DI Water with High presser Water (karcher)

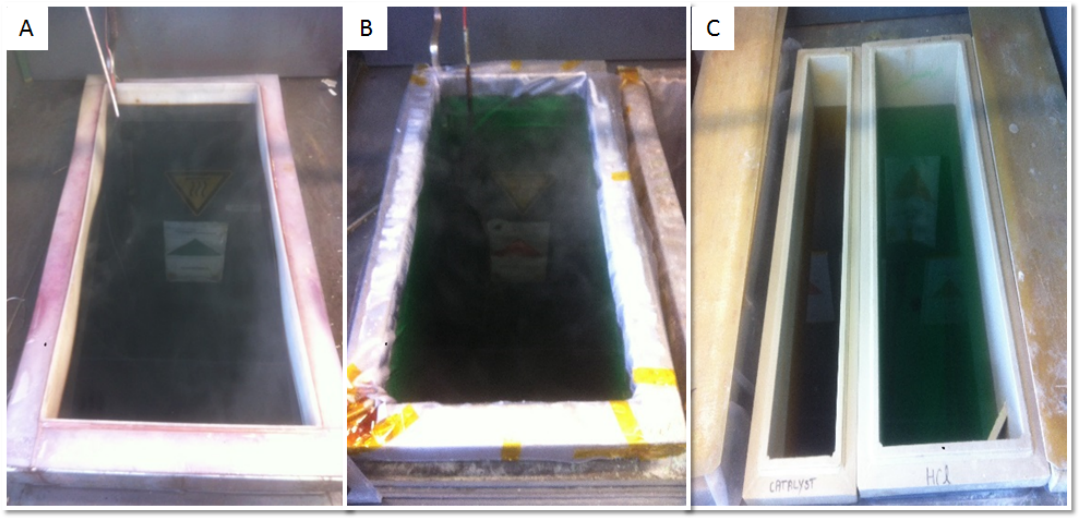

FIGURE 7.40: A. Gold (Au) bath; B. Nickel (Ni) bath; C. On the left Palladium (Catalyst) bath and on the right hydrochloric acid (HCL) bath.

The different steps performed during the procedure are shown in Fig.7.40. Some of the Au-coated THGEMs were transported to Trieste for a final validation and a few indeed failed this validation despite the good performance before the Ni-Au coating. All CsI coated THGEMs were later tested to stand nominal voltage, inside their storage box.

The solid reflective photo-cathode production procedure [71] [153] to achieve high QE, developed by RD-26 collaboration at CERN consists of:

- Proper substrate preparation: coating a Cu-clad PCB with 7μm Ni and 0.5 μm Au.
- Cleaning of the prepared substrate in ultra-sonic bath.
- Drying of the substrate in an oven (12h at 50 ^{0}C) to take out all the moisture present on the substrate (out gassing).

- Installation of the substrate inside the evaporation plant together with the gas tight chamber.
- Evacuation of the evaporation plant for about two days to assure $\sim 10^{-7}$ hPa.
- A slow deposition ($\sim$ 1 nm.s^{-1}) of a 300 nm thick CsI layer by thermal evaporation.
- A thermal treatment (8 h at 60 ^{0}C) to optimize the CsI photo-cathode response.
- Measurement of CsI response at 60 and 20 degrees.
- Extraction of the photo-cathode after closing the gas tight chamber (with 1 bar Ar).
- Flushing during transport, storage and handling with low-contamination gas.

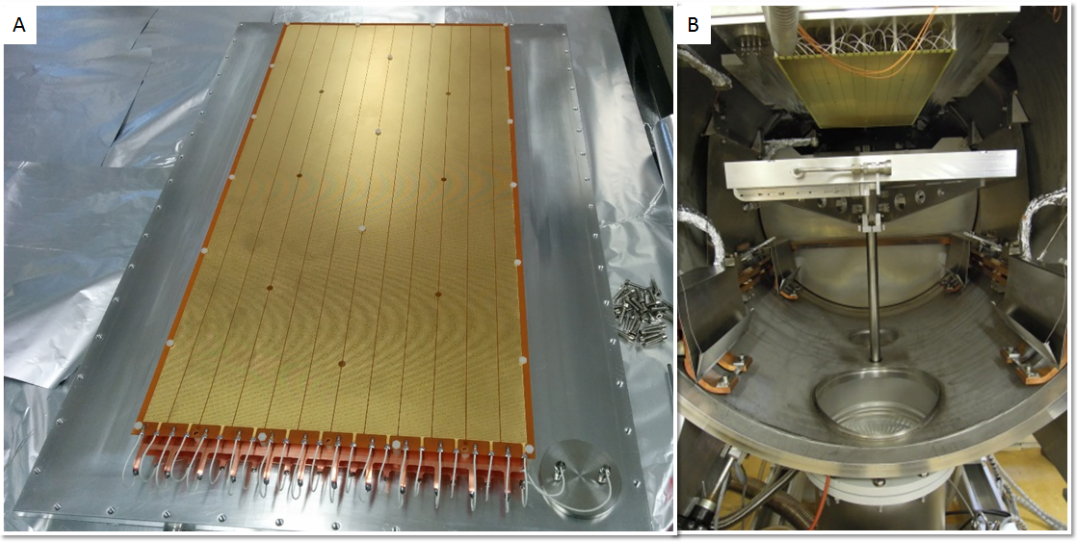

FIGURE 7.41: A. THGEM is mounted on the special frame ready to be coated with CsI. On the bottom right corner of the picture one can see two 'feed-through's for the wires. B. The special frame with THGEM mounted on it (Top) and the cover over the piston (bottom) inside the CsI evaporation plant.

After the Ni-Au coating, the THGEM was brought to the CsI lab where it was mounted on a special frame designed and produced at the INFN Trieste mechanical workshop. The frame has 24 pillars to assure the THGEM planerity while depositing CsI. A special Cu piece was used to apply HV bias to the sectors where the wires for TOP and Bottom of the THGEM were coming out through a special feed-through (see Fig.7.41) containing two lines one for the Top electrodes and the other for the bottom electrodes: this allowed biasing of the THGEM for further tests inside the CsI gas tight box. The CsI coating was performed inside the evaporation plant (Fig.7.42) according to the procedure described above.

The estimation of the quantum efficiency of the CsI photo-cathode was performed inside the evaporation plant by mapping the local CsI photo-cathode response. The measurement was performed using a D_2 UV light source and biasing the photocathode and the PMT accordingly. A scan of the photocurrents from the photo cathode and from the PMT was performed over the whole CsI photocathde surface. In

Fig.7.43 the setup used for the mapping of the local CsI photo-cathode response is shown.

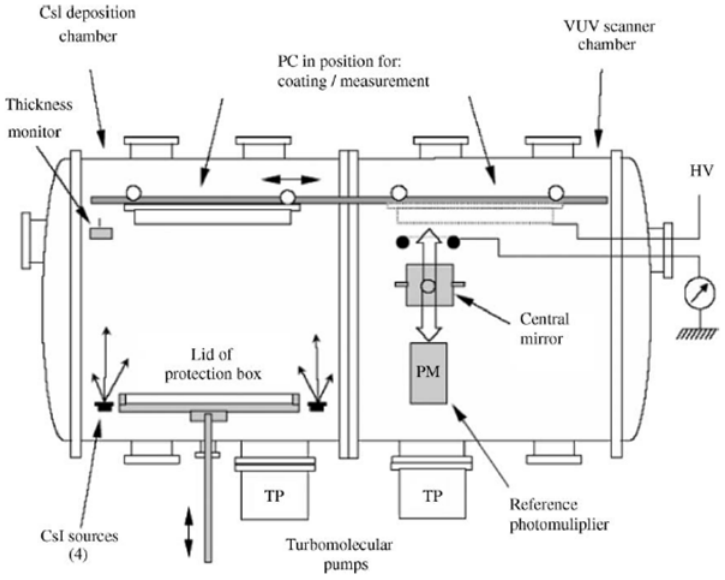

FIGURE 7.42: Layout of the CsI production chamber. Left: CsI evaporation side; Right: photo-current measurement side.

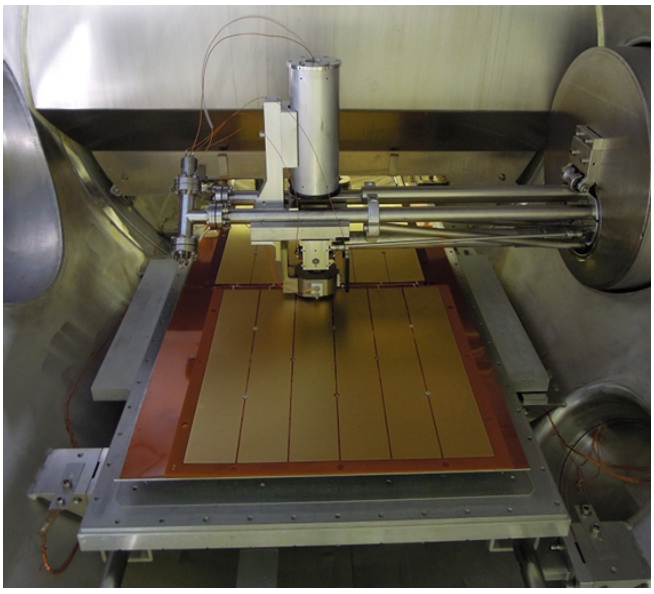

FIGURE 7.43: The setup to measure quantun efficiency of the CsI coated THGEMs.

The quantity $I_{Normalized}$, defined as in the Eqn.7.3, is used for the estimation of the local quantum efficiency of the CsI photo-cathode. It is the ratio of the locally measured photocurrents, of the CsI photo-cathode and of the PMT, corrected by subtracting the corresponding noise (which is measured in each step of the measurements).

$$I_{Normalized} = \frac{I_{CsI} - I_{CsI_{Noise}}}{I_{Ref} - I_{Ref_{Noise}}} \tag{7.3}$$

Where

- I_{CsI} is the measured photo-current from the CsI photo-cathode.
- $I_{CsI_{noise}}$ is the measured noise in measured current for I_{CsI}.
- I_{Ref} is the measured current in the reference PMT.
- $I_{Ref_{noise}}$ is the measured noise in the I_{Ref}.

TABLE 7.1: Details of evaporation performed for CsI coating of the COMPASS THGEM photo-cathodes on the year 2015-2016

THGEM No.	Evaporation date	at 60^0C	at 25^0C
THGEM 319	18-01-2016	2.36	2.44
THGEM 307	25-01-2016	2.65	2.47
THGEM 407	02-02-2016	2.14	2.47
THGEM 418	08-02-2016	2.79	2.98
THGEM 410	15-02-2016	2.86	3.14
THGEM 429	22-02-2016	2.75	2.74
THGEM 334	29-02-2016	2.77	3.00
THGEM 421 re-coating	10-03-2016	2.61	2.83

For the upgrade of COMPASS RICH-1, 8 photo-cathodes (shown in Table-7.1) were needed and 11 photo-cathodes were produced. The measurement of $I_{Normalized}$ was performed for each of them, with and without a fused silica quartz window in between the UV source and the photo-cathode. The use of the window allows to estimate the QE of the photopcathodes in the photon wavelength range similar to the real experiment like situation. In Fig.7.44 and Fig.7.45 the results of the measured $I_{Normalized}$ for THGEM photocahode #421 with and without the quartz window are shown.

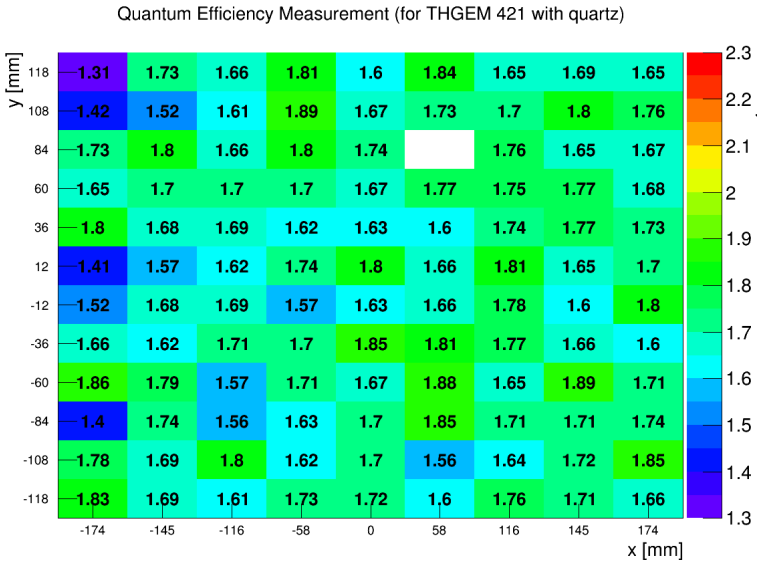

FIGURE 7.44: QE with Quartz window

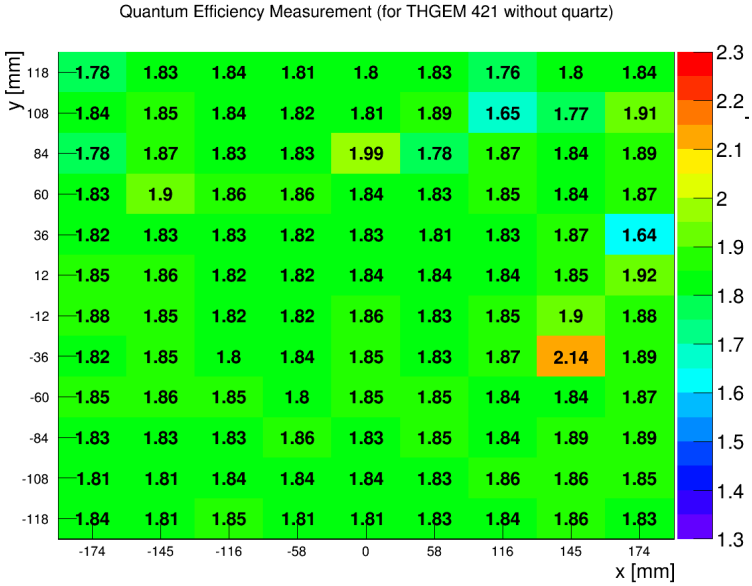

FIGURE 7.45: QE without Quartz window

A reference substrate, know to have good QE, was measured in the same condition to provide an approximate indication of the absolute QE. A "Quantum Efficiency" of $\sim 0.7 \div 1 \times (QE_{Max_{CsI}})$ was observed w.r.t. the reference substrate, which is fully compatible with the expectation since the THGEM has a 23% optical transparency. A slight increasing trend in QE had also been noticed during the production.

7.4 Installation on RICH-1

7.4.1 Assembling the hybrid PDs

The pre-assembled hybrid detectors were transported to CERN and a dedicated clean area in Bd-887 in Prevessin was equipped to open and manipulate PDs. Each chamber has been opened to extract the hybrid-frame, which was transported to COMPASS RICH-1 lab in Bd-892-R-A04. There the hybrid frame was equipped with THGEMs to build the final Hybrid PD.

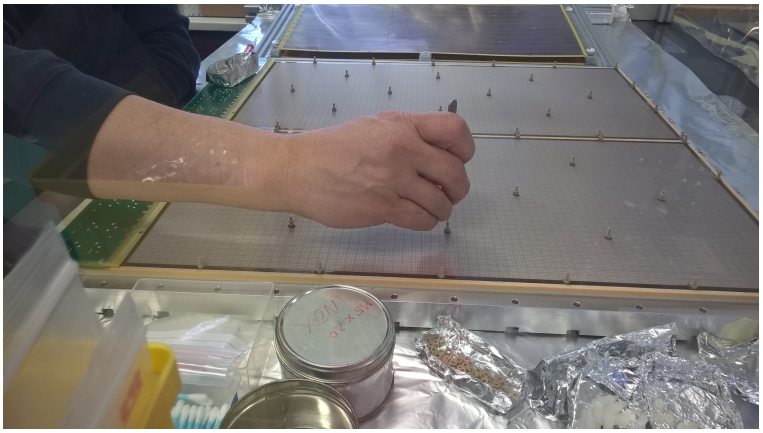

FIGURE 7.46: Putting the spacers before mounting of the THGEM-2

The mounting of THGEM-2 was performed in a dust free environment after putting on the pillars the PEEK spacers which provide the required 5 mm gap between the mesh and the THGEM-2 bottom (Fig.7.46). The electrical connection was provided by direct soldering of the THGEM-2 HV pads to the corresponding pads on the HV distribution PCB (Fig.7.47).

FIGURE 7.47: Mounting of THGEM-2 on the hybrid frame inside a dust free tent

A dedicated large glove-box was designed and built to perform the mounting of CsI coated photo-cathodes on to the hybrid detectors (Fig.7.48). The glove-box needs to accommodate the hybrid detector, a special cover made from a 30 mm thick aluminum plate to close the hybrid detector after the final assembly and two CsI coating

boxes with a photo-cathode inside each one. Also the required tools and soldering machines need to be put inside the glove box to perform the assembly operation.

FIGURE 7.48: The glove box inside the COMPASS RICH-1 lab at Bd-892-R-A04

The operation consists in flushing the glove-box with nitrogen until the inside environment reaches a level of 10 ppm oxygen contamination. The CsI-coating boxes are kept under constant flow inside the glove-box with independent lines. After reaching the desired oxygen contamination, the first CsI coating box is opened, The THGEM-1 is dismounted from the CsI coating box (Fig.7.49) and mounted on the hybrid detector. The same procedure is repeated for the second photo-cathode. After concluding the assembling operation the hybrid detector is closed with the special cover and a line used to flush the CsI coating box is connected to the hybrid detector to ensure no significant oxygen/moisture contamination ($\sim$10 ppm) inside.

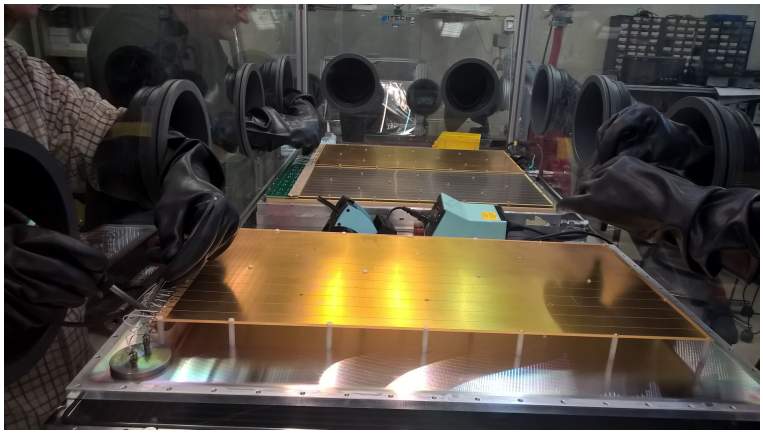

FIGURE 7.49: Soldering of the HV wires for the photo-cathode inside the glove box

The full operation of assembling hybrid PDs takes several hours. The fact that it is not possible to touch the CsI surface of the photo-cathodes, makes the operation very delicate and challenging. Special tools were used to safely perform the mounting of the nuts to fix the THGEM piece in place. For the same reason the wires which are providing the HV connection to the photo-cathode are pre- soldered on the THGEM-1 and the only soldering performed inside the glove box is the connection between

the wires and the HV distribution PCB. A direct soldering on the THGEM as performed for THGEM-2 could be too risky because if the soldering tip is too near to the CsI surface, the probability of spilling soldering Sn-drops over the photo-cathode is high (Fig.7.50).

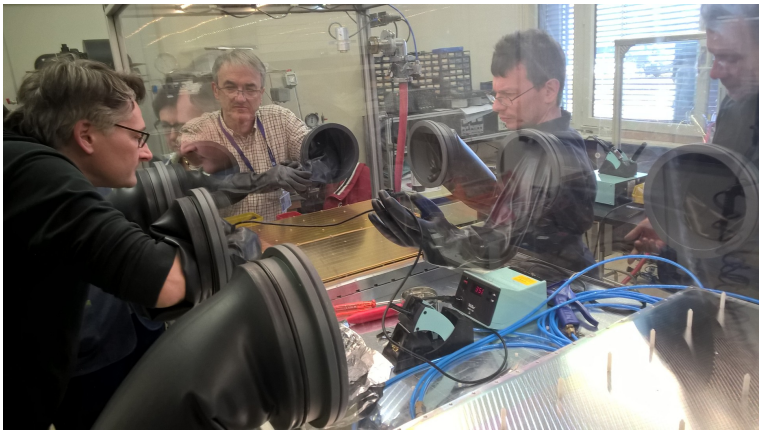

FIGURE 7.50: Soldering inside the glove box

7.4.2 Integration of MAPMTs and Hybrid PDs

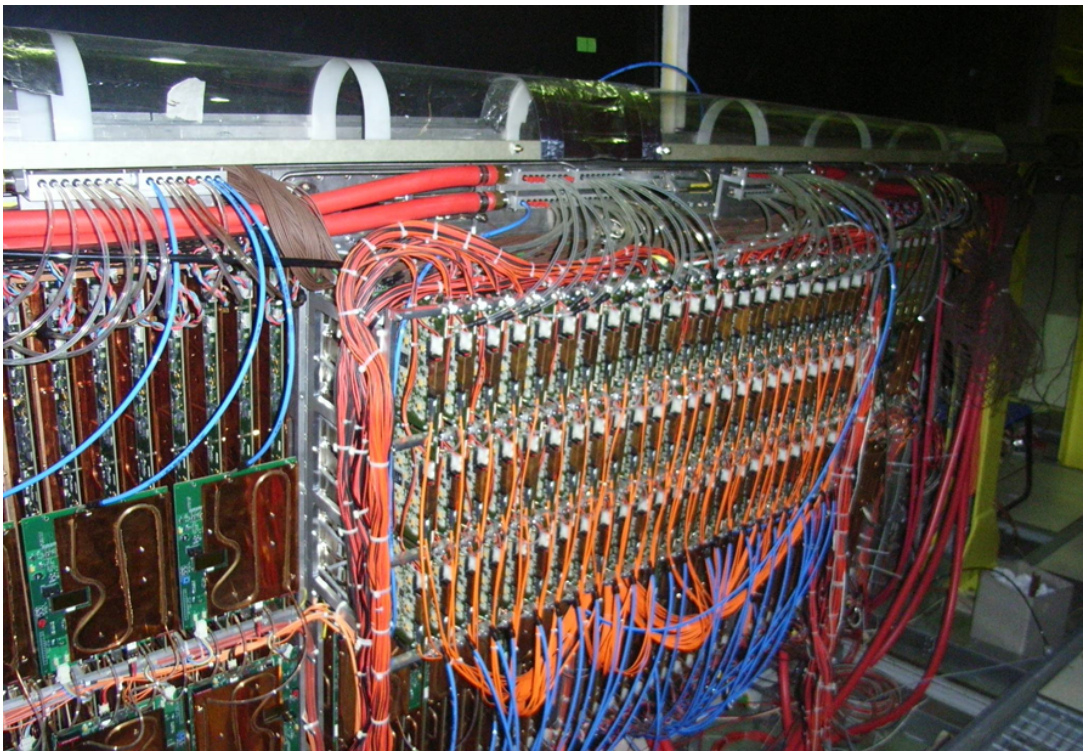

FIGURE 7.51: Old PDs with colling and FEE mounted

In parallel to the operation with the hybrid PD assembling, performed by one team, the operation of exchanging the old frames with the new ones was performed in Bd-887 clean area dedicated to COMPASS RICH-1 by another team after dismounting of the old PDs from COMPASS RICH-1.

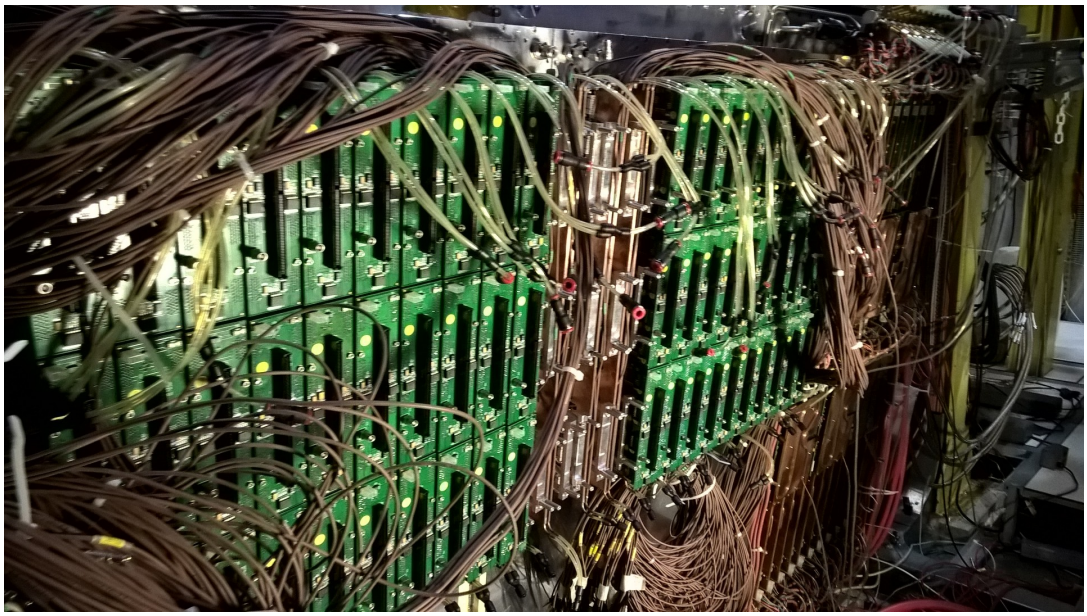

FIGURE 7.52: PDs to be dismounted after dismounting the cooling.

There were two options to take out the old PDs from RICH-1:

- Dismounting of an entire 4PDs holding frame (both for top and bottom PDs): this "standard operation" implies opening and contaminating the RICH vessel, requires a large amount of work (and man-power) and forces to face a risky and heavy disassembling and re-assembling.
- Dismounting a single PD keeping the quartz window in place: this requires complex operations never tried before but reduces the risks and the amount of work.

The latter option was chosen and all the services (Fig.7.51): readout optical fibers, water cooling pipes, Digital FEE, HV and LV cables, gas pipes have been disconnected. The analogue FEE, the MAPMTs with iron shielding and lens systems remained on the chamber (Fig.7.52) making its weight $\sim$ 400kg. Detaching the chamber from the RICH-1 vessel was risky as it has to be extracted perpendicularly from the quartz window which sits at an angle of 13 degrees w.r.t. the vertical reference.

After dismounting two chambers were put face to face on a special support in front of the RICH, craned out of the experimental hall and transported to the Bd-887 clean area. In Fig.7.53 the lenses of the MAPMT system can be seen as well as the shining rainbow effect from the 300 nm thick CsI layer of the old MWPC photo-cathode.

FIGURE 7.53: The old frame with MWPC with CsI photo-cathode (bottom part) and MAPMTs with fused silica lenses (top part), in CERN clean room facility

The operation of exchanging the MAPMT frames with lenses from the old frames to the new ones was performed with the help of a small crane inside the clean area: the old frames with MAPMT + lens system were laid horizontally over the marble top reference table. After taking out all the screws between the MAPMT frames and the old frames, they were craned up and hanged in the air (Fig.7.54). The old frames were exchanged with the new ones over the table, and then the MAPMT frames were inserted into the new frames and secured in place with screws (Fig.7.55). The whole operation was very delicate as the clearance between the border of the lens system

and the border of the frames is $\sim$ 0.5 mm, thus the operation had to be done with extreme care and took several hours.

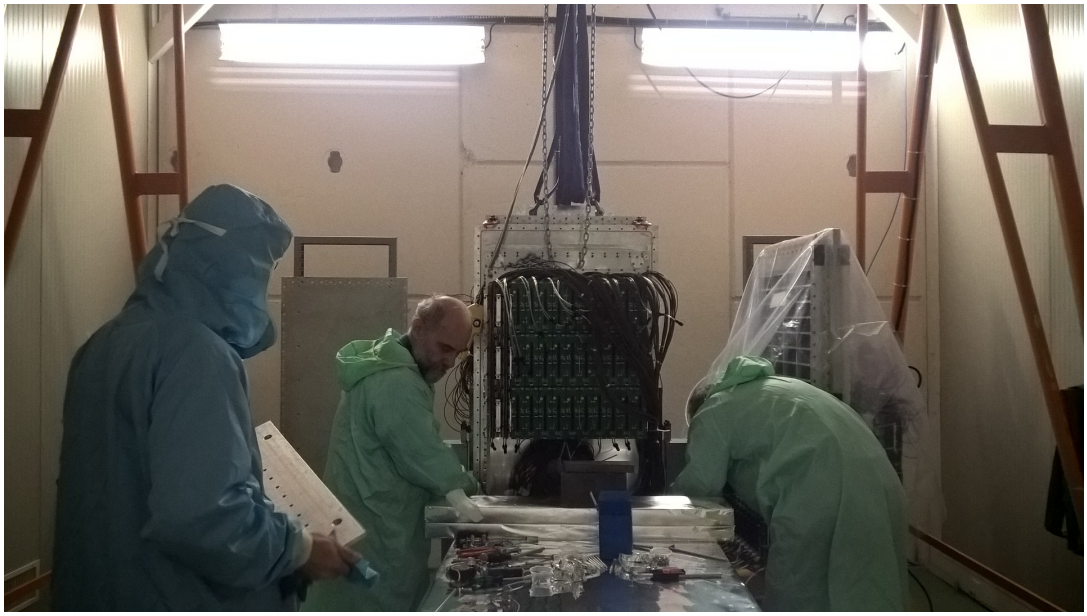

FIGURE 7.54: Preparing the MAPMT part for being dismounted from old frame.

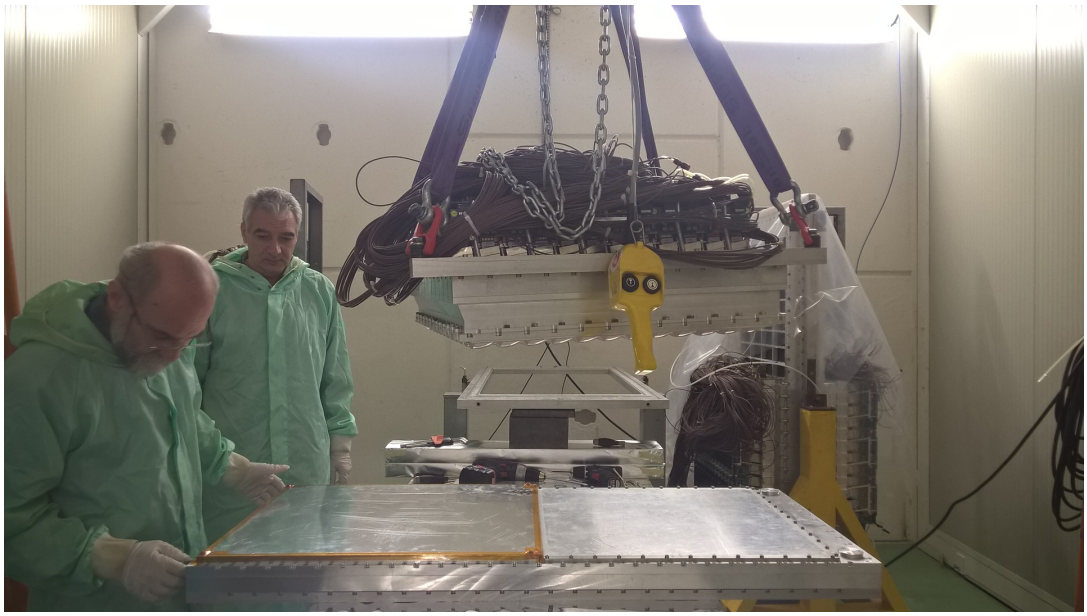

FIGURE 7.55: Mounting the MAPMTs with lenses to the new frame.

Two sets of new frames with MAPMT system were mounted on the special transport frame face to face. The empty portions of the new hybrid PDs were covered with aluminum closing plates. The transport frame with the two sets was then transported to Bd-888 to be mounted back to COMPASS RICH-1 (Fig.7.56).

FIGURE 7.56: Craning up the modified new frame with MAPMTs for trsnportation from the clean room to the area.

The quartz windows, which were exposed after removal of old PDs were protected with an aluminum plate (Fig.7.57-A and Fig.7.57-B) to prevent dust deposition and the risk of breaking. Before re-mounting the new frames with the MAPMT system, the protection was removed at the very last moment. A small support frame was designed and built (Fig.7.57C) to hold the heavy frames in a correct position during the mounting operation, which was risky and delicate due to the need to approach the windows, keeping the frames parallel to the quartz window (at a 13 degree angle w.r.t. the vertical). The small support frame was put in place in front of the corresponding quartz window. Then the Special transport frame with two PDs was craned down in front of the RICH-1. One by one the new frames with MAPMTs

were dismounted from the transport frame, craned up, and mounted on the RICH by resting them over the support frame (Fig.7.57D, E and F).

FIGURE 7.57: A: Fused SI Windows on COMPASS RICH-1 with protection cover. B: Fused Si windows after removing the protection. C: Special custom build support for mounting back PD frames with MAPMT system (marked with red circle). D, E and F: craning down of the PD frames with MAPMT system (D) and mounting on the RICH-1 (E and F)

7.4.3 Installation of the new PDs on COMPASS RICH-1

The newly assembled hybrid PDs with CsI photo-cathodes, closed by special cover and under continuous gas flow (to avoid moisture contamination), were transported to Bd-888 with special care. To provide an O_2 and moisture free environment (required for CsI), a big glove-box was mounted in front of the RICH-1 PDs. In Fig.7.58-A, the operation of craning down the big glove-box in front of RICH-1 is shown. In Fig.7.58-B the already mounted glove-box can be seen. The closed hybrid PDs with independent gas flow along with the required tools for the mounting operation, were placed and secured in position inside the big glove box before mounting it on the RICH-1. The operation was performed for both lower and upper PDs separately: for the lower PDs a difficult was to position and keep the viton o-ring inside the groove against gravity; for the upper PDs the operation was even more challenging than for the lower.

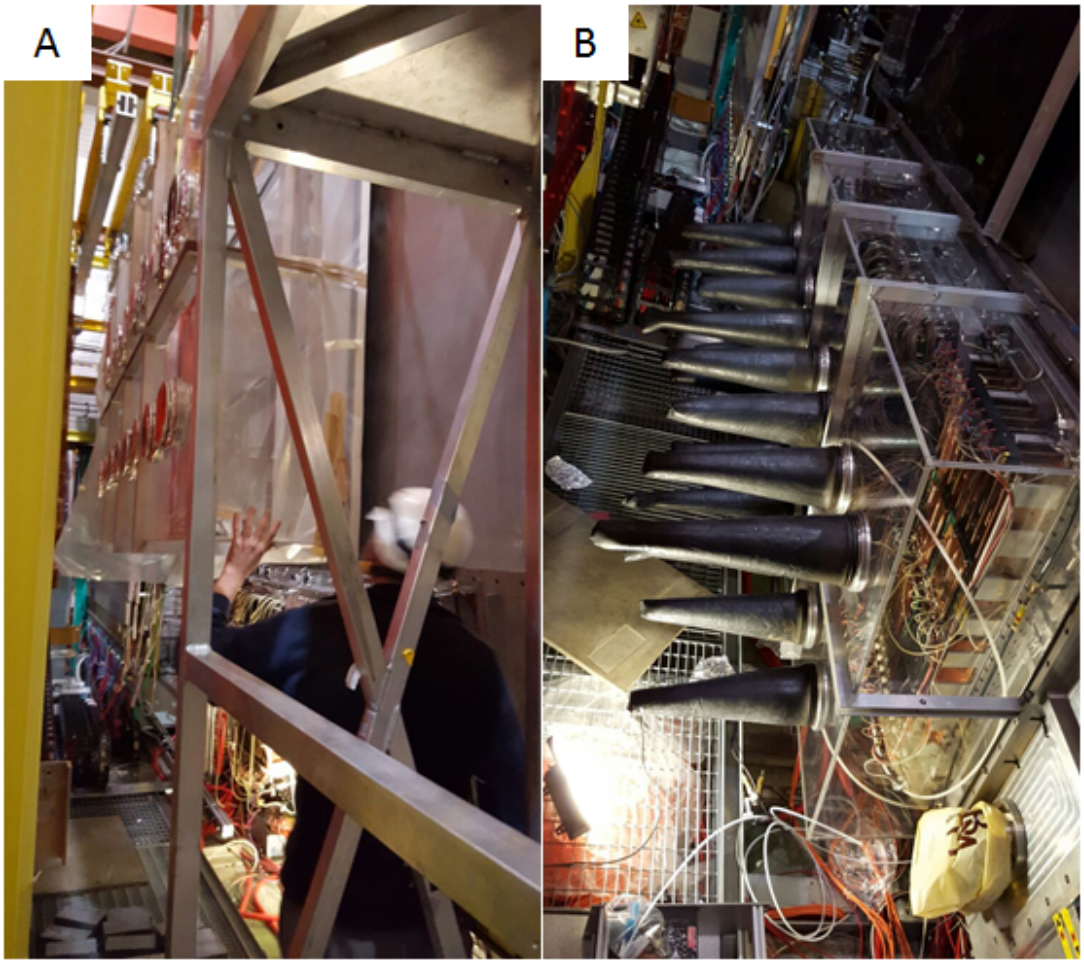

FIGURE 7.58: A: Craning Down the glove box to mount back the new hybrid PDs B: Glovebox in place flushed.

7.4.4 Equipping the new PDs

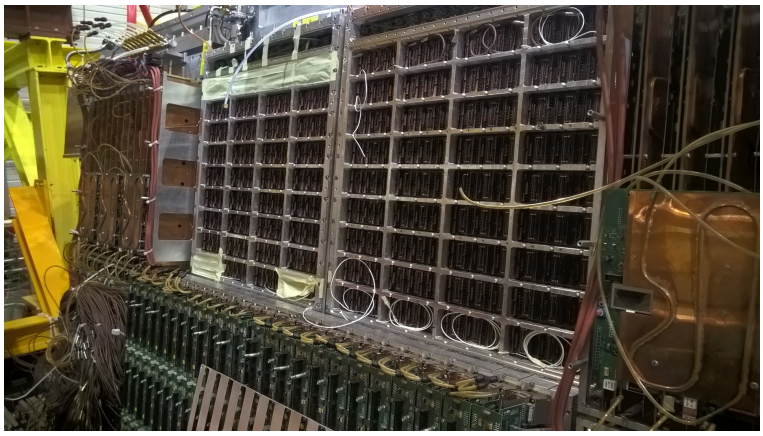

FIGURE 7.59

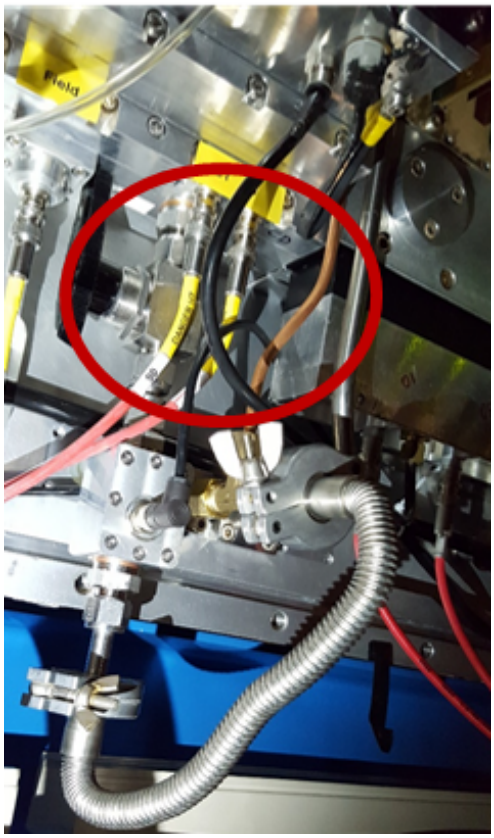

FIGURE 7.60: Presuure temperature sensors box in the gas input of a newly installed hybrid PD at COMPASS RICH1

Re-mounting of all the services was done immediately after the installation of the new PDs. The gas flow was the first service to be put in place as the PDs with CsI photo-cathodes cannot be left without flushing. During the gas pipes connection also the P-T sensors were mounted at the gas input and output of each chamber and then connected to a Raspberry-Pi embedded PC to read P-T values every 2s. The PC is connected to the COMPASS Detector Control System, which stores the data in the COMPASS database.

Colleagues from the different institutes responsible for the front-end electronics (INFN Torino and Freiburg University for the CMAD + Dreisam based electronics and the Technical University Munich with CEA Saclay, France for the APV-25 based electronics) mounted back the FEE with the corresponding LV systems.

For the MAPMT part of the new frames, the remounting operation was difficult but without surprises. After reconnecting the gas lines and the front-end electronics with their low voltage systems, the connection of the optical fibers to read the FEE was performed and tested. Eleven optical fibers within 144 fibers in total were found to be broken and new fibers were bought and replaced. The HV was connected back and validated too.

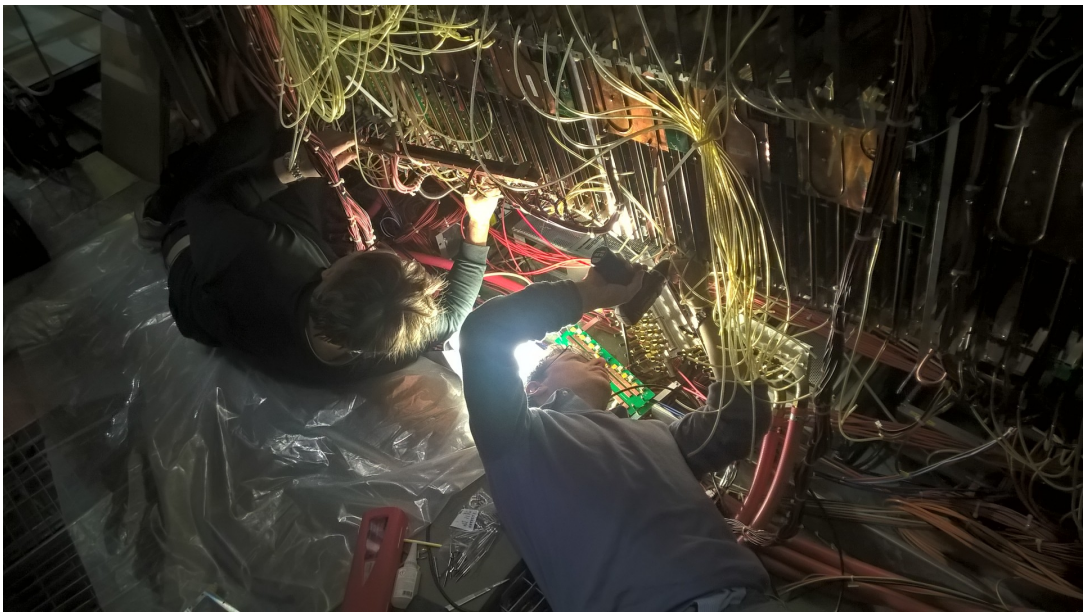

FIGURE 7.61: Colleagues performing difficult mounting operations

To mount the old APV-25 based electronics onto the new PDs, several small but delicate and unavoidable changes needed to be done on the systems responsible for holding, attaching cables LV distributions etc. A significant change in the grounding of the FEE was introduced. This work was really hard because of accessibility problems. In Fig.7.61 one can see that the re mounting of the LV distribution support for the new detectors needed some acrobatic skills.

The frontend electronics cooling system is based on water circulation in under pressure condition (400 mbar). Two independent PLC controlled circulation systems (for the top and the bottom detectors respectively) are present to provide the cooling. In Fig.7.62 the top view (left) and a side view of the bottom system (right) can be seen: a distilled water reservoir, hosting a heat exchanger cooled by CERN chilled water at 7 ^{0}C, is kept at 19 ^{0}C to avoid condensation of the air moisture on the FEE. A closed expansion vessel, placed above the height of the frontend, is kept at 400 mbar absolute pressure. The water circulates from the water reservoir to the FEE via 2 cm diameter pipes, distributors and 4 mm diameter plastic pipes, which are connected to 4 mm (2 mm inner) diameter Cu pipes braced to the heat exchanger Cu plates attached to all FEE cards. The hot water from the FEE cards is suck to the expansion vessel, from where it is transported back to the reservoir by a PLC controlled pump.

In 2016 a new system with increased cooling capacity was installed and fixed the previous problems of over heating during hot summer days.

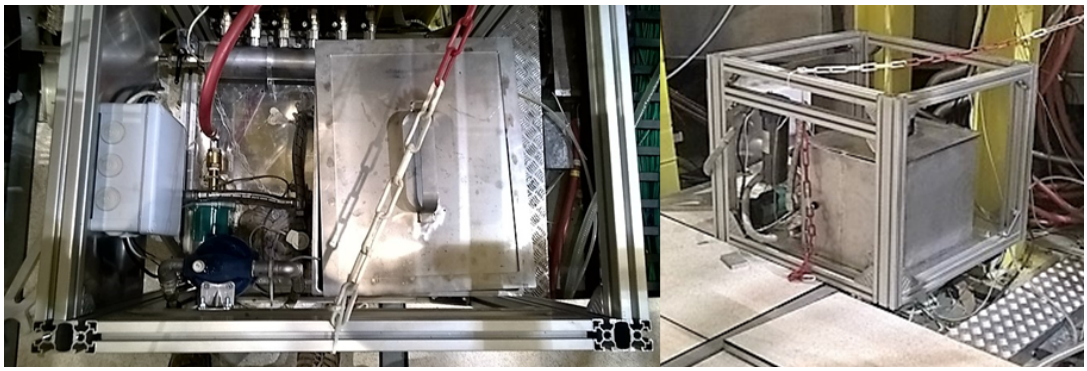

FIGURE 7.62: Left: Top view of the cooling system; Right: the cooling setup. Both the picture is for the bottom part

The control of the COMPASS RICH-1 hybrid PD HV system is a challenging task: If not grouped the total of 4 hybrid PDs have ~ 500 electrodes to be provided with high voltage. Each PD is segmented in four high voltage sectors. Each sector has 7 layers of electrodes (including the wire plains but excluding the mesh and the field shaping extra electrodes). Each Hv channel provides HV bias to the group of electrodes of a layer in a sector (6 THGEM segment electrodes for a sector).

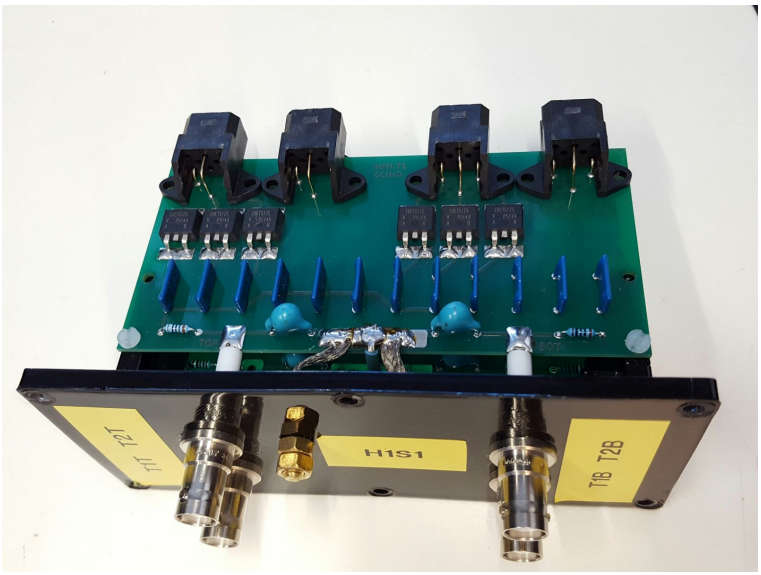

FIGURE 7.63

Special HV distribution PCBs were designed and equipped in our lab in Trieste (see Fig.7.63 and Fig.7.64).

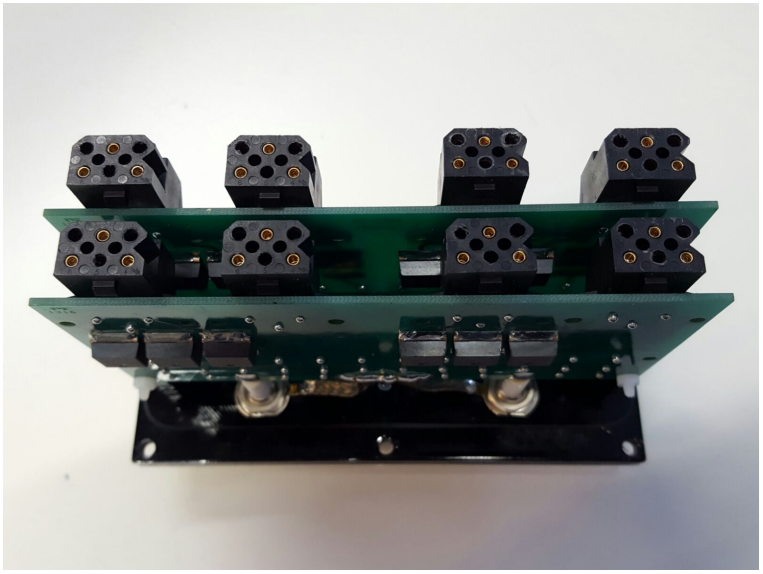

FIGURE 7.64

The HV distribution cards are providing HV to 6 electrodes from each HV inputs. They feed an entire sector: four inputs and 24 outputs. They include a filter (500 MΩ and 220 pF) against HV ripple propagation and 20ETS HV diodes to prevent cross-talk between THGEM electrodes.

Chapter 8

Results and Conclusion

8.1 Monitoring and Control of the High Voltage for the New PDs at CERN

As explained in Chapter-7 the control of the COMPASS RICH-1 hybrid PD HV system (108 HV channels) is a challenging task. For multistage detectors, not the individual voltages, but the relative biases are the main elements: therefore the control system has to handle all electrodes according to their correlations. Besides segmentation of electrodes, a single detector cell, called a **sector**, consists of three transfer and three amplification regions, and thus have six active electrodes (The MESH and the field wire plain are kept at ground potential). A hybrid PD consists of four **sectors**. The Hybrid High Voltage Control System (HVCS), developed by Gergő Hamar from INFN Treiste, uses two CAEN SY4527 series mainframes, eight CAEN HV modules A1561HDN -6 kV, 50 pA 12 channels power supplies and two CAEN HV module A7030DP, +3 kV, 12 channels power supplies. It controls four Hybrid PDs and can modify, control, monitor and log the HV values for all the electrodes. The software used for discharge study (described in section-6.1.2) is embedded in the HVCS and used to monitor, count and log the discharges in all the electrodes. Depending on the discharge rate it can reduce the biasing of an electrode to guarantee safe operating conditions.

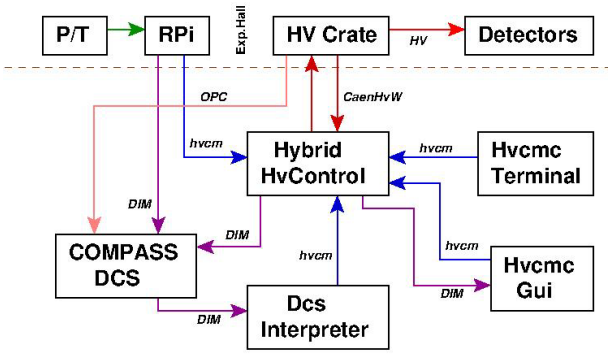

FIGURE 8.1: Scheme of the high voltage control system

It uses four Raspberry Pi embedded PCs to control and monitor 8 PT sensors to perform the automatic adjustment of the High Volatge to compensate the P-T variation. It is closely connected with the COMPASS Detector Control System (DCS). The scheme is shown in Fig.8.1 and a screen shot of the GUI can be seen in the Fig.8.2.

FIGURE 8.2: HVC GUI

In Fig.8.3 the discharge rates measured by the HVCS are plotted for two adjacent sectors for three days. A linear and low discharge rate/day is observed ($\sim$ 30 discharges/day/PD).

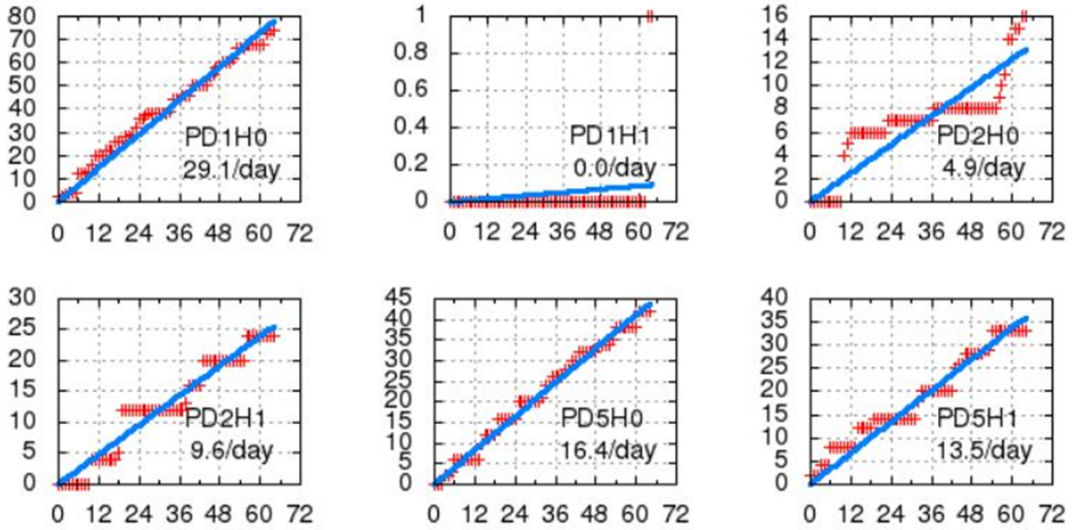

FIGURE 8.3: Discharges on each sector along time (X-Axis is presented in hours)

8.2 FrontEnd Electronics and Noise Analysis

8.2.1 APV25-S1 based front-end electronics

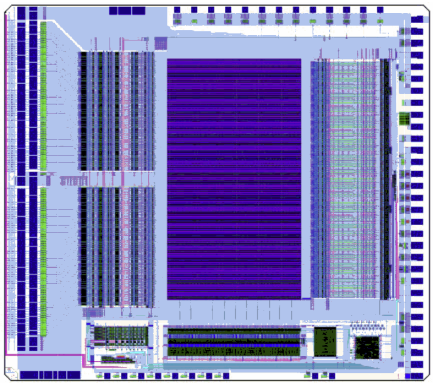

FIGURE 8.4: APV25-S1 chip Layout

The COMPASS RICH-1 hybrid readout is based on the APV25-S1 [151] Fig.8.4 which is an analogue pipeline ASIC developed for the read-out of silicon strip detectors in CMS. The APV25-S1 also contains many features including a programmable bias generator, an internal test pulse generation system, and a slow control communication interface. It was successfully adopted for the COMPASS RICH-1 MWPCs [154], GEM [155] and Silicon tracking detectors[156]. Each channel of the APV25 consists of a charge-sensitive preamplifier followed by an inverter stage with unit amplification to allow signals of both polarity to be processed, and a CR-RC type shaping amplifier. Its time constants are adjustable within a wide range from 50 to 350 ns by changing the bias of the analogue stages via feedback transistors, thus opening the possibility to use the APV25 to read "slow" detectors as MWPCs. The amplifier output amplitudes are sampled at a frequency of 40 MHz and stored in a 192 cell analogue pipeline. Upon arrival of an external trigger at the chip, the cells corresponding to the known trigger latency (up to 4 ms) are flagged for readout. The analogue levels of the flagged cells for 128 channels are then multiplexed at 20 or 40MHz onto a single differential output. In order to get information on the signal shape, and thus on the timing, not only the sample corresponding to the peak of the expected signal is transferred, but in addition two samples on the rising edge of the signal are read out, as shown in Fig.8.5. In our system, the time gap

between these individual samples sent out by the APV25 can be varied in steps of 25 ns from 25 ns to several hundreds of ns[1], depending on the shape of the input signal. For the COMPASS RICH-1 MWPCs, the optimum sampling gap is 150 ns, for MMs it is 75 ns and this value has been set for the Hybrid PDs too. Data were also collected using 150 ns sampling gap. The multiplexed analogue data stream from each APV25 chip is digitised by a 10 bit flash ADC. After digitization, individual pedestal values are subtracted from each channel and a possible shift common to all channels of one chip (mode noise) is corrected using one FPGA (Xilinx XCV400E) for 6 APV25 chips. This FPGA also performs zero suppression by sending out only channels with amplitudes higher than a programmable multiple of the respective individual noise figure. In this way, the data volume can be reduced to $\leq$5%.

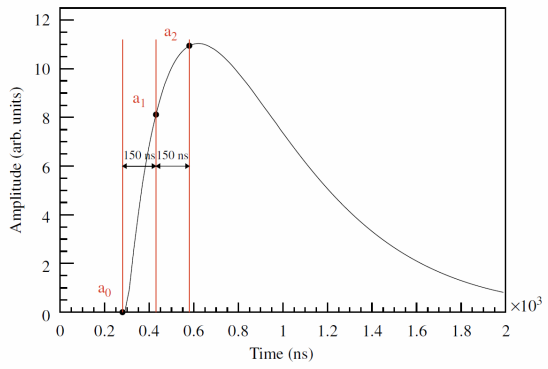

FIGURE 8.5: Principle of analogue signal sampling by the APV25 chip. The analogue signal on each pad is first preamplified and shaped by a CR-RC circuit with adjustable time constants, and then sampled at a frequency of 40 MHz. The charge measured in each sample is stored in an analogue pipeline while the external trigger is formed. The dots labelled a_0, a_1 and a_2 indicate the three samples which are read out from the APV25 pipeline per primary trigger.

The COMPASS RICH-1 readout system is described in detail in [154] and consists of a chain of four different types of printed circuit boards interconnected by cables or optical fibers (the schematic is shown in Fig.8.6). The front-end card was designed to match the size of the previously used GASSIPLEX board with dimensions of 580×150 mm^2 and nine Robinson Nugent connectors, each connecting 48 cathode pads to the front-end electronics. A total of 432 channels are fed into four APV25 chips on one front-end board, each chip reading 108 RICH pads. In order to guarantee stable operation of the chip with gas detectors, where large currents can be induced by occasional discharges, an external protection circuit is added between detector pads and chip input. It consists of a pair of inverted high-speed signal diodes (BAV99) connected to ground, and a coupling capacitor (220 pF) to avoid leakage currents into the chip. The APV25 chip is electrically connected via 25 mm Aluminum wire bonds. The required pitch of 44 mm for the signal inputs is achieved by a thin single-layer circuit on glass substrate, wire-bonded to the FR4 front-end motherboard and to the APV25.

[1]For this purpose the APV25 is not used in its so-called "multi mode", in which three samples with a fixed 25 ns time interval are transferred, but in the "peak mode". In this mode of operation, only one single sample is sent per trigger received by the APV25. Three samples at arbitrary time intervals can be read out by sending two additional artificially generated triggers at predefined time intervals in addition to the primary one.

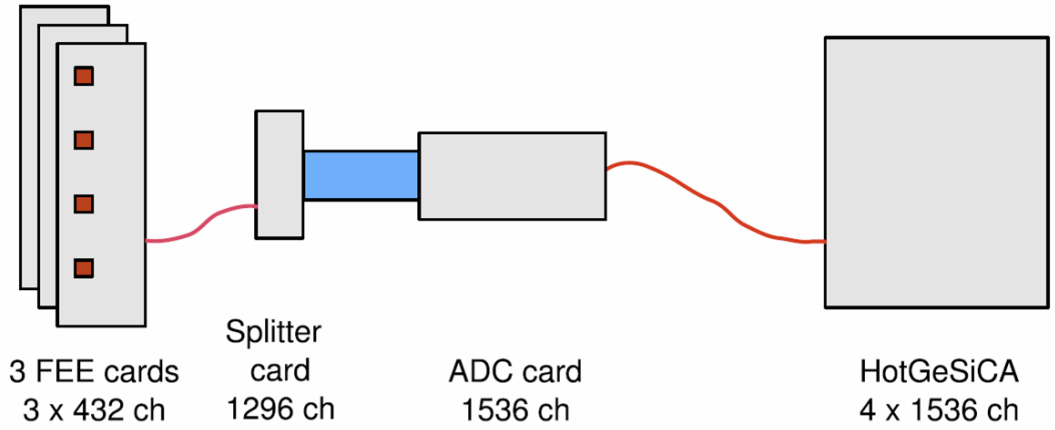

FIGURE 8.6: Schematics of the APV25 prototype readout chain for RICH-1.

The unused 20 channels of each chip are connected to ground via 6.8 pF capacitors, approximately matching the capacitance of connected channels. In this way the capacitive noise of all channels is of the same order of magnitude. This is necessary for the common mode noise correction algorithm to work properly, since it uses the median of all 128 input channels as reference. An adapter card (Splitter card in Fig.8.6) combines the differential analogue signals from three front-end cards into a single flat cable going to one ADC card, located $\sim$2 m further away.

The splitter card also splits the clock, trigger and I2C control signals from the ADC card to the front-end cards. Each ADC card hosts 12 pipelined ADC chips to sample the data stream from the APV25 chips. After digitization and zero suppression by two FPGAs, data are sent via optical fiber using the Hotlink protocol to a 6U VME module (HotGeSiCA in Fig. 3), which merges data from up to four ADC modules (48 APV25 chips) and sends them to the DAQ computers, again via optical fibers using the S-Link protocol.

The scheme of COMPASS RICH-1 PDs after the upgrade in 2016 is shown in Fig.8.7. The convention used in the scheme is:

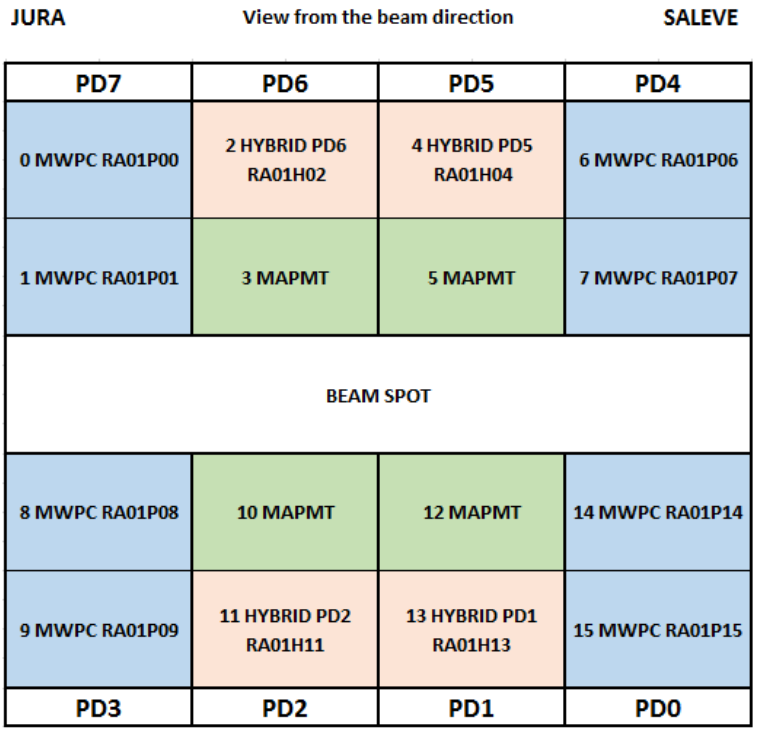

FIGURE 8.7: RICH layout from beam direction

- Sets of frames are called Photon Detectors (PDs) and they are numbered 0 - 7 as PD0 and so on.
- Detectors are called Photocathodes (P) for MWPCs and Hybrid (H) for new hybrid PDs. and they are numbered from 0 - 15 as RA01x00 and so on where x is either P or H.

After the upgrade in 2006 Detector 3, 5, 10 and 12 were replaced with MAPMTs and thus are out of the APV25-S1 based electronics mapping.

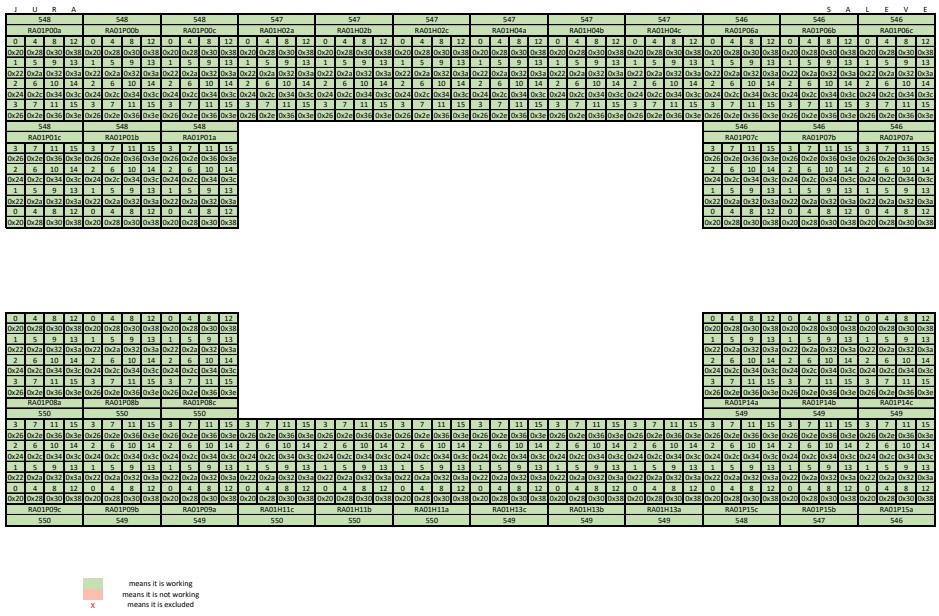

FIGURE 8.8: RICH APV Mapping

The mapping of the APV25-S1 based FEE is shown in Fig.8.8 where the a, b and c after the detector id stands for separating three splitter cards connected to the same chamber. The number in the top of each group (e.g. 547 in top of the group RA01H02c) shows the id of the HotGeSiCA the splitter card is connected to. The same convention is used for on-line monitoring and analysis of COMPASS data and also for data reconstruction and off-line analysis.

8.2.2 COMPASS On-line Analysis Softwares

In order to do an on-line monitoring and to perform basic analysis of the COMPASS data, a custom build software package, inside the CORAL (Chapter-2) framework, called COmpass Object Oriented On-line monitoring programme (COOOL) was developed. The main features of COOOL package are:

- It provides on-line as well as off-line access to the data.
- These data are decoded and processed, then they are shown typically as histograms and can be saved to a TTree structure for later processing using ROOT[2].
- All detectors are monitored, either they are tracking detectors or they are something else.
- COOOL is built on the top of the ROOT package, which supplies the framework for its graphical user interface (GUI) and data analysis.

[2]A modular scientific software framework. It provides all the functionalities needed to deal with big data processing, statistical analysis, visualization and storage. https://root.cern.ch/

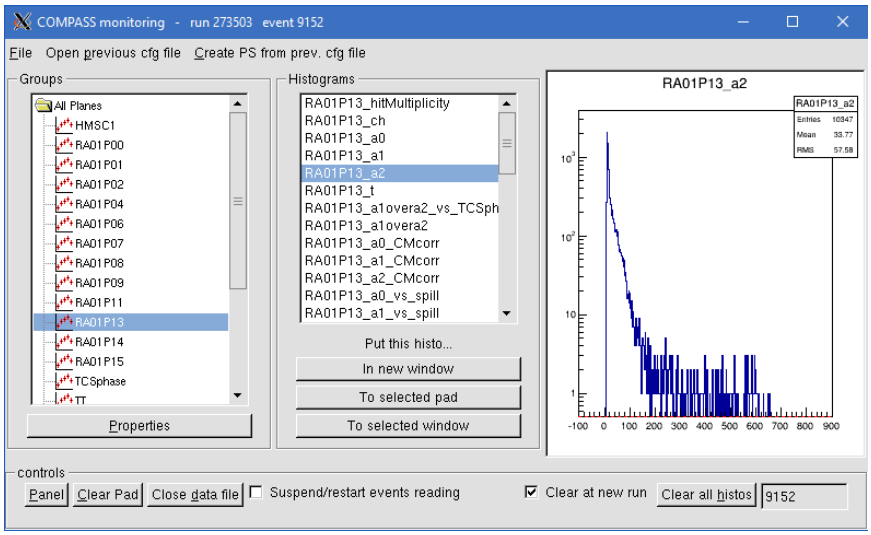

FIGURE 8.9: Screen shot of COOOL GUI for run 273503 showing the distribution of a_2 for the Detector RA01H13 (new Hybrid PD from PD1 in the scheme shown in Fig.8.7).

In Fig.8.9 a screen shot if the COOOL GUI can be seen where the detector RA01H13 (COOOL maintains the old names (P) for the Hybrid detectors in its GUI) has been selected and then its charge distribution histogram is selected in the middle panel, and plot on the right panel.

ROOT TTrees produced by running COOOL in batch mode (called BCOOOL) can be analyzed further for extracting interesting informations. The results shown in the next sections are mostly produced by BCOOOL analysis.

A specific online analysis tool called "GEM monitor"[3] is used for the analysis of the online data from APV on chip by chip basis. It runs in COMPASS or any other Scientific Linux based environment. This tool is also used for analyzing and producing pedestal files for FEE. A screen shot of the GUI of GEM monitor is shown in Fig.8.10.

To perform the commissioning and to analyze thoroughly all of the interesting online data from 2016 data taking period, it was convenient to run these tools (COOOL/ BCOOOL and GEM monitor) in the INFN Trieste computer farm, which has a COMPASS like environment. Installing these tools on the farm was non trivial as they require special libraries (with compatibility issues with the farm operating system) and a group of prerequisites (frameworks/environments) to be set up in the farm. I couldn't succeed without the remote help from Damien Neyret of CEA, Sacley, France.

[3]Originally developed for GEM detectors by our Munich colleagues

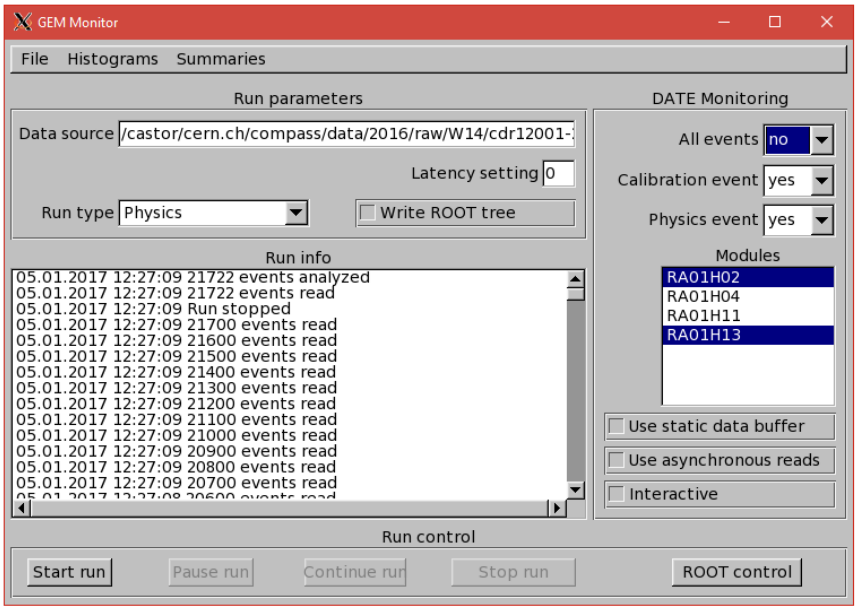

FIGURE 8.10: Screen shot of GEM monitor for a run showing the number of processed events for the selected Detectors in the right panel.

8.2.3 Noise analysis

For data taking, the correct pedestal information for each APV channel (mean and sigma of the pedestal) is essential. It is obtained by taking data with the ADC card set to "latch all" mode (turning off pedestal subtraction, common mode correction, thresholding and the zero suppression). The pedestal files (files containing the values of mean and sigma for all channels of AVP25-S1 chips) for each splitter card are produced by analyzing the "latch all" mode data using GEM monitor. To check the stability of the noise, several consecutive pedestal files were generated. The reproducibility was checked by correlating sets of values for the same splitter card. In Fig.8.11 the correlation between two consecutive runs for the splitter card RA01H11c, for the beginning of the run, is shown. The axes are expressed in ADC units corresponding to $\sim$150 equivalent electron. While the majority of the channels is providing similar values for the pedestals in the two sets, a systematic displacement of $\sim$10 ADC channels is present for an important number of channels (a minorty of channels shows an opposite displacement of about 20 channels).

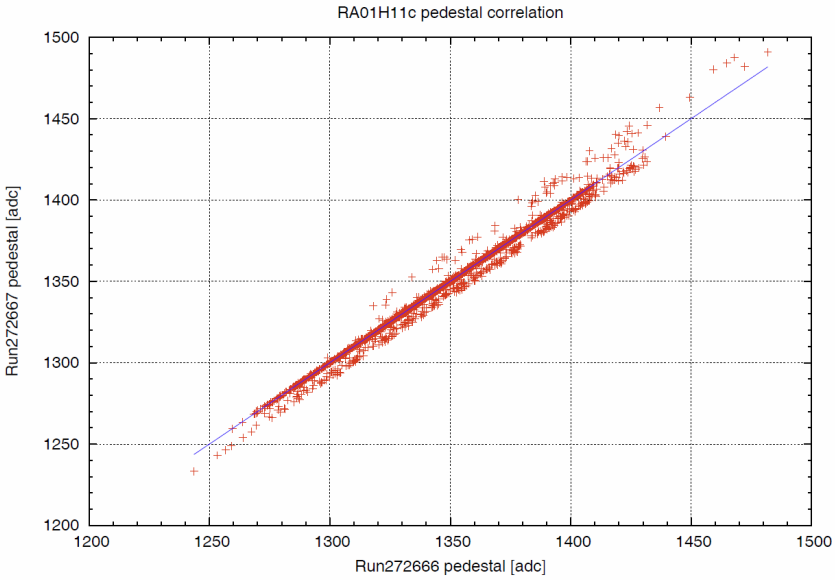

FIGURE 8.11: pedestal mean value correlation between two pedestal sets.

Analysis of the same data using COOOL/BCOOOL shows the random change of the noise is due to some of the HV sectors of the MESH only (Fig.8.12).

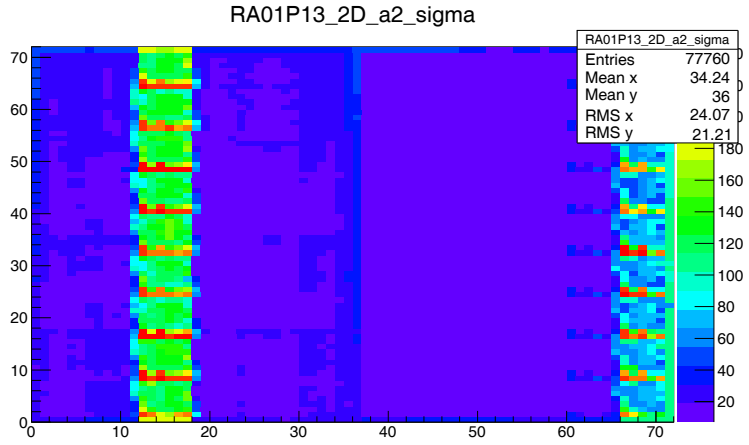

FIGURE 8.12: COOOL plot the for pedestal run 272666 showing the localizations of the noisy channels in two regions

A problem in the grounding connections of the two sectors was probably at the origin of this pathology. Excluding the large noise sectors, the problem was temporarily solved. In FIg.8.13 the correlation between mean value of the pedestals for two sets of data after the intervention is shown: a better reproducibility is achieved.

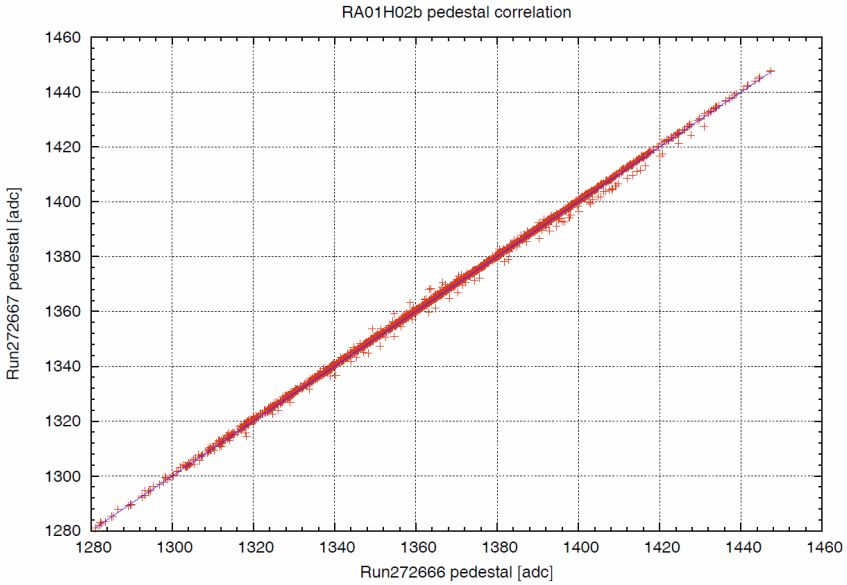

FIGURE 8.13: showing the plot of noise correlation as shown in Fig.8.11 after repairing the grounding

In Fig.8.14 the correlation between pedestal sigma values for two runs is presented. The noise figure for majority of the channels are reasonable, ranging between 5 and 10 ADC units, while the correlation is not good apart from the channels with the lowest noise figure.

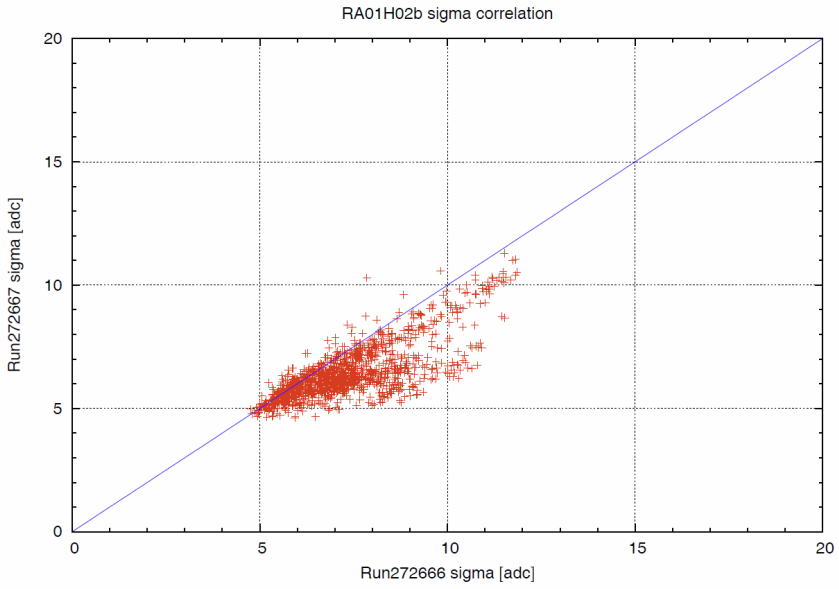

FIGURE 8.14: Correlation of pedestal sigma values for two runs.

8.3 Cherenkov Photon Signal

As it was previously described in Section-8.2.1, three amplitude samples are registered by the APV-25 S1 based FEE, 75 ns apart. These samples a_0, a_1 and a_2 are taken

before, during and after the rising edge of the signal

A latency scan was performed to find the optimal latency value using a pion beam to have larger hit rate in the new hybrid PDs. The latency was varied by one unit (25 ns) for each spill automatically by using a special firmware for the FPGA. The distribution of the a_2 amplitude for each spill was obtained using the analysis tool gemMonitor. In Fig.8.15 the distributions of a_2 amplitudes vs. spill number are shown. The scan was started with a latency value of 140 units and the firmware was decreasing this initial value by 1 unit for each spill: It was understood that the optimal latency for the chamber is around 122 units.

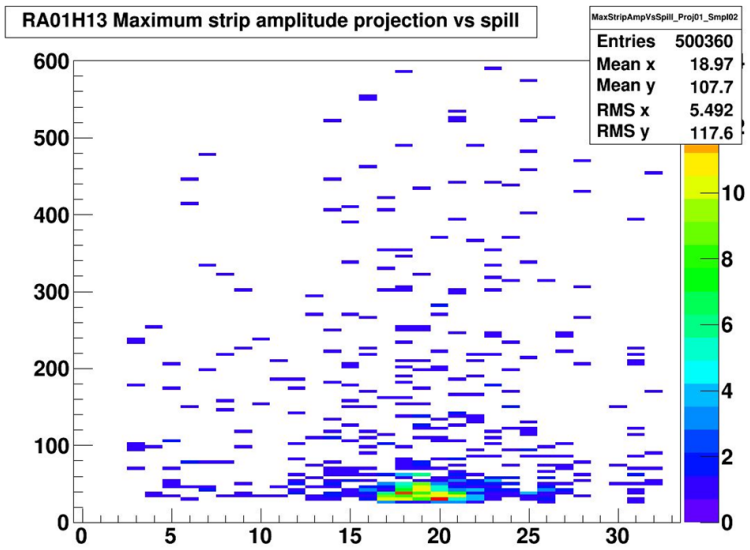

FIGURE 8.15: First Signal Seen at 2am from one of the Hybrid

An analysis using the BCOOOL tool and cuts to reject signals with raising edge not matching the required timing: $a_0 < 5$ to rejects those which raise too early and $a_1 > 5$, $a_2 > 13$ to select those which are perfectly in time. The number of accumulated hits with these cuts for each latency values for PD1 is shown in FIg.8.16. This exercise allowed to accurately determine the optimal latency to be imposed. A good signal to noise ratio for the peak at latency = 123 units can be seen.

All the results shown from now on are results of BCOOOL analysis performed mainly at farm TS computer facility.

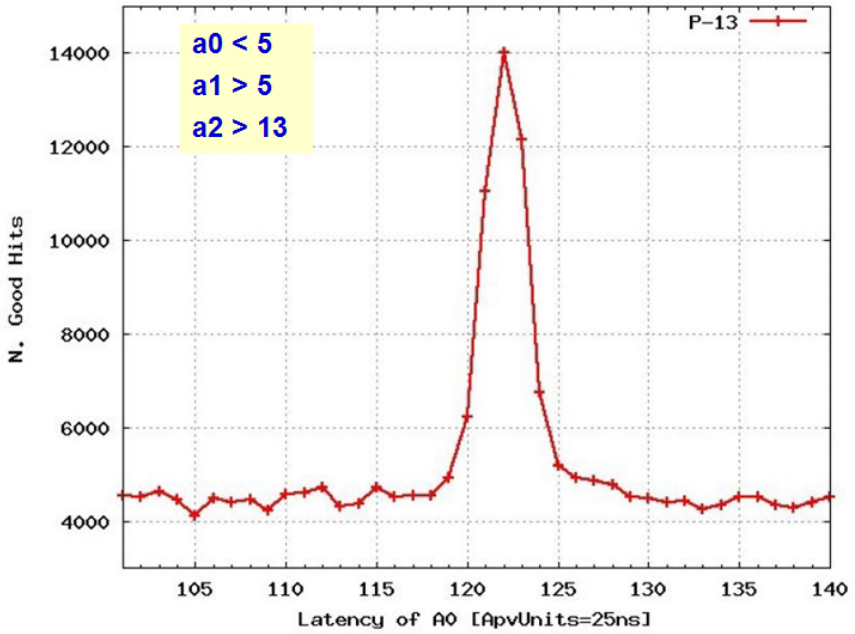

FIGURE 8.16: No. of good hits for different latency values.

The raw distribution of $\frac{a_1}{a_2}$ is shown in the Fig.8.17 with the latency = 123 units. The peak around 0.68 proves the fact that the latency values applied to the APV chips are the correct ones.

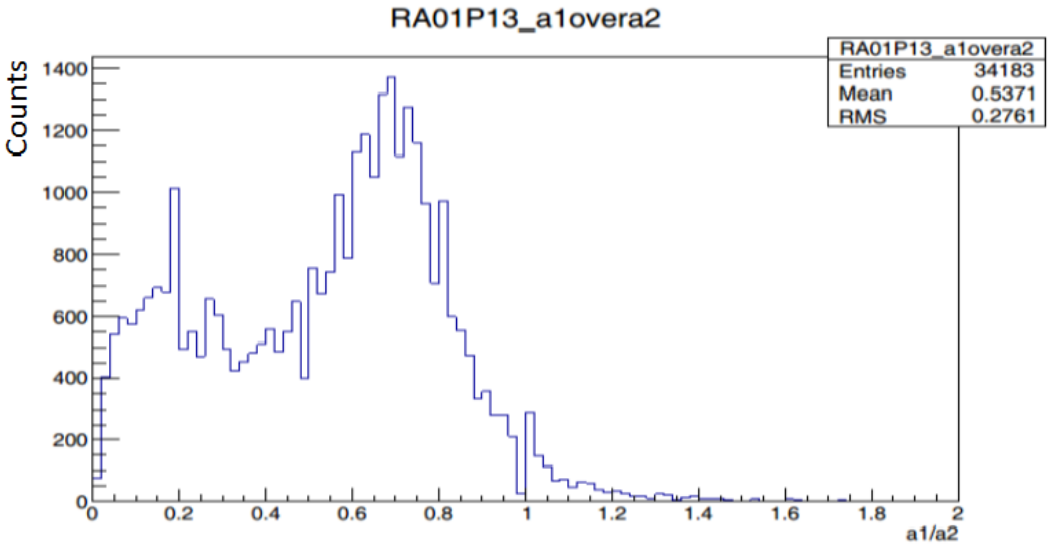

FIGURE 8.17: Distribution of Amplitude Ratios

In Fig.8.18 $\frac{a_0}{a_2}$ is plotted vs. $\frac{a_1}{a_2}$, . The specific shape of the plot called "banana plot" shows the correct accumulation of events.

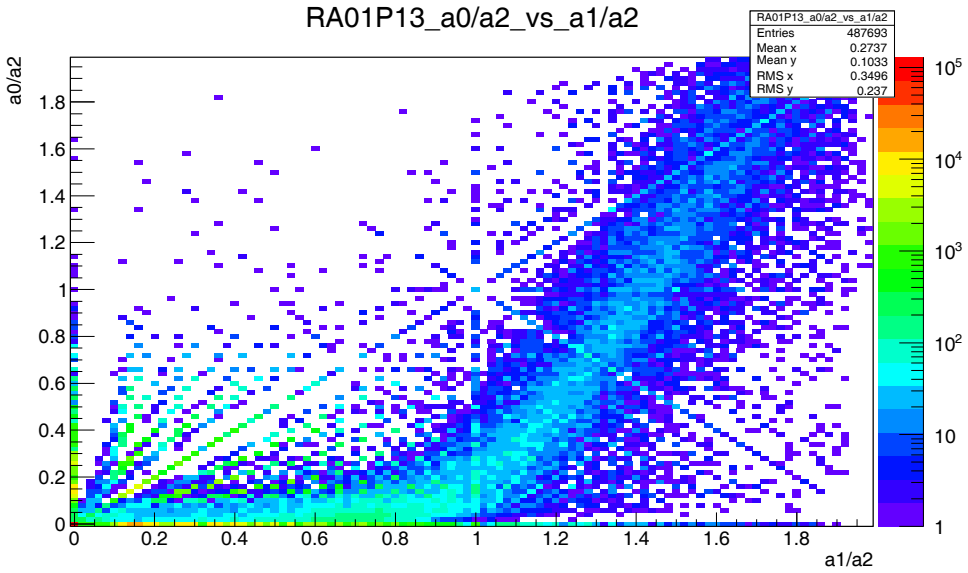

FIGURE 8.18: signal amplitude ratios

The TCSphase as shown in Fig.8.19 allows to fine tune the timing after finding the correct latency value.

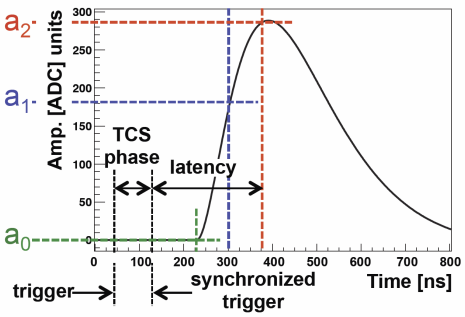

FIGURE 8.19: APV signal after amplification. The three samples a_0, a_1 and a_2 are taken off during the rising edge of the signal. The TCS phase is the duration between a physical trigger and the time of the next rising edge of the 38.88 MHz clock of the trigger control system. The latency is the duration between the rising edge of the TCS clock and a_2

The clusters are reconstructed with the amplitudes samples of every hits of all the channels of the detectors. The hits are regrouped by cluster and then the position of the cluster is calculated using a center of gravity method weighted with the a_2 amplitude. The main hit is the closest one to this center of gravity. The cluster time is reconstructed using the ratio a_1 over a_2 and the TCS phase Δt_{TCS} (duration between a physical trigger and the time between the next rising edge of the 38.88 MHz clock of the trigger control system) of the main hit of the cluster. The observation of $\frac{a_1}{a_2}$ as a function of Δt_{TCS} for all the main hits of an APV card shows the relation:

$$\frac{a_1}{a_2} = \alpha(\Delta t_{TCS}) + \beta \tag{8.1}$$

where α and β are free parameters of the time calibration for an APV card. These parameters were found using a gaussian fitting by slices. Once they are calculated, they are written in files for each APV cards and are communicated to COOOL/BCOOOL for the reconstruction of the tracks. The time of each hit can then be determined with:

$$t_{hit} = \frac{\frac{a_1}{a_2} - \beta}{\alpha} - \Delta t_{TCS} \tag{8.2}$$

Fig.8.20 shows the raw relation between $\frac{a_1}{a_2}$ with Δt_{TCS} (TCS phase). The slope of the signal band in case of hybrid PD (right) is larger than for the MWPC case (left) as expected from the different signal formation time for the two technologies.

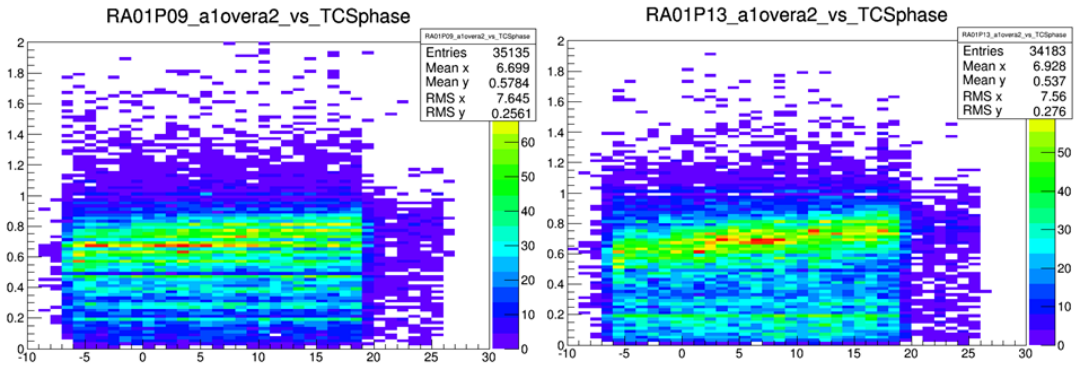

FIGURE 8.20: $\frac{a_1}{a_2}$ vs TCS phase: RA01P09 is a MWPC, RA01P13 is a Hybrid PD. The TCSphase axis unit is ns.

The a_2 amplitude distribution is presented in Fig.8.21a for a COMPASS run without beam using random triggers only and in Fig.8.21b for a run with beam taken immediately after the run with no beam, using the standard COMPASS physics trigger. The presence of signals from physics events is evident. A typical distribution of the a_2 amplitude for PD13 is shown in Fig.8.22. In the distribution three clear regions can be distinguished: the noise peak, a clear exponential region, and a less populated tail at higher value of amplitudes up to the APV saturations. The exponential part is clearly related to the detection of single electron initiated avalanches: this is what we expect from Cherenkov photoelectrons. Fitting the exponential part a gain of $\sim 8.4\times10^3$ was obtained (considering 300 e^- per ADC ch).

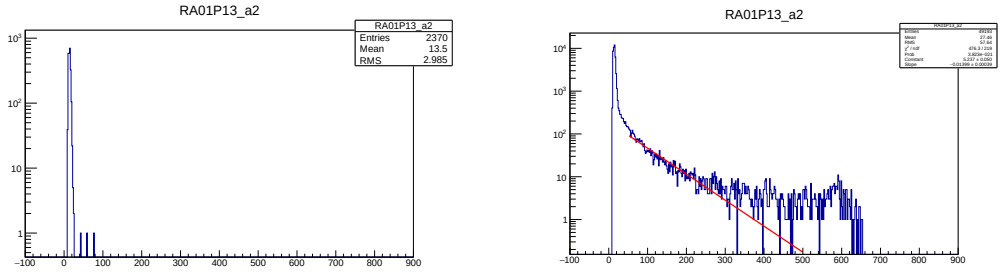

(A) (B)

FIGURE 8.21: A. amplitude a_2 spectrum from hybrid PD13 taken without beam (random trigger); B. aplitude a_2 spectrum from hybrid PD13 taken with beam (physics trigger).

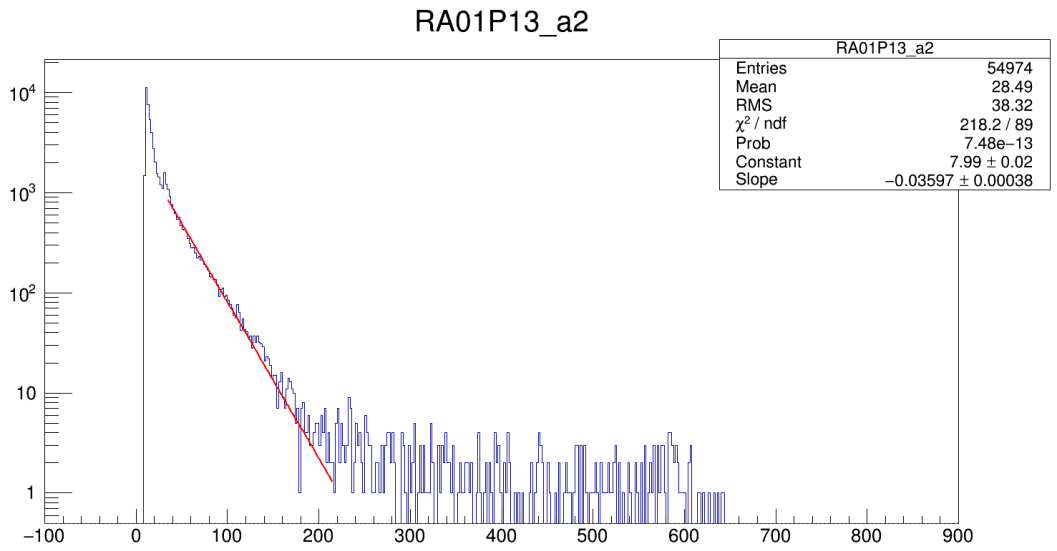

FIGURE 8.22: Typical SPectra with three parts. Noise, Single Photon Exponential and high amplitudes due to MIPs

To confirm the presence of the single photoelectrons effective gain scans were performed for different bias voltages for MM and THGEMs. In Fig.8.23 the exponential part of the a_2 distributions for different ΔV_{THGEM} (left) is shown: on the right similar distributions for different V_{MESH} are plotted. An increase in the effective gain with an increase in bias is observed. High voltage bias conditions providing effective gain values in the range between 1×10^4 to 4×10^4 were used for the data taking.

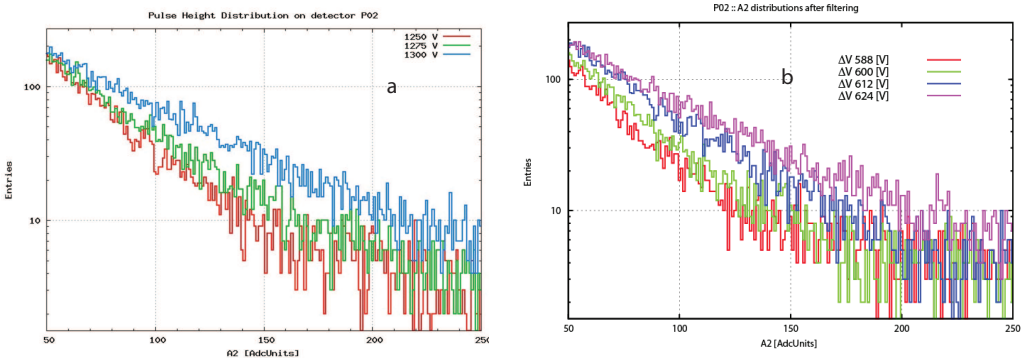

FIGURE 8.23: THGEM and MM gain scan with different biasing voltages.

A measurement of the accumulated good a_2 hits for each sectors for different E_{drift} values was performed. Fig.8.24 shows the No. of good (selected) a_2 hits as a function of E_{drift} for each sectors of all the PDs. A peak around +200 V.cm^{-1} of E_{drift} was observed: This result is in good agreement with the drift scan performed in the 2014 test beam at CERN (as described in Chapter-5).

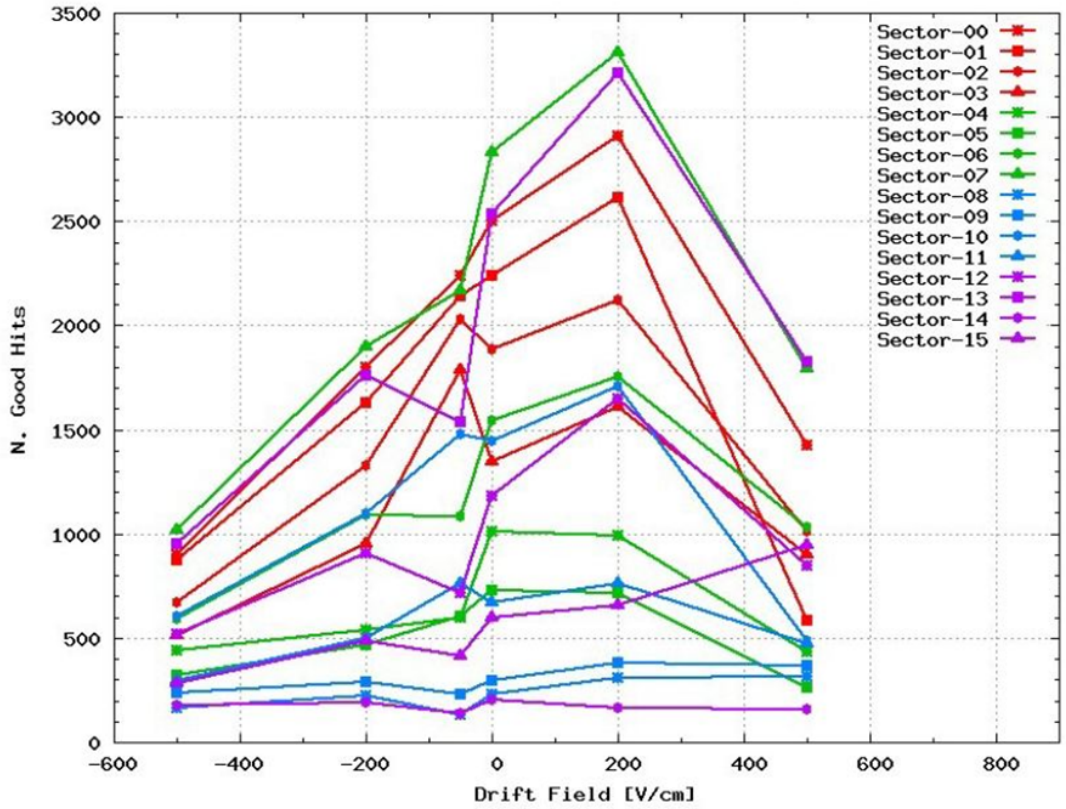

FIGURE 8.24: Scan of the integrated number of good hit for different E_{drift} values

To confirm this observation, two runs, one with +500 V.cm^{-1} of E_{drift} and the other with -200 V.cm^{-1} of E_{drift} were chosen from the drift scan exercise. In Fig.8.25 the distributions of good a_2 hits, for both of the E_{drift} conditions, are plotted in bins of ADC channels. A clear saturation of the a_2 amplitude can be seen for the case of +500 V.cm^{-1} of E_{drift} field (red curve) due to the collection of charged particle ionization. For the blue curve (-200 V.cm^{-1} of E_{drift} field value) a distribution without the saturation was observed. The same observation was made in the test beam at CERN, and is a clear indication of a good suppression of charged particle signals.

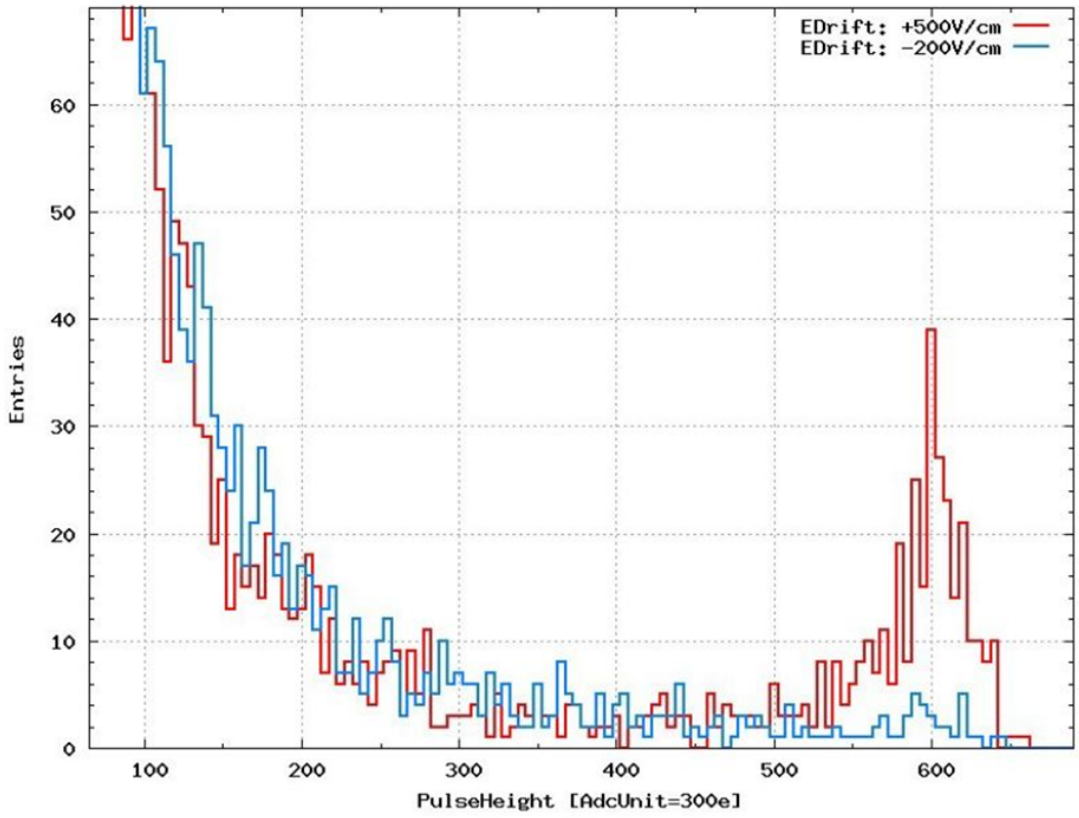

FIGURE 8.25: Study of the effect of the E_{drift} on ionizing particle collection.

To produce a complete characterization of the upgraded COMPASS RICH-1 (average number of photon per event, resolution, efficiencies etc.) the full offline analysis of the data is needed. The full data reconstruction and analysis are long, delicate, hard jobs: it generally takes several months to achieve preliminary results. To obtain a preliminary rough estimate of the number of Cherenkov photons in our hybrid PDs, we compared the number of accumulated good a_2 hits in the new Hybrid PDs with the same obtained from a MWPC based PD during a latency scan. In Fig.8.26 the result is shown for three different PDs (Two Hybrid PDs and one MWPC based PD). For the correct latency value, more good a_2 hits are observed for the new hybrid PDs ($\sim \times 2$) compared to the old MWPC based PD.

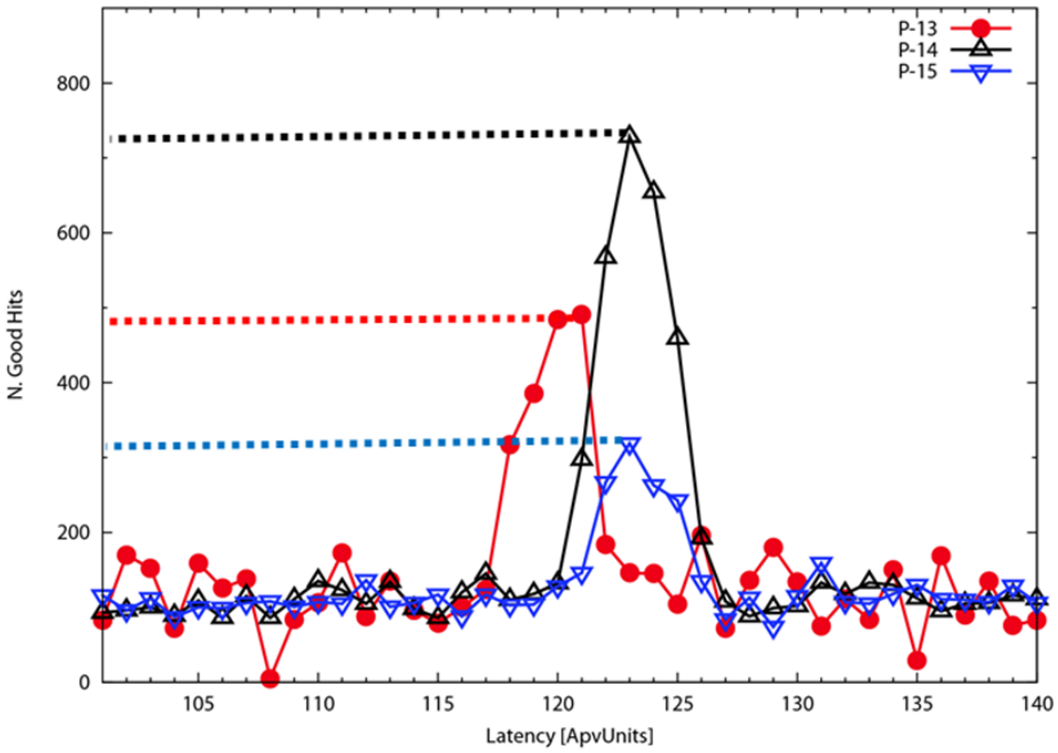

FIGURE 8.26: Latency scan result to estimate the relative hit rate between new Hybrid PDs and the old MWPC based PDs

Although being a very preliminary indication, this result is very promising. Reconstruction and analysis of 2016 COMPASS data are still ongoing and more interesting results will come soon.

8.4 Conclusions

The dedicated R&D program to develop an MPGD based detector of single photons for RICH applications has been finalized. The optimal choices for the photon detector to be used for the upgrade of COMPASS RICH-1 have been defined. The hybrid architecture combining double THGEMs and MicroMegas has been demonstrated to be the best option.

Several hybrid PD prototypes have been built and successfully tested providing validation of the hybrid architecture and of the parameters for the construction of the final PDs. Test beam validation demonstrated that the hybrid architecture is adequate for operation in the experimental environment.

The components for the final PDs have been built and validated by accurate quality control assessment. In particular a specific pre and post production treatment protocol has been developed and applied to assure good performance of the final THGEMs.

Bulk MMs built on PCBs with an innovative design based on the capacitive/resistive pad concept have been produced and used to build the final hybrid detectors. The

concept has been validated in our lab, in the beam test and in COMPASS experiment with the upgraded PDs.

Four hybrid PDs covering a total of 1.4 m^2 active single photon detection area have been built.

A complex and challenging assembly and installation of the new detectors with combined Hybrid PD and MAPMTs with Fused Silica lenses has been performed. It was an unique experience. Equipping and commissioning of the readout electronics was a long and delicate operation.

Almost 20k channels have a noise figure below 2000 equivalent e^-, obtained from the online analysis of the COMPASS data, after setting up a dedicated COMPASS like environment in the INFN Trieste computer farm, with custom COMPASS analysis tools.

All four new PDs have been operated during the entire 2016 COMPASS data taking period with a higher average effective gain with respect to the MWPC based PDs. 3 Sectors out of 16 needed to be operated with bias voltages lower than the nominal.

The first results obtained from the online analysis show that the new MPGD based PDs provide clear Cherenkov photon signals. A good suppression of the ionizing particles has been observed. A preliminary indication on the number of Cherenkov photons per event suggests an increase with respect to the previous MWPC based PDs.

The first MPGD based large area detectors of single photons operating in a physics experiment, open new perspective in this promising field.

8.5 Publications Signed by the Author Containing Results Presented in this Thesis

1. M. Alexeev, et. Al., Detection of Single Photon with HYBRID THGEM counter. (7 Pages Proceedings of Science (PhotoDet) 057 (2012))
2. M. Alexeev, et. Al., Ion Back Flow Reduction in a THGEM Based Detector; (2012) (7 Pages) IEEE Nuclear Science Symposium and Medical Imaging Conference Record (NSS/mic), 1165 (2012).
3. M. Alexeev, et. Al., Thick GEM-Based Detectors of Single Photons for Cherenkov Imaging Applications; (5 Pages) IEEE Nuclear Science Symposium and Medical Imaging Conference Record (NSS/mic), 763 (2012).
4. M. Alexeev, et. Al., THGEM-based photon detectors for the upgrade of COMPASS RICH-1; (5 Pages) Nuclear Instruments & Methods in Physics Research A 732, 264 (2013).
5. M. Alexeev, et. Al., Ion backflow in thick GEM-based detectors of single photons; (20 Pages) Journal of Instrumentation 8 (2013).
6. F. Tessarotto, et. Al., Development of Large Size Photon Detectors Based on THGEM and Hybrid MPGD Architectures; (8 Pages) IEEE Nuclear Science Symposium and Medical Imaging Conference (NSS/mic) (2013).

7. M. Alexeev, et. Al., MPGD-based counters of single photons developed for COMPASS RICH-1; (12 Pages) Journal of Instrumentation 9 (2014).
8. M. Alexeev, et. Al., Progresses in the production of large-size THGEM boards; (11 Pages) Journal of Instrumentation 9 (2014).
9. M. Alexeev, et. Al., Status and progress of the novel photon detectors based on THGEM and hybrid MPGD architectures; (5 Pages) Nuclear Instruments & Methods in Physics Research A 766, 133 (2014).
10. F. Tessarotto, et. Al., Long term experience and performance of COMPASS RICH-1; (17 Pages) Journal of Instrumentation 9 (2014).
11. P. Abbon et. Al., The COMPASS setup for physics with hadron beams; (47 Pages) Nuclear Instruments & Methods in Physics Research A 779, 69 (2015).
12. M. Alexeev, et. Al., The gain in Thick GEM multipliers and its time-evolution; (15 Pages) Journal of Instrumentation 10 (2015).
13. M. Alexeev, et. Al., Status of the development of large area photon detectors based on THGEMs and hybrid MPGD architectures for Cherenkov imaging applications; (4 Pages) Nuclear Instruments & Methods in Physics Research A 824, 139 (2016).
14. M. Alexeev et. Al., Status of COMPASS RICH – 1 upgrade with MPGD – based Photon Detectors. Submitted European Physics Journal Web of Conferences
15. Alexeev et. Al., The Development of MPGD based detectors of Single Photons Submitted European Physics Journal Web of Conferences
16. M. Alexeev et. Al., Investigation of the microstructure of Thick-GEMs with single photo electrons. Submitted European Physics Journal Web of Conferences

Bibliography

[1] David Bartlett et al. “Performance of the Cherenkov counters in the fermilab tagged photon spectrometer facility”. In: *Nuclear Instruments and Methods in Physics Research Section A: Accelerators, Spectrometers, Detectors and Associated Equipment* 260.1 (1987), pp. 55 –75. ISSN: 0168-9002. DOI: http://dx.doi.org/10.1016/0168-9002(87)90387-1. URL: //www.sciencedirect.com/science/article/pii/0168900287903871.

[2] P. Duteil et al. “Rev”. In: *Sci. Instrum.* 35 (1964), p. 1523.

[3] U Müller et al. “The recent performance of the Omega {RICH} detector in experiment {WA89} at {CERN}”. In: *Nuclear Instruments and Methods in Physics Research Section A: Accelerators, Spectrometers, Detectors and Associated Equipment* 371.1–2 (1996). Proceedings of the Second International Workshop on Ring Imaging Cherenkov Detectors, pp. 27 –32. ISSN: 0168-9002. DOI: http://dx.doi.org/10.1016/0168-9002(95)01137-4. URL: //www.sciencedirect.com/science/article/pii/0168900295011374.

[4] *DELPHI 82-1 CERN LPC 82-8 (1982), 31-1 (1982) and LPC-16 25/3/1982; DELPHI Technical proposal CERN-LPC 83-3, pp. 83-86 and DELPHI Progress Report, CERNLPC 84-16; W. Adam et al., Nucl. Instrum. Methods A, 371 (1996) 12.*

[5] *SLD Design Reports, SLAC 273 and 274 (1984); V. Ashford et al., IEEE Trans. Nucl. Sci. NS-33 (1986) 113; Abe K. et al., Nucl. Instrum. Methods A, 371 (1996) 8.*

[6] I Ariño et al. “The HERA-B ring imaging Cherenkov counter”. In: *Nuclear Instruments and Methods in Physics Research Section A: Accelerators, Spectrometers, Detectors and Associated Equipment* 516.2–3 (2004), pp. 445 –461. ISSN: 0168-9002. DOI: http://dx.doi.org/10.1016/j.nima.2003.08.173. URL: http://www.sciencedirect.com/science/article/pii/S0168900203024306.

[7] H.E. Jackson. “The {HERMES} dual-radiator {RICH} detector”. In: *Nuclear Instruments and Methods in Physics Research Section A: Accelerators, Spectrometers, Detectors and Associated Equipment* 502.1 (2003). Experimental Techniques of Cherenkov Light Imaging. Proceedings of the Fourth International Workshop on Ring Imaging Cherenkov Detectors, pp. 36 –40. ISSN: 0168-9002. DOI: http://dx.doi.org/10.1016/S0168-9002(02)02154-X. URL: http://www.sciencedirect.com/science/article/pii/S016890020202154X.

[8] “LHCb Reoptimized Detector Design and Performance, LHCb Collaboration, CERN/LHCC 2003-040, 2003; M. Adinolfi et al., Nucl. Instrum. Methods A 574 (2007) 39.” In: ().

[9] Alice Collaboration. “Technical Design Report of the High Momentum Particle Identification Detector, CERN/LHCC 98-19, ALICE TDR 1, 14 August 1998; ALICE collaboration, The ALICE high momentum particle identification system: An overview after the first Large Hadron Collider run, Nucl”. In: *Instrum. Meth. A* 639 (2011), p. 7.

[10] M. Artuso et al. In: *Methods in Physics Research A* 441 (2000), p. 374.

[11] I. Adam et al. “Nucl”. In: *Instr. Meth. A* 538 (2005), p. 281.

[12] A. Oed. “Nucl”. In: *Instr. and Meth. A* 263 (1988).

[13] Y. Giomataris et al. "MICROMEGAS: a high-granularity position-sensitive gaseous detector for high particle-flux environments". In: *Nuclear Instruments and Methods in Physics Research Section A: Accelerators, Spectrometers, Detectors and Associated Equipment* 376.1 (1996), pp. 29 –35. ISSN: 0168-9002. DOI: http://dx.doi.org/10.1016/0168-9002(96)00175-1. URL: http://www.sciencedirect.com/science/article/pii/0168900296001751.

[14] Nucl F. Sauli. "Instr. and Meth". In: *A* 531 (1997), p. 10.

[15] The Compass Collaboration and P. Abbon et al. "Nucl". In: *Instr. Meth. A* 577 (2007).

[16] M. Alfonsi et al. "Nucl". In: *Instr. and Meth. A* 535 (2004).

[17] M. G. Bagliesi et al. "Nucl". In: *Instr. and Meth. A* 617 (2010).

[18] N. Abgrall et al. "Nucl". In: *Instr. and Meth. A* 637 (2011).

[19] The Atlas Collaboration. "Technical Design Report for the New Small Wheel". In: *CERN-LHCC-* 20 (June 2013), pp. 2013–006.

[20] The Cms Collaboration. "CMS Technical Design Report for the muon endcap GEM upgrade". In: *CMS Technical Design RCERN-LHCC-* 13.30 (Sept. 2015), pp. 2015–012.

[21] The Alice Collaboration. "Technical Design Report for the Upgrade of the ALICE Time Projection Chamber". In: *Technical Design Report fCERN-LHCC-* 16.3 (Mar. 2014), pp. 2013–020.

[22] M. Krämer et al. "First results of the PixelGEM central tracking system of COMPASS, Nucl". In: *Sci. Conf. R* 197 (2009), p. 113.

[23] D. Neyret et al. "The COMPASS experiment gets its new hybrid GEM-Micromegas pixelized detectors to track high particle flux". In: *talk at MPGD* 2015 ().

[24] F. Hartjes et al. "Nucl". In: *Instrum.Meth. A* 706 (2013), p. 59.

[25] X. Llopart et al. "Nucl". In: *Instrum.Meth. A* 581 (2007), p. 485.

[26] "B. Dorney et al., R&D on a novel fast timing micro pattern gaseous detector (FTM), talk at MPGD2015." In: (). URL: https://agenda.infn.it/contributionDisplay.py?contribId=36&sessionId=2&confId=8839.

[27] *T. Papaevangelou et al., Fast Timing for High-Rate Environments with Micromegas, talk at MPGD2015.* URL: https://agenda.infn.it/contributionDisplay.py?contribId=83&sessionId=2&confId=8839.

[28] G. Bencivenni et al. "The micro-Resistive WELL detector: a compact spark-protected single amplification-stage MPGD". In: *Journal of Instrumentation* 10.02 (2015), P02008. URL: http://stacks.iop.org/1748-0221/10/i=02/a=P02008.

[29] *T. Geralis et al., Development of resistive Micromegas for sampling Calorimetry, talk at MPGD2015.* URL: https://agenda.infn.it/contributionDisplay.py?contribId=109&sessionId=2&confId=8839.

[30] *A. Teixeira et al., Micromegas Pad Resistive Read-Out with Embedded Protection Resistor Production, RD51 meeting, CERN, Switzerland, 9 December 2014.*

[31] *A. Mathis et al., Study of the dE/dx resolution of a GEM Readout Chamber prototype for the upgrade of the ALICE TPC, talk at MPGD 2015.* URL: https://agenda.infn.it/contributionDisplay.py?contribId=9&sessionId=2&confId=8839.

[32] *R. Majka et al., Combined Gas Electron Multipliers and Micromegas as Gain Elements in a High Rate Time Projection Chamber, talk at the 2015 IEEE Nuclear Science Symposium, San Diego, California, USA, 31 October - 7 November 2015.*

[33] *V. Bellini et al., JINST, vol. 7, p. C05013, 2012; E. Basile et al., Nucl. Instrum. Meth. A, vol. 718, p. 429, 2013.*

[34] B. Adeva et al. "DIRAC: A high resolution spectrometer for pionium detection". In: *Nuclear Instruments and Methods in Physics Research Section A: Accelerators, Spectrometers, Detectors and Associated Equipment* 515.3 (2003), pp. 467 –496. ISSN: 0168-9002. DOI: http://dx.doi.org/10.1016/j.nima.2003.08.114. URL: //www.sciencedirect.com/science/article/pii/S0168900203024082.

[35] *HERA-B INNER TRACKER collaboration, T. Hott et al., Nucl. Instrum. Meth. A, vol. 408, p. 258, 1998.*

[36] S. Aune et al. "Performance of the micromegas detector in the {CAST} experiment". In: *Nuclear Instruments and Methods in Physics Research Section A: Accelerators, Spectrometers, Detectors and Associated Equipment* 573.1–2 (2007). Proceedings of the 7th International Conference on Position-Sensitive DetectorsPSD-77th International Conference on Position-Sensitive Detectors, pp. 38 –40. ISSN: 0168-9002. DOI: http://dx.doi.org/10.1016/j.nima.2006.10.249. URL: //www.sciencedirect.com/science/article/pii/S0168900206021851.

[37] A. Balla et al. "Nucl". In: *Instrum. Meth. A* 628 (2011).

[38] *G. Cibinetto et al., "A Cylindrical GEM Detector with Analog Readout for the BESIII Experiment," in MPGD2015.* URL: https://agenda.infn.it/contributionDisplay.py?contribId=28&sessionId=2&confId=8839.

[39] S. Aune et al. "Nucl". In: *Instrum. Meth. A* 604 (2009).

[40] *M. Posik et al., "Barrel MicroMegas and Forward Triple-GEM," in EIC User's Meeting, Stony Brook, New York, USA, 2014.*

[41] *A. Vauth et al., "Studies on Gas Electron Multiplier (GEM) modules of a Large Prototype TPC for the ILC," in MPGD2015.* URL: https://agenda.infn.it/contributionDisplay.py?contribId=34&sessionId=8&confId=8839.

[42] *P. Colas et al., "Test of a new anode resi9stive coating for a MICROMEGAS TPC" in MPGD2015.* URL: https://agenda.infn.it/contributionDisplay.py?contribId=112&sessionId=8&confId=8839.

[43] *M. Cortesi et al., "Operation of a hybrid micropattern gaseous detector in low-pressure hydrogen, deuterium and helium , for active-target time projection chamber applications," in MPGD2015.* URL: https://agenda.infn.it/contributionDisplay.py?contribId=2&sessionId=2&confId=8839.

[44] *J. Ruz Armendariz et al., "The NIFFTE project," in MPGD2013, Zaragoza, Spain, 2014.*

[45] URL: https://www.ill.eu/instruments-support/instruments-groups/instruments/d20/description/instrument-layout/".

[46] B. Esposito et al. "Design of a GEM-based detector for the measurement of fast neutrons". In: *Nuclear Instruments and Methods in Physics Research Section A: Accelerators, Spectrometers, Detectors and Associated Equipment* 617.1–3 (2010). 11th Pisa Meeting on Advanced DetectorsProceedings of the 11th Pisa Meeting on Advanced Detectors, pp. 155 –157. ISSN: 0168-9002. DOI: http://dx.doi.org/10.1016/j.nima.2009.06.101. URL: //www.sciencedirect.com/science/article/pii/S0168900209013710.

[47] *G. Croci et al., "The BAND-GEM detector: An improved efficiency GEM-based solution for thermal neutrons detection at spallation sources," in MPGD2015.* URL: https://agenda.infn.it/contributionDisplay.py?contribId=3&sessionId=2&confId=8839.

[48] *S. Wu et al., "Recent R&D results on the double phase LAr LEM TPC," in MPGD2015.*

[49] *A. Sokolov et al., "Two-phase Cryogenic Avalanche Detector with electroluminescence gap and THGEM/GAPD-matrix multiplier," in MPGD2015.* URL: https://agenda.infn.it/contributionDisplay.py?contribId=18&sessionId=2&confId=8839.

[50] *E. Erdal et al., "Bubble-assisted Liquid Hole-Multipliers: bubble stability and electroluminescence in varying electrode configurations," in MPGD2015.* URL: https://agenda.infn.it/contributionDisplay.py?contribId=127&sessionId=2&confId=8839.

[51] *J. Galän et al., "Microbulk Micromegas for the search of DBD of 136Xe in the PandaX-III experiment," in MPGD2015.* URL: https://agenda.infn.it/contributionDisplay.py?contribId=42&sessionId=2&confId=8839.

[52] *T. Ikeda et al., "Study of Negative-Ion TPC using μ-PIC for Directional Dark Matter search," in MPGD2015.*

[53] *J. Garza, "Microbulk Micromegas as x-ray detectors for axion searches: CAST and developments for IAXO," in MPGD2015.* URL: https://agenda.infn.it/contributionDisplay.py?contribId=22&sessionId=2&confId=8839.

[54] S. Andreas et al. "Proposal for an Experiment to Search for Light Dark Matter at the SPS". In: *arXiV:* 1312 (), p. 3309.

[55] M. Raggi, M. Raggi V. Kozhuharov, and V. Kozhuharov. "Proposal to search for a dark photon in e+ on target cell, Advances in High Energy Physics, vol. 2014, p. ID 959802, 2014". In: ().

[56] *S. Bressler et al., "Recent progress with the RPWELL detector," in MPGD2015.* URL: https://agenda.infn.it/contributionDisplay.py?contribId=8&sessionId=2&confId=8839.

[57] *T. Fujiwara et al., "Development and application of scintillating Glass-GEM detector," in MPGD2015.* URL: https://agenda.infn.it/contributionDisplay.py?contribId=4&sessionId=2&confId=8839.

[58] *F. Murtas, in https://web2.infn.it/GEMINI/index.php/gempix-detector.*

[59] *A. Ochi et al., Nucl. Instrum. Meth. , vol. 471, p. 264, 2001; A. Ochi et al., JINST , vol. 9, p. C01039, 2013.*

[60] R. Baur et al. "The {CERES} {RICH} detector system". In: *Nuclear Instruments and Methods in Physics Research Section A: Accelerators, Spectrometers, Detectors and Associated Equipment* 343.1 (1994), pp. 87 –98. ISSN: 0168-9002. DOI: http://dx.doi.org/10.1016/0168-9002(94)90537-1. URL: http://www.sciencedirect.com/science/article/pii/0168900294905371.

[61] M. Adams et al. "π/K/p identification with a large-aperture ring-imaging cherenkov counter". In: *Nuclear Instruments and Methods in Physics Research* 217.1–2 (1983), pp. 237 –243. ISSN: 0167-5087. DOI: http://dx.doi.org/10.1016/0167-5087(83)90140-0. URL: http://www.sciencedirect.com/science/article/pii/0167508783901400.

[62] "The RD26 Collaboration, RD26 status reports:" in: *CERN/DRDC* 483 (), pp. 93–36.

[63] M. Spegel. "The impact of the {TIC} on the physics performance of {NA44}". In: *Nuclear Instruments and Methods in Physics Research Section A: Accelerators, Spectrometers, Detectors and Associated Equipment* 433.1–2 (1999), pp. 366 –371. ISSN: 0168-9002. DOI: http://dx.doi.org/10.1016/S0168-9002(99)00362-9. URL: http://www.sciencedirect.com/science/article/pii/S0168900299003629.

[64] J. Friese et al. "Enhanced quantum efficiency for CsI grown on a graphite-based substrate coating". In: *Nuclear Instruments and Methods in Physics Research Section A: Accelerators, Spectrometers, Detectors and Associated Equipment* 438.1 (1999), pp. 86 –93. ISSN: 0168-9002. DOI: http://dx.doi.org/10.1016/S0168-9002(99)00663-4. URL: http://www.sciencedirect.com/science/article/pii/S0168900299006634.

[65] H. Rabus et al. "Quantum efficiency of cesium iodide photocathodes in the 120–220 nm spectral range traceable to a primary detector standard". In: *Nuclear Instruments and Methods in Physics Research Section A: Accelerators, Spectrometers, Detectors and Associated Equipment* 438.1 (1999), pp. 94 –103. ISSN: 0168-9002. DOI: http://dx.doi.org/10.1016/S0168-9002(99)00665-8. URL: http://www.sciencedirect.com/science/article/pii/S0168900299006658.

[66] R. Gernhäuser et al. "Cesium iodide photon converter performance in a gaseous {RICH} detector". In: *Nuclear Instruments and Methods in Physics Research Section A: Accelerators, Spectrometers, Detectors and Associated Equipment* 438.1 (1999), pp. 104 –108. ISSN: 0168-9002. DOI: http://dx.doi.org/10.1016/S0168-9002(99)00666-X. URL: http://www.sciencedirect.com/science/article/pii/S016890029900666X.

[67] E. Albrecht et al. "Status and characterisation of {COMPASS} RICH-1". In: *Nuclear Instruments and Methods in Physics Research Section A: Accelerators, Spectrometers, Detectors and Associated Equipment* 553.1–2 (2005). Proceedings of the fifth International Workshop on Ring Imaging DetectorsFifth International Workshop on Ring Imaging Detectors, pp. 215 –219. ISSN: 0168-9002. DOI: http://dx.doi.org/10.1016/j.nima.2005.08.036. URL: //www.sciencedirect.com/science/article/pii/S0168900205016001.

[68] A. Braem et al. "Identification of high p particles with the STAR-RICH detector". In: *Nuclear Instruments and Methods in Physics Research Section A: Accelerators, Spectrometers, Detectors and Associated Equipment* 499.2–3 (2003). The Relativistic Heavy Ion Collider Project: {RHIC} and its Detectors, pp. 720 –724. ISSN: 0168-9002. DOI: http://dx.doi.org/10.1016/S0168-9002(02)01969-1. URL: http://www.sciencedirect.com/science/article/pii/S0168900202019691.

[69] F. Garibaldi et al. "A proximity focusing {RICH} detector for kaon physics at Jefferson lab hall A". In: *Nuclear Instruments and Methods in Physics Research Section A: Accelerators, Spectrometers, Detectors and Associated Equipment* 502.1 (2003). Experimental Techniques of Cherenkov Light Imaging. Proceedings of the Fourth International Workshop on Ring Imaging Cherenkov Detectors, pp. 117 –122. ISSN: 0168-9002. DOI: http://dx.doi.org/10.1016/S0168-9002(02)02166-6. URL: http://www.sciencedirect.com/science/article/pii/S0168900202021666.

[70] Antonio Di Mauro. "Recent CsI-RICH developments". In: *Nuclear Instruments and Methods in Physics Research Section A: Accelerators, Spectrometers, Detectors and Associated Equipment* 525.1–2 (2004). Proceedings of the International Conference on Imaging Techniques in Subatomic Physics, Astrophysics, Medicine, Biology and Industry, pp. 173 –177. ISSN: 0168-9002. DOI: http://dx.doi.org/10.1016/j.nima.2004.03.042. URL: http://www.sciencedirect.com/science/article/pii/S0168900204003845.

[71] H. Hoedlmoser et al. "Production technique and quality evaluation of CsI photocathodes for the ALICE/HMPID detector". In: *Nuclear Instruments and Methods in Physics Research Section A: Accelerators, Spectrometers, Detectors and*

Associated Equipment 566.2 (2006), pp. 338 –350. ISSN: 0168-9002. DOI: http://dx.doi.org/10.1016/j.nima.2006.07.047. URL: http://www.sciencedirect.com/science/article/pii/S016890020601312X.

[72] A. Breskin et al. "Field-dependent photoelectron extraction from CsI in different gases". In: *Nuclear Instruments and Methods in Physics Research Section A: Accelerators, Spectrometers, Detectors and Associated Equipment* 367.1–3 (1995). Proceedings of the 7th International Wire Chamber Conference, pp. 342 –346. ISSN: 0168-9002. DOI: http://dx.doi.org/10.1016/0168-9002(95)00639-7. URL: http://www.sciencedirect.com/science/article/pii/0168900295006397.

[73] A Di Mauro et al. "Photoelectron backscattering effects in photoemission from CsI into gas media". In: *Nuclear Instruments and Methods in Physics Research Section A: Accelerators, Spectrometers, Detectors and Associated Equipment* 371.1–2 (1996). Proceedings of the Second International Workshop on Ring Imaging Cherenkov Detectors, pp. 137 –142. ISSN: 0168-9002. DOI: http://dx.doi.org/10.1016/0168-9002(95)01146-3. URL: http://www.sciencedirect.com/science/article/pii/0168900295011463.

[74] M. Alexeev et al. "Micropattern gaseous photon detectors for Cherenkov imaging counters". In: *Nuclear Instruments and Methods in Physics Research Section A: Accelerators, Spectrometers, Detectors and Associated Equipment* 623.1 (2010). 1st International Conference on Technology and Instrumentation in Particle Physics, pp. 129 –131. ISSN: 0168-9002. DOI: http://dx.doi.org/10.1016/j.nima.2010.02.171. URL: http://www.sciencedirect.com/science/article/pii/S0168900210004389.

[75] C D R Azevedo et al. "Towards THGEM UV-photon detectors for RICH: on single-photon detection efficiency in Ne/CH 4 and Ne/CF 4". In: *Journal of Instrumentation* 5.01 (2010), P01002. URL: http://stacks.iop.org/1748-0221/5/i=01/a=P01002.

[76] J Escada et al. "A Monte Carlo study of photoelectron extraction efficiency from CsI photocathodes into Xe–CH 4 and Ne–CH 4 mixtures". In: *Journal of Physics D: Applied Physics* 43.6 (2010), p. 065502. URL: http://stacks.iop.org/0022-3727/43/i=6/a=065502.

[77] *E.Albrecht et al., Nucl. Instr. and Meth. A 502 (2003) 112; Nucl. Instr. and Meth. A 502 (2003) 236; Nucl. Instr. and Meth. A 502 (2003) 266; Nucl. Instr. and Meth. A 510 (2003) 262; Nucl. Instr. and Meth. A 518 (2004) 586; Nucl. Instr. and Meth. A 553 (2005) 53; Nucl. Instr. and Meth. A 553 (2005) 135; Nucl. Instr. and Meth. A 553 (2005) 215; Czech. J. Phys. 56, Suppl. F (2006) 307; Nucl. Instr. and Meth. A 567 (2006) 104; Czech. J. Phys. 56, Suppl. F (2006) 315; Czech. J. Phys. 56 Suppl. F (2006) 323; Nucl. Instr. and Meth. A 567 (2007) 114; Nucl. Instr. and Meth. A 572 (2007) 419; Nucl. Instr. and Meth. A 580 (2007) 906; Nucl. Instr. and Meth. A 581 (2007) 419; Nucl. Instr. and Meth. A 587 (2008) 371; Nucl. Instr. and Meth. A 595 (2008) 177; Nucl. Instr. and Meth. A 595 (2008) 194; Nucl. Instr. and Meth. A 595 (2008) 204; Nucl. Instr. and Meth. A 595 (2008) 233; Nucl. Instr. and Meth. A 616 (2010) 21; Nucl. Instr. and Meth. A 639 (2011) 15; Nucl. Instr. and Meth. A 639 (2011) 219; Nucl. Instr. and Meth. A 639 (2011) 271.*

[78] A. Braem et al. "Results from the ageing studies of large CsI photocathodes exposed to ionizing radiation in a gaseous RICH detector". In: *Nucl. Instrum. Meth. A* 553 (2005), p. 187.

[79] R. Chechik et al. "Progress in GEM-based gaseous photomultipliers". In: *Nuclear Instruments and Methods in Physics Research Section A: Accelerators, Spectrometers, Detectors and Associated Equipment* 502.1 (2003). Experimental Techniques of Cherenkov Light Imaging. Proceedings of the Fourth International Workshop on Ring Imaging Cherenkov Detectors, pp. 195 –199. ISSN: 0168-9002. DOI: http://dx.doi.org/10.1016/S0168-9002(03)00273-0. URL: http://www.sciencedirect.com/science/article/pii/S0168900203002730.

[80] D. Mörmann et al. "Operation principles and properties of the multi-GEM gaseous photomultiplier with reflective photocathode". In: *Nuclear Instruments and Methods in Physics Research Section A: Accelerators, Spectrometers, Detectors and Associated Equipment* 530.3 (2004), pp. 258 –274. ISSN: 0168-9002. DOI: http://dx.doi.org/10.1016/j.nima.2004.03.212. URL: http://www.sciencedirect.com/science/article/pii/S016890020401068X.

[81] D Mörmann et al. "A gas avalanche photomultiplier with a CsI-coated {GEM}". In: *Nuclear Instruments and Methods in Physics Research Section A: Accelerators, Spectrometers, Detectors and Associated Equipment* 478.1–2 (2002). Proceedings of the ninth Int.Conf. on Instrumentation, pp. 230 –234. ISSN: 0168-9002. DOI: http://dx.doi.org/10.1016/S0168-9002(01)01762-4. URL: http://www.sciencedirect.com/science/article/pii/S0168900201017624.

[82] W. Anderson et al. "Design, construction, operation and performance of a Hadron Blind Detector for the {PHENIX} experiment". In: *Nuclear Instruments and Methods in Physics Research Section A: Accelerators, Spectrometers, Detectors and Associated Equipment* 646.1 (2011), pp. 35 –58. ISSN: 0168-9002. DOI: http://dx.doi.org/10.1016/j.nima.2011.04.015. URL: http://www.sciencedirect.com/science/article/pii/S0168900211007534.

[83] *A. Bondar et al., Nucl. Instr. and Meth. A 496 (2003) 325; A. Breskin et al., Nucl. Instr. and Meth. A 478 (2002) 225.*

[84] *J.F.C.A. Veloso et al., Rev.Sc. Instr. 71 (2000) 2371; A.V. Lyashenko et al., JINST 2 (2007) P08004.*

[85] A. Lyashenko et al. "Efficient ion blocking in gaseous detectors and its application to gas-avalanche photomultipliers sensitive in the visible-light range". In: *Nuclear Instruments and Methods in Physics Research Section A: Accelerators, Spectrometers, Detectors and Associated Equipment* 598.1 (2009). Instrumentation for Collding Beam PhysicsProceedings of the 10th International Conference on Instrumentation for Colliding Beam Physics, pp. 116 –120. ISSN: 0168-9002. DOI: http://dx.doi.org/10.1016/j.nima.2008.08.063. URL: //www.sciencedirect.com/science/article/pii/S0168900208012060.

[86] M Alexeev et al. "Ion backflow in thick GEM-based detectors of single photons". In: *Journal of Instrumentation* 8.01 (2013), P01021. URL: http://stacks.iop.org/1748-0221/8/i=01/a=P01021.

[87] Gianluca Cavoto. "BaBar forward endcap {RPCs}". In: *Nuclear Instruments and Methods in Physics Research Section A: Accelerators, Spectrometers, Detectors and Associated Equipment* 533.1–2 (2004). Proceedings of the Seventh International Workshop on Resistive Plate Chambers and Related Detectors, pp. 46 –49. ISSN: 0168-9002. DOI: http://dx.doi.org/10.1016/j.nima.2004.06.127. URL: //www.sciencedirect.com/science/article/pii/S0168900204014007.

[88] Fuyuki Tokanai et al. "Newly developed gaseous photomultiplier". In: *Nuclear Instruments and Methods in Physics Research Section A: Accelerators, Spectrometers, Detectors and Associated Equipment* 766 (2014). {RICH2013} Proceedings of the Eighth International Workshop on Ring Imaging Cherenkov Detectors Shonan, Kanagawa, Japan, December 2-6, 2013, pp. 176 –179. ISSN: 0168-9002. DOI: http://dx.doi.org/10.1016/j.nima.2014.05.014. URL: //www.sciencedirect.com/science/article/pii/S0168900214005130.

[89] Fuyuki Tokanai et al. "Development of gaseous {PMT} with micropattern gas detector". In: *Nuclear Instruments and Methods in Physics Research Section A: Accelerators, Spectrometers, Detectors and Associated Equipment* 610.1 (2009). New Developments In Photodetection {NDIP08Proceedings} of the Fifth International Conference on New Developments in Photodetection, pp. 164 –168. ISSN: 0168-9002. DOI: http://dx.doi.org/10.1016/j.nima.2009.05.111. URL: //www.sciencedirect.com/science/article/pii/S0168900209010547.

[90] The Compass Collaboration. "Common Muon and Proton Apparatus for Structure and Spectroscopy". In: *CERN/SPSLC/* 297.1 (Mar. 1996), pp. 96–30.

[91] The Compass Collaboration. "COMPASS-II Proposal". In: *CERN/SPSC/* 340.17 (May 2010), pp. 2010–022.

[92] F. Gautheron. "The Newly Upgraded Large COMPASS Polarized Target". In: *AIP Conference Proceedings* 915.1 (2007), pp. 961–966. DOI: 10.1063/1.2750934. eprint: http://aip.scitation.org/doi/pdf/10.1063/1.2750934. URL: http://aip.scitation.org/doi/abs/10.1063/1.2750934.

[93] E. Bielert et al. "A 2.5 m long liquid hydrogen target for {COMPASS}". In: *Nuclear Instruments and Methods in Physics Research Section A: Accelerators, Spectrometers, Detectors and Associated Equipment* 746 (2014), pp. 20 –25. ISSN: 0168-9002. DOI: http://dx.doi.org/10.1016/j.nima.2014.01.067. URL: http://www.sciencedirect.com/science/article/pii/S0168900214001363.

[94] S. Scherrers. 2016.

[95] N. Makke. 2011.

[96] E. Albrecht et al. "{COMPASS} RICH-1". In: *Nuclear Instruments and Methods in Physics Research Section A: Accelerators, Spectrometers, Detectors and Associated Equipment* 502.1 (2003). Experimental Techniques of Cherenkov Light Imaging. Proceedings of the Fourth International Workshop on Ring Imaging Cherenkov Detectors, pp. 112 –116. ISSN: 0168-9002. DOI: http://dx.doi.org/10.1016/S0168-9002(02)02165-4. URL: http://www.sciencedirect.com/science/article/pii/S0168900202021654.

[97] E. Albrecht et al. "First performances of {COMPASS} RICH-1". In: *Nuclear Instruments and Methods in Physics Research Section A: Accelerators, Spectrometers, Detectors and Associated Equipment* 518.1–2 (2004). Frontier Detectors for Frontier Physics: Proceedin, pp. 586 –589. ISSN: 0168-9002. DOI: http://dx.doi.org/10.1016/j.nima.2003.11.092. URL: //www.sciencedirect.com/science/article/pii/S0168900203029590.

[98] P. Abbon et al. "The experience of building and operating {COMPASS} RICH-1". In: *Nuclear Instruments and Methods in Physics Research Section A: Accelerators, Spectrometers, Detectors and Associated Equipment* 639.1 (2011). Proceedings of the Seventh International Workshop on Ring Imaging Cherenkov Detectors, pp. 15 –19. ISSN: 0168-9002. DOI: http://dx.doi.org/10.1016/

j.nima.2010.10.102. URL: http://www.sciencedirect.com/science/article/pii/S0168900210023879.

[99] F Tessarotto et al. "Long term experience and performance of COMPASS RICH-1". In: *Journal of Instrumentation* 9.09 (2014), p. C09011. URL: http://stacks.iop.org/1748-0221/9/i=09/a=C09011.

[100] E. Albrecht. "et al". In: *The radiator gas and the gas system of COMPASS RICH-1* 502 (2003), p. 266.

[101] S. Dalla Torre. "et al". In: *A study of the RICH gas refractive index* 639 (2011), p. 271.

[102] E. Albrecht. "et al". In: *VUV absorbing vapours in n-perfluorocarbons* 510 (2003), p. 262.

[103] E. Albrecht. "et al". In: *The mirror system of COMPASS RICH-1* 502 (2003), p. 236.

[104] S. Costa. "et al". In: *CLAM, a continuous line alignment and monitoring method for RICH mirrors* 553 (2005), p. 135.

[105] E. Albrecht. "et al". In: *On-line mirror alignment monitoring method for COMPASS RICH-1* 595 (2008), p. 194.

[106] E. Albrecht. "et al". In: *Mirror alignment control for COMPASS RICH-1 detector* 639 (2011), p. 219.

[107] G. Baum. "et al". In: *The COMPASS RICH project* 433 (1999), p. 207.

[108] F. Piuz. "Ring Imaging CHerenkov systems based on gaseous photo-detectors: trends and limits around particle accelerators". In: *Nucl. Instrum. Meth. A* 502 (2003), p. 76.

[109] H. Hoedlmoser et al. "Long term performance and ageing of CsI photocathodes for the ALICE/HMPID detector". In: *Nucl. Instrum. Meth. A* 574 (2007), p. 28.

[110] G. Baum. "et al". In: *BORA: a front end board, with local intelligence, for the RICH detector of the Compass Collaboration* 433 (1999), p. 426.

[111] G. Baum. "et al". In: *The COMPASS RICH-1 read-out system* 502 (2003), p. 246.

[112] P. Abbon et al. "Fast readout of the COMPASS RICH CsI-MWPC photon chambers". In: *Nucl. Instr* 567 (2006), p. 104.

[113] M. J. French et al. "Design and results from the APV25, a deep sub-micron CMOS front-end chip for the CMS tracker". In: *Nucl. Instrum. Meth. A* 466 (2001), p. 359.

[114] M Alexeev et al. "Long term experience with CsI photocathodes in gas photon detectors". In: *Journal of Instrumentation* 9.01 (2014), P01006. URL: http://stacks.iop.org/1748-0221/9/i=01/a=P01006.

[115] P. Abbon et al. "Particle identification with {COMPASS} RICH-1". In: *Nuclear Instruments and Methods in Physics Research Section A: Accelerators, Spectrometers, Detectors and Associated Equipment* 631.1 (2011), pp. 26 –39. ISSN: 0168-9002. DOI: http://dx.doi.org/10.1016/j.nima.2010.11.106. URL: //www.sciencedirect.com/science/article/pii/S0168900210026422.

[116] P. Abbon et al. "Design and construction of the fast photon detection system for {COMPASS} RICH-1". In: *Nuclear Instruments and Methods in Physics Research Section A: Accelerators, Spectrometers, Detectors and Associated Equipment* 616.1 (2010), pp. 21 –37. ISSN: 0168-9002. DOI: http://dx.doi.org/10.1016/j.nima.2010.02.069. URL: //www.sciencedirect.com/science/article/pii/S0168900210002676.

[117] M. Alekseev et al. "Studies for a fast {RICH}". In: *Nuclear Instruments and Methods in Physics Research Section A: Accelerators, Spectrometers, Detectors and*

Associated Equipment 553.1–2 (2005). Proceedings of the fifth International Workshop on Ring Imaging DetectorsFifth International Workshop on Ring Imaging Detectors, pp. 53 –57. ISSN: 0168-9002. DOI: http://dx.doi.org/10.1016/j.nima.2005.08.006. URL: //www.sciencedirect.com/science/article/pii/S016890020501569X.

[118] P. Abbon et al. "Design and status of {COMPASS} FAST-RICH". In: *Nuclear Instruments and Methods in Physics Research Section A: Accelerators, Spectrometers, Detectors and Associated Equipment* 567.1 (2006). Proceedings of the 4th International Conference on New Developments in PhotodetectionBEAUNE 2005Fourth International Conference on New Developments in Photodetection, pp. 114 –117. ISSN: 0168-9002. DOI: http://dx.doi.org/10.1016/j.nima.2006.05.069. URL: //www.sciencedirect.com/science/article/pii/S016890020600876X.

[119] P. Abbon et al. "Fast photon detection for {COMPASS} RICH-1". In: *Nuclear Instruments and Methods in Physics Research Section A: Accelerators, Spectrometers, Detectors and Associated Equipment* 572.1 (2007). Frontier Detectors for Frontier PhysicsProceedings of the 10th Pisa Meeting on Advanced Detectors, pp. 419 –421. ISSN: 0168-9002. DOI: http://dx.doi.org/10.1016/j.nima.2006.10.220. URL: //www.sciencedirect.com/science/article/pii/S0168900206021450.

[120] P. Abbon et al. "Fast photon detection for particle identification with {COMPASS} RICH-1". In: *Nuclear Instruments and Methods in Physics Research Section A: Accelerators, Spectrometers, Detectors and Associated Equipment* 580.2 (2007). Imaging 2006Proceedings of the 3rd International Conference on Imaging Techniques in Subatomic Physics, Astrophysics, Medicine, Biology and Industry, pp. 906 –909. ISSN: 0168-9002. DOI: http://dx.doi.org/10.1016/j.nima.2007.06.081. URL: //www.sciencedirect.com/science/article/pii/S0168900207012879.

[121] P. Abbon et al. "The fast photon detection system of {COMPASS} RICH-1". In: *Nuclear Instruments and Methods in Physics Research Section A: Accelerators, Spectrometers, Detectors and Associated Equipment* 581.1–2 (2007). {VCI} 2007Proceedings of the 11th International Vienna Conference on Instrumentation, pp. 419 –422. ISSN: 0168-9002. DOI: http://dx.doi.org/10.1016/j.nima.2007.08.018. URL: //www.sciencedirect.com/science/article/pii/S0168900207016853.

[122] P. Abbon et al. "The characterisation of the multianode photomultiplier tubes for the RICH-1 upgrade project at {COMPASS}". In: *Nuclear Instruments and Methods in Physics Research Section A: Accelerators, Spectrometers, Detectors and Associated Equipment* 595.1 (2008). {RICH} 2007Proceedings of the Sixth International Workshop on Ring Imaging Cherenkov Detectors, pp. 177 –179. ISSN: 0168-9002. DOI: http://dx.doi.org/10.1016/j.nima.2008.07.074. URL: //www.sciencedirect.com/science/article/pii/S0168900208009698.

[123] P. Abbon et al. "Optical telescopes for COMPASS RICH-1 up-grade". In: *Czech. J Phys. Suppl. F 315* 56 (2006).

[124] P. Abbon et al. "Hartmann test of the COMPASS RICH-1 Optical telescopes". In: *Czech. J Phys. Suppl. F 323* 56 (2006).

[125] J. Hartmann. "Bemerkungen über den Bau und die Justirung von Spektrographen". In: *Z. Instrumentenkd.* 20 (1900), p. 47.

[126] L. J. Golden and Dynamic Hartmann test. "Appl". In: *Opt* 14 (1975), p. 2391.

[127] P. Abbon et al. "Read-out electronics for fast photon detection with {COMPASS} RICH-1". In: *Nuclear Instruments and Methods in Physics Research Section A: Accelerators, Spectrometers, Detectors and Associated Equipment* 587.2–3 (2008), pp. 371 –387. ISSN: 0168-9002. DOI: http://dx.doi.org/10.1016/j.nima.2007.12.026. URL: //www.sciencedirect.com/science/article/pii/S0168900207024576.

[128] P. Abbon et al. "The fast readout system for the {MAPMTs} of {COMPASS} RICH-1". In: *Nuclear Instruments and Methods in Physics Research Section A: Accelerators, Spectrometers, Detectors and Associated Equipment* 595.1 (2008). {RICH} 2007Proceedings of the Sixth International Workshop on Ring Imaging Cherenkov Detectors, pp. 204 –207. ISSN: 0168-9002. DOI: http://dx.doi.org/10.1016/j.nima.2008.07.063. URL: //www.sciencedirect.com/science/article/pii/S0168900208009777.

[129] M. Chiosso et al. "A fast binary front-end ASIC for the RICH detector of the COMPASS experiment at CERN". In: (Oct. 2008), pp. 1495–1500. ISSN: 1082-3654. DOI: 10.1109/NSSMIC.2008.4774697.

[130] F. Gonnella and M. Pegoraro. "CERN-LHCC-2001-034". In: *p.* 204 ().

[131] H. Fischer et al. "Implementation of the dead-time free {F1} {TDC} in the {COMPASS} detector readout". In: *Nuclear Instruments and Methods in Physics Research Section A: Accelerators, Spectrometers, Detectors and Associated Equipment* 461.1–3 (2001). 8th Pisa Meeting on Advanced Detectors, pp. 507 –510. ISSN: 0168-9002. DOI: http://dx.doi.org/10.1016/S0168-9002(00)01285-7. URL: //www.sciencedirect.com/science/article/pii/S0168900200012857.

[132] D.B. Ta et al. "Serial powering: Proof of principle demonstration of a scheme for the operation of a large pixel detector at the {LHC}". In: *Nuclear Instruments and Methods in Physics Research Section A: Accelerators, Spectrometers, Detectors and Associated Equipment* 557.2 (2006), pp. 445 –459. ISSN: 0168-9002. DOI: http://dx.doi.org/10.1016/j.nima.2005.11.115. URL: //www.sciencedirect.com/science/article/pii/S016890020502214X.

[133] P. Abbon et al. "Pattern recognition and {PID} for {COMPASS} RICH-1". In: *Nuclear Instruments and Methods in Physics Research Section A: Accelerators, Spectrometers, Detectors and Associated Equipment* 595.1 (2008). {RICH} 2007Proceedings of the Sixth International Workshop on Ring Imaging Cherenkov Detectors, pp. 233 –236. ISSN: 0168-9002. DOI: http://dx.doi.org/10.1016/j.nima.2008.07.015. URL: //www.sciencedirect.com/science/article/pii/S0168900208009844.

[134] T. Ypsilantis and J. Seguinot. "Theory of ring imaging Cherenkov counters". In: *Nuclear Instruments and Methods in Physics Research Section A: Accelerators, Spectrometers, Detectors and Associated Equipment* 343.1 (1994), pp. 30 –51. ISSN: 0168-9002. DOI: http://dx.doi.org/10.1016/0168-9002(94)90532-0. URL: //www.sciencedirect.com/science/article/pii/0168900294905320.

[135] P. Jeanneret. 2001.

[136] L. Periale et al. "Detection of the primary scintillation light from dense Ar, Kr and Xe with novel photosensitive gaseous detectors". In: *Nuclear Instruments and Methods in Physics Research A* 478.1-2 (Feb. 2002), pp. 377–383. URL: http://www.sciencedirect.com/science/article/pii/S016890020101779X.

[137] J. Ostling et al. "Study of hole-type gas multiplication structures for portal imaging and other high count rate applications". In: *IEEE Transactions on Nuclear Science* 50.4 (2003), pp. 809–819. URL: http://ieeexplore.ieee.org/document/1221880.

[138] P. S. Barbeau et al. "Toward coherent neutrino detection using low-background micropattern gas detectors". In: *IEEE Transactions on Nuclear Science* 50.5 (2003), pp. 1285–1289. ISSN: 0018-9499. DOI: 10.1109/TNS.2003.818237.

[139] R. Chechik et al. "Sealed GEM photomultiplier with a CsI photocathode: ion feedback and ageing". In: *Nuclear Instruments and Methods in Physics Research A* 478.1-2 (Feb. 2002), pp. 303–308. URL: http://www.sciencedirect.com/science/article/pii/S0168900201017521.

[140] C. Shalem et al. "Advances in Thick GEM-like gaseous electron multipliers—Part I: atmospheric pressure operation". In: *Nuclear Instruments and Methods in Physics Research Section A: Accelerators, Spectrometers, Detectors and Associated Equipment* 558.2 (2006), pp. 475 –489. ISSN: 0168-9002. DOI: http://dx.doi.org/10.1016/j.nima.2005.12.241. URL: http://www.sciencedirect.com/science/article/pii/S016890020502680X.

[141] C.K. Shalem et al. "Advances in thick GEM-like gaseous electron multipliers Part II: Low-pressure operation". In: *Nuclear Instruments and Methods in Physics Research Section A: Accelerators, Spectrometers, Detectors and Associated Equipment* 558.2 (2006), pp. 468 –474. ISSN: 0168-9002. DOI: http://dx.doi.org/10.1016/j.nima.2005.12.219. URL: http://www.sciencedirect.com/science/article/pii/S0168900205026793.

[142] M Cortesi et al. "THGEM operation in Ne and Ne/CH 4". In: *Journal of Instrumentation* 4.08 (2009), P08001. URL: http://stacks.iop.org/1748-0221/4/i=08/a=P08001.

[143] R Alon et al. "Time resolution of a Thick Gas Electron Multiplier (THGEM)-based detector". In: *Journal of Instrumentation* 3.11 (2008), P11001. URL: http://stacks.iop.org/1748-0221/3/i=11/a=P11001.

[144] A. Breskin et al. "A concise review on {THGEM} detectors". In: *Nuclear Instruments and Methods in Physics Research Section A: Accelerators, Spectrometers, Detectors and Associated Equipment* 598.1 (2009). Instrumentation for Collding Beam PhysicsProceedings of the 10th International Conference on Instrumentation for Colliding Beam Physics, pp. 107 –111. ISSN: 0168-9002. DOI: http://dx.doi.org/10.1016/j.nima.2008.08.062. URL: http://www.sciencedirect.com/science/article/pii/S0168900208012047.

[145] R Alon et al. "Time resolution of a Thick Gas Electron Multiplier (THGEM)-based detector". In: *Journal of Instrumentation* 3.11 (2008), P11001. URL: http://stacks.iop.org/1748-0221/3/i=11/a=P11001.

[146] E. Rocco. 2010.

[147] M. Alexeev et al. "The gain in Thick GEM multipliers and its time-evolution". In: *Journal of Instrumentation* 10.03 (2015), P03026. URL: http://stacks.iop.org/1748-0221/10/i=03/a=P03026.

[148] M Alexeev et al. "Development of THGEM-based photon detectors for Cherenkov Imaging Counters". In: *Journal of Instrumentation* 5.03 (2010), P03009. URL: http://stacks.iop.org/1748-0221/5/i=03/a=P03009.

[149] A. Bondar et al. "Study of ion feedback in multi-GEM structures". In: *Nuclear Instruments and Methods in Physics Research A* 496.2-3 (Jan. 2003), pp. 325–332. URL: http://www.sciencedirect.com/science/article/pii/S0168900202017631.

[150] D Mörmann et al. "Evaluation and reduction of ion back-flow in multi-GEM detectors". In: *Nuclear Instruments and Methods in Physics Research Section A: Accelerators, Spectrometers, Detectors and Associated Equipment* 516.2–3 (2004), pp. 315 –326. ISSN: 0168-9002. DOI: http://dx.doi.org/10.1016/j.nima.2003.08.156. URL: http://www.sciencedirect.com/science/article/pii/S016890020302504X.

[151] M.J. French et al. "Design and results from the APV25, a deep sub-micron {CMOS} front-end chip for the {CMS} tracker". In: *Nuclear Instruments and Methods in Physics Research Section A: Accelerators, Spectrometers, Detectors and Associated Equipment* 466.2 (2001). 4th Int. Symp. on Development and Application of Semiconductor Tracking Detectors, pp. 359 –365. ISSN: 0168-9002. DOI: http://dx.doi.org/10.1016/S0168-9002(01)00589-7. URL: http://www.sciencedirect.com/science/article/pii/S0168900201005897.

[152] M. Alexeev et al. "Progress towards a THGEM-based detector of single photons". In: *Nuclear Instruments and Methods in Physics Research Section A: Accelerators, Spectrometers, Detectors and Associated Equipment* 639.1 (2011). Proceedings of the Seventh International Workshop on Ring Imaging Cherenkov Detectors, pp. 130 –133. ISSN: 0168-9002. DOI: http://dx.doi.org/10.1016/j.nima.2010.10.117. URL: http://www.sciencedirect.com/science/article/pii/S0168900210024022.

[153] A. Braem et al. "Technology of photocathode production". In: *Nuclear Instruments and Methods in Physics Research Section A: Accelerators, Spectrometers, Detectors and Associated Equipment* 502.1 (2003). Experimental Techniques of Cherenkov Light Imaging. Proceedings of the Fourth International Workshop on Ring Imaging Cherenkov Detectors, pp. 205 –210. ISSN: 0168-9002. DOI: http://dx.doi.org/10.1016/S0168-9002(03)00275-4. URL: http://www.sciencedirect.com/science/article/pii/S0168900203002754.

[154] P. Abbon et al. "A new analogue sampling readout system for the {COMPASS} RICH-1 detector". In: *Nuclear Instruments and Methods in Physics Research Section A: Accelerators, Spectrometers, Detectors and Associated Equipment* 589.3 (2008), pp. 362 –369. ISSN: 0168-9002. DOI: http://dx.doi.org/10.1016/j.nima.2008.02.077. URL: http://www.sciencedirect.com/science/article/pii/S0168900208003148.

[155] B. Ketzer et al. "Performance of triple {GEM} tracking detectors in the {COMPASS} experiment". In: *Nuclear Instruments and Methods in Physics Research Section A: Accelerators, Spectrometers, Detectors and Associated Equipment* 535.1–2 (2004). Proceedings of the 10th International Vienna Conference on Instrumentation, pp. 314 –318. ISSN: 0168-9002. DOI: http://dx.doi.org/10.1016/j.nima.2004.07.146. URL: http://www.sciencedirect.com/science/article/pii/S0168900204016687.

[156] H. Angerer et al. "Present status of silicon detectors in Compass". In: *Nuclear Instruments and Methods in Physics Research Section A: Accelerators, Spectrometers, Detectors and Associated Equipment* 512.1–2 (2003). Proceedings of the 9th European Symposium on Semiconductor Detectors: New Developments on Radiation Detectors, pp. 229 –238. ISSN: 0168-9002. DOI: http://dx.doi.org/10.1016/S0168-9002(03)01898-9. URL: http://www.sciencedirect.com/science/article/pii/S0168900203018989.

[157] *The COMPASS Collaboration, CERN/SPSLC/96-14, SPSLC/P 297, March 1, 1996; CERN/SPSLC/96-30, SPSLC/P 297, May 20, 1996; CERN/SPSC/2010-014, SPSC-P-340, May 17, 2010; CERN/SPSC/2010-022, SPSC-M-772, September 3, 2010; Phys. Lett. B 612 (2005) 154; Phys. Rev. Lett. 94 (2005) 202002; Eur. Phys. J. C 41 (2005) 469; Phys. Lett. B 633 (2006) 25; Phys. Lett. B 647 (2007) 8; Phys. Lett. B 647 (2007) 330; Nucl. Phys. B 765 (2007) 31; Nucl. Instr. and Meth. A 577 (2007) 455; Eur. Phys. J. C 52 (2007) 255; Phys. Lett. B 660 (2008) 458; Phys. Lett. B 673 (2009) 127; Phys. Lett. B 676 (2009) 31; Phys. Lett. B 680 (2009) 217; Eur. Phys. J. C 64 (2009) 171; Phys. Rev. Lett. 104 (2010) 241803; Phys. Lett. B 690 (2010) 466; Phys. Lett. B 692 (2010) 240; Eur. Phys. J. C 70 (2010) 39; Phys. Lett. B 693 (2010) 227; Phys. Rev. Lett. 108 (2012) 192001; Phys. Lett. B 713 (2012) 10; Phys. Lett. B 717 (2012) 376; Phys. Lett. B 717 (2012) 383; Nucl. Phys. B 865 (2012) 1; Eur. Phys. J. C 72 (2012) 2253; Phys. Lett. B 718 (2013) 922.*

[158] M. Alexeev et al. "The quest for a third generation of gaseous photon detectors for Cherenkov imaging counters". In: *Nuclear Instruments and Methods in Physics Research Section A: Accelerators, Spectrometers, Detectors and Associated Equipment* 610.1 (2009). New Developments In Photodetection {NDIP08Proceedings} of the Fifth International Conference on New Developments in Photodetection, pp. 174 –177. ISSN: 0168-9002. DOI: http://dx.doi.org/10.1016/j.nima.2009.05.069. URL: http://www.sciencedirect.com/science/article/pii/S0168900209010560.

[159] M. Alexeev et al. "{THGEM} based photon detector for Cherenkov imaging applications". In: *Nuclear Instruments and Methods in Physics Research Section A: Accelerators, Spectrometers, Detectors and Associated Equipment* 617.1–3 (2010). 11th Pisa Meeting on Advanced DetectorsProceedings of the 11th Pisa Meeting on Advanced Detectors, pp. 396 –397. ISSN: 0168-9002. DOI: http://dx.doi.org/10.1016/j.nima.2009.08.087. URL: http://www.sciencedirect.com/science/article/pii/S0168900209017173.

[160] M. Alexeev et al. "Detection of single photons with THickGEM-based counters". In: *Nuclear Instruments and Methods in Physics Research Section A: Accelerators, Spectrometers, Detectors and Associated Equipment* 695 (2012). New Developments in Photodetection {NDIP11}, pp. 159 –162. ISSN: 0168-9002. DOI: http://dx.doi.org/10.1016/j.nima.2011.11.079. URL: http://www.sciencedirect.com/science/article/pii/S0168900211021498.

[161] F. Sauli. "GEM: A new concept for electron amplification in gas detectors". In: *Nuclear Instruments and Methods in Physics Research Section A: Accelerators, Spectrometers, Detectors and Associated Equipment* 386.2–3 (1997), pp. 531 –534. ISSN: 0168-9002. DOI: http://dx.doi.org/10.1016/S0168-9002(96)01172-2. URL: http://www.sciencedirect.com/science/article/pii/S0168900296011722.

[162] Y. Giomataris and G. Charpak. "A hadron-blind detector". In: *Nuclear Instruments and Methods in Physics Research Section A: Accelerators, Spectrometers, Detectors and Associated Equipment* 310.3 (1991), pp. 589 –595. ISSN: 0168-9002. DOI: http://dx.doi.org/10.1016/0168-9002(91)91104-4. URL: http://www.sciencedirect.com/science/article/pii/0168900291911044.

[163] L Periale et al. "Detection of the primary scintillation light from dense Ar, Kr and Xe with novel photosensitive gaseous detectors". In: *Nuclear Instruments and Methods in Physics Research Section A: Accelerators, Spectrometers, Detectors and Associated Equipment* 478.1–2 (2002). Proceedings of the ninth Int.Conf. on Instrumentation, pp. 377 –383. ISSN: 0168-9002. DOI: http://

dx.doi.org/10.1016/S0168-9002(01)01779-X. URL: http://www.sciencedirect.com/science/article/pii/S016890020101779X.

[164] R. Chechik et al. "Thick GEM-like hole multipliers: properties and possible applications". In: *Nuclear Instruments and Methods in Physics Research Section A: Accelerators, Spectrometers, Detectors and Associated Equipment* 535.1–2 (2004). Proceedings of the 10th International Vienna Conference on Instrumentation, pp. 303 –308. ISSN: 0168-9002. DOI: http://dx.doi.org/10.1016/j.nima.2004.07.138. URL: http://www.sciencedirect.com/science/article/pii/S0168900204016663.

[165] M. Alexeev et al. "THGEM-based photon detectors for the upgrade of {COMPASS} RICH-1". In: *Nuclear Instruments and Methods in Physics Research Section A: Accelerators, Spectrometers, Detectors and Associated Equipment* 732 (2013). Vienna Conference on Instrumentation 2013, pp. 264 –268. ISSN: 0168-9002. DOI: http://dx.doi.org/10.1016/j.nima.2013.08.020. URL: http://www.sciencedirect.com/science/article/pii/S0168900213011467.

[166] *M.Alexeev et al., Nucl. Instr. and Meth. A 610 (2009) 174; Nucl. Instr. and Meth. A 617 (2010) 396; Nucl. Instr. and Meth. A 623 (2010) 129; 2010 JINST 5 P03009; Nucl. Instr. and Meth. A 639 (2011) 130; 2012 JINST 7 C02014.*

[167]

[167] P.Jeanneret, Ph.D. Thesis, Neuchâtel University, 2001; L.Periale et al., Nucl. Instr. and Meth. A 478 (2002) 377; P.S.Barbeau, et al., IEEE Trans. Nucl. Sci. NS-50(4) (2003) 1285; R.Chechik et al., Nucl. Instr. and Meth. A 535 (2004) 303.

[168] Maxim Alexeev et al. "Development of THGEM-based photon detectors for Cherenkov Imaging Counters". In: *Journal of instrumentation* 5 (2010), p. 12.

[169] D. Mörmann et al. "GEM-based gaseous photomultipliers for UV and visible photon imaging". In: *Nuclear Instruments and Methods in Physics Research A* 504.1-3 (May 2003), pp. 93–98. URL: http://www.sciencedirect.com/science/article/pii/S0168900203007605.

[170] A. Breskin et al. "Sealed GEM photomultiplier with a CsI photocathode: ion feedback and ageing". In: *Nuclear Instruments and Methods in Physics Research A* 478.1-2 (Feb. 2002), pp. 225–229. URL: http://www.sciencedirect.com/science/article/pii/S0168900201017521.

[171] T.Schmidt. "PhD Thesis, A common readout driver for the COMPASS Experiment". 2001.

[172] A. Grenemaier. "Eine universelle Ausleseschnittstelle fur das COMPASS Experiment". 2002.

[173] B. Grube. "A trigger control system for COMPASS and a measurement of the Transverse Polarisation of L and X Hyperons from Quasi-Real Photo Production". 2006.